n

Firstbrook, David (2017) *Ultrasonically assisted penetration through granular materials for planetary exploration.* PhD thesis.

http://theses.gla.ac.uk/8256/

Available under License Creative Commons Attribution 4.0 International (CC BY-NC-ND 4.0):
https://creativecommons.org/licenses/by-nc-nd/4.0/

Glasgow Theses Service
http://theses.gla.ac.uk/
theses@gla.ac.uk

Ultrasonically Assisted Penetration through Granular Materials for Planetary Exploration

David Firstbrook

Submitted for the degree of

Doctor of Philosophy

From the University of Glasgow

University of Glasgow

School of Engineering

Glasgow, G12 8QQ

© David Firstbrook 2017

“I don’t like sand. It’s coarse and rough and irritating and it gets everywhere.”

- *Anakin Skywalker*

Abstract

Space exploration missions often use drills or penetrators to access the subsurface of planetary bodies. Protected by the conditions experienced at the surface, these regions have potentially been untouched for millennia. As such, the subsurface is a very attractive option for scientific goals, be it the search for extra-terrestrial life, to examine the history of the planet, or to utilise underground resources. However, many issues arise in such a task. Every other rocky body in our solar system possesses a surface gravity lower than our own, resulting in a lower available weight for a spacecraft to 'push' on a penetrating device. Add to this the low power availability and complications regarding remote operation, and this becomes a very difficult process to achieve. Mole devices which burrow through the ground whilst tethered to a surface-station to provide power and data have shown great promise in this regard. Using an internal mass to 'hammer' themselves into the ground, special care is required to ensure internal components are not damaged, and that they can arrive at their target depth in a reasonable period of time. There is continuous development in these types of drilling and penetrating technologies and anything that can penetrate with a lower weight-on-bit (WOB), and consume less power, could potentially be extremely useful for these situations.

High powered ultrasonic vibrations have been shown to reduce operational space and forces required in cutting bones for surgery. Additionally, they have been successful in reducing WOB requirements for drilling devices through rocky substrates. To maximise penetration depth, it is often favourable to progress though granular material rather than solid rock, however this also provides its own set of problems. This work looks at applying ultrasonic vibration to penetrating probes for use in granular material, with the aim of utilising it in low gravity or low mass scenarios.

Before this can be done however, the regolith used for testing must be fully characterised and consistent preparation methods established, ensuring that all other effects are accounted for. An ultrasonically tuned penetrator was designed and manufactured, and the effects it had on the surface of sand were investigated using a high-speed camera and

optical microscope. It was found that regions of sand immediately surrounding the penetrator were highly fluidised, localising any deformations to a small radial distance. Penetration tests were then conducted that showed ultrasonic vibration significantly reduces the penetration forces and therefore the overhead weight required, in some cases by over an order of magnitude. A similar effect was seen in power consumption, with some instances displaying a lowered total power draw of the whole system.

Experiments were then conducted in a large centrifuge to examine the trends with respect to gravity. Gravitational levels up to 10 g were tested, and the general trend showed that ultrasonic penetration efficiency indeed increased at lower gravities, suggesting that the force reduction properties would be enhanced at lower levels of g. Finally, the first steps to applying this technique as a fully-fledged penetration device were conducted. These tests oversaw combining ultrasonic vibration with the established hammering mechanism used by mole devices. Comparing this against a purely hammering penetration, it was found that the addition of ultrasonic improved performance significantly, greatly reducing the number of strikes required to reach the same penetration depth.

To conclude, the work presented in this thesis shows the potential that ultrasonic vibration can have with advancing low gravity/low mass penetrating devices. Reducing both the weight and power requirements can be a huge boon to small spacecraft, and the potential use as subsurface access or anchoring devices makes it an attractive avenue for future research and development.

Key words: Ultrasonic vibration, granular materials, penetration, subsurface exploration, force reduction, power optimisation, centrifuge testing, hammer-action penetration, moles.

Email: dfirstbrook@gmail.com

Acknowledgements

It is an amazing feeling to have this thesis completed in front of me, but it was only through the help and support of others that this could have been possible. I would first and foremost like to give my heartfelt thanks to my supervisor Dr. Patrick Harkness for allowing me the opportunity to work on this research, as well as always giving me the time for advice when I needed it. Additionally, I would like to thank Prof. Yang Gao for offering me guidance throughout my PhD, and for providing mentoring support whilst I was on placement with her at the Surrey Space Centre.

I would also like to acknowledge the Engineering and Physical Sciences Research Council (EPSRC, grant no. EP/K503058/1) for funding this project, as well as the ESA Education Office for the 'Spin Your Thesis' Campaign opportunity and funding. The University of Glasgow has been my home for the last four years, and I want to recognise the close friends and colleagues that I have made during my time here: Dan, Ryan, Kevin, Mat, Lee, and Michael. They made my days so much more enjoyable, whether they were spent lugging buckets of sand in the lab, or toiling away the wee hours writing in the office.

It was also important to realise that there was life outside of work, and I would like to give a special thanks to the University of Glasgow Squash Club for giving me an enormous welcome when I first arrived in this strange new city north of the wall. I almost certainly would not have finished had it not been for my adoptive squash family.

Outside of the University, I would like to thank Daniel, Karen, Alan, and Amy. You were always ready to lend an ear when things got tough, or to join in with celebrations when things went well. Finally, I can't imagine what my time would have been like without the support of my family, and the critical patience and proof-reading of my parents. You both really got me through this PhD, and nothing has been more valuable to me than your time and words of wisdom.

Contents

List of Figures

List of Tables

Symbols

Symbol	Unit	Definition
A	m	Amplitude of vibration
A_C	m^2	Cross-sectional area of the cone
A_S	m^2	Buried area of the sleeve of cone
B	m	Diameter of cone
c	N/m^2	Cohesion
c_u, c_{app}	N/m^2	Apparent cohesion
cc	cm^3	Cubic centimetres
D_0	m	Diameter of horn at origin
D_f	m	Final dimeter of horn
D_r	%	Relative density
e	-	Void ratio
e_{min}	-	Minimum void ratio
e_{max}	-	Maximum void ratio
f	Hz	Resonate frequency
F_a	N	Force of vibration due to acceleration
f_s	N/m^2	Sleeve friction
F_{shear}	N	Shearing force in DST
F_T	N	Total penetration resistance
g	$9.81\ m/s^2$	Earth gravity
Hz	1/s	Frequency
J	J	Energy
K_0	-	Coefficient of lateral pressure at rest
K_p	-	Passive coefficient of lateral stress
L	m	Lateral extension of slip lines
L	m	Length of DST box
ΔL	m	Lateral displacement of DST box
m	kg	Mass
n	-	Integer

N	N	Force
N_q	-	Bearing capacity factor
q_C	N/m^2	Cone resistance
S	m^2	Cross-sectional area of DST box
v	m/s^2	Velocity of wave in material
Z	m	Penetration depth
γ	N/m^3	Effective unit weight of sand
Γ	-	Relative acceleration
Γ_0	-	Critical relative acceleration for glassy state
Γ_1	-	Critical relative acceleration for fluidised state
ε	-	Shear strain
ϕ, φ	^{o}	Angle of internal friction
ρ	kg/m^3, g/cm^3	Bulk density of sand
ρ_{min}	kg/m^3, g/cm^3	Minimum density
ρ_{max}	kg/m^3, g/cm^3	Maximum density
σ_n	N/m^2	Normal stress on DST box
τ	N/m^2	Shear stress
τ_f	N/m^2	Maximum shear stress
τ_{cr}	N/m^2	Critical shear stress
ω	1/s	Angular frequency

Acronyms

ASLD	Apollo Lunar Surface Drill
ASTM	American Society for Testing Materials
BP	Block Paving sand simulant
Cc	Coefficient of curvature
CHIMRA	Collection and Handling for Interior Martian Rock Analysis
CNSA	China National Space Administration
CPT	Cone Penetration Test
Cu	Coefficient of uniformity
D_{10}	Diameter of grain at 10% passing
D_{30}	Diameter of grain at 30% passing
D_{60}	Diameter of grain at 60% passing
DAQ	Data Acquisition Device
DC	Direct Current
DRD	Dual Reciprocating Drill
DST	Direct Shear Test
EMA	Experimental Modal Analysis
ES-3	Engineering Soil simulant 3
ESA	European Space Agency
ESTEC	European Space research and TEchnology Centre
FEA	Finite Element Analysis
FRF	Frequency Response Function
HMI	Hydrargyrum Medium-arc Iodide
HP^3	Heat Flow and Physical Properties Package
IDDS	Inchworm Deep Drilling System
InSight	INterior exploration using Seismic Investigations, Geodesy and Heat Transport
ISAD	Icy Soil Acquisition Device
ISRU	In-Situ Resource Utilisation
ISS	International Space Station

JAXA	Japan Aerospace Exploration Agency
JPL	Jet Propulsion Laboratory
JSC Mars-1	Johnson Space Center Martian simulant 1
KSC	Kennedy Space Center
LDC	Large Diameter Centrifuge
LDV	Laser Doppler Vibrometer
MER	Mars Exploration Rovers
MIT	Massachusetts Institute of Technology
MMS	Mojave Mars Simulant
MRI	Magnetic Resonance Imaging
MUPUS	MUlti PUrpose Sensors for surface and subsurface science
NASA	National Aeronautics and Space Administration
NI	National Instruments
PAS	Polish Academy of Sciences
PLUTO	PLanetary Underground TOol
PZT	Lead Zirconate Titanate (Acronym of chemical formula $Pb[Zr_xTi_{1-x}]O_3$)
RTG	Radioisotope Thermoelectric Generator
SD2	Sample Drill and Distribution
SEIS	Seismic Experiment for Interior Structure
SMAA	Soil Mechanics Surface Sampler
SSAA	Surface Sampler Acquisition Assembly
SSC	Surrey Space Centre
SSC-1	Surry Space Centre Marian simulant 1
SSC-2	Surry Space Centre Marian simulant 2
SSC-3	Surry Space Centre Marian simulant 3
UPCD	Ultrasonic Planetary Core Drill
USDC	Ultrasonic/Sonic Driller/Corer
WOB	Weight On Bit

Chapter 1

Introduction

Throughout history, the great expanse of space has proved to be a long-held source of wonder and fascination for humanity. As naturally inquisitive beings, it is little wonder that we sought to find out more about what lies beyond our planet. At first it was simply by eye, but as technology progressed people had new ways to investigate the stars, with the invention of the telescope truly opening up the field of Astronomy. However, only relatively recently have we had the technology to physically travel to extra-terrestrial bodies.

The space race between the US and USSR was a period of unimaginable development in space exploration, from the first satellite Sputnik 1, to the first foot upon an extra-terrestrial surface in the Apollo 11 mission. Further developments allowed robotic landers that could even survive the harsh, acidic environment of Venus with the Venera missions, giving us our first glimpse at a planet other than our own. With the fall of the Soviet Union, more collaboration could occur between the two space powers at the time, USA and Russia, eventually seeing the construction of the largest ever artificial body in orbit around the Earth: The International Space Station (ISS). Scientific advancements have steadily progressed, with more and more countries joining the space faring community, such as Europe through ESA, Japan through JAXA, and China with CNSA.

Currently, one of the largest areas of research is the exploration of Mars. It is thought that Mars once had a very different climate, with flowing rivers and significant atmosphere and magnetic field. The view we have of the planet today is rather bleak, with a cold, dry, desolate surface. The reasons for this drastic change are still not fully understood, and a large number of missions have been launched to try and answer this question. Many past and current missions, such as the Mars Exploration Rovers (MER) and Curiosity, as well

as future missions, such as ExoMars and Mars 2020, aim to investigate the surface in an ever increasing amount of detail.

Exploration below the surface of extra-terrestrial bodies not only offers an exciting opportunity to better understand the geological history of the planetary body, but also extends the potential for scientific discovery. Shielded from the harsh realities of space, the sub-surface is a likely place in which to find material that has been left undisturbed since the creation of our solar-system, or the location of organic signatures or even life-forms that have stowed away aboard a rocky vessel for millennia. Accessing these depths in the far reaches of the solar system is a tricky endeavour in these harsh environments, and the constraints involved in these missions continually drive the development of new technology.

1.1 Aims and objectives

It is suspected that ultrasonic vibration will reduce the required overhead weight required for penetration, due to the use of ultrasonics in other force-reducing devices such as medical scalpels and ultrasonic machining. This work will set out to determine whether this force-reducing effect is present in the penetration of granular material, as well as any additional effects that might occur. As such, the aims can be summarised as:

1. Investigating the phenomena associated with ultrasonic vibration and the penetration of granular material.
2. Establishing the limits of this effect with respect to a variety of variables.
3. Provide operational information based on empirical results.
4. Develop systems that can utilise and exploit any benefits of ultrasonic vibration that are discovered.

To the best of the author’s knowledge this is the first investigation into this phenomenon and, as it could be beneficial to low-mass/low-gravity planetary exploration scenarios, a key objective will be to acquire this knowledge in the context of extra-terrestrial sub-surface burrowing. Providing useful design assistance to these burrowing devices is the ultimate impact sought from this research.

1.2 Structure of thesis

Chapter 2

The current state of extra-terrestrial sub-surface access, as well as an overview of the physics involved in granular material is presented. Additionally, the production and versatility of ultrasonic vibration is covered, describing the considerations that are needed when designing an ultrasonic device.

Chapter 3

When testing a penetrating device, the substrate used must be clearly and adequately defined. Here, descriptions of the defining characteristics of the different granular materials used in this work are given, as well as an in-depth look at the experimental techniques required to do so.

Chapter 4

The design of the ultrasonic probe is detailed here, including the experiments conducted in order to validate the performance of the probe.

Chapter 5

Using the newly manufactured probe, a microscopic look at the interactions of ultrasonic vibration and granular material are examined. This is a very qualitative chapter, however it is invaluable information with which to assay the results from future experiments.

Chapter 6

Here the first penetration experiment through granular material using an ultrasonically assisted penetrator is conducted. Using a continuous penetration rate, it examines the effect that ultrasonic vibration has on the penetration forces.

Chapter 7

Encouraged by the effects seen in the force experiments, these tests set out to expand it and examine the effects that ultrasonically assisted penetration has on the total power consumption of the system.

Chapter 8

As this work is motivated by space applications, it is scientifically prudent to conduct experiments at other levels of gravity. This chapter covers the redesign of the experiment and methodology so that tests can be conducted in various high gravity levels, through the use of a Large Diameter Centrifuge (LDC).

Chapter 9

All previous tests have been conducted with the aim of understanding the properties of ultrasonic vibration and penetration, investigating the underlying science and phenomena. This chapter lays out the first steps taken to apply this knowledge into an actual device to be used for sub-surface access. Working on similar principles to existing penetrating moles, ultrasonic vibration is combined with a hammer-action, and the improvements and limitations examined.

Chapter 10

To conclude, a summary of the main conclusions are provided, emphasising the main accomplishments and achievements of this work. A list of the publications resulting from this thesis is also provided.

Chapter 11

With the information gained from this research and looking ahead, some possible applications of ultrasonic vibration and penetration are discussed, as well as some potential avenues for future research.

COMMENTS ON TERMINOLOGY

NOTE: Whilst the term ‘soil’ might have a certain connotation on Earth (i.e., containing organic compounds, or to refer to the aptly named substrate ‘earth’), throughout this report it can used interchangeably with ‘regolith’, and ‘granular material’ as a description for any loose, heterogeneous unconsolidated rock-based media. There has been some attempt to make a distinction, by using ‘regolith’ to describe larger particles, however as of yet there has been no formal consensus on the matter, so for ease of reading this text will make no distinction. There is however a formal definition for the term ‘dust’, which refers to very fine particles smaller than 30 μm.

Chapter 2

Literature Review

This section will provide the necessary background information needed to investigate ultrasonic penetration through granular material. Firstly, an explanation is given as to why it is important to access the subsurface, and a summary of some of the methods conducted to do so. Space missions that have utilised the different methods of subsurface access will be covered, as well as some of the concepts in development now for future missions. An account of the mechanics involved in ultrasonic vibration will be given, as well as some of the experimental processes used in characterisation. Finally, a description of some of the physics involved in soil and sand will be covered, involving the various methodologies and associated phenomena.

2.1 Subsurface exploration

2.1.1 Motivation for subsurface

Broadly speaking, the exploration of a planetary body can be split roughly into five stages: Long distance (via telescopes), orbital (via satellite imaging), atmospheric (via entry vehicles), surface (via landers and rovers), and subsurface (via drills and penetrating probes). Each one affords a progressively closer examination of the planetary surface.

Accessing the subsurface allows examination at a micro-scale, and is perhaps the only solid evidence to indicate life on other planets. In fact, the reasons to access the subsurface are three-fold: geological, astrobiological, and for In Situ Resource Utilisation (ISRU).

Oceans and rivers on Earth are the cause of much of the erosion on the surface, but due to the absence of liquid water on Mars, the erosion rate is very low [1]. For this reason, even at relatively shallow depths, the geology of the terrain will be extremely old, allowing

us glimpses into the history of the planet. Accessing these depths is therefore a key component in establishing the history of Mars.

As for astrobiological incentives, the subsurface offers a region that is somewhat protected from the harsh UV and cosmic radiation that bombards the surface of Mars. Due to the lack of an appreciable atmosphere and magnetic field, the surface is left vulnerable to these forms of radiation, with a surface radiation level 100 times greater than on the surface of Earth, or the equivalent of a mammogram of radiation per day [2]. This radiation is blocked by the ground, reducing in intensity at depth, and it has been estimated that at 3 m depth the levels drop to equal the surface radiation levels of Earth [2].

A promising area of biology for organisms that can survive these sort of intense environments is the study of ‘extremophiles’ [3], such as Tardigrades [4] or the micro-organism *Deinococcus Radiodurans* [5]. *D. Radiodurans* especially are known to be able to withstand enormous doses of radiation, 3,000-6,000 times the lethal dose for humans [5]. Whilst they possess the ability to survive high acute doses, it is theorised that even these radio-resistant organisms would be completely eradicated from the surface of Mars over a time scale of a few million years. However, the radiation reduces to survivable levels at 1 m depth [2]. Accessing these depths therefore could prove crucial for the discovery of extra-terrestrial life.

Finally, it is generally agreed upon that the technicalities of bringing enough fuel for a return flight would make human exploration of Mars extremely difficult. Instead, significant research has been done to establish whether it would be possible to re-fuel at the surface of Mars. By harvesting the solid ice-water that is known to exist at the Martian poles, it could be possible to produce via electrolysis two of the main components of rocket fuel; Hydrogen and Oxygen [6]. This also extends to using available resources for other requirements such as power and habitat shielding [7], and can also be considered for other planetary bodies such as the Moon [8] or the mining of asteroids [9].

2.1.2 Terrestrial heritage

2.1.2.1 Classic Drilling

Classical drilling relies on two separate processes. Firstly, the substrate must be broken in some manner, and secondly, the resultant cuttings must be removed. Without both processes working in tandem, drilling progress will come to a halt. There are a variety of ways in which these steps can be achieved. For substrate breaking, the most common method is by mechanical action, physically taking the rock past its shear, tensile, or compressive strength and thus inducing a failure in the material. There are also drills that use heat, lasers, or chemicals to achieve this material failure, however these can contaminate or modify the sample beyond the point of scientific value.

Mechanical action can be split further into ‘percussive’ and ‘rotary’, and to a lesser extent ‘rotary percussive’. Rotary drilling is the form that most of us are accustomed to, as it is used in most common electric drills. It breaks the material by shear failure at the bit-substrate interface. A particular advantage that rotary drilling has is that the rotational motion can also support augering to enable removal of the resulting cuttings, with cuttings removal often taking place simultaneously using a spiral flute to bring them to the surface.

Percussive drilling works by hammering the substrate and causing fractures and cracks to form within the material (often propagating far past the point of impact). This ultimately causes fragmentation, breaking off into small pieces which can then be evacuated. The most basic way to achieve this is to physically remove the drill and evacuate the cuttings manually. This is extremely time consuming, but it is also cheap and is thus often used in areas of low technology. The hammering mechanism can also be accompanied by rotational action, known as the rotary/percussive drilling mechanism. This enables augering for chipping evacuation, and also allows the possibility of any of the three material failure mechanisms discussed, sometimes simultaneously. This combined action often significantly increases the efficiency of drilling over solely rotational or percussive [10].

In large-scale drilling, such as industrial drilling through rock for oil, liquids are often pumped into the area being drilling to bring the cuttings to the surface. This also has the

advantage that it will cool the drill bit, as heat generation tends to be more of an issue with larger rigs. Using liquids is not acceptable for space applications, due to both contamination issues, as well as needing to supply liquid which will increase the weight of a drill. This issue with weight is not an arbitrary one when it comes to space missions, as the cost of launching a vehicle into space is largely determined by the weight of the payload. A promising direction of design for subsurface exploration probes are small, lightweight penetrators and drills, however care is needed in the design to ensure a sufficient weight-on-bit (WOB), and this will be discussed further in the literature review.

2.1.2.2 Pile driving

A common terrestrial use of probe insertion is in construction engineering, using piles to provide foundations for buildings in otherwise unstable areas. These piles are long support structures made from metal, wood, or concrete, and transmit overhead structural forces underground to levels that are capable of supporting the loads. These piles are driven through the ground by a variety of means, and are subject to very complicated civil engineering mathematics. A full discussion of pile engineering is outwith the scope of this thesis, and as such it will only touch on the immediately applicable information; the reader can be directed to Bement, R.A.P. [11] if they wish to learn more on this topic.

Piles can be installed in the ground by two main methods: Impact hammers, and vibratory hammers. Impact hammers, as the name suggest, rely on an impulse delivered by a hammer to drive the pile through the ground. Vibratory hammers on the other hand use an eccentric rotating mass to supply a continuous sinusoidal signal to the pile and, by extension, into the surrounding soil. Vibrodrivers can further be classified into sub-sonic (6 – 50 Hz), and sonic (140 – 150 Hz) [11], each one tailored to the substrate in question. Vibrodrivers have been shown to display large benefits over the traditional hammering technique; it has been reported that during field trials, a steam-driven hammer drove a pile 20 m in 90 minutes, whereas a vibrodriver operating nearby managed 21 m in 42 seconds [11].

Performance is highly dependent on the properties of the soil, with one study showing that through a soil at a medium-dense (65% relative density), energy consumption was lower for vibrodriving than for impact driving, however at 90% relative density the opposite was true [12]. In these particular tests, using a frequency range of 5 – 60 Hz, the

optimum frequency of vibration that yielded the greatest rate of penetration was determined to be 20 Hz.

2.1.3 Extra-terrestrial applications

Most missions to the surface of an extra-terrestrial body incorporate some sort of sub-surface access device. In these extreme environments, sub-surface access proves to be a difficult endeavour. The low gravity on all other rocky bodies in our solar system results in a lower WOB available, reducing the efficiency of drilling. Additionally, the vast distances create a delay in any operating signal, resulting on the reliance on a high-degree of autonomy.

Methodologies of accessing the subsurface can loosely be divided into four distinct categories: Drilling, penetration, excavation, and impaction [13]. Drilling specifically involves the breakage of substrate and subsequent removal from the hole, whereas penetration refers to softer material such as sand or soil, displacing the material to the front and side to allow progression. Whilst this process is not necessarily as complex as drilling, it also comes with its own set of problems that can be exacerbated in low gravity environments. Excavation is accomplished by scoops and shovels and limited to the near-surface, and hypervelocity impactors strike the surface at high velocities, destroying the device in the process.

2.1.3.1 Drills

Drilling on the surface of other planetary bodies has a long heritage, and has been the most common method out of the four subsurface access categories described above. Constraints due to the realities of space result in slightly different approaches to drilling than from a terrestrial stand-point. For example, whilst the use of cutting fluid is nearly ubiquitous for tough materials or large-scale operations on Earth, the low temperatures and pressure of space means that any fluid would either freeze or instantly evaporate. In addition, not only is it extra weight to carry where mass budget is tightly constrained, but fluids are also liable to contaminate any samples acquired, reducing the scientific validity of any results.

Due to the substantial history of space drilling operations, only a few of the most important systems will be covered here. To learn more, please refer to [10].

Drilling on the surface on another planetary body began in 1970 with the Soviet Luna 16 lander, shown in Figure 2.1(a), which was the first autonomous mission to successfully return a drilled sample of the lunar regolith back to Earth [14] (note that the first actual sample return was with the Apollo 11, which used scoops and hammered-tubes to sample the terrain by hand [15]). This drill, a rotary/percussive corer, penetrated to a depth of 35 cm in 7 minutes, before encountering an obstacle and required a halt to drilling [14]. In total, 101 g of lunar regolith was collected.

This was quickly followed by the USA the following year with the Apollo 15 mission; the fourth human landing on the surface of the Moon. The astronauts David Scott and James Irwin used the Apollo Lunar Surface Drill (ASLD), a 500 W rotary/percussive drill and shown in Figure 2.1(b), to core to a depth of 2 m beneath the lunar surface. This was a meter short of the target depth. The drill subsequently became stuck and required *"the two of us, working at the limit of our combined strength"* in order to release it [16], during which Scott sprained his shoulder under the strain [17].

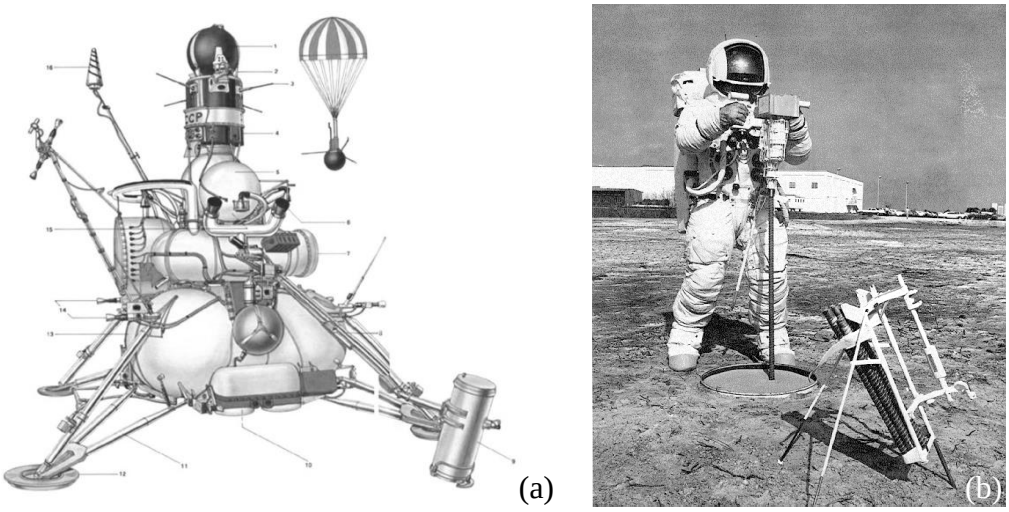

Figure 2.1: First instances of extra-terrestrial drilling with (a) the Luna 16 lander [14]*, and (b) the Lunar Surface Drill as used by the Apollo 15 astronauts, shown here during testing at the Kennedy Space Center (NASA photo S70-29673).*

The first instances of drilling on another planet were the Soviet Venera 13 and 14 landers in 1982, shown in Figure 2.2(a) [14] (Note that the previous missions, Venera 11 and 12, were both successful in landing and had drilling devices in the scientific payload, however neither of these were successful in obtaining a sample). The drill sampler, shown

in Figure 2.2(b) was successful on both landers in drilling to the target depth of 3 cm, acquiring core samples of 3 cc in total. Penetrometers were also present on both landers; however for Venera 14 in an extraordinary stroke of bad luck, the probe was deployed in the exact location that a recently-ejected lens cap had landed, rendering any data useless.

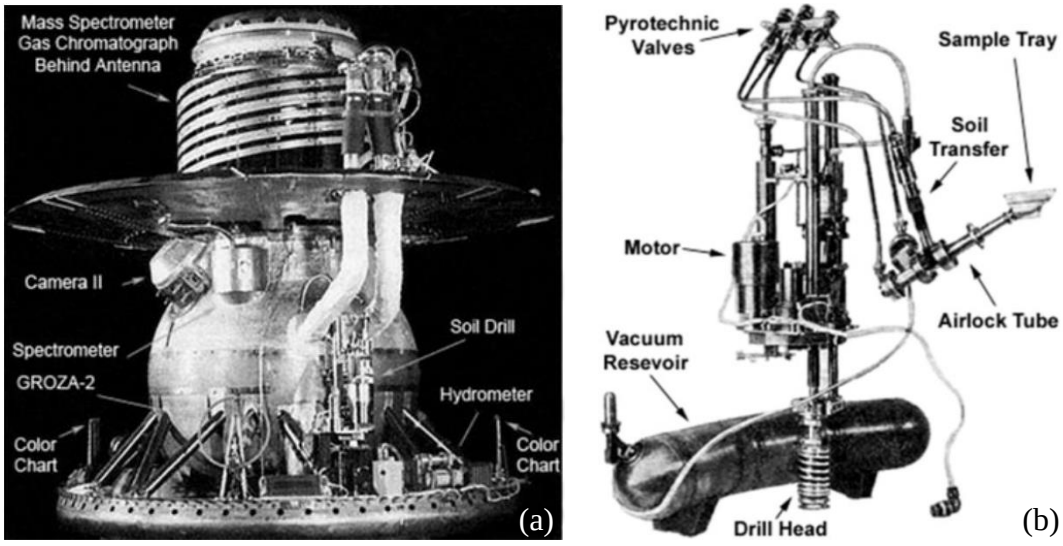

Figure 2.2: Overview of the Venera 13 and 14 missions showing (a) the lander and scientific payload, and (b) the drilling mechanism [14].

Drilling research and design has continued since these early days of space exploration, and has featured on many missions during that time. They are often limited to the very near surface, such as with the sampling drill on-board the Curiosity rover as part of the Mars Science Laboratory mission, with a drill depth of 5 cm [18], [19]. This rotary/percussive drill allows the rover to collect the resulting cuttings and process them in the Collection and Handling for Interior Martian Rock Analysis (CHIMRA) unit. With a hammering frequency of 1,800 blows per minute, the drill is able to impart impact energies between 0.05 and 0.8 Joules [20]. Another drill, the Sample Drill and Distribution (SD2) device was flown on-board Philae as part of the Rosetta mission to land on and sample a comet [21]. Designed to drill to a depth of 23 cm with a sample size of 0.2 cc the drill was ultimately unable to sample the comet due to complications in landing.

Looking further ahead, some of the most exciting Mars exploration missions are the proposed Icebreaker mission by NASA, and the ExoMars programme by ESA/Roscosmos. Whilst it does not yet have an assigned mission date, the Discovery-class Icebreaker concept has gone through heavy development, proposing to drill 1 m through the icy surface of the Martian poles on board a lander based on the Phoenix chassis [22]. Using a

rotary/percussive mechanism, it claims to be able to drill to a 1 m depth in 1 hour, using a 100 N weight-on-bit and 100 W of power [22]. The drill, shown in Figure 2.3(a) is able to deliver a large impact energy of up to 2.5 J per blow, taking samples in 10 cm sections before brushing the resulting cuttings for subsequent analysis [23].

The ExoMars rover, shown in Figure 2.3(b) and planned for a launch date in 2020, is the second half of the two-part Martian exploration mission 'Exobiology on Mars' (ExoMars). At the time of writing and to the best of the author's ability, not much specific information regarding the drill could be found, however it is stated that it will drill to depths of up to 2 m below the surface, with the drill-stem split into 4 sections that will be assembled in situ [24], [25].

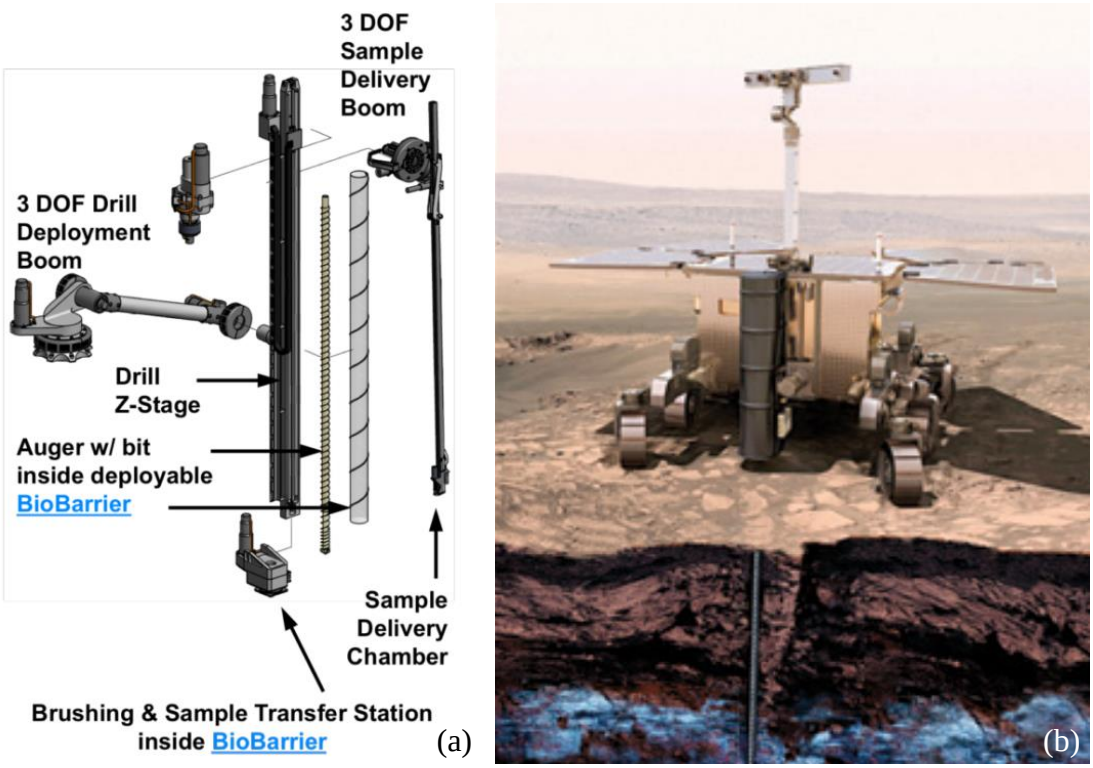

Figure 2.3: Proposed Martian drills showing (a) Icebreaker [23]*, and (b) ExoMars* [24].

Due to the level of flexibility that it affords, most of the drills described operate using the rotary/percussive drilling method, using cams to deliver the hammering blow. However, novel ways in which to deliver this percussive action using high-power ultrasonic vibration are in development, such as the Ultrasonic/Sonic Driller/Corer (USDC) [26] and Auto-Gopher [27] devices by JPL or the Ultrasonic Planetary Core Drill (UPCD) by the University of Glasgow [28], [29]. These drills work on a similar principle to each other, whereby a free-mass (similar to a ball-bearing) is allowed to come into

contact with the tip of an ultrasonically vibrating horn. Due to the rapid vibration of the horn, the free-mass will then rebound at high velocity, subsequently impacting a drill-bit and thus transferring momentum onto the drilling substrate. This process repeats itself thousands of times a second, and is able to deliver high impact forces for a low weight-on-bit and power consumption.

2.1.3.2 Penetrators and penetrometry

The terms ‘penetrator’ and ‘penetrometer’ are often used interchangeably in the literature, however they do possess specific differences in their definition [13]. Penetrometry is the field of measuring properties of a material using a penetrating probe. These properties are often mechanical in nature, such as measurements of force, penetration rate etc, but can also incorporate other physical properties. As such, a ‘penetrometer’ is a device that is used for penetrometry, and is outfitted with sensors in order to carry out those measurements (the CPT test described later is an example of this). ‘Penetrators’ on the other hand are purely delivery vehicles of a payload to the sub-surface. A penetrator can also be a penetrometer if outfitted with sensing devices, which is the most usual route in the scientific community. Common penetrators are needles for injecting medicine, or some methods for planting seeds in soil. Most of the devices described in this work are used for scientific measurements and are thus penetrometers, however many could also be considered penetrators.

Penetrometers can be split into two groups according to their relative velocity; fast or slow. Fast penetrometers, also known as “kinetic” penetrometers, are released above the surface and utilise the gravitational potential to gain momentum and impact the surface, gaining access to the sub-surface and coming to a standstill in a short duration of time [13]. In contrast, low speed penetrometers start from a stationary point on the surface from a lander or rover, and use an axial force to progress into the subsurface. This axial force can take the form of a steady penetration force (known as “static” or “quasi-static” penetration), or from internal hammering (known as “dynamic” penetrometers) [13]. This work will mainly be focussed on low-velocity penetrators.

Static penetration is rarely used to access any significant depths, as the penetration depth will ultimately be limited by the weight of the spacecraft. It is most commonly used

in civil engineering as a method of determined properties of the soil, as part of the 'cone penetration test', or CPT [30], [31]. By relating the penetration force to the depth of insertion with a calibrated penetrometer, certain inferences can be made about the strength and structure of the soil. Dynamic penetrometers, such as those utilising a hammer action, have the advantage that they provide their own penetration force, and is more unrestricted in its ability to overcome obstacles in its path. Several missions have thus used this technique to gain access to the sub-surface.

Although it was never successfully tested in situ, the PLUTO (PLanetary Underground TOol) probe was such a device, used on the Beagle 2 lander for an ESA mission to search for organic material on Mars [32], [33]. The PLUTO probe was able to travel unhindered except for a connecting tether to the main lander, giving rise to the terminology 'mole'. This tether acted as both a power supply and a method of data transmission. It could also be used to winch the probe back to the lander for storage and translation to a different area of interest. The probe utilised a linear percussive technique (no rotary or cutting action), having an internal mass to drive a metal spike into the ground as shown in Figure 2.4. It does this by repeatedly raising the mass with a DC motor and striking the inside of the casing, displacing and compressing the medium ahead of it to advance [33].

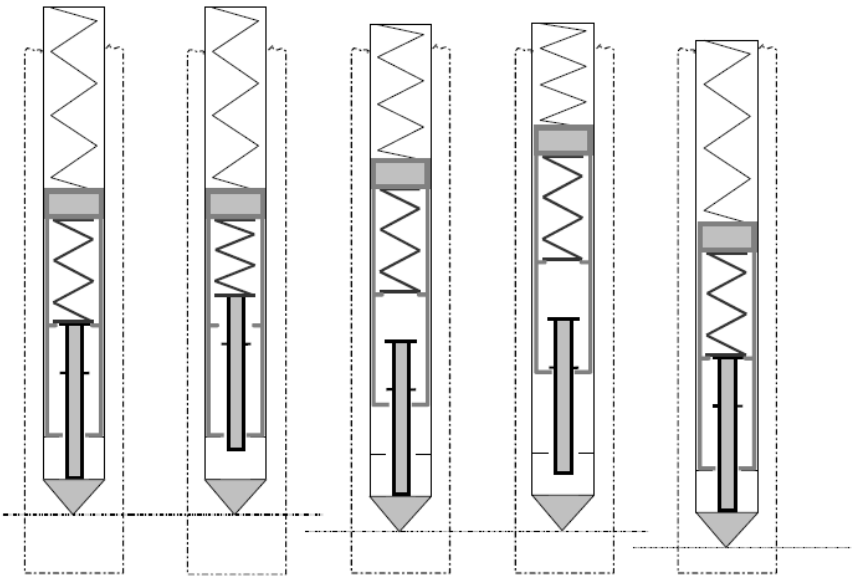

Figure 2.4: The PLUTO probe and hammering mechanism [35].

A significant complication with this method is that the motion of releasing the mass will act to pull the mole out of the soil, cancelling out any progress made. This is solved by including a 'suppressor' in the system. The hammering mass is sprung against this

suppressing mass, and at the moment of release the suppressor mass is moved backwards. A weaker back-spring then slowly decelerates the suppressor, eventually causing it to start moving forward and cause a smaller secondary strike. The break-spring behind the suppressor must be finely tuned to ensure that the force of decelerating of the suppressor mass is kept below the skin friction of the penetrator, otherwise the probe will move back up out of the hole [34].

An advantage of this mole, shown in Figure 2.5, is that it allows the probe to travel along the surface of the ground, giving it a higher degree of manoeuvrability and enabling it to re-locate to an area of easier penetration or higher scientific vale without moving the main lander or rover. Also, by striking the top of the housing instead of the bottom, this effectively reverses the direction of penetration, and studies have shown a ten-fold reduction in the retrieval force required [35]. It is important to note that this method can result in very high impact forces within the probe, with accelerations as high at 8,000 m/s^2 noted [34]. Whilst not directly mentioned within the literature, personal communications with some of the scientists involved revealed that these impact forces were cause for concern, potentially damaging internal components.

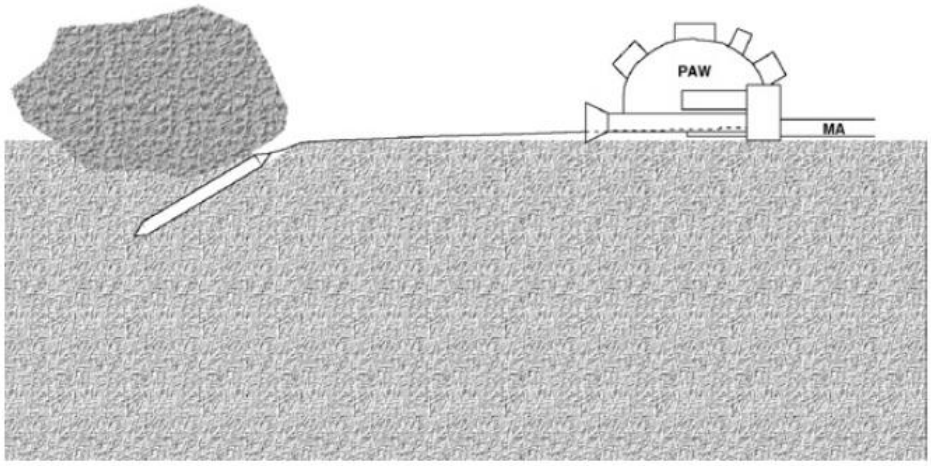

Figure 2.5: Example of the flexibility of the PLUTO probe's deployment [41]

A similar design of mole, HP^3, is being used as part of the InSight mission and is heavily based on the PLUTO design. The spacecraft, using the Phoenix Mars chassis, was due to launch in November 2016, but due to technical issues with the SEIS seismometer during testing, the launch was delayed until May 2018. The aim of this mission is to investigate the interior and origin of Mars, including the composition, size, and state of the

core, the crust thickness, and thermal gradients within the crust [36]. To achieve these goals, InSight will use the Heat Flow and Physical Package (HP^3); a mole and tether probe system, shown in Figure 2.6, illustrating the cylindrical cam that compresses the force springs, as well as the suppressing mass and brake spring.

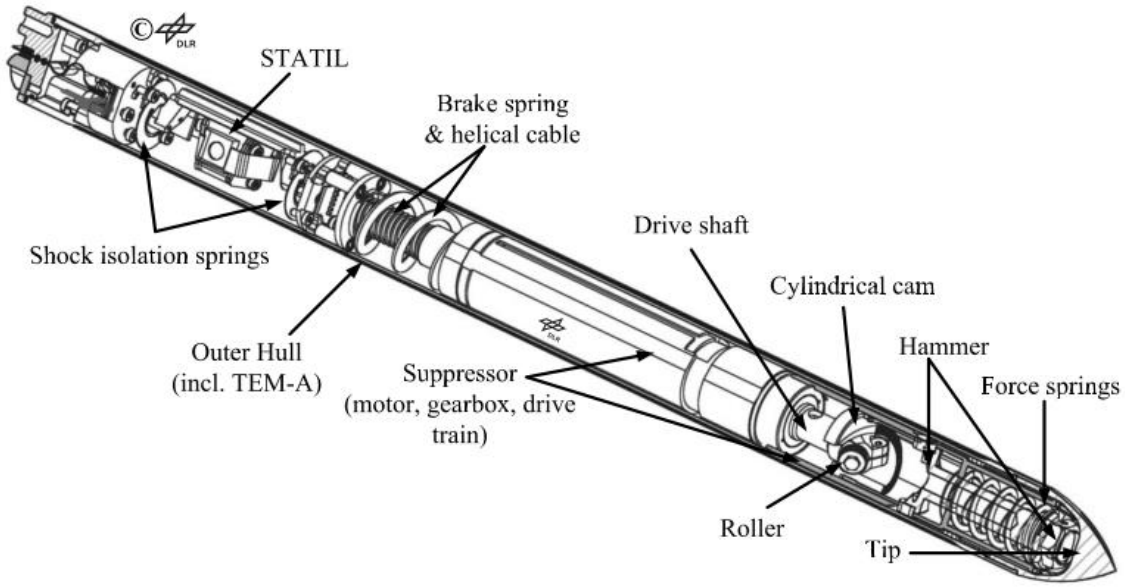

Figure 2.6: Cut-away of the HP^3 mole system [44].

Other important devices to mention in the field of moles and penetrometers are the KRET mole [37], the MUPUS probe on the Rosetta mission [38], and the CHOMIK device developed for the Phobos Grunt mission [39], [40]. KRET is a tethered mole that has been in development at the Polish Academy of Science (PAS) in Poland, functioning in a similar way to HP^3, whereas MUPUS and CHOMIK utilise a solenoid-driven hammer and are limited in depth to the left of the penetrating shaft. Due to complications in the Philae landing on the Rosetta mission, the MUPUS probe was not positioned ideally and was not able to reach its anticipated depth. The CHOMIK device possessed a higher energy-per-stroke that the MUPUS probe, and was included on the Phobos-Grunt mission to return regolith sample from the surface one of the Martian moons, Phobos. Unfortunately the mission was ultimately not able to leave Earth orbit, and the device was never tested in situ. A summary of some of these penetrating devices are given in Table 2.1.

Table 2.1: Specification of the flown probes and moles.

	PLUTO mole [41], [33]	**MUPUS probe** [38]	**HP^3 mole** [36], [42]–[44]
Mass	0.9 kg	2.35 kg	< 2 kg
Length	280 mm	360 mm	350 mm
Diameter	20 mm	20 mm	26.4 mm
Drilling depth	1.5 m	320 mm	3 – 5 m
Power	3 W	2.2 W	< 5 W

2.1.3.3 Excavator

Perhaps the easiest method of acquiring samples is through the use of scoops. Generally these are limited to a few centimetres depth and provide a simplistic and robust method of sub-surface access. They do have some drawbacks, such as struggling in frozen or highly compacted regolith, however they have successfully been used on several missions, such as the Soil Mechanics Surface Sampler (SMSS) on the Surveyor 3 and 7 Lunar landers [45], [46], the Surface Sampler Acquisition Assembly (SSAA) on the Viking 1 and 2 Martian landers [47] (the first mission to sample the Martian surface), and the Icy Soil Acquisition Device (ISAD) on the Phoenix lander [48]–[50], also on the Martian surface, and shown in Figure 2.7.

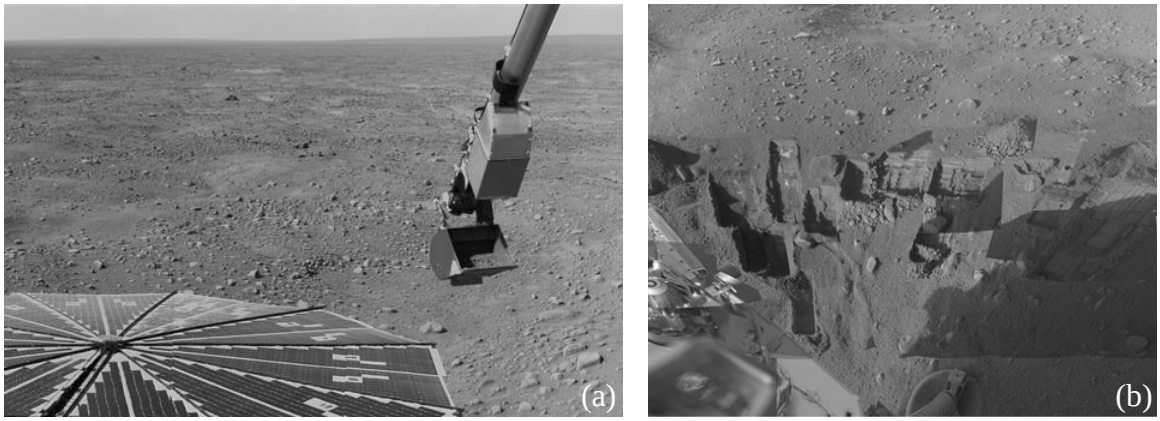

Figure 2.7: The Phoenix lander showing (a) the ISAD after scooping, and (b) and example of the trenches left after scooping. (credit NASA/JPL)

2.1.3.4 Hypervelocity

Hypervelocity impactors access the sub-surface by striking the group at an extremely high speed. The technique differs from fast-velocity penetrators in that the probe is destroyed in the process and a crater formed. The NASA Deep Impact mission investigated the comet Tempel 1 by releasing an impactor that collided with the surface, forming a crater 150 m in diameter and sending up a plume of ejecta that the parent spacecraft could analyse [51].

2.1.4 Bio-mimetic Drills

Nature has provided inspiration for countless inventions and mechanisms for hundreds, if not thousands of years. Through natural selection and a significant time-period, nature has often solved many common problems faced by engineers, and through reverse-engineering these solutions it can be possible to apply this knowledge to very novel applications [52]. It is not always the perfect solution however, as specific scenarios might call for very different approaches, but in the field of low-gravity/low-mass drilling there are a few examples that have shown great promise.

2.1.4.1 Wood-wasp

As stated earlier, penetration and drilling under low-loads is a difficult process to undertake. However, there are many insects that are able to drill or burrow through a variety of substances extremely effectively for their small size. Two of the most promising candidates for space applications are the locust and the wood wasp, which both burrow to lay their eggs. Currently this research is concerned mainly with the wood-wasp method, but for more information on both please refer to [53].

“Wood wasp” is the generic name given to a variety of different families of insect that use an ovipositor to bore into wood and lay their eggs (‘wasp’ in this regard is a misnomer, as many of these families would not be classed as true wasps). There are many different kinds of ovipositor, be it long and flexible or short and rigid, however they all use a reciprocating motion for drilling. A typical ovipositor is shown Figure 2.8.

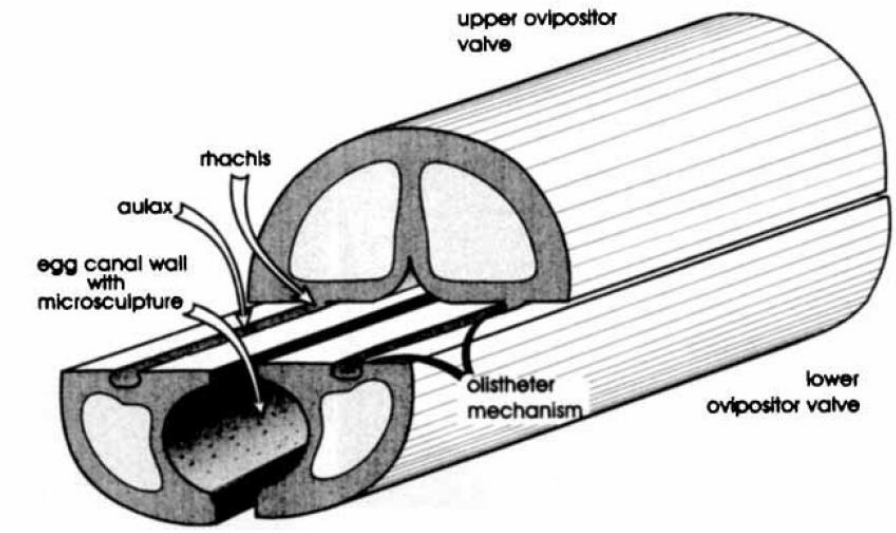

Figure 2.8: Overview of the ovipositor [54].

The single upper valve is connected by a groove-like joint (the olistheter) to the two lower valves, enabling the lower valves to slide back and forth independently. They also form a tube along which eggs or venom can pass, and are covered in backwards facing teeth [54]. Here the reciprocal motion is key, as the backwards teeth on the retracting valve engage with the substrate, providing a reactive force which pushes the other valve further into the material. This is repeated until the required depth is achieved. The advantage of this method is that the force needed for penetration comes from the reactive force and not any overhead mass, meaning a smaller overall device is sufficient [55]. A simplified schematic of this process can be seen in Figure 2.9.

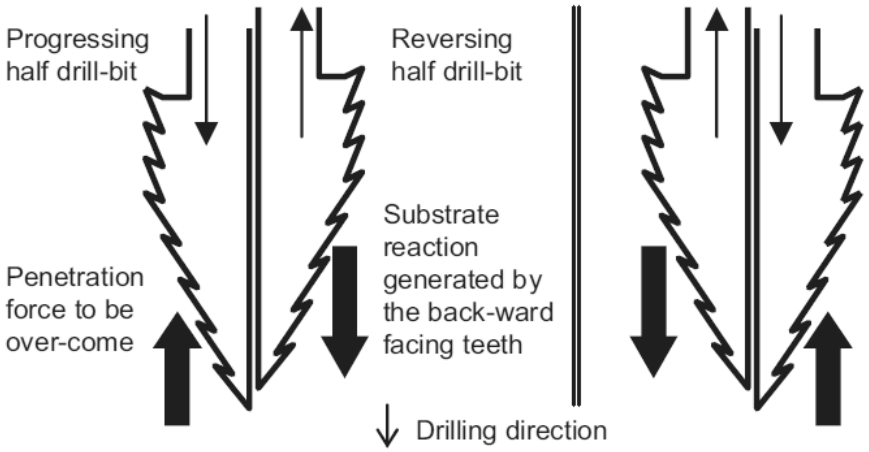

Figure 2.9: The DRD mechanism [55].

Drills based on this design have shown some success at reducing the overhead mass required for penetration into sand [53], [56]–[61], however the biggest issue that arises is the fact that sand is not as rigid as wood. Sand, being a loose material, will not engage with the backwards teeth as well as the cellular walls of wood and significant slippage is observed at depths on the order of 15 cm [56]. This novel design is a relatively recent field of research, and is still in heavy development [62].

2.1.4.2 Razor clam

Research at the Massachusetts Institute of Technology (MIT) has looked at the burrowing methods of the razor clam (Atlantic jackknife clam, *Ensis directus*), for the design of the RoboClam robot [63]–[65]. Based purely on the pulling strength of the razor clam's 'foot', about 10 N, the mollusc should only be capable of burying itself a few centimetres into the sea bed, however it is able to reach depths up to 70 cm [66]. The reason for this is that it takes advantage of the non-Newtonian nature of saturated sand, quickly contracting its valves and causing the surrounding media to liquefy. The region of liquefied sand extends 1 – 5 body radii out from the bivalve, and allow it to travel to depths with significantly less drag. A comparison of the RoboClam with the animal it took its inspiration from, and the locomotion mechanisms are given in Figure 2.10.

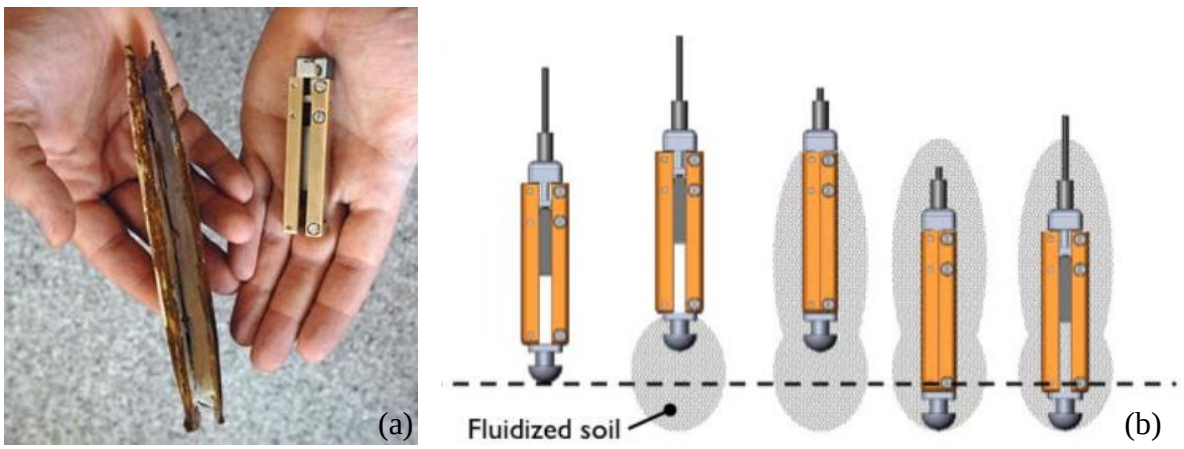

Figure 2.10: The RoboClam, showing (a) comparison with the razor clam [123]*, and (b) illustration of the liquification mechanism and progression* [64].

Travelling through liquefied sand rather than static-sand results in a reported order of magnitude decrease in the energy required to reach the 70 cm depth [65]. Using a genetic algorithm several different evolutions of the RoboClam design were simulated to find the optimum solution, and a final device has been manufactured that displays burrowing

performance on a par with the razor clam through its natural mudflat habitat [65]. Due to this burrowing performance, the RoboClam is being marketed as a “smart” anchor that is able to set and un-set itself, making a firm anchoring point whilst also being able to make retrieval easier when required. Whilst this is a terrestrial application, due to its relation to the field of low-mass penetrometry it could be an attractive option for space environments, and the concept of liquefying the surrounding media is an interesting one.

2.1.4.3 Inchworm

An untethered mole, the Inchworm Deep Drilling System (IDDS), was based on the movement of a worm, and was designed to progressively penetrate its way through high-strength, rocky material to depths greater than 100 m [10]. This self-contained device was split into two segments, with ‘shoes’ on the fore and aft sections able to grip against the inside of the bore hole to increase friction. With the aft-shoes engaged, a rotary drill bit at the front of the device could operate, reacting the torque against the bore-hole wall via the contact of the shoes. The forward section could then progress via a linear actuator, engage the fore-shoes, and then retract the aft section forward. In this way, the IDDS is able to drill in a piece-wise fashion [67]. An overview of this mechanism is shown in Figure 2.11.

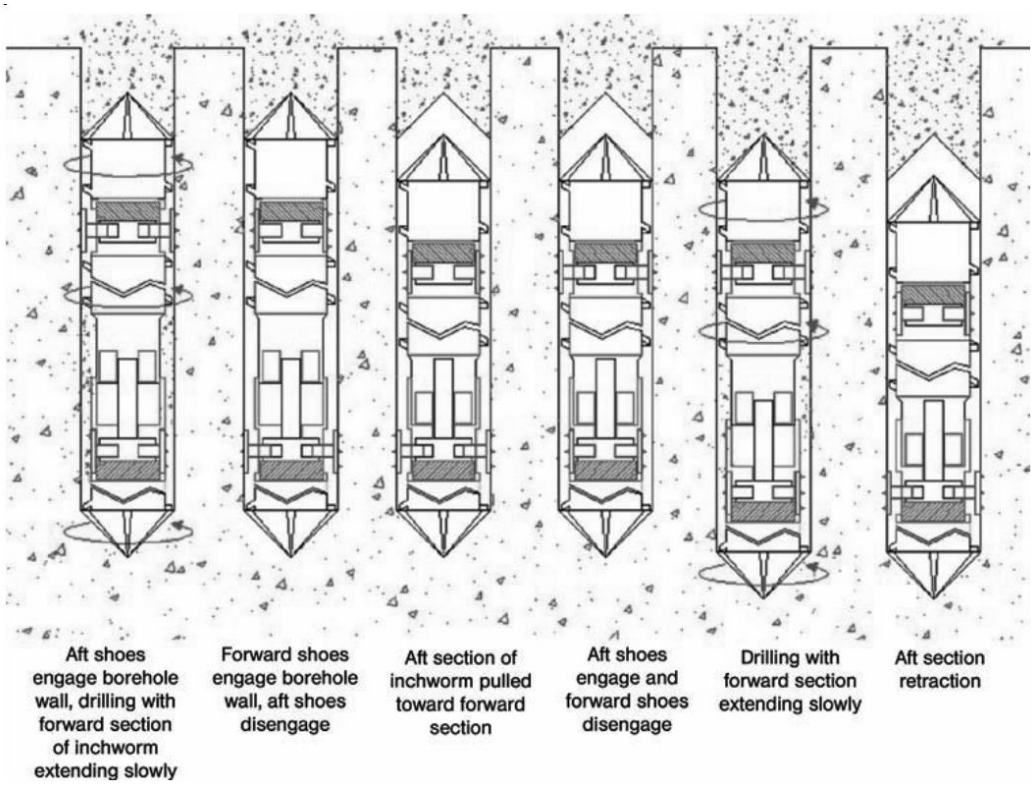

Figure 2.11: Drilling and “inch-worm” mechanism of the IDDS [10].

The IDDS is designed with low power in mind, such that it is able to be powered by a Radioisotope Thermoelectric Generator (RTG), and not require an umbilical cable for power supply. Whilst the IDDS is no longer presently in development, similar concepts are currently being studied and improved upon [68]–[70].

2.2 High-powered ultrasonics

Ultrasound is defined as any frequency of sound that lies beyond the upper threshold of human hearing of roughly 20 kHz (as opposed to infrasound, which lies below the lower threshold at 20 Hz). The concept of ultrasound dates back to Pythagoras and Aristotle, but it was not until the 19th century that the foundations were laid, with the most significant developments in the 20th century [71], [72].

It is also important to make the distinction between low and high powered ultrasonics. Low powered ultrasonics, as the name suggests, involves processes using ultrasonics at a low enough power to avoid significantly disrupting the surrounding environment. These processes use ultrasound and ‘echolocation’ for sensing purposes, where it is difficult or impossible to examine things optically, such as prenatal scans. High powered ultrasound on the other hand uses sufficient power to disrupt the surrounding environment significantly, albeit very locally. Obviously for cutting and drilling purposes this is intentional, and this is exactly what this research will focus on.

2.2.1 Ultrasonic production

For audible frequencies, the most common method of producing sound electronically is with the loudspeaker. Many different designs of loudspeaker exist, however the basic principle involves applying an alternating electrical current to a coil of wire that is located within a permanent magnetic field. The alternating current induces within the coil a varying opposing magnetic field, thus causing the coil to rapidly oscillate. Attaching a membrane or cone to the coil allows the production of pressure waves within the surrounding media, which is normally air for common sound production. The frequency afforded by this method ranges from tens of hertz to several thousand hertz, but it is difficult to sustain very high frequencies with this method.

Ultrasonic vibration is created by exploiting the phenomenon of certain materials that, when stressed, generate an electric charge. The inverse of this is also true, where the

piezoelectric material will undergo a deformation when applied with an electric field [73], which can create a vibration if an alternating voltage is used.

Originally, quartz was the material of choice for the production of ultrasound, however great developments have been made in materials that display a higher efficacy to this effect since then, with complex ceramics such as Lead Zirconate Titanate (PZT) becoming a current popular choice. The first direct application of ultrasonics was developed shortly after the Titanic disaster in order to detect obstacles at sea, which later evolved into submarine detection during World War I [74]. Paul Langevin pioneered the effective use of ultrasonics by sandwiching the quartz crystals between two steel plates, reducing the resonant frequency to a manageable 50 kHz, shown in Figure 2.12.

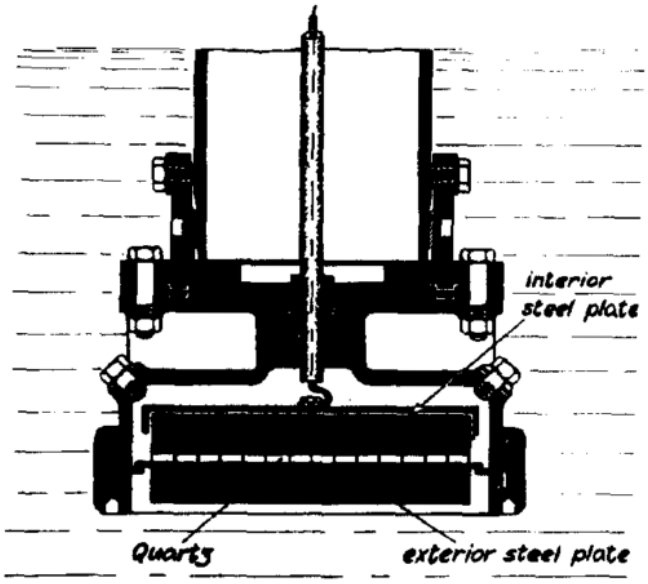

Figure 2.12: Langevin's device for underwater depth sounding [74].

This design later became known as the Langevin transducer, as is one of the most common types used today. At its most basic form it is composed of four different parts: a front mass, a back mass, piezo-ceramics placed between them, and a connecting bolt that compresses the whole stack together under load. Of course, in reality there are often additional components such as glues and electrodes to power the piezo-ceramics. This construction, like all objects in nature, has specific frequencies at which it resonates, known as the 'natural' or 'resonant' frequencies. The Langevin transducer is often excited with an alternating electric signal that matches one of these resonant frequencies, thus giving a maximum amplitude for the input signal.

2.2.2 Acoustic horns

These ultrasonic transducers (Langevin or otherwise) typically have very small tip amplitude of vibration on the order of 1-10 µm, however these are usually too low to be of practical use. To increase these amplitudes, acoustic horns (also referred to as ultrasonic horns, acoustic amplifiers, or mechanical transformers) are used to amplify the vibration. The 'gain' of the system is the ratio of final amplitude over initial amplitude, e.g. a system with a gain of 10 and an excitation amplitude of 5 µm will have a tip displacement of 50 µm. There are many different designs of horn, each suited to specific tasks. However, the basic principle remains the same: for a metal rod resonating at ultrasonic frequencies, the amplitude of the tip of the rod will increase with decreasing cross-sectional area.

The rate at which this gain increases depends on the specific shape and profile of the horn, such as those shown in Figure 2.13. Also shown are the gain of each design with respect to the diameter of the horn at the origin, D_0, and the final diameter, D_f. The stepped horn provides the greatest gain, followed by the exponential horn and the conical horn [75]. The gain of a cylindrical horn is simply unity, or 1, as it has no change in cross sectional area or diameter, therefore retaining the original vibrational amplitude.

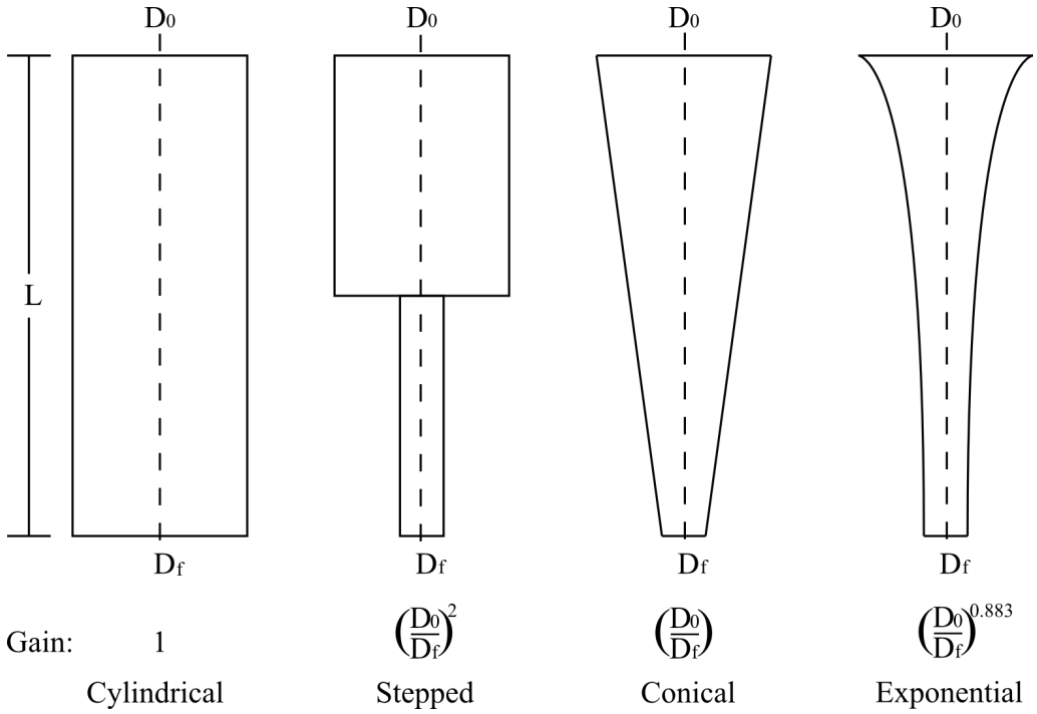

Figure 2.13: Common shapes for ultrasonic horns.

Whilst the stepped horn provides the greatest gain, it also causes the greatest fatigue of the metal since stress tends to concentrate at sharp angles. This stress can be reduced by filleting the sharp angles, but this then reduces the gain. A large part of the design of a horn is the compromise of increasing the gain as much as possible whilst still staying within the material's fatigue limit. For this reason hard metals such as steel and titanium are used as they normally have very high stress thresholds. Titanium additionally expresses a particularly low acoustical loss (known as having a high quality, or 'Q factor') and is usually the material of choice for many applications.

Increasingly novel designs have been designed to try to optimise and maximise this response, and this is a continuing area of research [76]–[79]. These horns are often manufactured separately from the transducer and designed to resonate at the operational frequency of the transducer, with a grub screw used to connect the two. Note that the specific definition of a 'transducer' is a device that transforms one form of energy into another; in this case electrical energy to mechanical energy. Whilst the transducer and horn are often referred to separately, once they are connected together the entire device is technically a transducer, with the piezo-ceramic transforming electrical energy into mechanical motion at the tip of the horn.

High-powered ultrasonics is a significant area of research, and has been used in a wide variety of fields. As discussed earlier, it has been used in the depth-sounding of submarines during World War I. More recently, it has shown promise as methods of bone-cutting for surgical requirements, reducing the amount of operating space needed [80]. In these bone-cutting devices, the ultrasonic vibration is utilised in direct contact with the material to be cut, as opposed to the USDC and UPCD drilling devices detailed in section 2.1.3.1 which use the ultrasonic vibration to react a sonic percussion onto the substrate.

2.2.3 Validation of ultrasonic vibration

Once a transducer has been designed and manufactured, it should be measured and calibrated to ensure the location of its natural frequencies are in the anticipated locations. Several variables can affect these natural frequencies, and so accurate measurements are essential for the design of any horn that is to be used with the transducer. This subsection

will include a short discussion about two of the more important experimental methods: The impedance sweep, and the Experimental Modal Analysis (EMA)

2.2.3.1 Impedance response

When an object is in resonance, the amount of force required to drive that object is at a minimum. An analogy of this is pushing someone on a swing; if the driving force (the pusher) matches the resonant frequency of the system (the swing), then this will result in the greatest amplitude of swing. This concept illustrates the *mechanical impedance* of a system, which for our purposes dictates the amplitude of vibration at the horn tip at resonance.

The concept of mechanical impedance is often represented by an analogous electrical system, as electrical systems are highly characterised and possess a wealth of research and information. Measurements of the acoustical impedance of a transducer are done by sweeping a constant voltage across a range of frequencies. The resultant current draw, and thus impedance (resistance), will accordingly be lower at frequencies of resonance, and higher at frequencies of anti-resonance. This is a quick method of determining the locations of resonance in the frequency domain, but it does not convey the mode of vibration, which requires Experimental Modal Analysis.

2.2.3.2 Experimental modal analysis

The modes of vibration define the specific manner in which an object vibrates. Taking an example of a simple cylinder, it is possible to describe the three main modes of vibration. The bending mode occurs when the cylinder vibrates in a bending fashion, similar to vibrating a ruler off the end of a desk. The longitudinal mode is a compressional "in-and-out" vibration along the axial direction, similar to how sound waves travel through a medium. Finally, there is the torsional mode, where the cylinder vibrates in a twisting fashion. All three modes, as well as the second bending mode are shown in Figure 2.14.

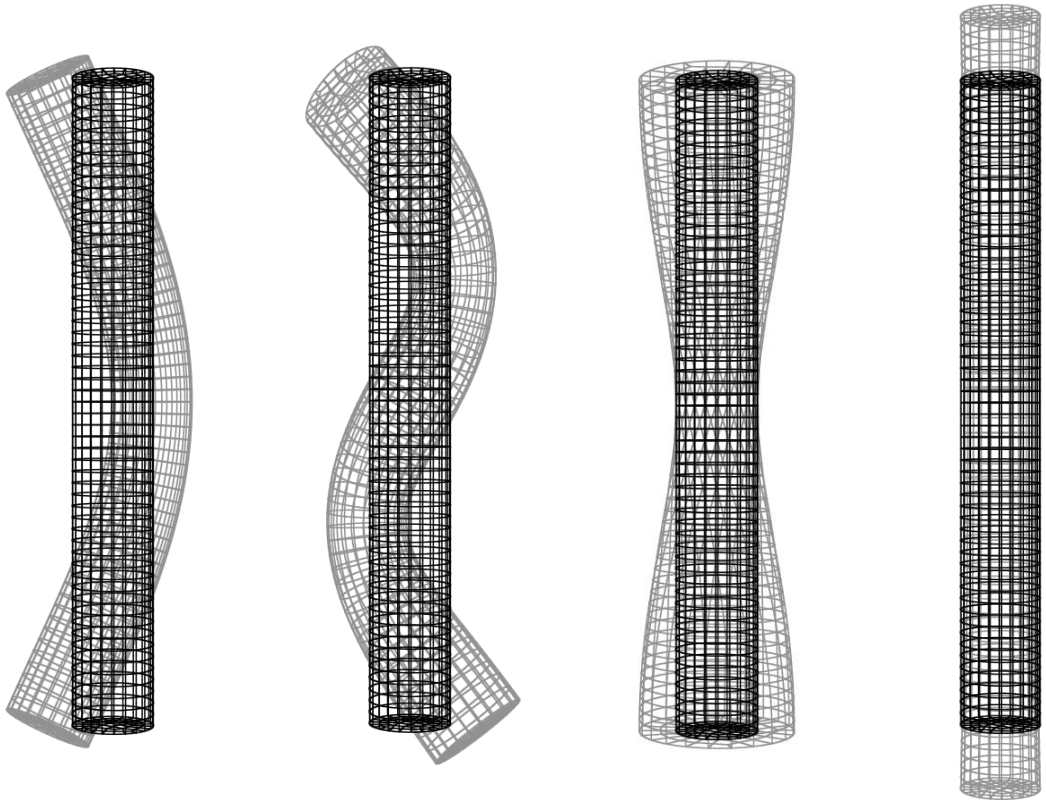

(a) (b) (c) (d)

Figure 2.14: Example of some vibrational modes of a cylinder showing (a) the 1st bending mode, (b) the 2nd bending mode, (c) the 1st torsional mode, and (d) the 1st longitudinal mode. The undeformed cylinder is shown in black outline, whilst the deformed shapes are shown in light-grey outline.

Experimental Modal Analysis (EMA) is the process in which these vibrational modes can be experimentally determined. Several methods exist, such as accelerometers attached to specific parts of an object, however the method most applicable to this research is through the use of Laser Doppler Vibrometers (LDVs), as this is able to measure very small displacements, and does not impinge the vibrational motion as other physical methods do, especially with the small vibrations used with ultrasonics.

LDVs work by focusing a laser onto a specific point on a vibrating surface, and measuring the reflected light. The velocity of that point relative to the laser beam will cause the reflected frequency of light to be either red-shifted or blue-shifted due to the Doppler Effect, depending on the direction of velocity. This change in frequency can be measured by an internal interferometer, and thus the velocity measured. Integrating this velocity can then provide information about the displacement of the point on the surface of the object, and subsequently the frequency and motion.

Comparing the magnitude of the displacement at specific frequencies to the input frequency will yield the Frequency Response Function (FRF), which is the measurement of the relative magnitude of vibration in the frequency domain of the point measured. Using a one-dimensional LDV uses a single laser beam to measure the velocity of a point in one direction. There are also three-dimensional LDVs which measure the velocity in all three directions, allowing a full understanding of the vibrational movement of specific points on an objects surface [81].

2.3 Soil mechanics

In the design for penetration experiments, it is very easy to become too focussed on just the drill itself. However, the drilling medium itself can be thought of as half of the whole system, and this section will set forth some of the most important concepts in this area.

Testing in a variety of mediums will also ensure the most adaptability in a drilling device, and clear characterisation of substrates is essential for this. This is especially true for space applications, as it would not be feasible to carry a very large range of interchangeable bits suited for specific circumstances, due to weight restrictions and the complexity involved with autonomous bit changing.

2.3.1 Vibrated soil and compaction

Sand mechanics, or psammomechanics, is an extremely complex area of research, with granular media being neither strictly a solid nor strictly a liquid, and can exhibit properties of both under different circumstances (for example, convective behaviour [82]). The main areas of interest for this research are *densification* and *fluidisation*. These are two phenomena commonly attributed to cyclic loading of granular media.

Densification is the process in which vibration of the media leads to a higher compaction, and therefore a higher density, whereas fluidisation is when a granular media behaves like a fluid. Vibrating a container of sand gives the particles motion, and in doing so allows them to re-organise themselves into a better packing structure, following an inverse logarithmic trend in density [83]. Raihane et al [84], [85] undertook some experiments to investigate how a box of sand reacts to a horizontal sinusoidal motion of the form:

$$x(t) = A\sin(\omega t) \tag{2.1}$$

where *A* and ω are the amplitude and angular frequency of vibration respectively. Using the acceleration of this sinusoidal motion, we can find a force due to this acceleration, F_a, acting on the sand particles in the shaken box to give:

$$F_a = mA\omega^2 \sin(\omega t) \tag{2.2}$$

The ratio of the maximum of this force to the weight of the contained sand (F=mg) is proportional to the ratio of the shear stress to the normal stress [86]. This governs whether the particles can overcome the static friction and mobilise, thereby becoming more fluid-like. The result is a relative non-dimensional acceleration, Γ, which is a control parameter generally accepted within the literature [85].

$$\Gamma = \frac{\omega^2 A}{g} = \frac{(2\pi f)^2 A}{g} \tag{2.3}$$

where g is the gravitational acceleration. It is very important to note at this point that 'g' is not just an arbitrary constant chosen for the sake of creating a non-dimensional entity, but actually comes out of the method of derivation. This means that the relative acceleration in equation (2.3) is dependent on what the value of gravity is on the particular astronomical body it is on. However, it also means that any drilling testing done on earth will not be truly representative to the same process on Mars. Regardless of any measures taken to simulate a low-gravity drill (e.g. by lowering the weight through the use of counterbalances), it would not be possible to precisely simulate a low-gravity sand sample without the use of drop-towers, parabolic flights, ISS experiments etc.

Research by Raihane et al. [85] showed that horizontal vibration (50 Hz) of a box of sand leads to three different states or regions, shown in Figure 2.15. Raihane identified two critical accelerations, Γ_0 and Γ_1, above which the sand exhibits "glassy" and "fluidized" characteristics respectively (here the glassy region is an intermediate state that is neither fully solid nor fluid like). The dynamic density (the density during vibration) increases in both the solid and glassy regions, but decreases in the fluidized region. This shows that both densification and fluidisation can occur simultaneously in the same system, making it difficult to discuss the concepts as singular, independent phenomena. The graph also shows

that for higher relative accelerations, the height of the sand actually increases, giving a larger total volume for the same mass, and therefore a decrease in the total bulk density decreases.

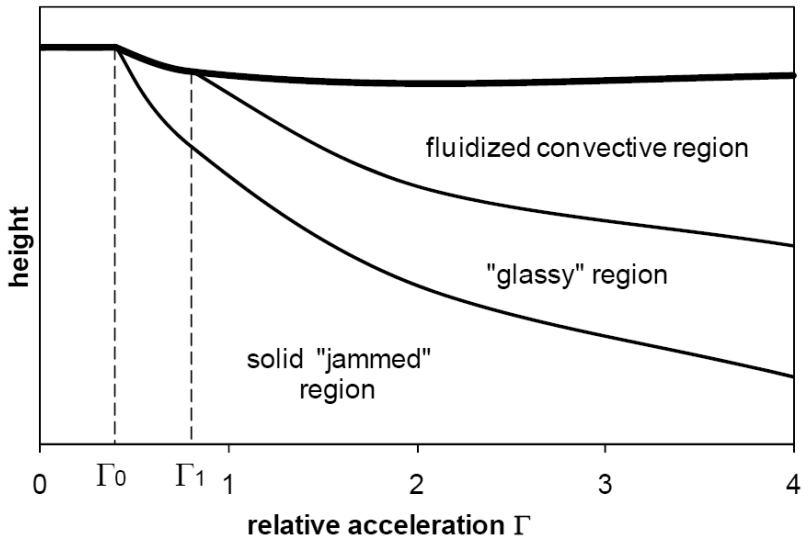

Figure 2.15: Representation of the regions present within a container of sand under vibration, as a function of the relative acceleration Γ [85].

It is important to distinguish between the dynamic density and the relaxed density, which is the density of the rested sand after vibration. As shown in Figure 2.16, after the vibration has stopped, the sand settles into a final state giving an overall increase in the density. Glassy and fluid characteristics only exist whilst the soil is being actively vibrated, and will return to a typical solid-state when stationary.

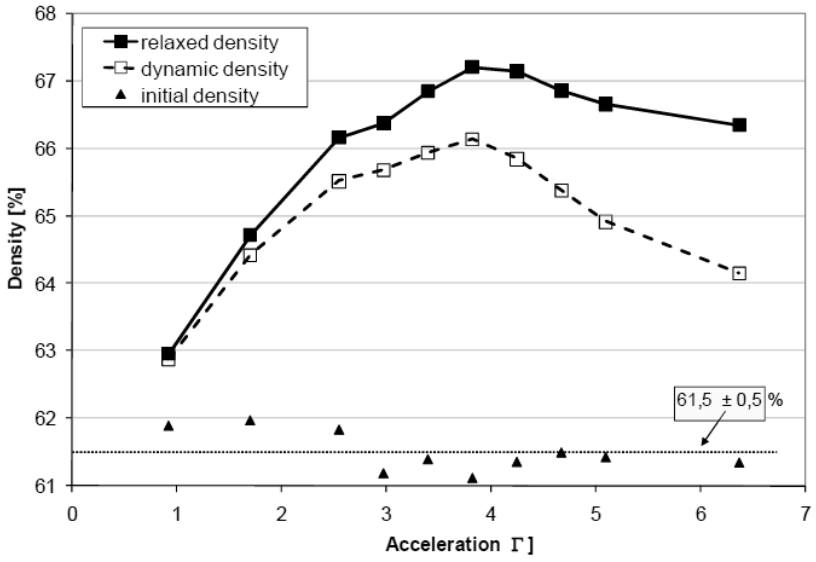

Figure 2.16: Comparisons of the dynamic density and the resultant density after vibration, as a function of the relative acceleration Γ [85].

Notes on Soil Mechanics Literature

Whilst reviewing the literature, it became apparent that there is some ambiguity over the terms 'fluidization' and 'liquefaction'. Liquefaction has been defined as "the nullity of the inter-granular stress between grains for some particular loading paths" [87], in essence, to show fluid-like behaviour. The most common area of research to find the term liquefaction is in relation to earthquakes. In these papers it was common to read about saturated soils, with earthquakes or vibrations causing the liquid within the soil to exhibit its properties to a greater extent; i.e., it is not about turning the sand into a fluid, but about the existing fluid taking on a larger role. Perhaps to add confusion, the additional term 'liquefy' or 'liquidation' appear to occasionally be used to describe both the fluidization of dry sand, as well as the liquefaction of saturated soils. As this work is for environments that are unlikely to have liquid water present, we will use the term 'fluidisation' strictly to describe the fluid-like behaviour of dry sand in motion.

There is very little research to be found in relation to ultrasonic vibration and sand, with all of the work described above dealing with frequencies on the order of 50 Hz. This low-frequency vibration will be important in terms of sand preparation (to achieve different densities for testing), however it does not enlighten us at all about how sand reacts to high-powered ultrasound. Taking equation (2.3) and using typical values for an ultrasonic horn (f = 20 kHz, A=5 μm), a relative acceleration on the order of Γ=8,000 is realised. This is far above the values used in the literature discussed, and it would not be good scientific practice to extrapolate results this far from the experimental data. Whilst the trend showed that increasing Γ produced a higher exhibition of fluidisation, it might be that equation (2.3) does not hold true for very high frequencies. The proposed research will investigate this to fill in some of these gaps in literature, hopefully providing some useful and original work.

2.3.2 Soil preparation

To examine the operational performances of devices intended for use on an extra-terrestrial body, materials that simulate the substrates on that body are used in testing. These are known as 'regolith simulants' and will be discussed in more detail in Chapter 3. It is crucial for testing that these substances are prepared in a controlled and repeatable manner.

It has been shown that pouring simulant into bucket from above 50 cm results in a homogeneous distribution of sand [88], [89], which is beneficial as differing layers of sand during penetration are hard to predict and account for. The density can then be varied by vibrating the container. Even a relatively small change in density (a +16% change) has been shown to cause a force increase of 1430% for a static penetration of 15cm into JSC Mar-1 simulant [90].

Rain

The rain method consists of filling a hopper with the sand, and opening a slit in the bottom of it. The hopper is moved back and forth over a container in a controlled manner, whilst allowing the sand to ‘rain down’ in a sweeping curtain. Each pass that the hopper makes across the container, a new layer of sand is deposited.

Pour

The pour method is perhaps the simplest way to fill a container with sand: sand is poured from a bucket into the container. The idea behind this is that the falling sand mixes with air, creating a homogeneous mixture (as opposed to the rain method, which creates a layered mixture). A large contributing factor to this method is the falling velocity of the sand, which will increase with increasing pouring height until the terminal velocity has been reached. Tests have been done to see the effect that the pouring height has on the final density, reporting that pouring heights above 50 cm have no further bearing on the density of the sand [89], [91].

Vibrate

The vibrate method utilises a vibrating container, to further compact the medium as it is poured into the container. The amplitude and frequency of vibration needs to be monitored and controlled properly to produce reproducible results.

Figure 2.17 describes all three of these methods [91].

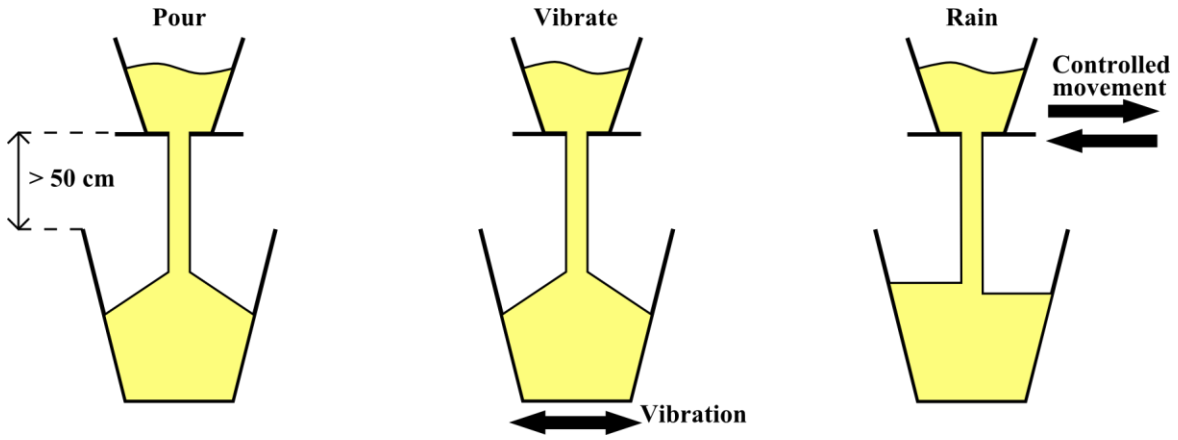

Figure 2.17: Three different methods of filling a container with sand.

2.3.3 Bearing capacity theorem

The bearing capacity of soil relates the loading that a soil takes from foundations or buildings, and is a fundamental aspect of civil engineering. The maximum loading a soil can take before failing is known as the 'ultimate bearing capacity', and governs at what point a footing will sink into the ground. Whilst failure of the ground can be catastrophic for the civil engineer, it is quite advantageous for those looking to drill or penetrate through soil, and serves as a basis for modelling penetration behaviour.

The mechanisms of soil failure are a highly complex field, and many assumptions are required in the formulations of bearing capacity theories. Prandtl assumed an active pressure zone forming a wedge in the soil directly beneath a foundation, with a passive wedge of soil near the surface that would be pushed up and away from the foundation. In-between these zones is a radial shear zone undergoing plastic deformation, following a logarithmic spiral [92]. Terzaghi then refined these equations by including the weight of the displaced soil, however as the foundation progresses in depth, it is assumed that soil above the lowest point of the foundation does not undergo shear deformation, and thus this method is only applicable to depths smaller than the diameter of the foundation [93]. This was further adapted by Meyerhof that accounted for this volume of soil, incorporating a logarithmic-spiralling yield surface that extended all the way up to the level of the surface for shallow foundations. For deep foundations, the failure zone takes the shape of a logarithmic spiral surrounding the bottom of the foundation [94].

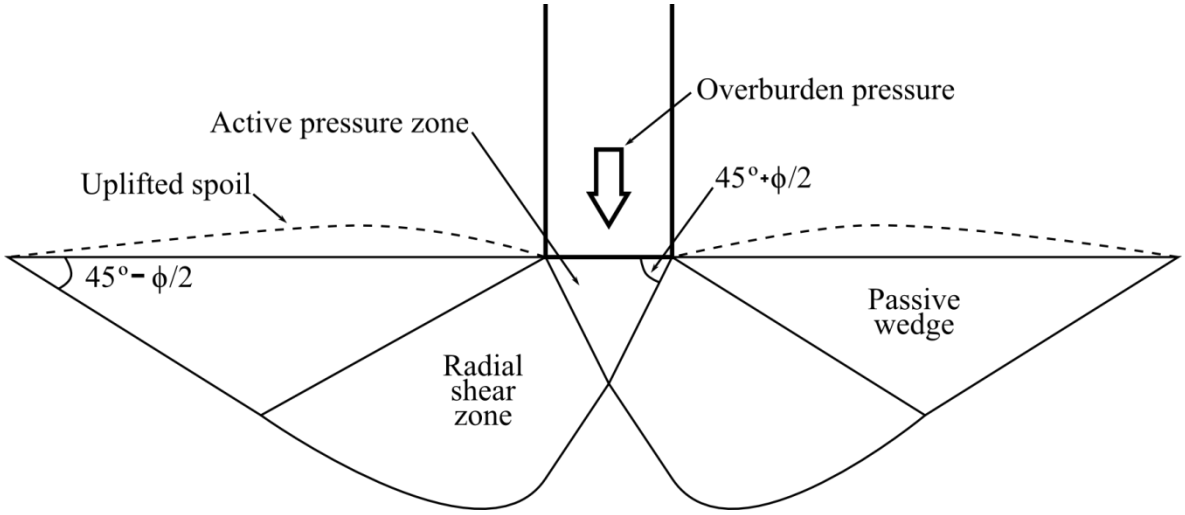

Figure 2.18: Ideal failure mechanisms in soil due to a foundation using Prandtl's theory. Noted are some angles between certain planes of failure, where ϕ is the angle of internal friction [92], [93].

This is a brief overview of some of the methods used to determine soil resistance, however it should be noted these are all approximations in a highly empirical field, with no single 'de-facto method' that accurately models all situations. For more a more thorough examination of these models, please refer to [92]–[94].

2.3.4 Penetration force predictive models

Despite these approximations, models can be extremely valuable in predicting trends, and benefit from empirical data to improve upon. The methods described above are designed for buildings, and are thus not directly applicable to small penetrators. In response to this, a researcher from the University of Arkansas, Ahmed ElShafie, has developed formulas that aim to predict the penetration profiles of probes through granular materials. He then extends these formulas to low gravity scenarios, with theoretical results from past space missions.

These formulas are quite complex, so for ease of the reader, each section will be broken down into the four components of the total penetration resistance, F_T shown in equation (2.4). Symbol definitions will be presented after each set of formulas in the order that they are displayed. In this work, the terms 'cone', 'penetrator', 'penetrometer' are interchangeable [95].

2.3.4.1 ElShafie penetration equations

The total penetration resistance (F_T) is the sum of two terms: the cone resistance (q_c) and the sleeve friction (f_S).

$$F_T = q_C A_C + f_S A_S \tag{2.4}$$

where A_C is the cross-sectional area of the penetrator, and A_S is the buried area of the sleeve of the penetrator. The cone resistance q_c can be calculated as a function of penetration depth Z as:

$$q_C = \gamma \times Z \times N_q \left(1 + \left(K_0 \times \sin\varphi \times \frac{Z}{L}\right)\right) \tag{2.5}$$

where γ is the effective unit weight of sand (N m^{-3}), Z is the penetration depth (m), N_q is the bearing capacity factor (dimensionless), K_0 is the coefficient of lateral pressure at rest (dimensionless), φ is the friction angle of sand (º), and L is the lateral extension of the slip lines (m). The effective unit weight of sand γ is the weight per unit volume of sand, calculated by:

$$\gamma = \rho \times g \tag{2.6}$$

where ρ is the bulk density of sand, and g is the gravitational acceleration. The dimensionless terms Nq and K, the bearing capacity factor and coefficient of lateral stress, are given as:

$$N_q = a \times e^{b \tan\varphi} \tag{2.7}$$

$$K = 1 - \sin\varphi \tag{2.8}$$

where a=1.0584 and b=6.1679 for sand [19]. The lateral extension of slip lines L (how far horizontally sand is moved due to penetration) is defined as:

$$L = B \times e^{\frac{\pi}{2} \times \tan\varphi} \times \tan\left(\frac{\pi}{4} + \frac{\varphi}{2}\right) \quad (2.9)$$

where B is the diameter of the penetrator. The cross-sectional area of the penetrator A_C is then given by:

$$A_C = \frac{\pi \times B^2}{4} \quad (2.10)$$

The sleeve friction, f_S, in the second term of equation (2.4) is also a function of penetration depth Z:

$$f_S = \frac{K_p \times \gamma \times Z}{3} \quad (2.11)$$

$$K_p = \frac{1 + \sin\varphi}{1 - \sin\varphi} \quad (2.12)$$

where K_p is the passive coefficient of lateral stress. The area of sleeve buried under the sand A_S is then defined as:

$$A_S = \pi \times B \times Z \quad (2.13)$$

Whilst this may seem like a confusing list of formulas, they combine so that the total penetration resistance, F_T in equation (2.4) depends solely on bulk density (ρ), penetrator diameter (B), penetration depth (Z), and angle of internal friction (φ).

Using these formulas, a bulk density of 1.8 g/cm^3 and a probe of 1 cm diameter, ElShafie created a series of theoretical penetration forces as a function of depth in accordance to different planetary bodies, shown in Figure 2.19.

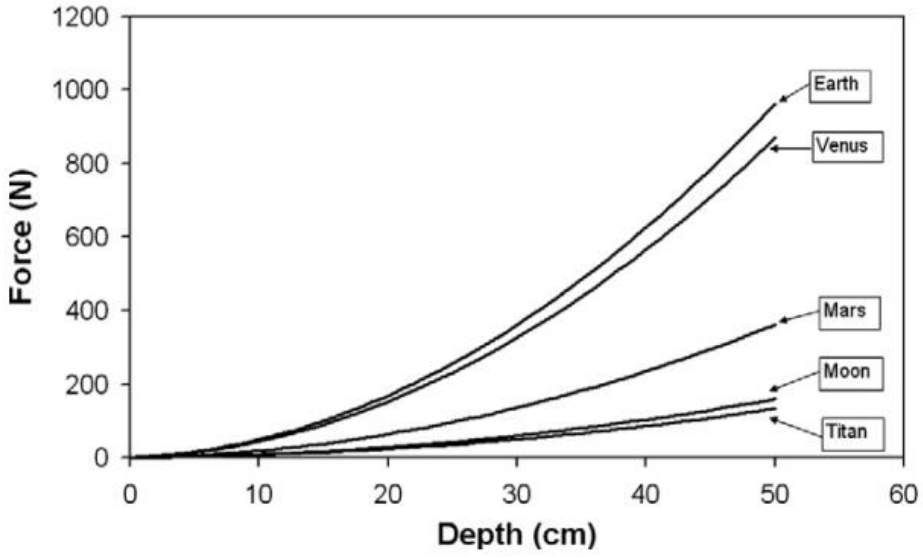

Figure 2.19: Predicted penetration performance on different planetary bodies according to the model by ElShafie [95].

Comments on the model

F_T in this equation is the total force required for penetration. The cone resistance and sleeve friction, q_c and f_S, have units of pressure, however the formulations are not trivial and they are difficult to visualise in this sense. The area of the cone, A_C, is the cross sectional area of the probe, which is independent from the shape of the tip. The area of the sleeve is the surface area of the cylindrical portion of the probe that is buried beneath the sand. The shape of the tip has been experimentally shown to have an impact on the penetration force [96], however as this model is an approximation, it is not considered.

The effective unit weight of sand, γ, is the weight of sand per unit of volume. N_q is a factor of bearing capacity, which is a function of the friction angle of the sand. The coefficient of lateral pressure at rest, K_0, is defined as zero lateral strain in a sand deposit. The angle of internal friction, φ, is defined as the angle on failure envelope of the shear stress and normal effective stresses, and increases with denser sand. L represents the distance that the slip lines of penetration extend horizontally, and D_r is the relative bulk density of the sand as a percentage between absolute minimum and maximum compaction.

Additionally, some concerns were found in the literature regard these formulas. In some work [95] there is an inclusion of the term for the area of the sleeve, A_S, in equation (2.11). However, this results in the units of the sleeve friction, f_S, to be force, rather than pressure.

It is assumed that this is an error, and so the A_S term is omitted from equation (2.11) for these purposes.

Gravitational acceleration, g, appears in these formulas, suggesting that the force of penetration, F_T, is dependent on the strength of gravity on the planetary body it is on, seen in Figure 2.19. This model assumes that penetration will be easier in lower gravity, quoting [95]:

"When the gravity of the planetary body decreases, density, porosity, friction angle and relative density will decrease and therefore, force needed for penetration will decrease as well"

Note, that this quote is slightly incorrect, as the porosity of sand is inversely proportional to relative density, as will in fact increase if the relative density decreases. Tilman Spohn, the principal investigator for the MUPUS probe, speaking on the initial progress of the Philae lander in its attempt at penetrating the surface of comet 67P/Churyumov-Gerasimenko said on a Rosetta progress blog [97]:

"The probe then started to hammer itself into the subsurface, but was unable to make more than a few millimetres of progress even at the highest power level of the hammer motor."

These two statements apparently contradict each other, as according to ElShafie the comet should require negligible force due to the negligible gravity. This is not shown by the Philae results, so a deeper complexity of granular penetration in low gravity environments is evident. Of course, these results could indicate that Philae had landed on a very frozen surface, however experimental testing is warranted in various levels of gravity in order to investigate ElShafie's model, and empirical results could potentially assist in formulating a stronger model.

2.4 Chapter conclusions

This chapter has covered the main topics needed for an understanding of the upcoming work on ultrasonic vibration and the penetration of granular materials. It has highlighted the cross-disciplinary nature of the work, involving information from civil engineering, biomimetics, ultrasonic vibration, soil mechanics, space systems, and drilling mechanisms.

Sand in particular was singled-out as a particularly problematic material to work with and anticipate, and much work will be required in order to deal with it in a scientific and consistent manner. Examples of models and methods used in civil engineering gave an insight into some of the complications involved, but as this remains a highly empirical field, these models are unlikely to be able to directly translate to the small scale. A model that has been specifically tailored to penetration of granular materials in space was covered, which will prove to be an exciting aspect to test out experimentally.

As this work involves using an ultrasonic penetrator, a brief history of ultrasonics was given and some background information on the phenomena involves was described. A summary of some of the most important space applications of penetration were also provided, allowing all of the other information to be put into perspective.

Chapter 3

Regolith Characterisation

This chapter will cover the characterisation of the regolith simulants used in experiments. Of the five simulants used in testing, three of them (SSC-1, SSC-2, and ES-3) were created by the University of Surrey and used solely during visitation to their facilities. These regoliths have already been fully characterised [56], so will only be mentioned here briefly. An additional sand from the University of Surrey, SSC-3, had only the particle size distribution completed at time of use and was used at both the University of Glasgow and the University of Surrey. A regolith simulant from the University of Glasgow, BP, was also used at both these facilities. This chapter is mainly tasked with categorising the simulants SSC-3 and BP, and a description of the processes and steps taken to do so.

3.1 Regolith simulant justifications

Studies of the composition of Mars have shown that there is rarely any liquid water present on the surface. The pressure and temperature on Mars are near the triple point of water, causing any liquid water to be highly unstable. This means that any soil analogue used must be as dry as possible. Even the presence of a relatively small amount of water can have huge changes on the soil mechanics, as we all discover at a young age when trying to build sand castles at the beach.

This means that the ground encountered on the surface on Mars is likely to be very different to most of that found on Earth. For experimental testing, it is necessary to reproduce the anticipated environment on the planetary body where drilling is intended. Therefore, for a drilling or penetrating device, it is imperative that the equipment is tested on specialised substrate that is designed to replicate the ground found on Mars, known as a ‘Martian simulant’ or ‘Mars analogue’. It is important to define exactly what is meant by this term, and what specifically constitutes whether something can be defined as an analogue or not. This is not an arbitrary task, as a regolith analogue can be required to

simulate a variety of different properties including; chemical, mechanical, physical, magnetic, and organic [98]. A definition given by McKay and Blacic [99] in a 1989 workshop on lunar soil defines a soil simulant as:

"any material manufactured from natural or synthetic terrestrial or meteoritic components for the purpose of simulating one or more physical and/or chemical properties of a (lunar) rock or soil."

The key aspect of this definition is that a soil simulant only needs to mimic "one or more" of the properties discussed above, and not "all". The property that is chosen to for a particular simulant should be selected for a particular purpose, i.e. if an experiment is done to decide how well an electric signal can pass through Martian soil, it would require a simulant that mimics the conductive properties of real Martian soil, but not necessarily one that mimics the reflectivity of Martian soil. This is very useful, as attempts to manufacture an analogue soil that exactly replicates all properties will be; a) lengthy and costly, and b) unnecessary [100].

For the purposes of the experiments conducted in this thesis, only a few properties are required to replicate those found on Mars, known as a 'Martian simulant'. These parameters are concentrated on the mechanical properties of sand, including the size and distribution of particles, the particle shape, and relative density of the preparations. Chemical and biological parameters are out of the scope of this research.

3.2 Regoliths considered

All five regoliths will be described briefly here, and then compared against the other measured characteristics in the conclusion of this chapter. Additionally, a few other well-known regoliths will be mentioned for reference, however these were not able to be used for tests due to being cost-prohibitive.

SSC-1

This quartz-based sand has rounded particle shapes, and has a relatively broad particle size distribution from 70 – 300 μm. It was procured by the University of Surrey from a local building supply dealer in Guildford, U.K. as "builders' sand", and had all particles above 1.3 mm removed after being dried.

SSC-2

This garnet-based sand has very angular particle shapes, and a very uniform particle distribution centred around 40 µm. It is normally used as an additive for blast cleaning and waterjet cutting, and was procured by the University of Surrey from the GMA Garnet Group.

SSC-3

This quartz-based sand has sub-angular particle shape, and a very uniform particle distribution centred around 180 µm. It was procured by the University of Surrey from West Wittering beach on the U.K. south coast, and sieved to only contain particles between 150 – 212 µm.

ES-3

This quartz-based sand has sub-rounded particle shape, and a relatively broad particle distribution between 300 – 600 µm. It was procured by the University of Surrey from Sibelco™ as the off-the-shelf product "Leighton Buzzard DA 30".

BP

This quartz-based sand has sub-rounded particle shape, and a uniform particle distribution centred around 212 µm. It was procured by the University of Glasgow from a local building supplier as "block paving sand", and was chosen to be in-between SSC-1 and ES-3 in size distribution, as well as have a low percentage of fine-particulate content for low risk.

Other Regolith Simulants

Two commonly used regoliths used to simulate the terrain on Mars are the regoliths from the Johnson Space Centre, JSC Mars-1 [101] (and the corresponding newer batch produced JSC Mar-1a), and later the Mojave Mars Simulant (MMS) [102], [103]. Both of these are designed to simulate the particle size, shape, and density of Martian sand [98], and are often used to test mechanical devices. MMS was developed to address some issues with JSC Mars-1 being too hydroscopic, absorbing too readily for the researchers needs.

3.3 Particle size distributions

SSC-3 was obtained from the Surrey Space Centre, and as such was already dried and prepared before experiments at the University of Glasgow. After purchase, BP was left to completely dry over a number of days by spreading it out in a dry room and passing an air current over it with occasional mixing to ensure all moisture was removed. The regoliths SSC-1, SSC-2, and ES-3 were used on-site during visits to the Surrey Space Centre, and were already completely characterised [56].

To measure the size distribution of sand, a weighed sample of it is passed through a stack of sieves with progressively smaller mesh size. The stack is vibrated, and the resulting mass from each sieve recorded calculated as a percentage of the original mass. For these tests, the stack of sieves was vibrated for 10 minutes at 50 Hz using an Endecott's 'Minor' sieve shaker, shown in Figure 3.1. The sand remaining in each sieve was then measured, repeated three times, and the average passing weight recorded, shown in Table 3.1 and Table 3.2 for BP and SSC-3 respectively.

Figure 3.1: The Endecott sieve shaker and mounted set of sieves.

Table 3.1: Particle distribution results for BP.

Sieve size (mm)	Passing weight in % of total mass			Average % passing weight
	Run 1	Run 2	Run 3	
1.4	99.98	99.96	99.98	99.97
0.6	99.60	99.62	99.64	99.62
0.355	92.19	93.44	92.76	92.80
0.3	81.24	81.78	80.41	81.14
0.25	54.05	54.85	52.99	53.96
0.212	30.12	31.74	30.20	30.68
0.18	13.89	15.63	15.06	14.86
0.15	3.84	4.70	4.13	4.22
0.09	0.40	0.62	0.54	0.52
0	0.00	0.00	0.00	0.00
Mass of original sample (g)	115.67	109.18	132.83	-

Table 3.2: Particle distribution results for SSC-3.

Sieve size (mm)	Passing weight in % of total mass			Average % passing weight
	Run 1	Run 2	Run 3	
1.18	99.99	100.00	100.00	100.00
0.6	99.98	99.99	99.99	99.99
0.425	99.95	99.97	99.96	99.96
0.3	99.74	99.80	99.80	99.78
0.212	88.13	88.67	89.21	88.67
0.15	17.75	18.36	19.70	18.60
0.075	0.13	0.16	0.15	0.15
0.063	0.04	0.05	0.05	0.04
0	0.00	0.00	0.00	0.00
Mass of original sample (g)	112.32	145.93	124.72	-

A common method of displaying this data is by plotting the cumulative percentage of weight passing the sieves, shown in Figure 3.2. An initial run for BP (not shown) included a sieve of 0.425 mm, however this was removed and replaced with 0.3, 0.25, and 0.18 mm sieves to allow for better resolution in the range 0.212 – 0.25 mm.

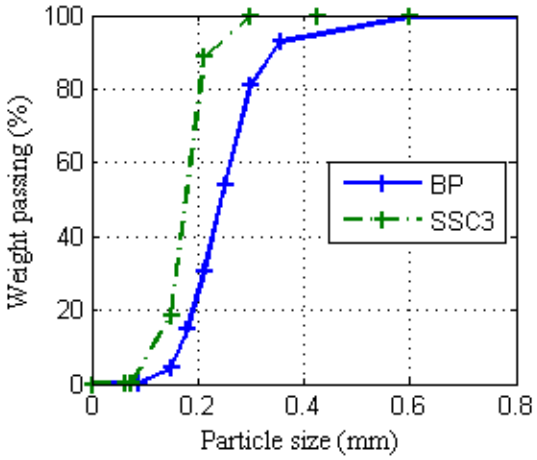

Figure 3.2: Particle size distribution of BP and SSC-3 by percentage of total weight passing.

From the figure, it is straightforward to see that SSC-3 is very uniform, with the sharpest percentage passing between 0.15 and 0.212 mm, and a low percentage passing of other sizes. BP on the other hand has a slightly larger average particle size around 0.25 mm, and a more even distribution as indicated by a slightly shallower gradient of curve. This gradation can be quantified with the use of two parameters, known as the coefficient of uniformity, C_u, and the coefficient of curvature, C_c [104]:

$$C_u = \frac{D_{60}}{D_{10}} \tag{3.1}$$

$$C_c = \frac{(D_{30})^2}{D_{10} \times D_{60}} \tag{3.2}$$

where D_{60} is the grain diameter at 60 percent passing, D_{30} is the diameter at 30 percent casing, and D_{10} is the diameter at 10 percent passing. A coefficient of uniformity, Cu, close to 1 indicates that the sand is very uniform, mostly containing particles of the same size. The coefficient of curvature, Cc, quantifies the curvature of the passing percentage graph, and a value between 1 and 3 indicates a well graded sand.

For the calculation of these formulas, in the likely case that a value of percentage does not correspond exactly to a sieve size, it is assumed that the distribution is linear between data points. It is possible that some variation in size distribution occurs between the sieve sizes, however this is the closest approximation without conducting the sand sieving process with custom-made sieves. The grain diameters at 10, 30, and 60 percent passing, as well as the corresponding coefficients are listed in Table 3.3.

Table 3.3: Diameter values and coefficients of SSC-3 and BP.

Sand	**D_{10}**	**D_{30}**	**D_{60}**	**C_u**	**C_c**
SSC-3	0.116	0.16	0.188	1.621	1.174
BP	0.166	0.21	0.26	1.566	1.021

From these values, it can be confirmed that both of these sands are very uniform, with coefficients of uniformity so close to unity. Additionally, the coefficient of curvature satisfies the requirement of falling between 1 and 3, so we can call both of these sands well graded, meaning that they have an even distribution of particle sizes.

3.4 Density measurements

3.4.1 Particle density

The particle density of a given sand is the density of a particle within a sample, and is constant for a specific sand, unlike bulk density which depends on the level of compaction. For sand that is made entirely from a single mineral, the particle density would simply be the density of that mineral. In practice however, sand is often a mixture of several different types of minerals.

To calculate this density, the volume of the particles must be calculated. This is most easily achieved by submerging a known mass of sand in a fluid (in this case, water was used), and measuring the volume displaced. Dividing the mass by the displaced volume will then yield the particle density of the granular material. This method was used on the returned lunar samples from the Apollo missions to calculate the lunar particle density [105].

Care must be taken when submerging to avoid either dry conglomerates, or trapped air pockets within the particles. These tests can be run in a vacuum chamber to assist in this by evacuating the air from the mixture, as advised in the American Society for Testing Materials (ASTM) standard [106], however this equipment was not available at the time of experiments.

A glass measuring cylinder graduated every 10 ml was used to measure the volume change of water. The cylinder was placed on a set of electronic scales (sensitivity 0.1 g), filled with a starting volume of 300 ml, and then the initial mass recorded. Sand was then added to the cylinder until the volume reached 350 ml, 370 ml, or 400 ml, with no variations noted with the different displaced volumes. The set-up is shown in Figure 3.3, illustrating the glass cylinder and electric scales used. Three measurements were taken and averaged to produce the final value of particle density, shown in Table 3.4. The fact that SSC-3 is cloudier than BP when submerged in water is indicative of a higher fine particulate content, an observation that is directly seen in Figure 3.2.

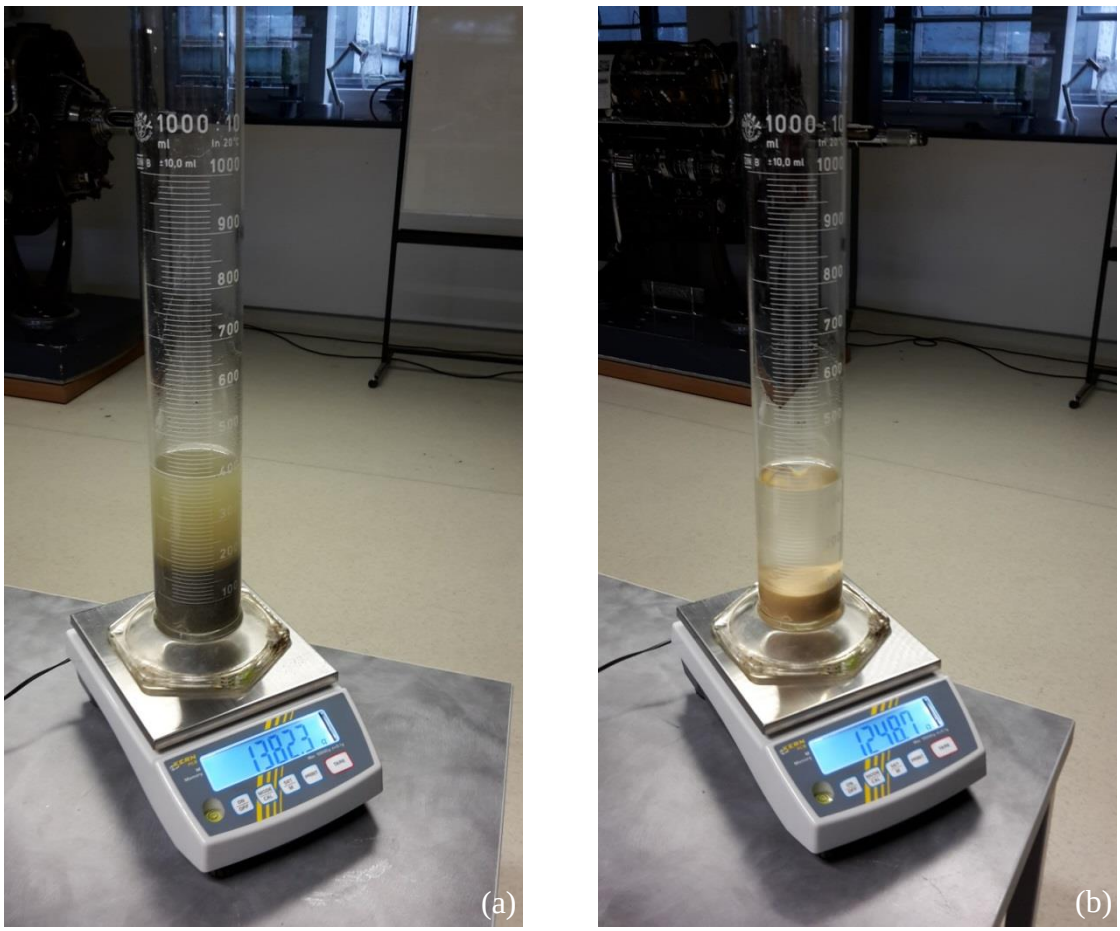

Figure 3.3: Submerged samples of sands in water for (a) SSC-3, and (b) BP. The mass and volume change was measured, determining the particle density.

Table 3.4: Particle density measurements of SSC-3 and BP sand. Each was measured three times at various masses and volumes, and no discernible differences were noted.

Sand		Mass of sand (g)	Volume displaced (ml)	Particle density (g/cc)	Average density (g/cc)	SD
SSC-3	Run 1	128.6	50	2.572	2.630	0.0504
	Run 2	186.6	70	2.666		
	Run 3	265.1	100	2.651		
BP	Run 1	130.7	50	2.614	2.629	0.0126
	Run 2	184.5	70	2.636		
	Run 3	263.6	100	2.636		

3.4.2 Minimum bulk density

The bulk density of sand can vary considerably depending on the method in which it is prepared, and so it is difficult to define what the absolute minimum or maximum density of a given sand should be. Experimentally determining the minimum bulk density is especially tricky to define, as loose sand is inherently unstable and will collapse with very little external influence, making any experiments dealing with it particularly problematic.

Instead of trying to define the absolute lowest density that can possibly be prepared, it is more prudent to establish a standardised method that can reproduce low density samples of sands, as it is more valuable to have a benchmark figure on which to compare other sand samples. These experiments used the ASTM "standard methods for minimum index density and unit weight of soils", which suggests three different methods to use, depending on the particle size distribution of the sand in question [107]. Method C is suggested for cohesionless sands in which 100% of particles fall below 9.5 mm, 90% or more falls below 2 mm, and up to 15% falls below 75 μm in size. As can be seen in Figure 3.2(a), both SSC-3 and BP satisfy all of these criteria.

Method C involves placing a known mass of granular material in a glass graduated cylinder (1 litre volume with 10 ml graduations for this case), and sealing the top with a rubber stopper. The cylinder is then tipped upside down and quickly tilted back to the original position, aerating the material. It is advised that this procedure be repeated until a constant volume is produced, in case the sand started in a compacted state. The surface of

the sand will often not be perfectly flat either so some amount of judgement is required by the operator to determine the average height of sand within the graduated cylinder.

Table 3.5: Minimum density measurements of SSC-3 and BP sand. Each was measured using three different masses, with no significant difference between the resulting densities.

Sand		Mass of sand (g)	Volume (ml)	Bulk density (g/cc)	Average density (g/cc)	SD
SSC-3	Run 1	414.3	300	1.381	1.381	0.00189
	Run 2	677.4	490	1.382		
	Run 3	854.8	620	1.378		
BP	Run 1	436.8	310	1.409	1.405	0.00342
	Run 2	715.5	510	1.403		
	Run 3	813.9	580	1.403		

3.4.3 Maximum bulk density

The ASTM standard method for determining maximum bulk density uses a specialised vibrating table and compression unit, which was not available for this work. Instead, the method used in the literature for the other sands SSC-1, SSC-2, and ES-3, was followed [56], which involves using the particle density of the sand and estimating the void ratio at maximum bulk density. The void ratio can vary from one sand to the next depending of the size distributions (as smaller particles will tend to fill in the voids left by larger particles), and particle shape (which can lead to irregular and inefficient packing). Following on from previous work that analysed the SSC-1, SSC-2, and ES-3 regoliths, a void ratio of 25% was used. The void ratio for the optimal packing structure of uniform spheres is defined as:

$$1 - \frac{\pi}{3\sqrt{2}} \approx 0.25952 \rightarrow 26\% \tag{3.3}$$

And the void ratio of 25% was chosen to reflect the fact that some smaller sized particles will tend to fill the voids, leading to slightly lower void ratio [56]. Using this value and the calculated value of particle density, the estimated maximum bulk densities of the sands are shown in Table 3.6.

Table 3.6: Estimated maximum bulk density values for SSC-3 and BP. These were calculated by assuming a void ratio of 25%, as used in [56].

Sand	Maximum density (g/cc)	SD
SSC-3	1.972	0.0378
BP	1.971	0.00947

3.5 Soil preparation techniques

At this stage, most of the necessary characteristics of the sand used have been experimentally established. These values can be considered ‘constants’ for the type of sand used, however a sample of sand can exist in nature at varying levels of bulk density, with a very loose sample being a low bulk density, and a compacted sample a very high bulk density. Precise reproduction of a specific bulk density is vital for accurate results and comparisons during testing, and this section involves establishing a method to produce consistent preparations of both a loose and a compact sample of test, for use in future testing. The regolith BP was used during these calibration tests.

Note that whilst the loose and compact density values are measured here, this value can slightly vary depending on the environment, such as the temperature and humidity etc. This is alleviated in several ways, such as ensuring the temperature in the laboratory is kept constant, and endeavouring to complete all tests for one sand in the same day, to ensure the conditions are the same. Additionally, the bulk density used in each test will be measured, allowing the user to track any large changes in density, should they arise.

3.5.1 Low density sand preparations

A mentioned in section 2.3.2, low density samples of sand can be produced by pouring it into a final container. For ease of use, the ‘rain’ method was not considered for these tests, focussing instead on the ‘pour’ method. A pour height of above 50 cm is required to result in a homogeneous final distribution of sand, and the following sections examine the different methods of pouring.

3.5.1.1 Low density consistency

Due to the huge effect on penetration force that sand density can have [90], consistency in sand sample production is arguably more important than producing the absolute maximum or minimum bulk density achievable. One way to achieve consistency is to ensure that the conditions and manner of the sand preparation are identical between different iterations.

To test the consistency in density from pouring sand into a container, two methods were tried: pouring sand by hand from one container to another at a certain distance, shown in Figure 2.17 and utilised by Gouache et al [91] (which is referred to as the ‘hand-pour method’), and a method involving containers suspending at specific heights, which is referred to as the ‘suspended-pour method’.

For the suspended pour method, a bucket with a 2 cm diameter hole was used. A small aluminium plate, tied to a length of string, was placed to cover this hole, and the bucket was filled with an excess of sand. This was then suspended from a long supporting bar, and supported by two tripods raised to a specific height, as shown in Figure 3.4(a). The testing container was placed directly below the bucket, and the string pulled to remove the aluminium cover plate, allowing the sand to flow from the hopper to the testing container below. Care was taken to ensure none of the apparatus was touched as the testing container filled, with the intention that the less human interaction involved, the more likely consistent reading could be achieved. Due to the fact that the sand rises as it fills the container, a height of 100 cm from the bottom of the bucket to the bottom of the sand container was used in this method to ensure that the sand always falls at least 50cm; the minimum height required for ideal mixing to occur [89].

Figure 3.4: Different pouring methods using (a) the suspended-pour method, and (b) the hand-pour method.

Shown in Figure 3.4(b) the hand-pour method involved filling a bucket with sand and then pouring it into the sand container below. As this was done by hand, the pouring height could only be approximated at 100 cm, and the pour rate was determined by the operator. In both cases, the preparation caused a build-up of sand on the top of the container. After the pour was completed, this mound was scraped off to the level of the top of the container. This ensures a constant volume of sand to facilitate calculating the bulk density of the sand with the measured mass.

The sand container was filled and the density recorded 10 times for both of the preparation methods. As can be seen in Table 3.7, the suspended-pour method not only resulted in a more consistent density (a standard deviation of 0.0029 as opposed to 0.0034), but it also resulted in lower average density (1.441 g/cc as opposed to 1.472 g/cc). Both of these results are beneficial, so the suspended-pour method was used as the method for all

future experiments. This method was also used for the production of any low bulk density containers of sand.

Table 3.7: Comparisons in resultant density of BP between different preparation methods.

Run	Suspended-Pour Density (g/cc)	Hand-Pour Density (g/cc)
1	1.443	1.464
2	1.442	1.473
3	1.441	1.475
4	1.444	1.475
5	1.442	1.473
6	1.443	1.468
7	1.436	1.471
8	1.437	1.470
9	1.437	1.470
10	1.441	1.470
Average Density	1.441	1.471
SD	0.0029	0.0034

3.5.2 High density sand preparations

Due to its granular nature, sand can exist at a variety of different bulk densities, depending on environmental factors such as local geography and air currents. To fully test the limits of a penetration device, the consistent production of both low and high density sand is required. As discussed in section 2.3.1, any vibration or shock will generally result in the sand settling into a more efficient packing structure, thus increasing the density. Controlling the way in which this is done should allow consistent reproduction of higher density sand.

3.5.2.1 Consistency and accuracy with high density sand

Experiments were conducted to see if vibration resulted in a non-homogenous distribution of sand particle size. For example, it is known that shaking a box containing many differently sized particles causes the larger particles to rise to the surface, known as

the ‘Brazil Nut effect’ [108]. In these tests, the container of sand was half-filled with sand and vibrated horizontally at various frequencies, amplitudes, and durations. Samples were then taken from the bottom and top of the container and put through the sand sieving process. No significant difference was noted in particle size distribution between samples taken from the top and from the bottom of the container.

The reason for the lack of size separation is likely due to the fact that the samples of sand used were especially uniform, with most sizes of particle within 100 μm size of each other. Indeed, it has previously been confirmed that particle size is the major controlling factor for the segregation of granular material under vibration [109]. The Brazil nut effect is most clearly seen in granular material that has a vastly varied particle size distribution (e.g., the large difference in size between Brazil nuts and other, smaller nuts). In any case, it is advantageous for future experiments that the vibration did not affect the distribution of sand enough to cause concern.

The advantage of this particular set-up was that the frequency and amplitude were controllable, allowing fine-tuning of the vibration if required. However, the mass of a full container was too great for this shaker, resulting in portions of the container to be jammed and thus would not be fully reset. Many different designs and method of vibrations were considered, eventually settling on the design shown in Figure 3.5. Here, an electric powered sander (‘Power Performance’ sheet sander, PSS300A 300 W) is bolted to the back of the container of sand, and placed upon a platform that allows movement of the container. The plate of the sander vibrates in a circular motion, with a dial labelled 1 - 6 that allowed control over the input power, referred to as ‘Power 1’, ‘Power 2’ etc. where applicable.

Figure 3.5: The sand shaker design.

To test the reliability of this vibration method, the suspended-pour technique described in section 3.5.1 was repeated, but with the additional step of leaving the container to vibrate as it fills up with sand. The top of the container was then scraped flat and the mass of sand measured as before, allowing accurate calculation of the bulk density. Measurements were taken at Power 1, 3, and 6, resulting in final bulk densities of 1.628, 1.604, and 1.604 g/cc respectively. The Power 1 setting, whilst being the lowest power, still provided more than enough vibration to completely fluidise all of the sand within the container, thereby eliminated any jammed regions. It also resulted in the highest density, so the decision was taken to only use this level of vibration for future experiments

Different amplitudes of vibration and frequency have a large influence on the final density, and a finely controlled shaker might indeed produce a denser sample of sand. For the purposes of this work, however, a density value that is simple and consistent to reproduce is of more value, so the Power 1 setting was deemed sufficient for all experiments outlined in this thesis. Additionally, the sand shaker design allows the container to be manoeuvred very easily without disturbing the sand, whereas a more complicated rig would potentially disturb and alter the sand during removal. Sand production using barrel shakers could be useful for further tests if warranted, in which case a new rig would need to be designed.

3.5.3 Relative density

With the method of sand preparation finalised, it is possible to measure what the bulk density of the sand for testing can be. Since the bulk density can lie anywhere between its theoretical minimum and maximum bulk density, often it is easiest to refer to the *relative density* of a sample of sand. This is often expressed as a percentage, where 0% relative density is the theoretical minimum density and measured in section 3.4.2, and 100% is the theoretical maximum density and measured in 3.4.3. More precisely, it is commonly defined as the ratio of the difference between the maximum void ratio and the void ratio of the sample, to the difference between its maximum and minimum void ratio [107]:

$$D_r = \frac{e_{max} - e}{e_{max} - e_{min}} \times 100 \tag{3.4}$$

where e_{max} is the maximum void ratio, e_{min} is the minimum void ratio, and e is the void ratio of the sand in its current state. For our purposes, it is perhaps easier to express this equation in its corresponding dry density form:

$$D_r = \frac{\rho_{max}}{\rho} \times \frac{\rho - \rho_{min}}{\rho_{max} - \rho_{min}} \times 100 \tag{3.5}$$

where ρ_{max} is the maximum density, ρ_{min} is the minimum density, and ρ is the bulk density of the sand after preparation.

As mentioned in section 3.4.2, the method of obtaining the value of minimum bulk density is to enable a benchmark figure, and not to create the absolute lowest density possible. This means that a user producing a loose density sample of sand might end up creating bulk density that is actually below the value for minimum bulk density, thus resulting in a negative relative density.

To obtain an average value of the bulk density of low and high density samples, ten preparations were conducted for each of the sands used, including the pre-characterised sands from SSC. This is shown in Table 3.8 along with the standard deviations. The full data can be found in the appendix CD.

Table 3.8: Results of preparing the regoliths.

Sand	Loose preparation		Relative Density (%)	Compact preparation		Relative Density (%)
	Density (g/cc)	SD		Density (g/cc)	SD	
SSC-1	1.408	0.0023	7.4	1.709	0.0047	83.0
SSC-2	1.882	0.0061	-20.3	2.229	0.0043	71.3
SSC-3	1.384	0.0000	0.7	1.595	0.0000	44.7
ES-3	1.470	0.0000	-8.8	1.671	0.0000	47.7
BP	1.432	0.0013	6.5	1.626	0.0013	47.4

3.6 Friction angle measurements

The Direct Shear Test (DST) is an experimental method to determine the internal friction angle φ and the cohesion *c* of a granular material. This subsection will cover the experimental protocol, as well as an examination of the results and implications. Most notably, the values of friction angle obtained in these tests will be useful for the predictive models discussed in section 2.3.4.

3.6.1 Apparatus and protocol

3.6.1.1 Testing principles

The Direct Shear Test measures the force required to create a shear plane within a sample of granular material. A container, 6 cm by 6 cm, and 3 cm deep is used within the DST apparatus, and is filled with a sand sample to a desired relative density level. This container is horizontally split into two halves, with the bottom half able to slide underneath the top half, illustrated in Figure 3.6.

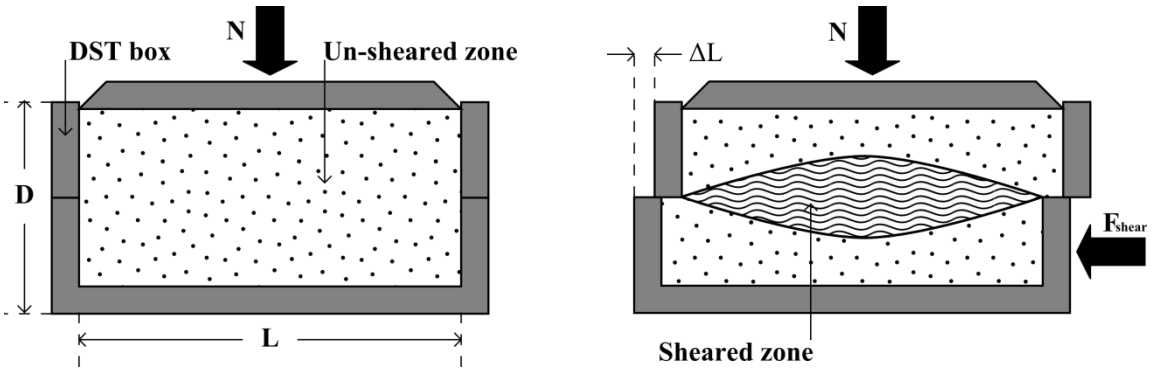

Figure 3.6: Overview of the direct shear test apparatus and operating principles.

A top cap is placed on the sample and a normal force *N* applied, containing the sand within the container. This gives a normal stress of:

$$\sigma_n = \frac{N}{S} \tag{3.6}$$

where σ_n is the normal stress, *N* is the applied normal force, and *S* is the cross-sectional area of the sample box (*L*x*L*), equal to 36 cm^2 in this set-up. With the top half of the container fixed in place, a shearing force F_{shear} pushes the bottom half of the container, resulting in a lateral displacement, ΔL. Likewise, the shear stress can be calculated as:

$$\tau = \frac{F_{shear}}{S} \tag{3.7}$$

where τ is the shear stress, and F_{shear} is the applied shear force. The shear strain, ε, can be calculated as the displacement over the original length:

$$\varepsilon = \frac{\Delta L}{L} \tag{3.8}$$

where ΔL is the displacement between the box-halves, and L is the internal length of the box.

The full DST set-up can be seen in Figure 3.7, with the hanging weight providing the normal force, and the displacement crank supplying the shearing movement. The proving ring consists of a sprung steel ring with a displacement gauge inside. For small deflections, the ring follows Hooke's Law, and the acting force can be calculated using the

displacement and a calibrated constant, in this case 1.384 N/div. With the container filled and the normal force applied, the lower box-half is slowly displaced, and the resultant shear force measured via a proving ring.

Figure 3.7: The DST machine. The sand container section is displayed in Figure 3.8.

A close up of the DST box is shown in Figure 3.8, showing the physical device compared to the simplified overview in Figure 3.6.

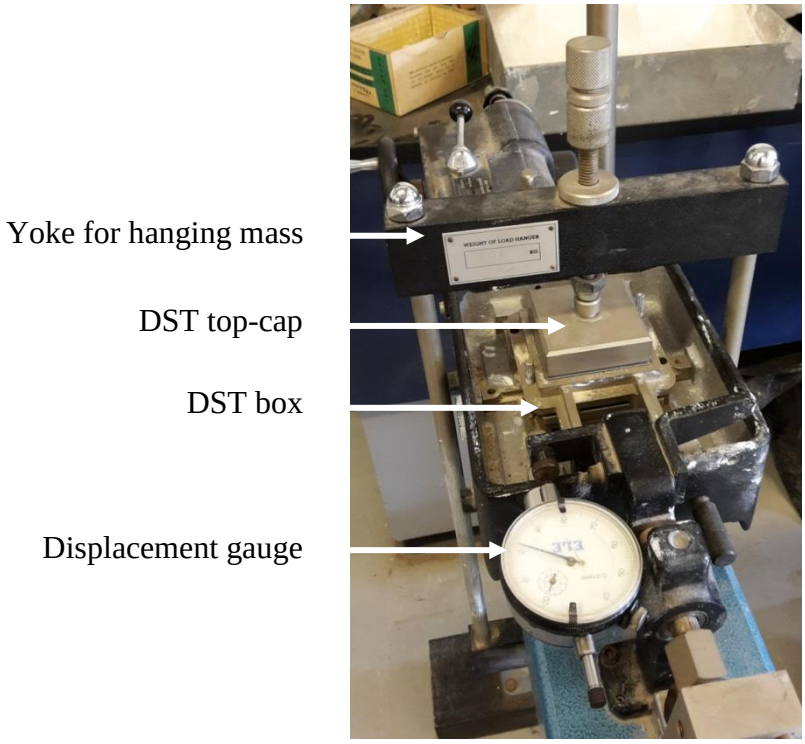

Figure 3.8: Close up of the DST sand container.

3.6.2 Results

A reading of the force was taken every 0.5 mm, the shear force measured via the proving ring gauge, and the shear strain and shear strain calculated accordingly. This was conducted three times using normal forces of 41.7, 83.3, and 152.8 kPa. The weight of the hanging yoke, 4.5 kg, caused any low density sand to compress, resulting in an unknown density. For this reason, only high density samples of SSC-3 and BP were tested, both at 1.60 g/cc. As will be seen in further chapters, the most interesting effects of ultrasonic penetration are seen in the high density samples, so it is perhaps more beneficial to obtain the friction angles at high density.

Plotting the shear stress against shear strain gives a classic stress-strain graph, shown in Figure 3.9 for SSC-3 and in Figure 3.10 for BP.

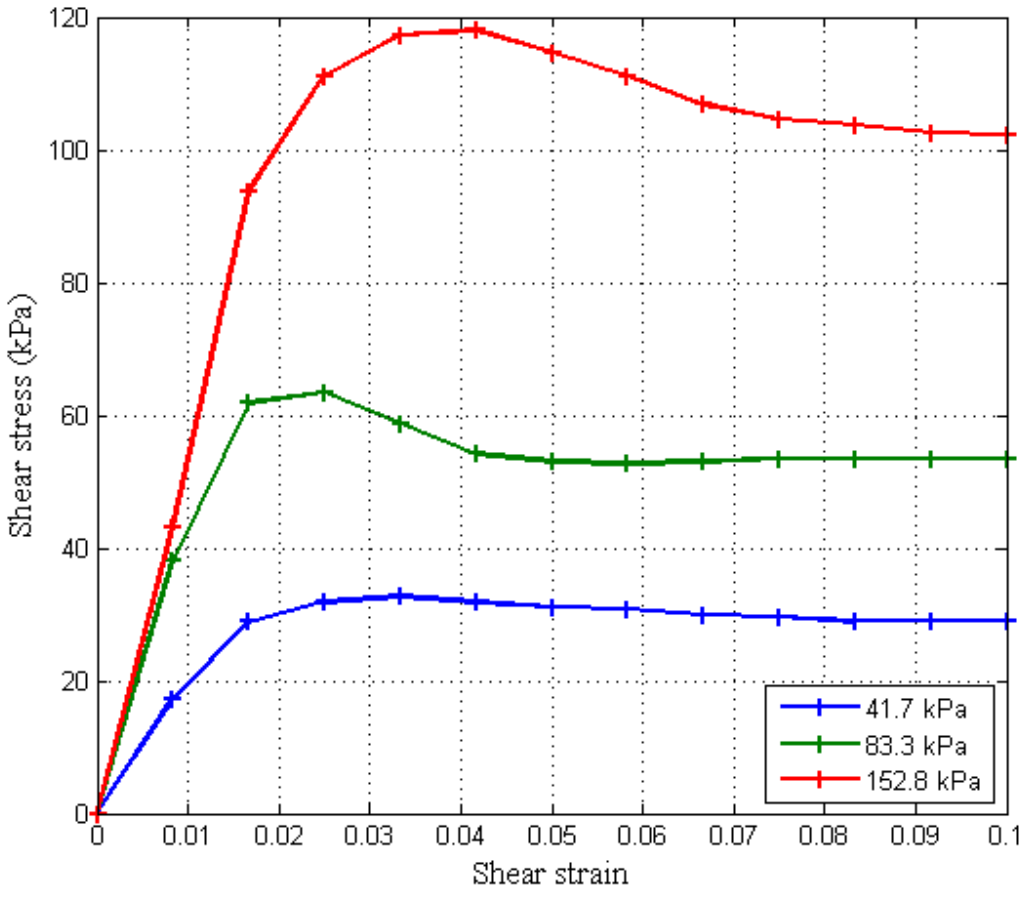

Figure 3.9: Shear stress for SSC-3 at three different normal stresses.

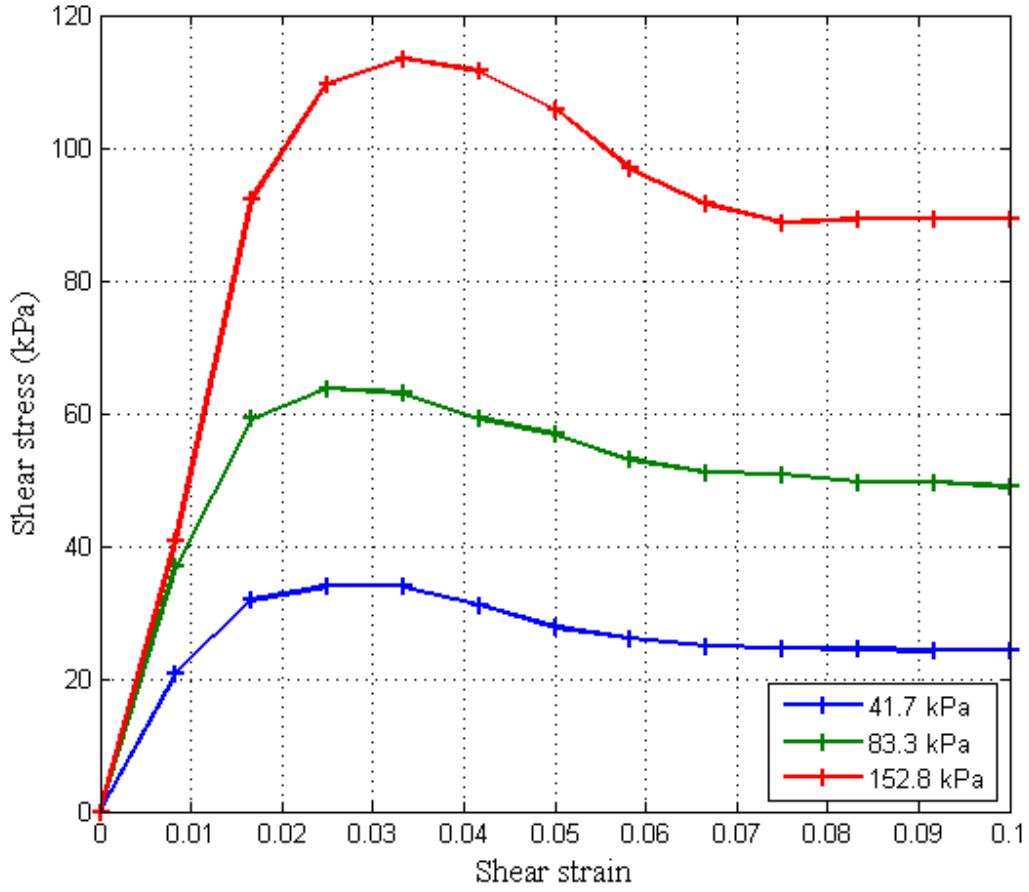

Figure 3.10: Shear stress for BP at three different normal stresses.

3.6.2.1 Shear stress at failure

The maximum values of shear stress shown in Figure 3.9 and Figure 3.10 correspond to the failure point of the sand. At this point, the friction of the sand at that particular normal force is overcome, causing the particles to slide over each other. In the foundation of building this can be catastrophic, but for penetration this is a vital stage, and allows the probe to progress through the sand once this limit is overcome. It is important to note that at small changes in distance, sand can exhibit elastic properties, as shown by the initial linear relation in the 152.8 kPa normal stress plot in Figure 3.9 and Figure 3.10. This effect is only apparent at very small strains however, due to the nearly perfectly-plastic nature of sand.

Plotting this maximum shear stress, τ_f, against the corresponding normal stress, σ_n, gives the failure envelope of the granular material, shown in Figure 3.11.

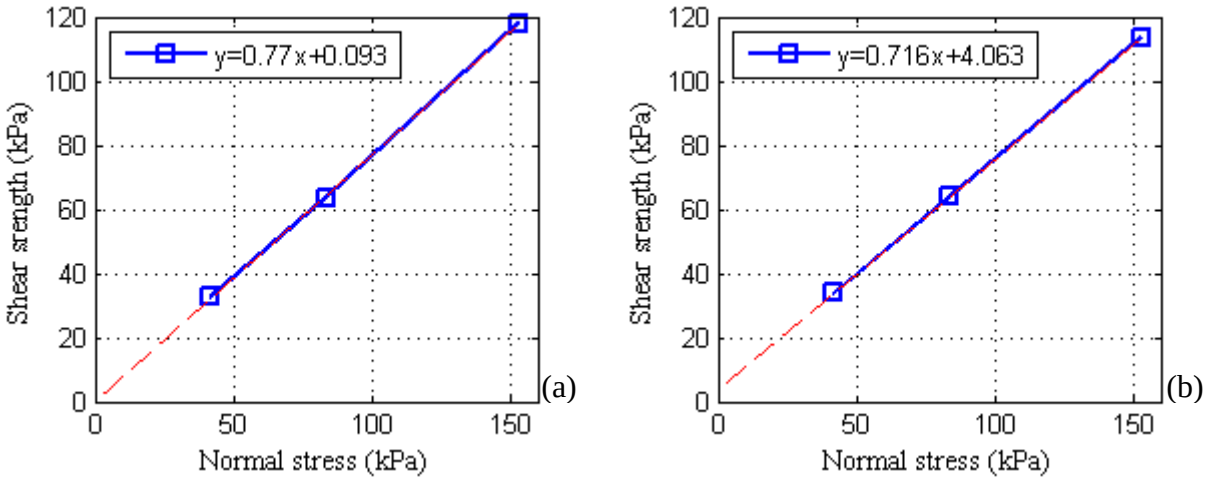

Figure 3.11: The shear strength failure envelopes for high density (a) SSC-3, and (b) BP. A line of best fit is taken of the three values to compare to Coulomb's law, giving R^2 values of 0.9997 for SSC-3, and 1 for BP.

Any combination of shear stress and normal stress that fall above this line will result in a failure of the soil. This failure can generally be approximated as a straight line [110], known as 'Coulomb's law', and defined as:

$$\tau_f = \mathrm{c} + \sigma_n \tan(\varphi) \tag{3.9}$$

where τ_f is the shear stress at failure, c is the cohesion, σ_n is the normal stress, and φ is the friction angle [110]. Taking a best-fit line through the data points results in a straight line of the form y=mx+c, where in this case y= τ_f, the y intercept c= c, and the gradient m=tan(φ). Taking the inverse tan of the gradient therefore gives the value of internal friction, shown in the friction angle summary in section 3.6.3.

3.6.2.2 Critical shear stress

The peaks seen in Figure 3.9 and Figure 3.10 are only seen in high density sand. This is due to the movement of the grains during shearing, and in high density sand, the low void ratio means that the grains have nowhere to move, other than up and over their neighbouring grains. The extra force required to 'lift' these grains is represented by the peak in shear stress. Since the sand has expanded, the density will always be lower at the end of shearing. Figure 3.12(a) shows the movement of grains whilst shearing along plane XX in high density sand.

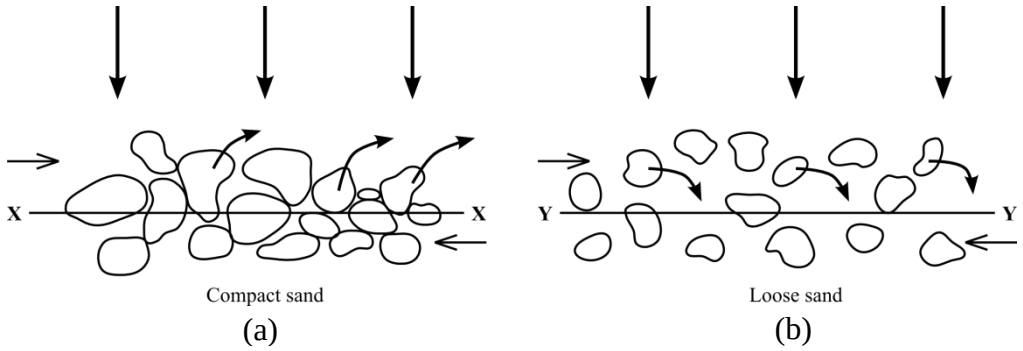

Figure 3.12: Movement of particles in DST tests for different relative densities. [110]

Low density sand, on the other hand, possesses the necessary voids for particles to move into, shown in Figure 3.12(b) when sheared along the plane YY. This results in a general collapse of the grains, and a steadier increase in shear stress.

For large displacements, both the stress-strain plots of low and high density sand approach the same common point, known as the 'residual shear strength', or the 'critical shear strength', τ_{cr}. Low density tests were not conducted for this work, due to the apparatus not able to sufficiently provide normal forces low enough so that the sand is not compressed and compacted, but an example of this effect is shown in Figure 3.13. The difference in stress between peak and critical shear strength, E, represents the extra work required to produce the vertical component of motion illustrated in Figure 3.12.

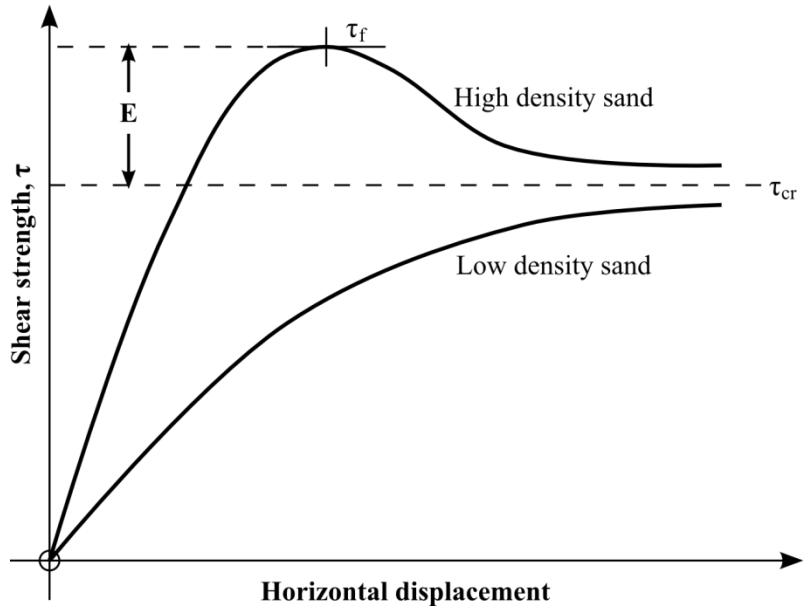

Figure 3.13: Shear strength characteristics of high and low density sand, approaching the same critical strength value. [110]

Taking the critical shear stress, denoted by the final values from the stress-strain curve, we get a critical shear strength envelope, shown in Figure 3.14. A new set of values for friction angle and cohesion can thus be calculated from this critical strength envelope, shown in the friction angle summary in section 3.6.3.

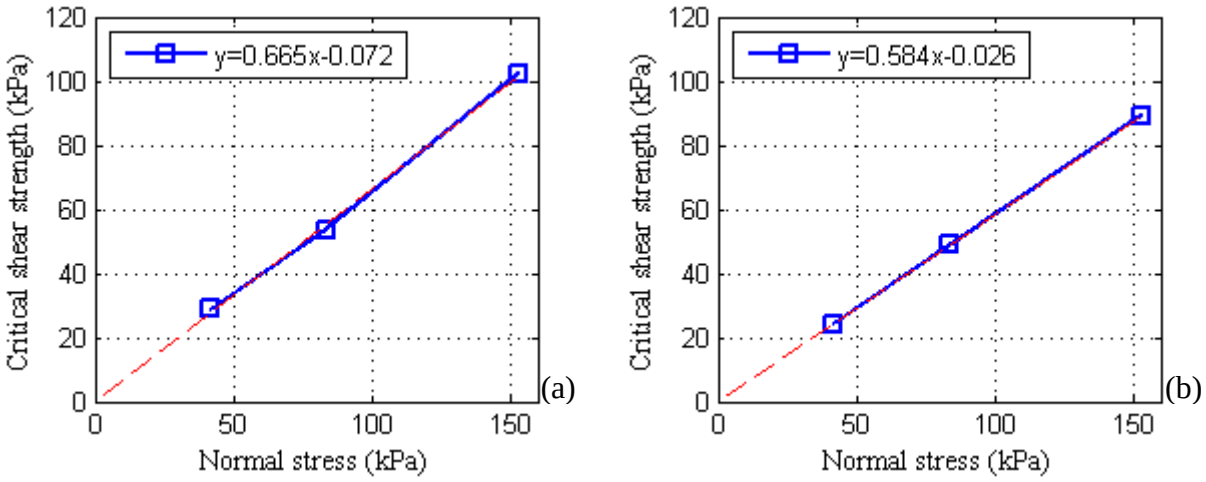

Figure 3.14: The critical shear strength envelopes for high density (a) SSC-3, and (b) BP. A line of best fit is again taken to compare to Coulomb's law, giving R^2 values of 0.998 for SSC-3 and 1 for BP. Note, the gradients are lower than for the strength failure envelopes.

3.6.2.3 Cohesion

The term 'cohesion', included in equation (3.9), refers to the internal forces holding particles together from causes other than friction, such as water tension for saturated soils, or electrostatic effects for charged particles. According to Coulomb's law, it is the shear stress required, if any, to shear a sample of sand with no normal stresses applied, and it represented by where the strength envelope intersects the y-axis in Figure 3.11 and Figure 3.14.

Normally, dry sands and soils should exhibit zero cohesion, since there are no forces holding the particles together. However, there is ambiguity in the literature as to what cohesion really is, how it should be defined, and if it is appropriate to ignore it. Additional terms such as 'adhesion' can further confuse the operator.

It is generally agreed that the cohesion resulting from water effects is called the 'apparent cohesion', denoted by c_u or c_{app} [110]. The binding resulting from the electrical forces between dry, fine grains is called the 'true cohesion', denoted by c' [111]. Water

tension in civil engineering is normally the dominant value, where it can reach 10,000 kPa, as opposed to *c'* which rarely reaches more than 25 kPa in all but the most highly consolidated clays [111].

Indeed, some argue that the purpose of direct shear test is to only measure the shear strength as a function of normal load. The test does not directly measure friction or cohesion, but rather these are in fact simply *"mathematical parameters derived from the laboratory test results"* [112].

Our usage of cohesion is most similar to this final definition, simply defined as the value of the intercept between the shear strength envelope and the vertical axis. As these sands are all dry, this could also be considered the true cohesion of the soil. The associated values of cohesion from both the critical shear strength envelopes and the peak shear strength envelopes are shown in the friction angle summary in section 3.6.3.

3.6.2.4 'Secant' or 'tangent' angle of friction

It is worth noting that there are in fact two common ways of calculating friction angle, known as the 'tangent' and the 'secant' angle. The 'tangent' value is obtained from conducting a set of experiments and plotting the shear strength failure envelope as we have done, taking the inverse tan of the gradient to give the tangent angle of internal friction.

The 'secant' angle is often used in civil engineering where a large number of DST experiments are unable to be conducted, and normally uses just one data point. Taking the highest envisioned normal and shear stress, the secant angle is thus the inverse tan of a single value of shear stress at failure divided by the corresponding normal stress. This takes the value of cohesion to be zero, and in essence is the angle of the straight lines drawn from the data point to the origin [112].

These tests have sampled enough points in order to create a line for the shear strength envelopes, and thus will use the more accurate 'tangent' angle of friction.

3.6.3 Friction angle summary

Using both the critical and the peak shear strength envelopes, we are able to get two values of friction angle and cohesion for each sand. These are summarised in Table 3.9.

Table 3.9: Experimental values of the internal friction angle and cohesion for the sands SSC-3 and BP. Also shown are the values obtained from the critical shear stress.

	Critical shear stress		Peak shear stress	
Sand	Angle φ (º)	Cohesion (kPa)	Angle φ (º)	Cohesion (kPa)
SSC-3	33.63	-0.072	37.60	0.093
BP	30.30	-0.026	35.60	4.063

It is interesting to note that the cohesion value is actually negative for both sands in the critical state. This would imply that the particles actually repel each other, but it is unlikely that this is the case. The cohesion values of all cases but peak shear stress BP are so low that they can be taken as essentially zero for our tests. However in lower gravity environments such as Mars, cohesion is more significant, so should not be assumed to be zero for these situations [113].

The critical shear strength represents the strength over large displacements, and is often used in civil engineering. The peak, or failure, shear strength of the sand represents the point at which the soil starts to fail, and is often used to 'play-it-safe'. Failure of the soil is what penetration relies on, so it is the peak friction angle that is of most interest.

3.7 Overviews and conclusions

Four characterised Martian regolith simulants, SSC-1, SSC-2, SSC-3, and ES-3, along with an additional block-paving sand referred to as 'BP' were tested and fully characterised. These gave a total of five different regoliths for ultrasonic testing, covering a broad range of sizes and final densities. An overview of the regolith characteristics is shown in Table 3.10, with the particle size distributions shown in Figure 3.15 and a visual representation of them in Figure 3.16. Note that for the information in this subsection, all measurements for BP and SSC-3 were conducted in Glasgow by the author, whereas the

regoliths SSC-1, SSC-2, and ES-3 were already measured and characterised previously [56], and combined in this section for reference and comparison purposes.

Table 3.10: Overview of the five regolith simulants chosen for experiments.

Regolith	Distribution	Size	Shape	Material
SSC-1	Broad	Medium	Sub-rounded	Quartz
SSC-2	Uniform	Very fine	Angular	Garnet
SSC-3	Uniform	Fine	Sub-angular	Quartz
ES-3	Broad	Coarse	Sub-rounded	Quartz
BP	Uniform	Medium	Sub-rounded	Quartz

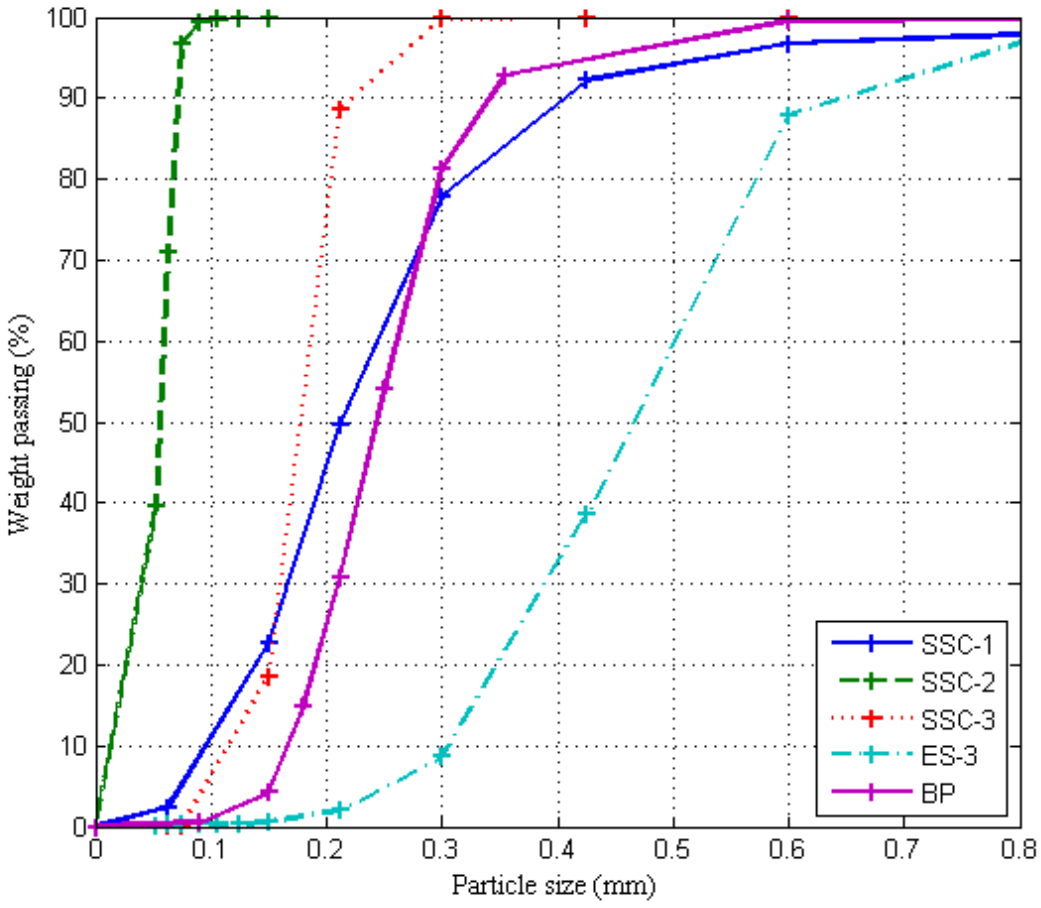

Figure 3.15: Particle size distributions of the five regoliths.

Figure 3.16: The five regoliths used in these experiments. (a) SSC-1, (b) SSC-2, (c) SSC-3, (d) ES-3, (e) BP.

Measurements on the maximum and minimum densities of BP and SSC-3 were also conducted, using the same ASTM standard methods used previously for SSC-1, SSC-2, and ES-3. The friction angle, one of the most important values in penetration mechanics, was experimentally calculated for BP and SSC-3 using an ELE™ Direct Shear Test apparatus, and will be especially useful in comparisons with predictive models. The equipment was not able to measure the friction angle of low density samples of sand due to the weight of the yoke, so these values are for high density samples only.

As well as characterising the regoliths, a procedure to acquire consistent low and high density samples of sand was also established, allowing accuracy for future experiments. Table 3.11 summarises the minimum and maximum densities of all sands used, as well as the value of relative densities of the low and high densities obtainable using the preparation methods described in sections 3.5.1 and 3.5.2 respectively. It should be noted, however, that the specific value of bulk density could vary slightly day-to-day due to small differences in environmental conditions, so the bulk density will always be measured for each experiment.

Table 3.11: Summary of the properties of the sands used. The values for minimum, maximum, and particle densities, as well as the friction angles for the sands SSC-1, SSC-2, and ES-3 are all taken from previous work [56]. *All other values were experimentally established in this chapter.*

Sand	**Bulk Density (g/cc)**				**Particle Density (g/cc)**	**Relative Density (%)**		**Friction Angle (º)**	
	Min	**Loose**	**Compact**	**Max**		**Loose**	**Compact**	**Crit**	**Fail**
SSC-1	1.384	1.408	1.709	1.795	2.394	7.4	8.3	45	48
SSC-2	1.949	1.882	2.229	2.366	3.154	-20.3	71.3	43	43
SSC-3	1.381	1.384	1.595	1.972	2.630	0.7	44.7	33.6	37.6
ES-3	1.498	1.470	1.671	1.914	2.599	-8.8	47.7	35	48
BP	1.405	1.432	1.626	1.971	2.629	6.5	47.4	30.3	35.6

Chapter 4

Ultrasonic Horn Design

One of the most common designs for ultrasonic horns is resonance at the operating frequency to occur at the L1 mode (the 1st longitudinal vibration mode). This means that the horn will have a single nodal point (normally located around halfway along the shaft), and each end of the horn vibrating out of phase with each other. As described in section 2.2.2, the step in a step horn should be located at a nodal point for maximum amplification, and thus requires the step to be located roughly halfway along the shaft as well. This significantly reduces the maximum allowable penetration depth, as the straight section of shaft is limited to only half of the horn. The overall length is determined by the chosen resonance frequency and material choice (which dictates the acoustical velocity), with the following equation relating them:

$$f = \frac{nv}{2L} \tag{4.1}$$

where f is the resonant frequency, n is an integer, v is the velocity of the wave in the material, and L is the length of the material. For resonant frequency of 20 kHz (the operating frequency of the transducer) and titanium as the material, this equation gives a maximum penetration distance of roughly 8 cm (half of 16 cm). This is a significant constraint on the penetration experiments, so it was decided to design the horn to resonate at the L2 mode. This mode effectively doubles the allowable length of the horn by allowing an additional half-wavelength, creating two nodal points at ¼ and ¾ along the length. Since the step has to be located only at one of these nodal points, the maximum penetration distance is three-times greater than a corresponding L1 horn. The horn itself was designed in Abaqus, and the final design shown in Figure 4.1

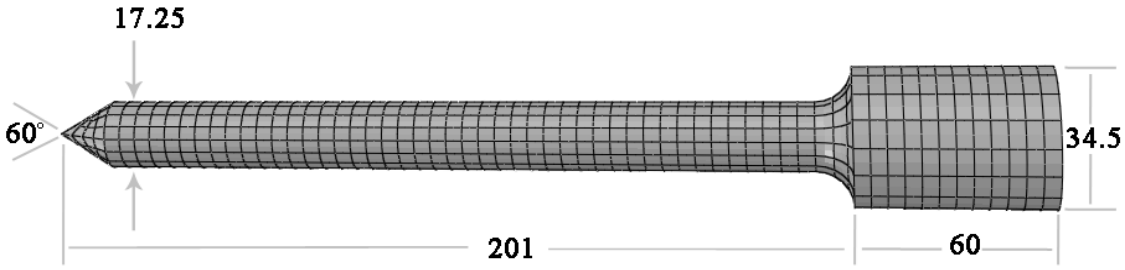

Figure 4.1: Ultrasonic horn. Measurements are in mm.

4.1 Experimental modal analysis

After the horn was produced, an impedance analysis was run on it to check the resonant frequencies. Unfortunately it had a resonant frequency of 21.2 kHz instead of the designed frequency of 20 kHz, most likely due to the cutting tool running too hot during manufacture. The range of frequencies that the transducer and amplifier can track across is 19.5-20.5 kHz, meaning that the horn would not function as intended. The general solution to this is to alter the resonant frequency of a horn is to change the length. This however was difficult in this particular case, due to the fact that the resonance was too high, and therefore required an addition of length to lower the frequency (it is much easier to take material off, than to put material on). A simple titanium washer 24mm long was produced, which was inserted between the base of the horn and the transducer and the whole set-up tightened together. This increased the overall length, and brought the resonance down to 20.3 kHz and within the workable range.

Impedance analysis allows a user to identify resonances within a material, however a full Experimental Modal Analysis (EMA) must be run in order to determine what mode these resonances are in, e.g. torsional, longitudinal, bending etc. This process involves passing a white noise signal into the transducer, effectively making the horn vibrate randomly at all frequencies. The range of frequencies in the white noise signal can be chosen by the user, with the range 16-40 kHz being chosen for this experiment to encompass the main 20 kHz resonance, plus any nearby resonances that might be significant. A Polytec CLV 3D laser vibrometer, Figure 4.2, was focused onto a single point on the horn at a time, measuring the displacement in 3 dimensions. 72 points and measurements were taken in total; 12 longitudinal points every 20 mm along the length, with a 6-fold rotational symmetry.

Figure 4.2: Probe in the EMA equipment

Each result from each point is attributed to its relative position on the horn. The software ME'scope, by Vibrant Technology Inc., then combines all of this information, giving an animated model of the horn's vibration at different frequencies. A frame of this animation is shown in Figure 4.3 as an example.

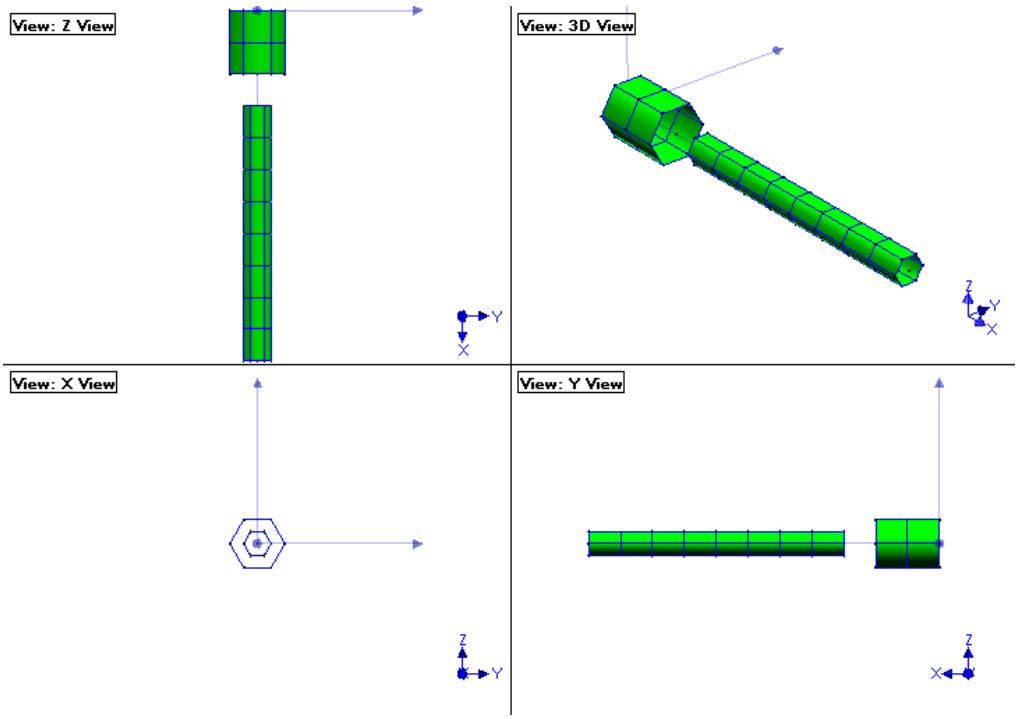

Figure 4.3: Frame of the resulting animation of motion from the EMA.

The software can also give the frequency response for each point on the horn, identifying the location of the resonant frequencies. An example of the response at the tip of the horn is shown in Figure 4.4. The large peak shown at 20.4 kHz is the resonance that is of interest, and the animation confirms that the mode is completely longitudinal. The next nearest mode at 25 kHz is a bending mode, but this is far enough away that it should not be a big problem in further experiments.

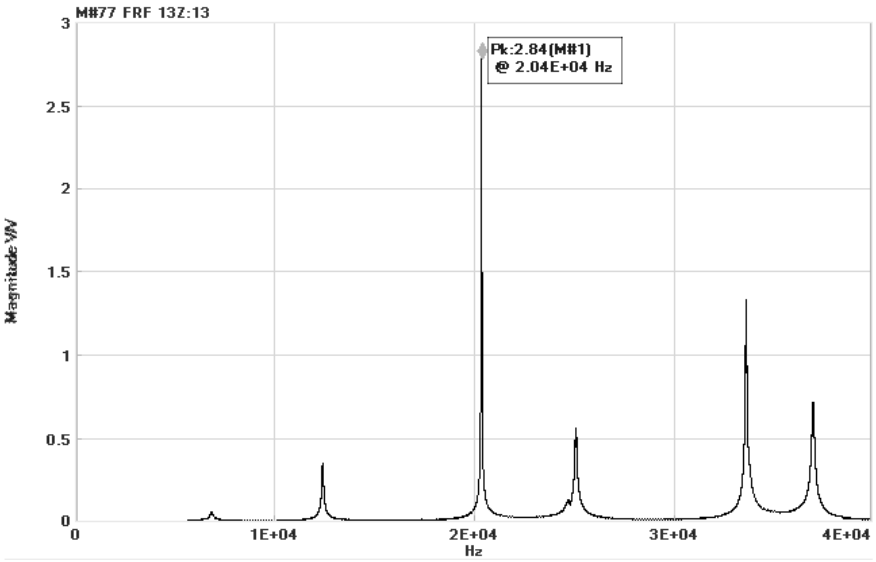

Figure 4.4: EMA results of the probe

Chapter 5

High-Speed Camera Tests

To understand the physical process of what would happen to the sand during ultrasonic penetration, a high-speed camera test was designed to record the motion of the sand and view it at a much slower speed. The biggest issue with trying to see the motion of particles during a penetration run is that it is extremely difficult to get a clear visual line-of-sight without severely disrupting the layout. Some tests have been conducted where the penetration probe is cut in half length-ways and placed against a glass or Perspex wall of the sand container, allowing a clear view of the sand immediately surrounding the probe during penetration [55]. This solution is not perfect however, and can suffer from wall-effects from the penetration being conducted so close to a boundary [114]. Additionally, an ultrasonic horn that has a non-rotationally symmetric cross-sectional profile will exhibit significant bending forces, and could result in a reduced operational life-span.

Initial investigations were done to see if it were possible to use MRI scanners to measure the sand near the surface of the probe, but this was dismissed due to lack of accuracy (high resolutions on the tens of microns scale are needed) and feasibility (large MRI machines only have a small working volume, and the penetrator and additional apparatus are metallic).

5.1.1 High-speed camera apparatus

With no ideal solution available, it was decided to position the horn horizontally, Figure 5.1(a), and cover it with sand so that it is just below the surface. Whilst the direction of gravity is not in-line with the penetrator, this test served as a qualitative measurement and thus will still allow a visual depiction of the interactions that high-powered ultrasonics has with sand; something that has not been done before. An Olympus SZX16 Stereo Microscope with an available magnification of 0.7 - 11.5x was lent to us by the Olympus representative for the University of Glasgow, Paul Edwards. This was attached to an

Olympus i-Speed 2 high-speed camera to allow magnified high-speed recording, shown in Figure 5.1(a).

Figure 5.1: High-speed camera set up.

The biggest issue faced with this set up was the lack of sufficient light, due to both the high frame rate and the large amount of optical elements in the microscope and camera (each element reduces light transmission by a certain percentage). High speed filming also requires special lamps that do not flicker at 50 Hz like mains powered lights. For this experiment a high power flicker-free Arri 2.5kW HMI (Hydrargyrum medium-arc iodide) lamp, normally used for theatre stage lighting, was hired for the day. With a Fresnel lens attached, this lamp was focussed onto a very small area around the horn, providing a high concentration of light, as seen in Figure 5.1(b). At 2,500W, this lamp also produced a huge amount of heat, so appropriate safety precautions were taken. Five kilograms of block-paving sand was dyed black and left to dry, then mixed together with the un-dyed sand. This achieved two goals: Reducing the overall albedo of the sand and therefore reducing the glare into the microscope, and facilitating visual discrepancy between individual grains of sand.

5.1.2 High speed camera experimental procedure

Two main aims of this experiment were to record the motion of the interaction of sand and ultrasonic vibration, and record the physical vibration of the ultrasonic horn. Neither of these effects have been recorded before, so much of this experiment was to garner whether either of these were indeed possible. The second aim is particularly problematic, as the camera was only able to record at a maximum of 33,000 frames per second by reducing the resolution to 92x72 pixels. In order to avoid aliasing artefacts, it is generally accepted that the sampling rate must be at least twice the highest frequency component of the source. This is known as the 'Nyquist Rate' or 'Nyquist Criterion', and ensures that the full motion of the horn can be captured.

5.1.2.1 33 kHz recording

Since the penetrator's operational frequency is 20 kHz, the Nyquist Criterion is not satisfied. This means that it is not recording a full representation of the physical vibration. Whilst this is unfortunate, it was not the primary aim of the experiment and so will serve as a preliminary investigation into the feasibility of this type of recording. The lens was focussed at the tip of the horn, the amplitude set to 5 µm, and the frame rate set to the maximum of 33,000 per second. At such a high frame rate, even the high powered lamp struggled to illuminate the area sufficiently, and the resulting images, as seen in Figure 5.2, were extremely dark and had to undergo post-processing to increase the brightness and contrast. A displacement of 17.5 µm (excitation amplitude of 5 µm, and a horn gain of 3.5) at the tip of the horn correlates to roughly 1-2 pixels on the recording sensor, further making it difficult to discern any vibration. Since this was the first time that any of the people involved had done an experiment like this, most of the day was spent in setting up and testing the limits of the equipment. Whilst we did not obtain the result that we had hoped from this experiment, we did overcome many issues in the set-up, and have shown promising results that recording the physical vibration of an ultrasonic horn could be achieved using different equipment, with suggestions as follows:

1. A higher speed camera, capable of recording at least 40,000 fps, and ideally 50,000 - 100,000 fps.

2. A camera with a higher resolution sensor. Higher magnification microscopes is not advised, as the working distance between the horn and lens gets very close, making it very difficult to sufficiently illuminate the area.

3. High-directional lamps. It would have been possible to use additional 2,500W lamps, however too many of them located in one area would lead to significant heating issues. Lamps that can direct a high-intensity area using fibre optics would be better, as the physical area to be illuminated is quite small.

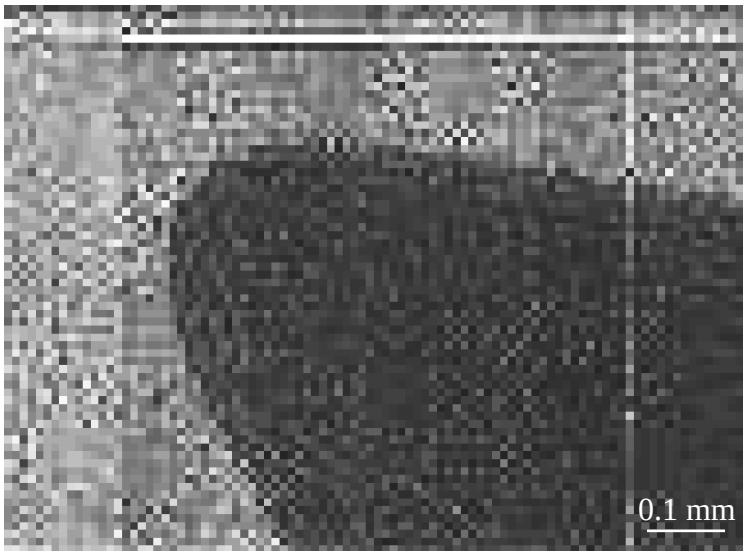

Figure 5.2: Close up view of the penetrator tip at 33,000 frames per second.

5.1.2.2 1 kHz recording

The primary aim of the experiment, to record the motion of the sand under ultrasonic excitation, was much more successful however. The full video is available on request with the University of Glasgow library, however a selection of still frames are given in Figure 5.3 to illustrate the main effects. As soon as vibration starts, sand is quickly projected away from the tip of the horn, as is to be expected from the oscillating manner of the vibration at the tip. However, what was surprising to see was that the sand in contact with the shaft of the horn appears to instantly fluidise, and rapidly move in the opposite direction, away from the tip and along the shaft. It is important to realise that this is not sand flowing down a slope, it is flowing purely horizontally. In fact, some sand particles actually flow up a gradient, as can be seen by the raised pile of sand along the shaft in Figure 5.3(f). This is a very unexpected result, and serves as a reminder that vibration of sand is an extremely complex field of research.

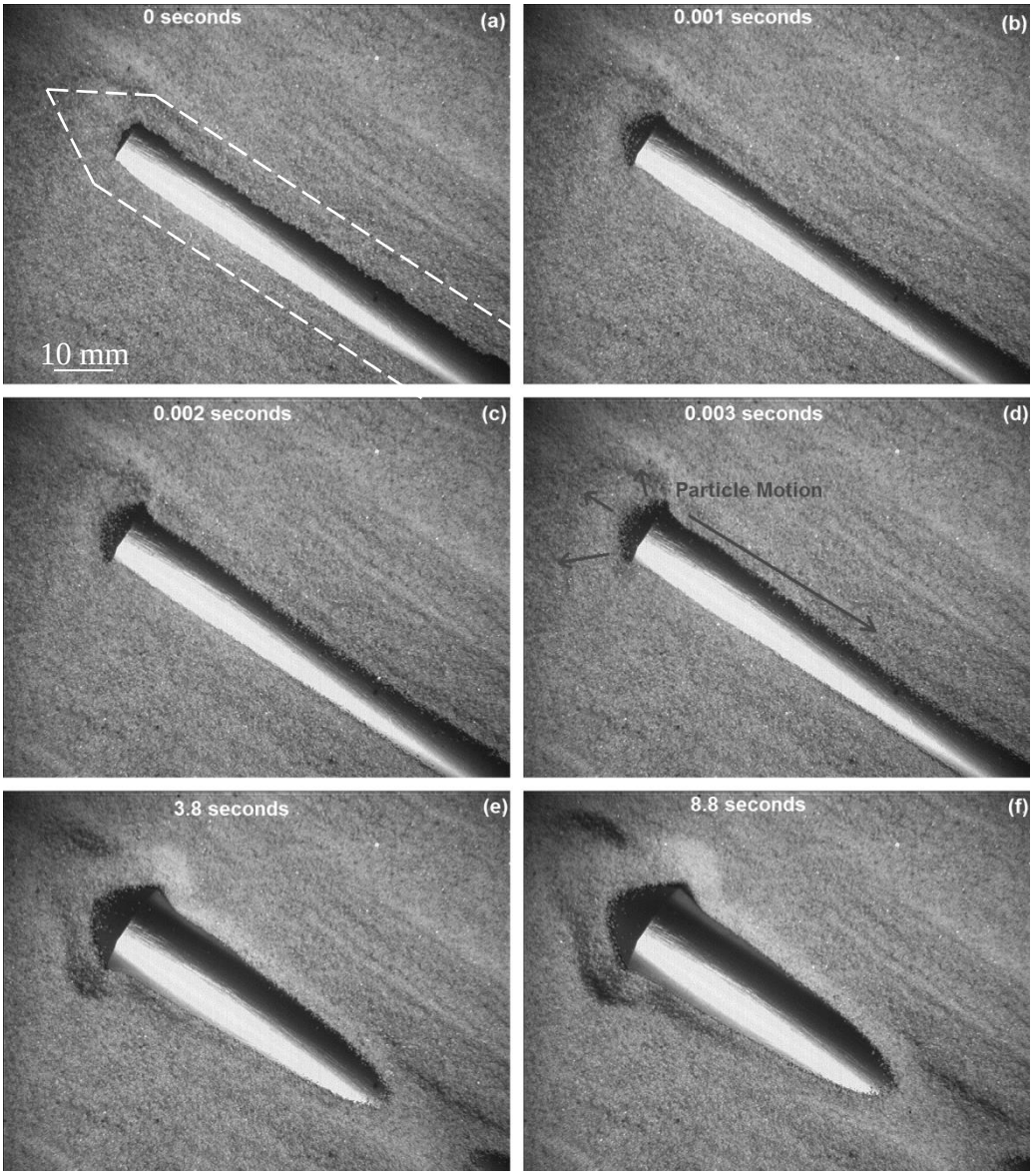

Figure 5.3: Snapshots of the motion of BP under ultrasonic vibration of the half-buried penetrator, outlined as a dashed line.

A side-on view of the resultant distribution of sand is shown in Figure 5.4. It is clear to see the level of sand is highest at the built-up section along the shaft, gradually decreasing in height towards the pit caused by the tip of the horn, followed by another pile of sand where the tip-ejected sand eventually came to rest. Whilst not entirely captured on video, there was a similar flow of sand along the shaft towards the built-up section, but on the opposite side. These two flows then result in the build-up of sand that can be seen in Figure 5.4.

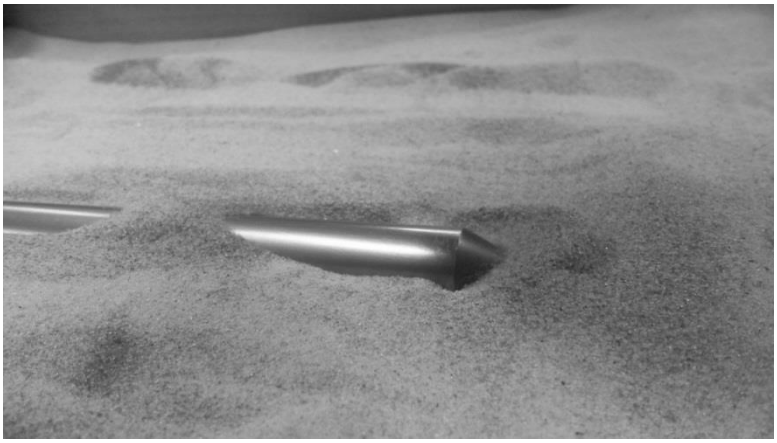

Figure 5.4: Build -up of sand around the nodal point with a 5 µm vibration after being half buried in the sand. The sand in front of the probe has also been evacuated forward from the vibration.

This build-up point coincides with one of the nodal points of the horn. The effect is reminiscent of Chladni patterns, where sand on a vibrating plate will collect at the nodes, sketching out elaborate patterns from the vibration [115]. The flow of sand is likely due to similar principles, however it is interesting to see it occur on a rod which is undergoing purely longitudinal vibration, rather than the transverse vibration of a vibrating plate.

5.2 Chapter conclusions

The experiment showed that ultrasonic vibration has a clear impact on the structure and movement of the sand particles. During penetration, it is possible that sand in front of the penetrator will be pushed forward and to the side, and sand along the shaft of the penetrator will travel towards the nodal points. This was also noted in qualitative testing of the probe in saturated sand, where clumps of wet sand would stick to the penetrator and travel up against gravity to collect at the nodal points In the future, it could be possible to create a device that uses this nodal-collection point to its advantage. For example, any device that is designed to move sand up a drill, such as an augured flute, would have the greatest impact if it were positioned near the nodes of an ultrasonic horn.

For the purposes of this work however, this experiment shows that even the relatively small amplitude of ultrasonic vibration can interact with sand in a significant way. The effects of fluidisation are kept to a small distance immediately surrounding the probe, something that is not seen in larger vibro-drills where the vibration extends a significant distance away, occasionally causing issues with the foundations of nearby buildings. Armed with this knowledge, it will give us a better understanding of any effects that might be seen in the following experiments and chapters.

Chapter 6

Penetration Forces Using Ultrasonic Probes

As discussed in the literature review, high powered ultrasonic vibration has been used to reduce forces in a variety of fields, most notably in small cutting devices for surgical requirements. If this phenomenon can also apply to reducing the forces for penetration through granular material, it could potentially be hugely beneficial for space exploration, where low available forces are of immediate concern in the low gravity environment of space. It is suspected that ultrasonic vibration, due to the fluidisation of sand, would result in lower overhead forces for penetration. These experiments look to establish the limits of this effect, what other additional outcomes exists, and how they might be applied.

6.1 Experimental rig design

In designing an experiment to test the effectiveness of ultrasonic vibration in granular material, a number of aspects require consideration. Firstly, an accurate and consistent method of providing the penetration action is required. In the interest of reducing the number of possible variables, it would be beneficial to have the penetration rate at a constant value. Both of these features are able to be fulfilled by a linear actuator.

Secondly, the penetration depth and force must able to be measured. This can be done by hand using rulers and force springs, however in the interest of obtaining smooth data and rapid experiments, it would be more efficient for this to be done electronically. Linear actuators can have internal potentiometers that are able to provide extension read-outs, allowing easy penetration depth measurements. Measuring the penetration force digitally is a little bit less straight forward, however force transducers are available that convert pressure into electrical signals via piezo-ceramic elements. Both of these devices are able to provide electronic read-outs in the form of voltage readings. This voltage can be fed into

a data acquisition device (DAQ), which in turn can be connected to a PC to allow the data to be recorded.

Thirdly, the force reacted from the probe must solely travel through the point of force measurement, in this case through the force transducer.

The finished rig, individual components and the break-down of their order can be seen in Figure 6.1. A Kistler force transducer was chosen to measure the force, located at the top of the rig, with all other components being supported from this point. It was important that all moving parts were only supported through the force transducer, as this ensures all the reacted force from penetration passes through this one point, giving an accurate representation of the penetration force. For stability, the penetrator and transducer needed to be contained in a cage that could slide vertically along rails. This has the potential to add some unwanted friction into the system, but care was taken to ensure the bearings were kept well lubricated and correctly aligned.

The linear actuator is able to drive the horn up and down, as well as provide read-outs of the extension via an internal potentiometer. The data acquisition device, a National Instruments USB DAQ 6009, serves as the connection between the actuator and force read-outs, and the computer. MATLAB running on this computer can then access the DAQ device, and record all of these measurements for evaluation. A MATLAB script was written to automatically save all results and display a calibrated force vs. penetration graph immediately after measurements have been completed.

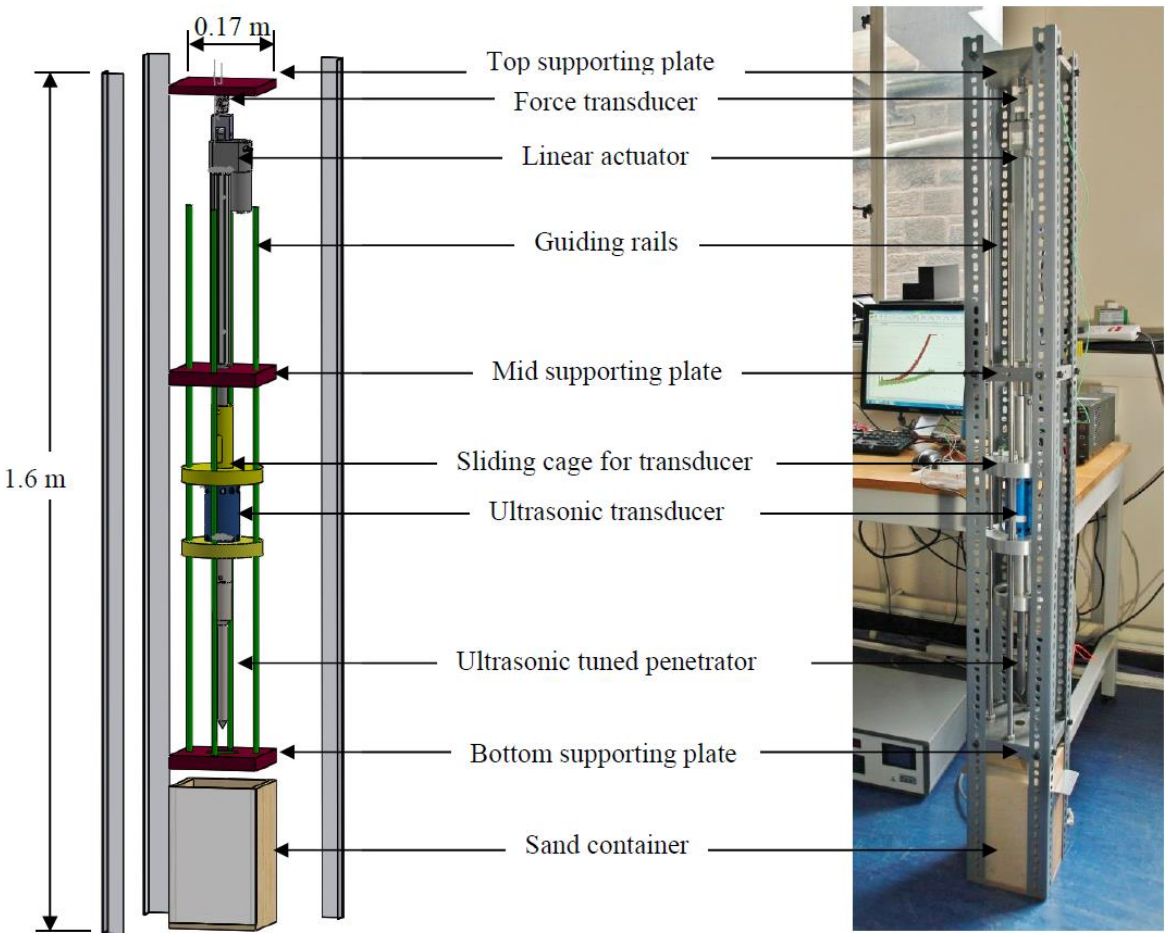

Figure 6.1: The rig for measuring reacted force during penetration. The linear construction allows an accurate measurement of force at the top of the structure.

6.2 Initial studies

Initial tests were conducted at the University of Glasgow, with the aim to assist in planning the full set of experiments at SSC. This section covers the steps taken to calibrate the experimental rig, the justifications of the parameters chosen, and finally the first results of ultrasonically assisted penetration into granular material, in this case in BP.

6.2.1 Linear actuator calibration

The linear actuator possess an internal potentiometer that varies its resistance depending on how extended the actuator is. A particular extension will have an associated resistance attributed to it, but it must first be calibrated. To do so, the actuator was clamped to a desk next to a meter ruler, with a pin attached to the end of the actuator to provide sub-millimetre accuracy. The DAQ device supplied a 5V input, and the resultant output voltage was measured when the actuator was extended in 1 cm increments. The results are shown

in Figure 6.2, along with the equation of a line-of-best-fit. The trend of voltage with true distance was perfectly linear with an R^2 value of 1, so using the equation of the fitted line and measuring the resultant voltage will give an accurate method of measuring penetration depth. Additionally, the actuator was loaded whilst extending, and the penetration rate was measured to be constant.

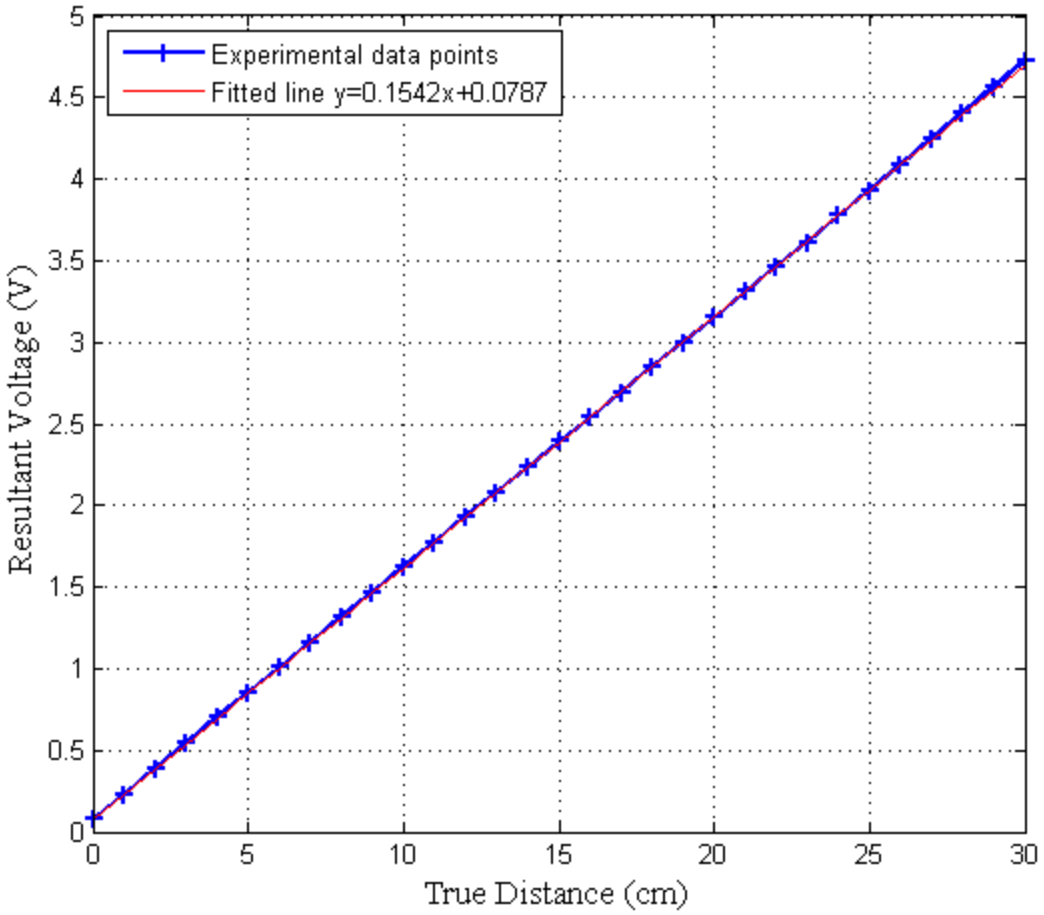

Figure 6.2: Calibration of the linear actuator.

6.2.2 Parameters and justifications

Before experiments can commence, it is necessary to choose which variables to use within the experiment, and what values they should take.

Sand density

As discussed in section 3.5, two different regolith densities could be prepared at low and high density. For the regolith used in initial test, BP, this corresponds to 1.43 and 1.63

g/cc respectively. Relative density has previously been shown to be one of the leading contributors for higher penetration forces, and testing both the maximum and minimum relative densities possible through the sand preparation method will help in examining this.

Penetration rate

The linear actuator (Duff Norton LT255-1-300) extension rate can be varied by the input voltage, keeping a constant penetration rate by drawing a higher current when loaded. Two different penetration rates were chosen to investigate whether this has an effect on penetration. A fast penetration rate of 9 mm/s was used as it was the rate corresponding to the optimum rated voltage of the linear actuator, 12 V. The lowest voltage that the power supply could go to (3V) resulted in a very inconsistent penetration rate, due to not being able to supply enough current to keep the rate constant. The limits of the actuator were tested and a compromise of a slow rate, yet stable voltage was needed, eventually settling on an actuator voltage of 4.8 V, corresponding to a penetration rate of 3 mm/s.

Ultrasonic amplitude

The Langevin transducer was connected to a Sonic Systems™ L500 power supply, allowing the supply of the ultrasonics signal, as well as tracking capabilities. The range of excitation amplitudes capable from this particular power supply was 1 – 10 µm, with an additional point at 0 µm from turning the ultrasonics supply off. Several intermediate values of 1-9 µm would give the highest resolution of data, however the number of required experiments starts to rapidly increase with additional variables. Amplitudes of 0, 1, 2, 5, and 10 µm were chosen due to the convenience in logarithmic scales and even spacing.

Consecutive penetrations

Consecutive penetrations were used to try and investigate how the fabric of sand evolves during the experiments. Previous work on granular material has touched upon this subject [100], noting how the penetration force increases with consecutive penetrations. Due to the fact that consecutive penetrations can be done relatively quickly, without re-setting the container of sand, it was decided to include this variable in the experiments, choosing six repetitions to replicate the previous work.

Variables summary

It is good experimental practice to only change one variable at a time whilst keeping all others constant. The full summary of chosen variables is shown in Table 6.1. The number of experiments is then simply the number of possible combinations of the different variables, giving (2 x 2 x 5 x 6) 120 separate runs.

Table 6.1: Variable space of the initial penetration tests into BP.

Variable	Data points	Notes
Relative Densities	2	High and Low relative densities defined in section 3.5.
Penetration Rate	2	Fast (9 mm/s) and Slow (3 mm/s) correspond to actuator supply voltage of 12 V and 4.8 V respectively.
Ultrasonic Amplitude	5	Transducer amplitudes of 0, 1, 2, 5, and 10 μm.
Consecutive Penetrations	6	Penetrations taken consecutively without resetting the sand.
Total Data Points:	120	

Additionally, the DAQ device also required input instruction for how to record the data. A sampling rate of 500 Hz was chosen to sufficiently capture the data in high resolution, with a sampling time of 25 s for the fast penetration rates, and 65 seconds for the slow penetration rates.

6.2.3 Experimental technique

To increase the accuracy of results, the experiment followed a set procedure to ensure that all tests were taken in the same conditions. The BP sand was prepared to either low or high density. The full container was then positioned inside the penetration rig, and a measurement taken of the position of the linear actuator when the tip of the probe was at the surface of the sand. This would set the location of the surface, and was subtracted from the linear actuator distance recorded during experiments to give the calibrated depth.

The probe was raised to the starting position and the linear actuator voltage set. A level of ultrasonic amplitude was chosen and switched on, the MATLAB script was set to record data, and the linear actuator switched on to commence penetration. After the probe reached the maximum depth (16.5 cm) and the MATLAB script finished recording data, the

ultrasonic supply was turned off and the penetrator raised to its starting point. The sand container was then removed and taken to the preparation area, and the process repeated.

6.2.4 Initial results and observations

All of the primary penetrations are shown together in Figure 6.3. Without exception, the application of ultrasonics resulted in a reduction of the force required for penetration. In both low and high density cases, even the lowest value of ultrasonics amplitude (1 µm) gives a significant decrease in the penetration force required. It is interesting to note that whilst higher amplitudes give a higher decrease in penetration force, it appears that any improvement is very small compared to smaller amplitudes. Higher amplitudes also require a larger amount of power to run, so in the interest of power consumption the larger amplitudes might not be viable.

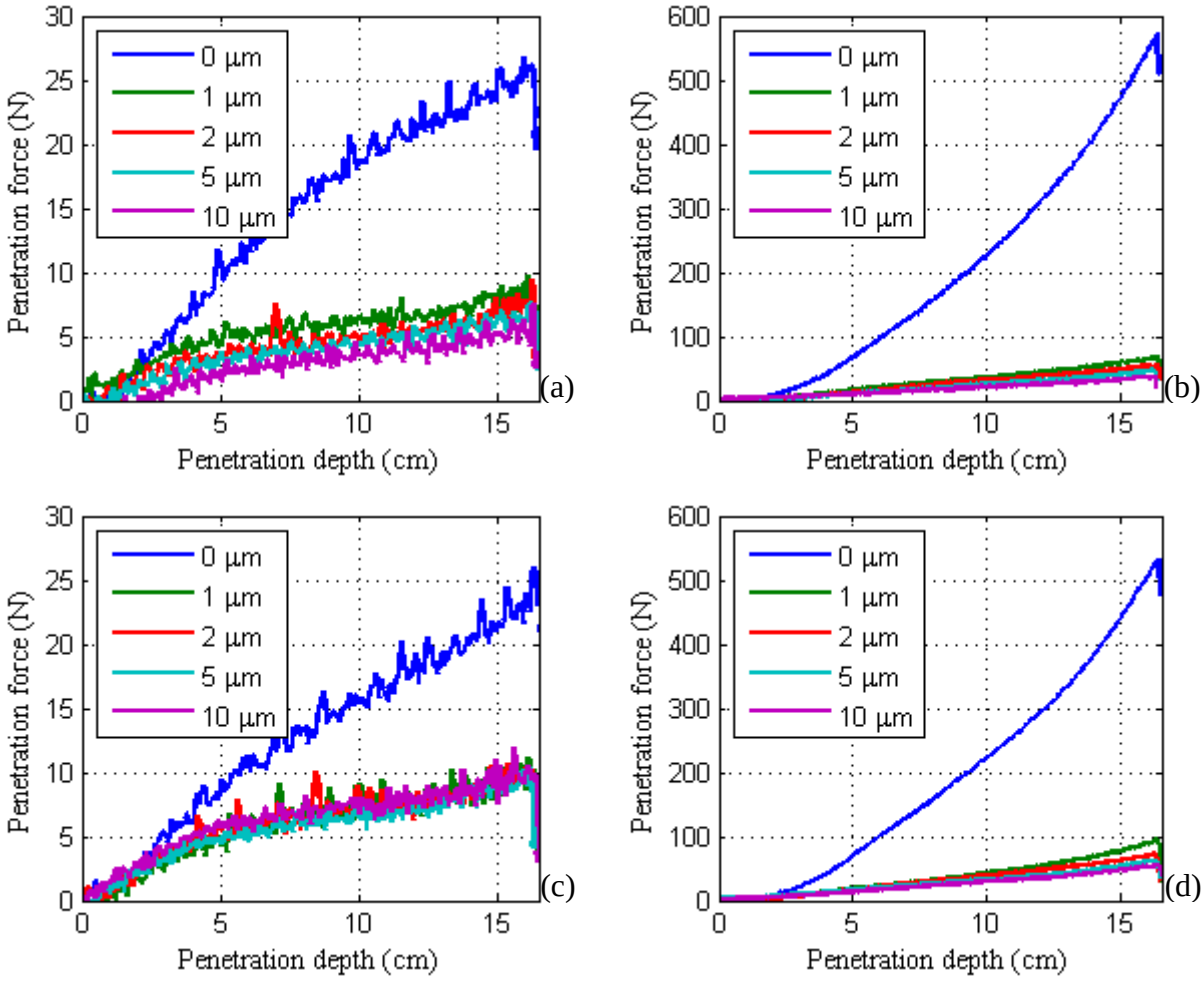

Figure 6.3: Penetration force profiles with different ultrasonic amplitudes into BP at (a) low density and slow rate, (b) high density and slow rate, (c) low density BP and fast rate, and (d) high density and fast penetration rate.

The largest reduction in penetration force is seen in the high density, low penetration rate experiment. Here, the maximum force for non-ultrasonic penetration is 571.9 N, compared to the maximum force at 10 µm of 36.47 N, giving a 93.6% reduction in peak force. Power consumption was not measured electronically, and could only be noted from the analogue dial during penetration. For this level of vibration, a peak power consumption of approximately 120 W was seen. Conversely, the peak power consumption for the 1 µm run was only 5 W, whilst still reducing the peak force by 88%. This is a slight reduction in the effectiveness of penetration but at significantly reduced power consumption, illustrating the diminishing returns at higher amplitudes. If a rover or lander has very tight power capabilities, then a lower ultrasonic amplitude could be used. If power is in excess and the main goal is to go as deep as possible, then a higher amplitude could be used.

This amount of power is extremely high when compared to lower amplitudes, and if run for a long period of time it will consume a large amount of energy. This energy needs to go somewhere, usually ending up as heat dispersed into the surrounding environment. After some of the runs, especially the low rate run (which had a duration of 60 seconds), it was noted that the titanium horn became excessively hot. This was very concerning, as not only does it mean that the horn is more apt to fatigue failure, but it also means that the sand immediately surrounding the horn would have become significantly heated. This would be problematic in planetary exploration, as it could potentially alter the composition of the surrounding media, or even destroy any organic substances. This was only an issue with the 10 µm case, with the next highest power consumption at 110 W for the 6th run of the 5 µm, high density, high rate experiment. All the data for the consecutive runs are included in the appendix CD.

6.2.5 Variable choices for further experiments

For all future tests, the decision was taken to exclude experiments using 10 µm of excitation vibration. The power consumption at this level of amplitude at high overhead loads regularly reached hundreds of Watts. This was not only was extremely energy inefficient, but it also created a possible hazard to the user and increased chance of fatigue of the horn. The results showed diminishing returns at higher amplitudes with very little benefit from using 10 µm compared to 5 µm, so the higher amplitudes were left out of any future experiments. The final variable space for the full set of experiments is shown in Table 6.2.

Table 6.2: Variable space of the full penetration force experiments.

Variable	Data points	Notes
Relative Densities	2	High and Low relative densities defined in section 3.5.
Penetration Rate	2	Fast (9 mm/s) and Slow (3 mm/s) correspond to actuator supply voltage of 12 V and 4.8 V respectively.
Ultrasonic Amplitude	4	Transducer amplitudes of 0, 1, 2, and 5 µm.
Consecutive Penetrations	6	Penetrations taken consecutively without resetting the sand.
Sands used	5	SSC-1, SSC-2, SSC-3, ES-3, and BP
Total Data Points:	480	384 of these done at SSC, remaining were conducted at Glasgow during initial testing.

6.3 Full experiment

The Surrey Space Centre (SSC), part of the University of Surrey, allowed the use of its state of the art facilities for these experiments. In addition to the four regolith simulants discussed at the start of this chapter, they also had a dedicated sand preparation lab, which had been equipped with special extractor fans to deal with the dust generated from preparing sand. This allowed the opportunity to test a broader range of sands that can contain a higher percentage of fine-particulates. The possibility of using their large vacuum chamber for doing tests at simulated Martian pressure was discussed, but due to time constraints this never came to fruition.

With two relative densities and five different sands, a total of ten different regolith environments that a rover or lander might encounter could be simulated. Two penetration rates, fast and slow, and four different ultrasonic amplitudes then give 80 different experimental runs. For each of these runs, six successive penetrations were performed in the same container without disturbing or resetting the sand, in order to identify how the force profiles change if multiple attempts at penetration in the same location are done. This resulted in a total of 480 separate experiments over the course of the time spent at the University of Surrey and the University of Glasgow.

6.3.1 Peak penetration forces

To measure the effectiveness of ultrasonic vibration on penetration force, the maximum penetration force encountered was taken from every run conducted into a fresh container of sand (i.e., a primary run, not a consecutive run). These force values were then plotted against their respective ultrasonic amplitudes, allowing a direct comparison of all ten different regolith environments (which include the initial tests taken at the University of Glasgow), shown in Figure 6.4. This figure condenses 80 experimental runs, with each point representing the peak force from a primary run.

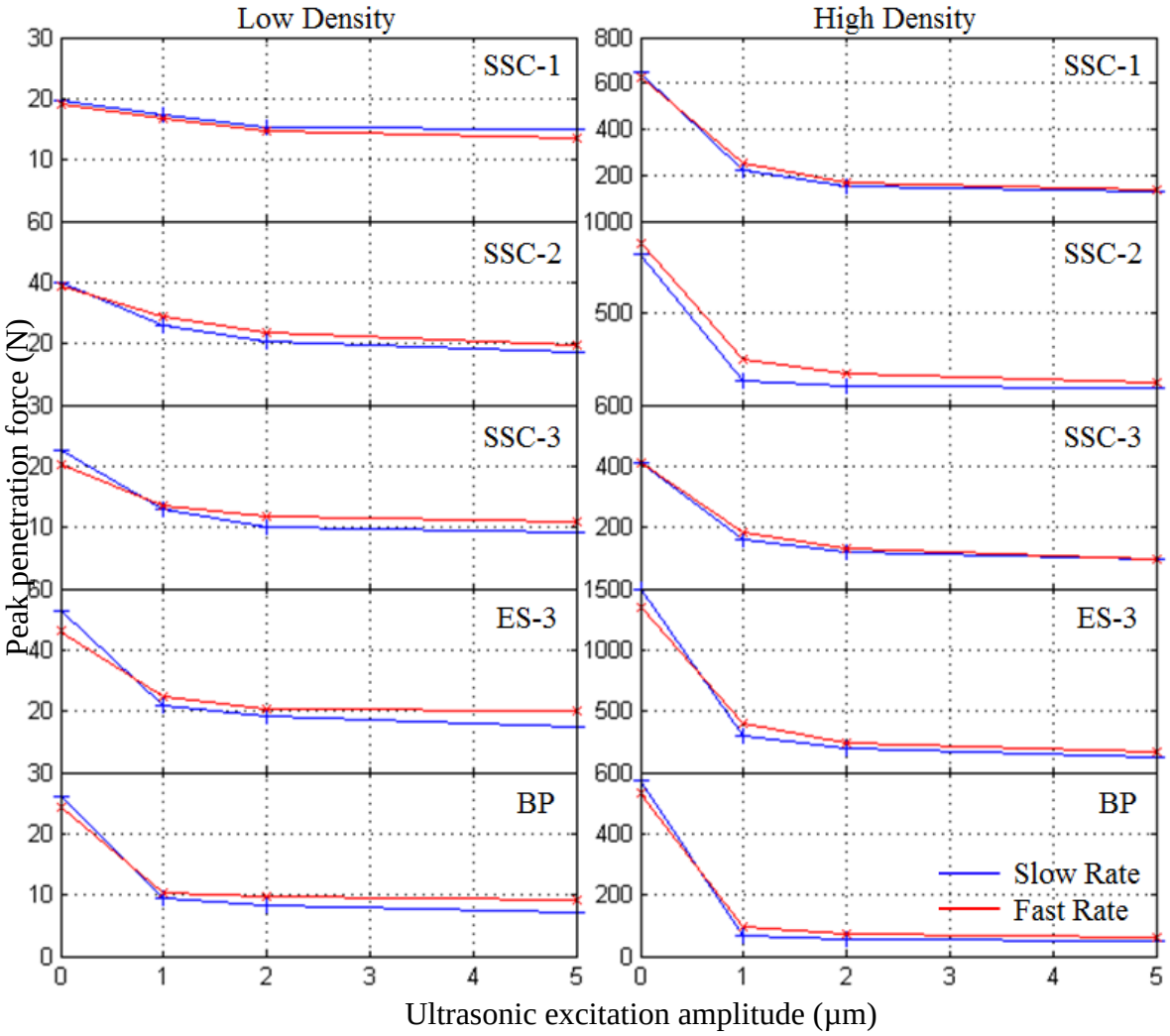

Figure 6.4: Peak penetration forces for all sands in low and high density, and at slow and fast penetration rates.

As with the initial BP experiments, there is a clear decrease in maximum penetration force upon application of ultrasonic vibration for all runs. Higher values of amplitude lead to larger reductions, however the diminishing returns at higher amplitudes appear to be

apparent with all sands, not just with BP. The largest reductions all appear to be in high density sand, with most of the reductions occurring at the lowest level of vibration used, 1 µm. This appears to be the area of most interest, and future experiments should concentrate on the lower levels of vibration.

Barring high density SSC-2, all non-ultrasonic penetration forces were higher with a slow penetration rate than with a faster one, possibly suggesting that there is a lower dynamic friction between the grains and the probe at higher velocities. Curiously, for most of the regolith environments, the opposite is true when ultrasonics is active, with the faster penetration rates resulting in a higher penetration resistance. This could be due to the duration of time that the grains of sand have in contact with the vibrating probe, possibly resulting in a larger volume of vibro-induced fluidised sand with a longer contact duration. In any case, this difference again highlights the significant differences between regular and ultrasonic penetration.

Using Figure 6.4, it is difficult to directly compare the effect that ultrasonics has had in all of the ten environments, due to the relative differences in penetration force between the different sands. This can be solved by normalising all of the peak forces, i.e. dividing all the forces by their non-ultrasonic counterpart. This allows a direct comparison between the *effectiveness* of ultrasonic vibration between different sands and densities, shown in Figure 6.5. The values here refer to what percentage (as a fraction) the penetration forces have been reduced to upon application of ultrasonic vibration. The further down the plot lines, the more effective ultrasonic vibration has been in reducing the force.

Low density sands especially appear to have much more variance in their effectiveness compared to the high density tests. For example, for low density and a fast penetration rate (Figure 6.5(c)), a vibration amplitude of 2 µm reduces the overhead force by 20% in SSC-1, whereas for BP it is reduced by 60%. High density sands on the other hand showed a much higher susceptibility to ultrasonic vibration, with all sands reducing by at least 50% using the lowest level of vibration, 1 µm, with the force reducing by roughly 90% in BP. This is advantageous, as high density sand yields a higher resistive force, and would therefore benefit the most from a higher ultrasonic effectiveness. Very compact densities have also been recorded on the Moon during the Apollo 11 missions, where they

discovered regolith almost at the point of incompressibility just a few centimetres below the surface [10].

Across all different variations of density and penetration rate, BP consistently showed the greatest reductions in force. SSC-1 performed the worst in the low density experiments, whereas SSC-3 was the worst at high density. Interestingly, at high density, the performance of SSC-2 and ES-3 were almost identical, despite being the most dissimilar regoliths with regards to the characterising parameters.

These results also serve to illustrate the principle that penetration and drilling is extremely dependent on the substrate or material, highlighting the need for empirical research such as this. The values of the data points in Figure 6.5 can be found in the appendix CD.

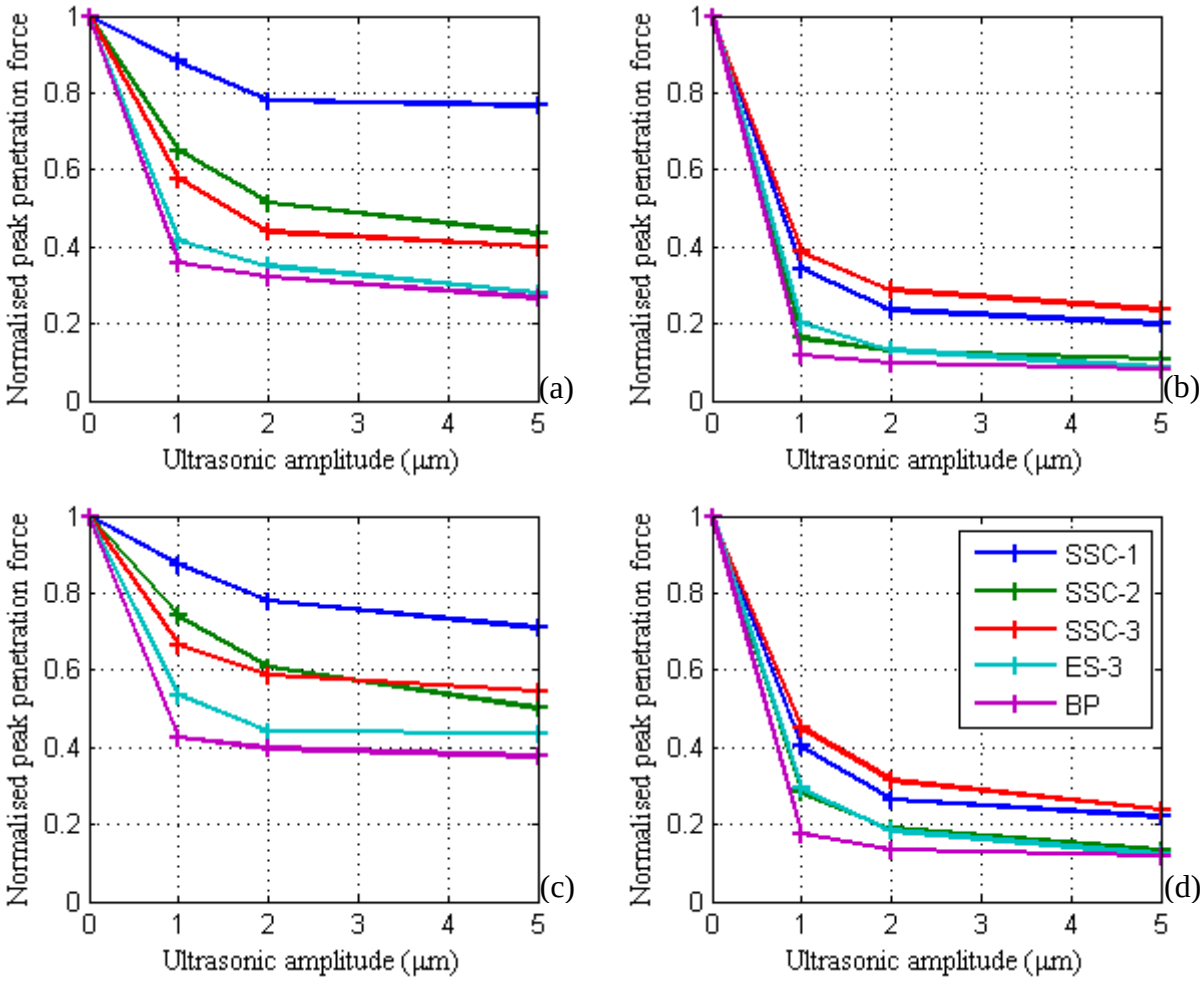

Figure 6.5: Normalised peak penetration forces for all sands at (a) low density and slow rate, (b) high density and slow rate, (c) low density and fast rate, and (d) high density and fast rate.

6.3.2 Consecutive penetrations

Each experiment also consisted of five additional penetrations into the same container of sand, without resetting the container first. An example of these tests, taking BP and a slow penetration rate are shown in Figure 6.6(a) and Figure 6.6(b) for low and high density preparations respectively. In every single case, consecutive penetrations resulted in higher required force. Seiferlin et al noticed this result previously, but it was not expanded upon [100].

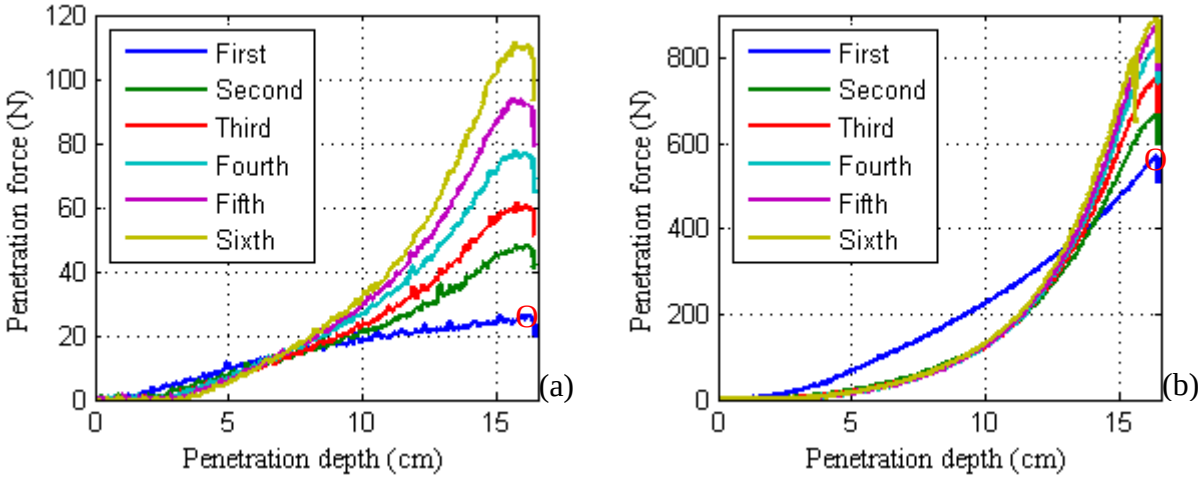

Figure 6.6: Consecutive 0 µm penetrations at a slow penetration rate into (a) low density BP, and (b) high density BP. Circled in red is an example of the peak penetration force data points used in Figure 6.4.

As a probe is pushed into sand or soil, it must displace the material either below or to the side of the penetrator if there are no mechanisms in place to bring the soil to the surface, such as an auger. This will lead to soil compaction in the regions immediately surrounding the probe, resulting in a more difficult environment for subsequent penetrations. This effect is more prominent in the low density environments, due to the fact that there is more potential for further compaction compared to high density preparations. Removal of the probe will also tend to cause additional material to fall into the cavity. Additionally, in higher density sand the resistive force increased to the point where the probe could potentially be drawing huge power at the highest amplitude settings, occasionally in excess of 200 W. For this reason it is advised that repeated penetrations into the same region are kept to a minimum.

An interesting effect is seen at about 7 cm depth for low density BP, and at 13 – 14 cm depth for high density BP. Up until this depth, the penetration force of consecutive penetrations is actually lower than the primary penetration force. The force then ramps up steeply, before progressing past this 'cross-over' point, to eventually result in a higher penetration force at the full depth. This is likely to be the result of the primary penetration pushing sand out in front of the probe, creating a highly compacted region out near the tip, but also essentially 'clearing the path' to some extent for following penetrations.

6.3.3 Plateauing of consecutive penetrations

As can be readily seen in Figure 6.6(a), and to a lesser extent in Figure 6.6(b), the force profiles of consecutive penetrations can be seen to level-off or plateau towards the end of the penetration. It was noted that this was only seen in consecutive penetrations and never in the primary runs (which displayed a much more regular increase in penetration force), and so an additional test was conducted.

With a high density preparation of SSC-3 and a fast penetration rate, a 0 µm penetration was conducted using the same experimental procedure as before. For this run however, the primary penetration was to just 7 cm (referred to as the 'half-depth' primary penetration). The probe was then retracted, and inserted again for a secondary penetration, this time to the full 16.5 cm depth (referred to as the 'follow-up' secondary penetration. These two runs, as well as an example of a regular full-depth primary and secondary penetration, are shown in Figure 6.7.

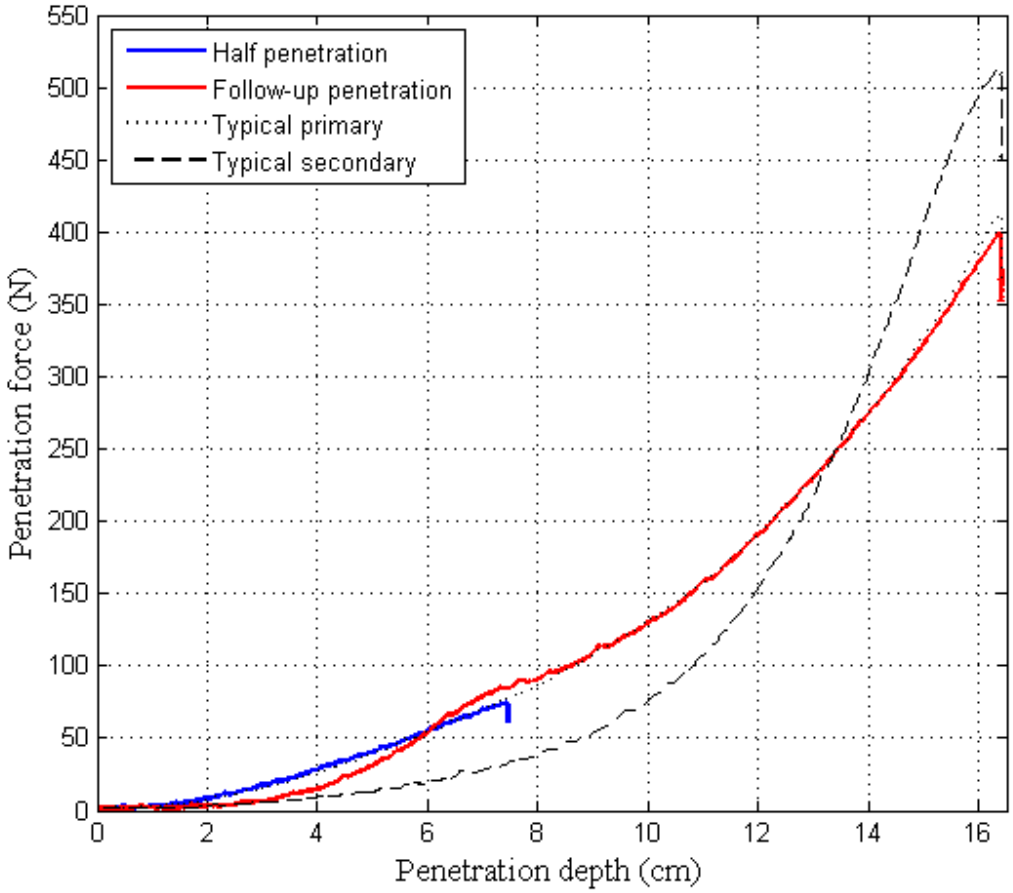

Figure 6.7: Half penetration and follow-up penetration compared to typical primary and secondary penetration profiles. Regolith used was high density SSC-3 with a fast penetration rate.

The follow-up secondary penetration exhibited the same peak penetration force as a typical primary penetration, however it experiences a deviation at around 7 cm, clearly as a result of the half-depth penetration before it. The force appears to plateau for a time, then return to the penetration profile of a regular primary run. This would confirm the fact that the plateauing effect is caused by the previous run, and not by boundary conditions of the container of sand.

The follow-up penetration follows the profile of a typical primary penetration after 7 cm depth, which is to be expected as the fabric of the sand is unaltered after this depth. However, following the same logic, it does not follow the profile of a typical secondary before 7 cm, as illustrated by the dashed line in Figure 6.7, instead exhibiting penetration force profile closer in force to a primary run. Additionally, the ‘cross-over’ point of the follow-up penetration occurs at a shallower depth of 6 cm compared to the 13.5 cm of the typical full-depth penetration runs. Comparing the depth of the cross-over points with the

depth of the previous primary run reveals that it coincides with a depth 82% of the previous depth, for both the half-depth and full-depth penetration runs. In a surface exploration situation, this would mean that a secondary penetration into the same hole would require less overhead force up until 82% of the depth, whereupon more overhead force would be required to penetrate the rest of the way.

6.3.4 Effects caused by ultrasonic penetration

An additional test designed to further investigate the differences between ultrasonic and non-ultrasonic penetration was conducted near the end of the experimental trip at SSC. This test, with the results shown in Figure 6.8, compares the penetration profiles of two non-ultrasonic secondary penetrations. For one of these profiles, the primary penetration was non-ultrasonic, whilst for the other the primary was a 5 µm amplitude vibration. The conditions used were: fast rate, high relative density, and regolith SSC-3.

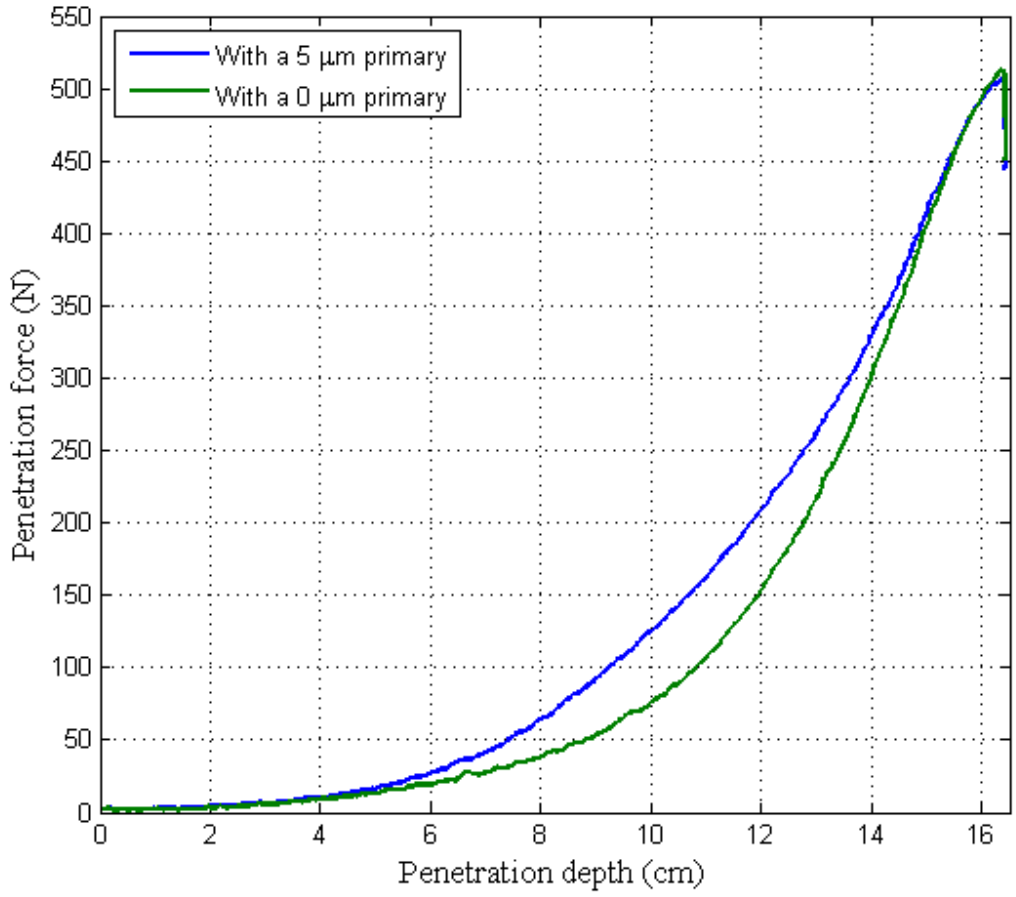

Figure 6.8: Non-ultrasonic secondary penetrations after either a 0 µm or a 5 µm primary penetration. This was conducted into high density SSC-3 at a fast penetration rate.

Both secondary penetrations reached the same maximum penetration force in the end, but the gradient of their respective curves are quite different. The run with an ultrasonic primary penetration had a much steadier curve, suggesting that the resistive force during penetration increased in a more predictable manner. The run with a non-ultrasonic primary penetration on the other hand initially required much less force, suggesting that ultrasonic vibration might make the surrounding sand harder to penetrate for subsequent attempts. However, the force quickly ramps up near the end, resulting in the same maximum penetration force. The larger area under the 5 µm primary curve also points to a higher total amount of work done, perhaps indicative of the densification of the sand due to ultrasonic vibration.

Currently, it is not fully clear why there is such a difference between the two curves, and an examination of the internal structure would be required in order to do so. Based on experience working with ultrasonic vibration however, it is likely that the ultrasonic vibration densifies the sand around it all the way through penetration, rather than just simply pushing sand forward as in regular penetration. This would mean that an ultrasonic primary and subsequent non-ultrasonic secondary penetration would be traveling through denser sand throughout the entire distance, and therefore feel a steadier increase in resistance. A non-ultrasonic primary and secondary penetration on the other hand would only feel this resistance near the end of travel. The fact that both penetration forces end up at the exact same final force is quite remarkable, and suggests that on the macro scale there is very little difference to the fabric of the sand whether an initial penetration was ultrasonic or not.

6.4 Chapter conclusions

The chapter covered the first examination at using high-powered ultrasonic vibration for use in penetration of sand, specifically looking at the force-reduction qualities. Several sands were tested, and ultrasonic vibration was found to reduce overhead force requirements for all sands and all densities.

The efficiency of this force reduction varied considerably, with low density sand showing relatively minor improvements over high density sand, which showed reductions of over 90% in some cases. The largest reductions coincided with the highest level of vibration (10 µm for BP, 5 µm for the remaining sands), however the level of improvement

over the lowest level of vibration (1 μm) were not so great, with significant diminishing returns apparent. As ultrasonic vibration requires power to sustain, it is yet to be seen if it is beneficial with respect to overall power consumption.

Additional effects from penetration were also seen and examined. Consecutive penetrations into the same container of sand without resetting showed increasing levels of peak penetration force. Initial penetration force, however, was lower than the primary penetration up until a certain depth. For high density SSC-3, initial results suggest that this cross-over depth appears to be at 82% of the full penetration depth for non-ultrasonic penetration, however more data would be required to confirm this value. This behaviour appears to be less pronounced in ultrasonically active runs, however the peak consecutive penetration forces do also rise.

Chapter 7

Power Optimisation for Ultrasonic Penetration

Previous sections have shown that ultrasonic vibration is able to significantly reduce the force of penetrating through granular material. This section is based upon that work, furthering it by investigating how the power consumption behaves for ultrasonically-assisted penetration. Other ultrasonic related systems, such as the UPCD from the University of Glasgow [28], [29], and the USDC from JPL [116] have reported a decrease in the total power consumption for drilling, and it would be interesting to see whether this response also applies to penetration and, if so, what the limits are.

Ultrasonic vibration reduces penetration force, and therefore reduces the strain and power consumed by the motor supplying the penetration. However, ultrasonic vibration itself requires power, with higher amplitudes requiring more power. It is predicted that there will be some balance point between the two power consumptions, theoretically resulting in an optimum value of excitation amplitude that minimises the total power consumption. If this were the case, then this could potentially be very useful for any space mission, but particularly for small landers where power availability is a severe concern.

7.1 Variable choice

Based on the knowledge gained from previous experiments, such as the high sensitivity of sand even at low vibrational amplitudes, it is important firstly to put some thought into what experimental variables to concentrate on. This information would then assist in the design of the experiment.

The force reduction experiments described in Chapter 6 showed a dramatic decrease in force at the lowest value tested, 1µm, with diminishing results for higher amplitudes. There is clearly some regime change happening between 0 and 1 µm, and these tests should concentrate on this lower-amplitude region. The L500 power supply from Sonic Systems™ can only supply a minimum amplitude of 1 µm, however their P100 system is able to supply 0.4 µm with a 0.1 µm resolution. A higher number of amplitudes would be preferable; however increasing the number of variables has the potential to dramatically increase the length of experiments. Several variables would therefore need to be dropped to compensate.

For ultrasonic amplitude, the full ultrasonic range was reduced from 1 – 5 to 0.4 – 2 µm. To investigate the low amplitude effects in higher resolution, the increments were 0.1 µm in the range 0.4 – 1 µm, then increased to 0.2 µm in the range 1 – 2 µm, resulting in 13 different values of amplitude, including the 0 µm control tests.

The different regolith environments displayed noteworthy differences in the effectiveness of ultrasonic penetration. To encompass the greatest range, the regoliths SSC-3 and BP were chosen for these experiments, as these sands showed the greatest variation in the normalised penetration forces in Figure 6.5(d). The two relative densities, loose and compact, were both kept for these experiments, as they also showed large differences between them.

Whilst a difference does emerge between the two penetration rates, it was not deemed sufficient enough to effectively double the experimental time. As 12 V was the rated voltage for the linear actuator, the fast penetration rate of 9 mm/s was used for these tests. Consecutive penetrations were also omitted from these experiments, concentrating on just the effects from primary penetrations. The full variable space for this experiment is shown in Table 7.1.

Table 7.1: Variable space of the power measuring experiments.

Variable	Data points	Notes
Relative Densities	2	High and Low relative densities defined in section 3.5.
Penetration Rate	1	Fast (9 mm/s) corresponding to actuator supply voltage of 12 V.
Ultrasonic Amplitude	13	Amplitudes of 0, 0.4, 0.5, 0.6, 0.7, 0.8, 0.9, 1.0, 1.2, 1.4, 1.6, 1.8, and 2 µm.
Sands used	2	SSC-3 and BP
Total Data Points:	52	

Additionally, the sampling rate of the DAQ was increased from 500 to 3,000 Hz to record any high-frequency effects in the power measurements the DAQ device also required input instruction for how to record the data.

7.2 Experimental apparatus

During the force reduction tests, power consumption of the ultrasonic transducer could be approximated by reading it off the dial of the L500 ultrasonic power supply, showing levels of power consumption ranging between 1 W and 200 W for the very high force and vibration levels, and no method to record this data. To accurately discern the differences in power consumption between different amplitudes, it was imperative that an accurate method of power measurement was established. The new ultrasonic supply, the P100 from Sonic Systems™, had an additional electronic output from the power display that enabled the digital recording of the power consumption. Using the pin for this and connecting it to a DAQ device (National Instruments USB-6009), it was possible to directly measure and record the active power supplied to the transducer in real-time.

For the power consumed by the linear actuator, the current and voltage of the power supply to actuator were measured, and multiplied via a custom-built multiplier circuit. The output of this was then recorded by the DAQ device. The voltage of the linear actuator was simple to measure, and consisted simply of routing an additional cable from the linear actuator power supply into the multiplier circuit, giving the real-time voltage of the actuator. Current measurement is a little bit more complex, requiring special circuits such as shunts; these, however, can interfere with the power supplied to the actuator, especially at the potentially large amounts of current used in these experiments. It was eventually

decided to use a Hall-effect current probe, model AEMC SL261, as this required no modifications to the existing actuator circuit, and had a minimal impact on the power delivered to the actuator. The output of this probe was routed to the multiplier circuit, providing the real-time measurement of current.

The penetration force and the penetration distance were recorded using the same methods as with the previous force reduction experiment, namely, via the force transducer and linear actuator potentiometer respectively. The inputs for the DAQ device were therefore: Penetration distance (via the potentiometer), force (via the force transducer), actuator power (via the multiplier circuit), and ultrasonic power (via the output from the ultrasonic supply). A custom MATLAB script recorded these values and saved them as a .csv file. The penetration rig was physically unchanged from the force experiments in Chapter 6, but included additional circuitry and measurement devices shown in Figure 7.1.

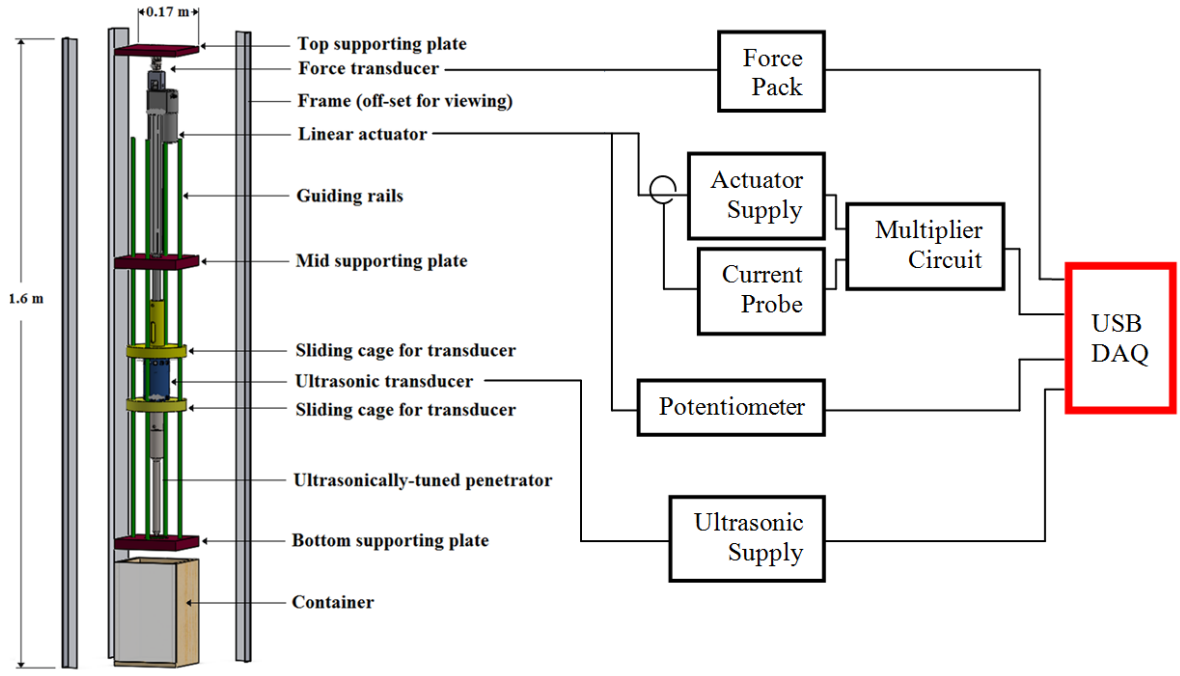

Figure 7.1: Schematic of the power rig and associated power measuring equipment

7.3 Results and discussion

The experiments were conducted at the University of Glasgow and split evenly over two days, with a single sand investigated for each day to minimise any environmental effects of the sands. Otherwise, the experimental procedure remained unchanged from the force experiment.

7.3.1 Higher resolution force reduction

This experiment was designed with two main aims. Measuring the power consumption properties was the foremost goal, however it was also possible to simultaneously investigate the force reduction properties of ultrasonic vibration at both a lower vibration amplitude, and also with higher fidelity.

These results are seen in Figure 7.2 (in a similar manner to the lower resolution force reduction results in section 6.3.1), showing the decreasing penetration force with increasing ultrasonic amplitudes for the four different regolith environments: sands BP and SSC-3, in both low and high relative densities. As before, a clear decrease in force is seen with increasing amplitudes. The results also match up quite well with the forces shown in Figure 6.4, with only a small difference in force. Due to the finer resolution of amplitudes though, it can be seen that in high density sand the transition is much smoother, indicating that there is a much more gradual change in regime. Low density sand on the other hand still displays a sharp drop 0.4 µm, with little further improvement at higher amplitudes.

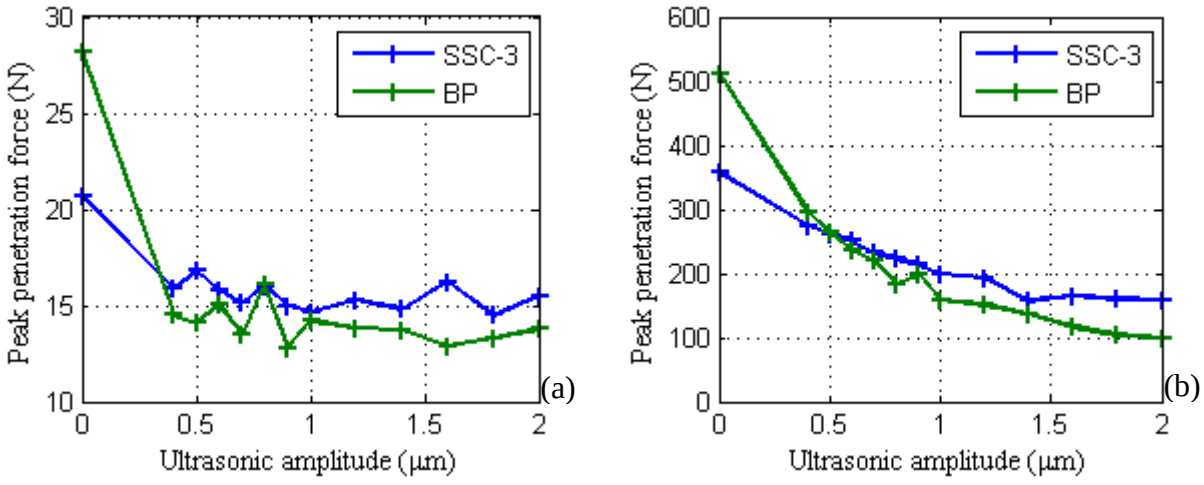

Figure 7.2: Peak penetration forces in SSC-3 and BP for (a) low density and (b) high density preparations.

Again, it is most beneficial to normalise the forces in order to compare the effectiveness of ultrasonic vibration, which is shown in Figure 7.3(a) for low density sand and Figure 7.3(b) for high density. Here is it clear to see that in low density sand, very little improvements are seen after 0.4 µm. In fact, at this lowest level of vibration, the percentage decrease in peak force is slightly greater in low density than in high density BP, with a decrease of 48.5% compared to 42.2%. For SSC-3 this is not the case, with a decrease of 23.4% and 23.6% for low and high density sand respectively. The peak forces continue to drop at higher amplitudes however, resulting in a decrease of 80.7% in BP at the highest level of vibration of 2 µm, compared to a decrease of just 51.1% for low density BP.

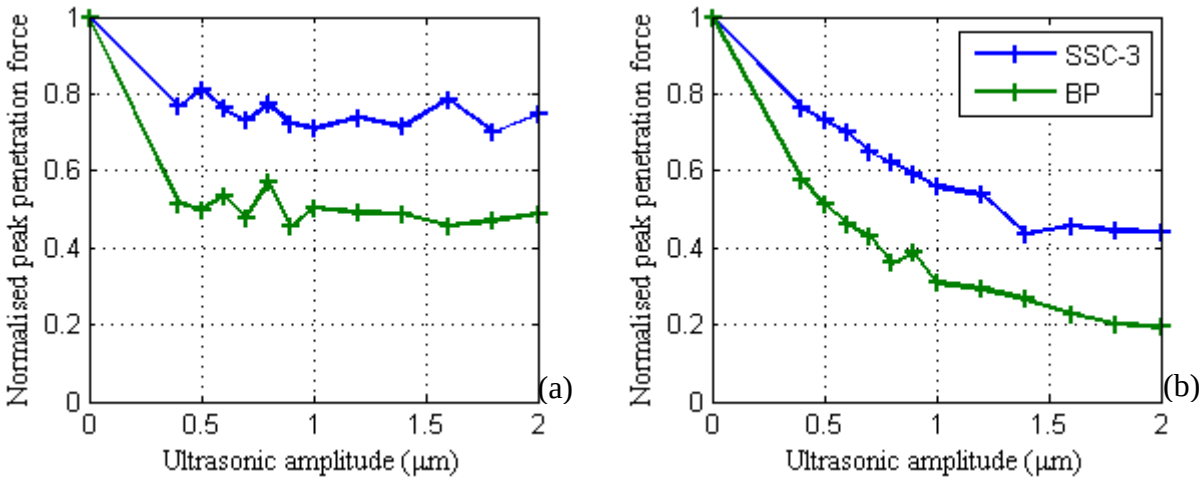

Figure 7.3: Normalised peak penetration profiles in SSC-3 and BP for (a) low density, and (b) high density sand.

It is possible that amplitudes below 0.4 µm would yield a smoother transition in low density sand, however that would require an ultrasonic power supply that was able to reach those levels. Regardless, it can be inferred that if a device were to penetrate through low density regolith, then it would be unnecessary to use vibrations above 0.4 µm.

7.3.2 Power measurement results

The additional devices included on this rig were used to measure the power consumption of both the linear actuator and the ultrasonic transducer. A lower penetration force requires less power to drive the linear actuator, however this will simultaneously increase the power to drive the ultrasonics.

An example of the power consumed by the actuator is shown in Figure 7.4(a) and (b) for low density and high density BP respectively, using a penetration amplitude of 0.8 μm. It is apparent that the motor in the linear actuator is quite inefficient, consuming a baseline of 6 W to operate the actuator without any loading, as well as a relatively noisy signal. For low density sand, the penetration resistance encountered is so low that no increase in actuator power is noted, getting lost within the base-line power consumption. For high density sand, the penetration resistance is high enough that it registers an increase in actuator power consumption, however the signal is still quite erratic.

This appears to be an issue with the linear actuator chosen, and a more efficient motor perhaps would not have such a high base-line operating power. Whilst a perfect motor would not be physically attainable, it could still be worthwhile calculating what the power consumption of a theoretical perfect actuator would be. This can be calculated by multiplying the penetration force by the penetration rate of 0.009 m/s, and is shown in Figure 7.4(c) and (d) for low and high density BP respectively, using an excitation amplitude of 0.8 μm. Here, the power consumption increases much more regularly, showing a peak penetration power of just 0.15 W for low density sand. This would explain the reason why no power increase was seen in the actuator, as the low density state of sand poses little resistance to penetration. High density sand on the other hand increases to just over 1.5 W of peak power consumption, enough so that it can be noted above the actuator base-line consumption and noise.

Finally, an example of the ultrasonic power consumption measurements are shown in Figure 7.4(e) and (f) in the same conditions as before. Low density sand displays a lower magnitude of ultrasonic power consumption compared to high density, due to the lower resistance and therefore loading on the vibration of the probe. However, the profiles of ultrasonic power consumption with respect to penetration depth do not appear to follow the same trend as with penetration force, increasing rapidly at a shallow depth and then levelling off after approximately 6 cm depth. This would suggest that ultrasonic power consumption is not directly proportional to penetration force, and that there might be other interactions that govern ultrasonic power consumption other than the resistance of the sand.

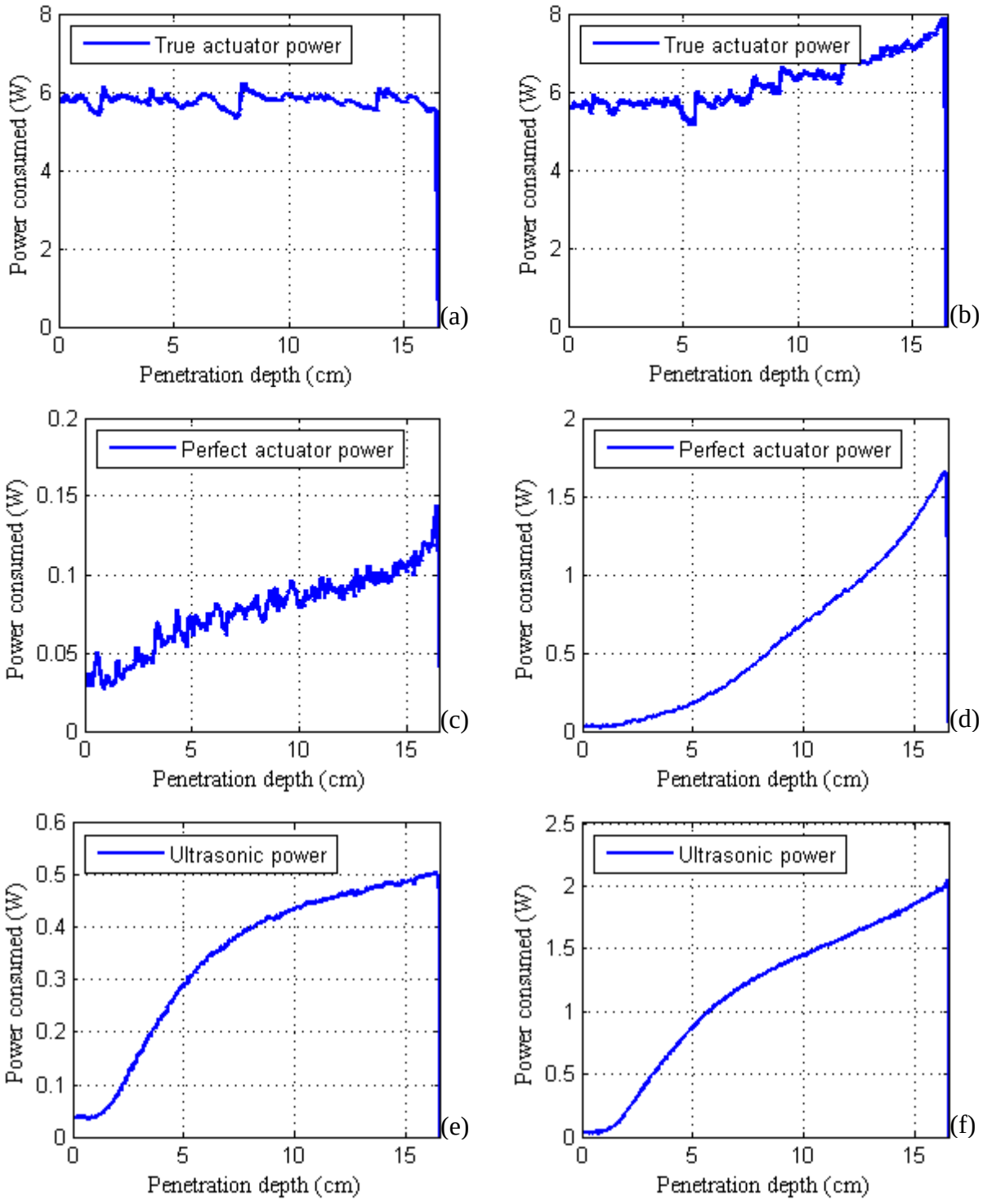

Figure 7.4: BP at 0.8 microns for low and high density

The rest of the analysis of the results will be conducted using the power consumption of the theoretical perfect motor, due to the high inefficiencies of the linear actuator. Different motors will yield different results, but this is an unavoidable reality of the operation of devices. Reducing the number of variables is more advantageous for this stage

of investigations, allowing more direct comparisons and examination. Optimisation of the motor would come at a later stage in the development of a penetration device.

With the choice of which power measurement to use clarified, it is possible to investigate whether there is a potential 'optimised' vibration level in which the total of actuator and ultrasonic power consumption is minimised. Figure 7.5 shows the relation between total power consumption and ultrasonic amplitude used in all four of the regolith environments.

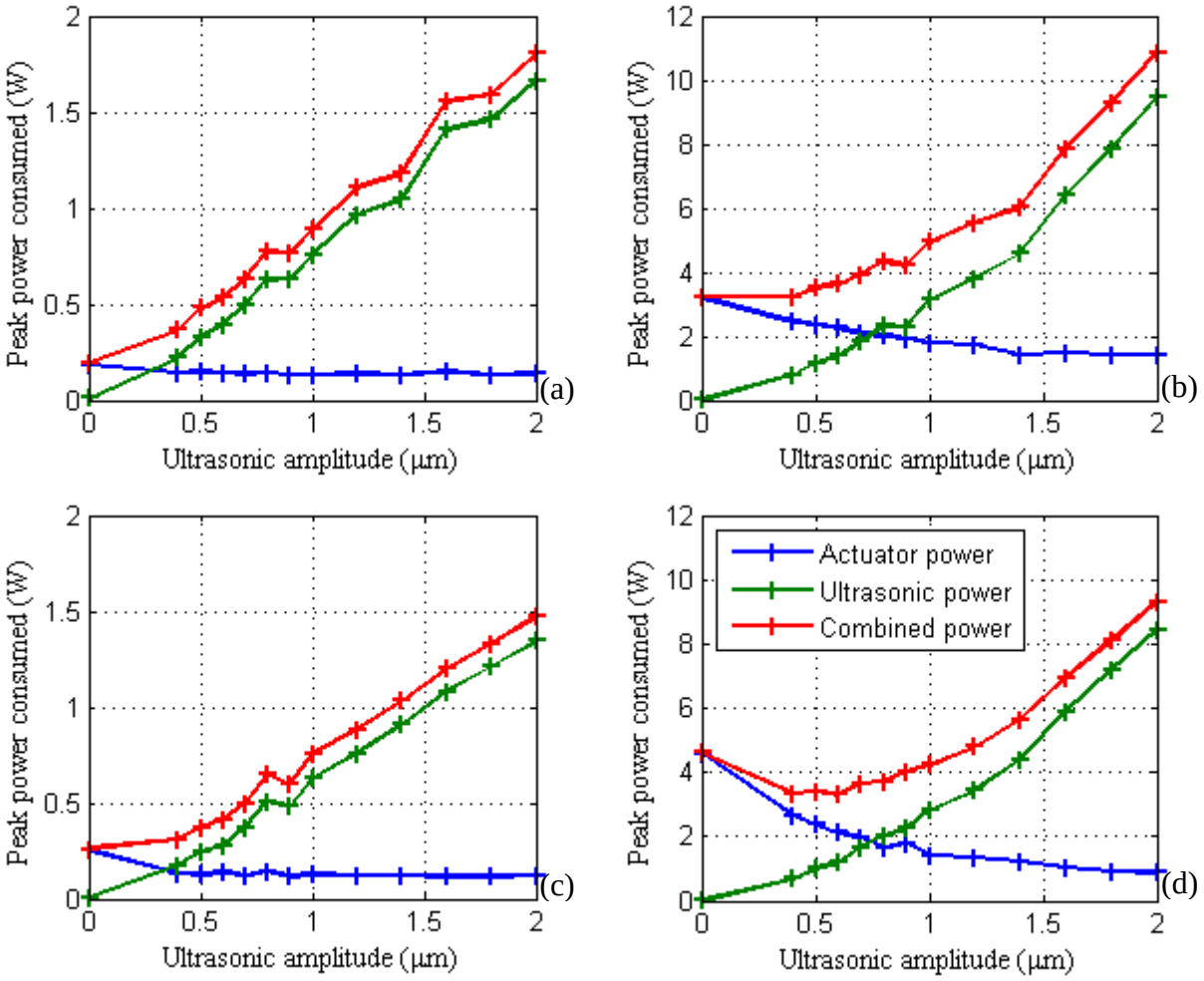

Figure 7.5: Peak power consumption using the perfect motor values for (a) low density SSC-3, (b) high density SSC-3, (c) low density BP, and (d) high density BP.

The ultrasonic power for all environments is shown to increase with higher amplitudes, as expected, with a clear optimum ultrasonic amplitude in high density BP at 0.6 µm. SSC-3 does not display this optimum level, with the decrease in actuator power equalling the

corresponding increase in ultrasonic power at 0.4 µm, showing that the power-saving properties of ultrasonic vibration can be dependent on the substrate.

For low density, both sands display a higher total power consumption for any level of ultrasonic vibration. This is likely due to the fact that the perfect-motor actuator power consumption is so low that it immediately gets overcome by the ultrasonic power, even at the lower amplitude. This illustrates that the regolith environment that penetration is conducted in can have a huge impact on the effectiveness of ultrasonically assisted penetration.

In Chapter 6, normalising the peak penetration forces allowed a quick and easy way of comparing the different sands and density. This can also be done for the total power consumption, with the results shown in Figure 7.6. The only environment to display a reduction in combined power consumption was high density BP, showing a decrease up to 1 µm, with the largest reduction of 28.1% at 0.6 µm. In all other instances, the total power was greater than just a non-ultrasonic penetration, with the higher amplitudes of vibration consuming a significant amount of power.

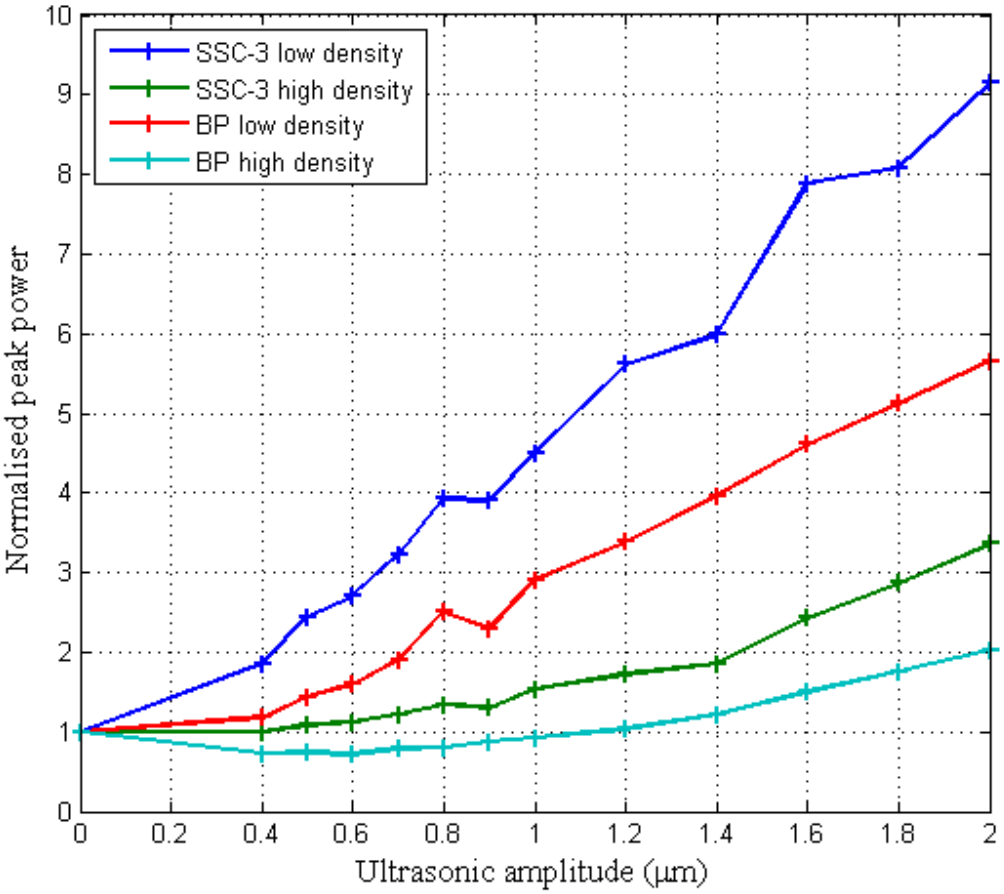

Figure 7.6: Normalised combined peak penetration powers.

7.4 Chapter conclusions

Ultrasonic vibration has been proven to reduce the forces involved in the penetration of granular material. By doing so, the load on the penetrating motor would correspondingly decrease, and therefore the consumed power would decrease. The tests in this chapter set out to investigate whether the penetrating power could decrease by such an extent that the additional power required for the ultrasonics would be off-set, potentially giving rise to an optimum level of vibration.

The results showed that it is indeed possible to achieve a lower total power consumption. It appears that this is not a global effect though, with only high density BP displaying a minimum at 0.6 µm excitation amplitude. This is likely due to the fact that BP showed a high sensitivity to ultrasonic vibration, with much larger relative reductions in force compared to SSC-3, which was chosen as it showed the lowest sensitivity out of all

sands. If a penetrating device were to incorporate ultrasonic vibration, any power reductions would be highly dependent on the specific substrate encountered.

Other interesting effects were also noted with the ultrasonic power consumption as the probe progressed through the sand. As the loading on the probe increases, ultrasonic power will increase, however this was not seen to increase proportionally with the penetration force, indicating that the vibration could be loaded in a different manner. This could potentially be due to the fact that the penetrator is vibrated at resonance, and therefore exhibits nodal points along the shaft that do not vibrate. The tip of the penetrator has the highest amplitude and thus maximum fluidisation will occur near the tip. Once the probe is a few centimetres in, little additional fluidisation will occur, and thus power consumption will not ramp up as much accordingly. As it stands, this could only be fully investigated by manufacturing a large array of ultrasonically tuned penetrators, and is out of the scope of this research.

Chapter 8

Penetration Experiments in High Gravity

The European Space Agency has a selection of opportunities available for student teams to conduct experiments in either microgravity or hypergravity. This involves a highly competitive application process, whereby the best four proposals are selected to develop their experiments alongside ESA experts, culminating in a trip to ESA facilities to conduct their tests.

A student team composed of the author David Firstbrook, Masters student Philip Docherty, and PhD student Ryan Timoney, was accepted for the 6th 'Spin Your Thesis' campaign in 2015 to conduct penetration experiments in hypergravity from 1 to 20 g. This experiment required a complete redesign, development, and manufacture of the penetration apparatus over a period of 6 months. The campaign then concluded with a visit to the Large Diameter Centrifuge (LDC) at the ESTEC facility in the Netherlands in September 2015.

8.1 Experiment concept overview

The experiment proposed for this campaign was largely based on repeating the penetration experiments described earlier in this thesis, but in a variety of gravitational levels. The main measurements stay the same, namely: penetration distance, penetration force, actuator power, and ultrasonic power. With gravity as a variable, this allows us to also provide empirical data for comparisons with existing penetration models. As such, the aims of the centrifuge experiment were thus to:

1. Measure the penetration force profiles of a probe in various levels of gravity, and compare it against the theoretical model.
2. Investigate the WOB reduction of ultrasonically assisted penetration, and see how this varies at higher gravity.
3. Establish the optimum ultrasonic amplitude that results in the lowest combined power consumption of components.

The first part deals with investigating how the penetration force profile in granular material progresses under various values of gravitational acceleration. This will then be compared against predicted results using ElShafie's model described in section 2.3.4, allowing experimental data to test the theory. This particular aim does not depend on ultrasonic vibration; however, if the model proves to be accurate, it could potentially be modified to incorporate ultrasonic effects on penetration force.

The second aim is to investigate how ultrasonic vibration can assist in these penetrations by lowering the required WOB. This is an evolution of the force reduction experiments conducted in Chapter 6. The tests conducted at the LDC investigated the limitations of the force reduction effect in high levels of gravity, with the aim of giving a better understanding of the force-reduction processes of ultrasonic vibration. It is theorised that the ultrasonic vibration reduces the friction between the sand grains and the surface of the cone, but the specific manner in which this is achieved is still to be determined.

The third aim involves the power requirements of penetration through granular material and is an evolution of the experiments conducted in Chapter 7, where it was found that in some sands there was an optimum ultrasonic amplitude at which the total power consumption of penetration was reduced to a minimum. By investigating how this relationship varies with gravity, it is hoped that this data could better advise the potential future use of ultrasonics for planetary missions.

High gravity justifications

The model presented by ElShafie [95] aims to predict penetration profiles in any gravitational environment. Since Earth (1 g) is the largest solid body in our solar system, data regarding penetration at <1 g is the most applicable, however low gravity experiments also come with their own inherent difficulties.

Parabolic flights, in which a special aircraft flies on a parabolic trajectory, can provide around 20 seconds of microgravity, with longer times available for levels of gravity above 0 g. Drop towers can also facilitate microgravity experiments for a few seconds by allowing the experiment to free-fall in a large tower. Indeed, ESA also offer these as student led projects as well as part of their 'Fly Your Thesis' and 'Drop Your Thesis' campaigns. It should be noted though that for the year that I was available for experiments, the 'Fly Your Thesis' opportunity was not running.

Both of these methods, however, can only be sustained for short periods, and experiments that require more time need to be performed in orbit around the Earth, such as on small satellites or on the international space station. Due to the difficulties of sending an experiment into orbit, and the time constraints given by the parabolic flights/drop towers, other methods had to be investigated.

Whilst high-gravity research will not be able to directly simulate drilling on Mars or the Moon, it will aid enormously in establishing a trend for drilling and penetration where gravity is a variable, providing predictions of penetration force-profiles in low gravity by extrapolation. For this reason the centrifuge is a good option, as it allows an unrivalled single experimentation time, as well as a much longer campaign duration in which many individual tests can be completed. The ability to conduct a large number of tests is particularly useful in granular material experiments, as sand, by its very nature, is notoriously troublesome to model on the small scale with any reasonable amount of accuracy. Empirical evidence is thus highly valued in this field.

8.2 Experimental rig re-design

8.2.1 Penetration action

The rig used in previous experiments stood at nearly 1.5 meters tall, whereas the working height of the gondola, shown in Figure 8.1, is just over 70 cm. The entire experimental apparatus therefore had to be completely re-designed to fit within these limitations, and indeed this proved to be one of the most difficult aspects of the whole campaign. To solve this problem, it is first important to understand why the original rig needed to be nearly 1.5 meters tall to begin with. Knowing this, it will then be possible to come up with alternative methods or space saving ideas.

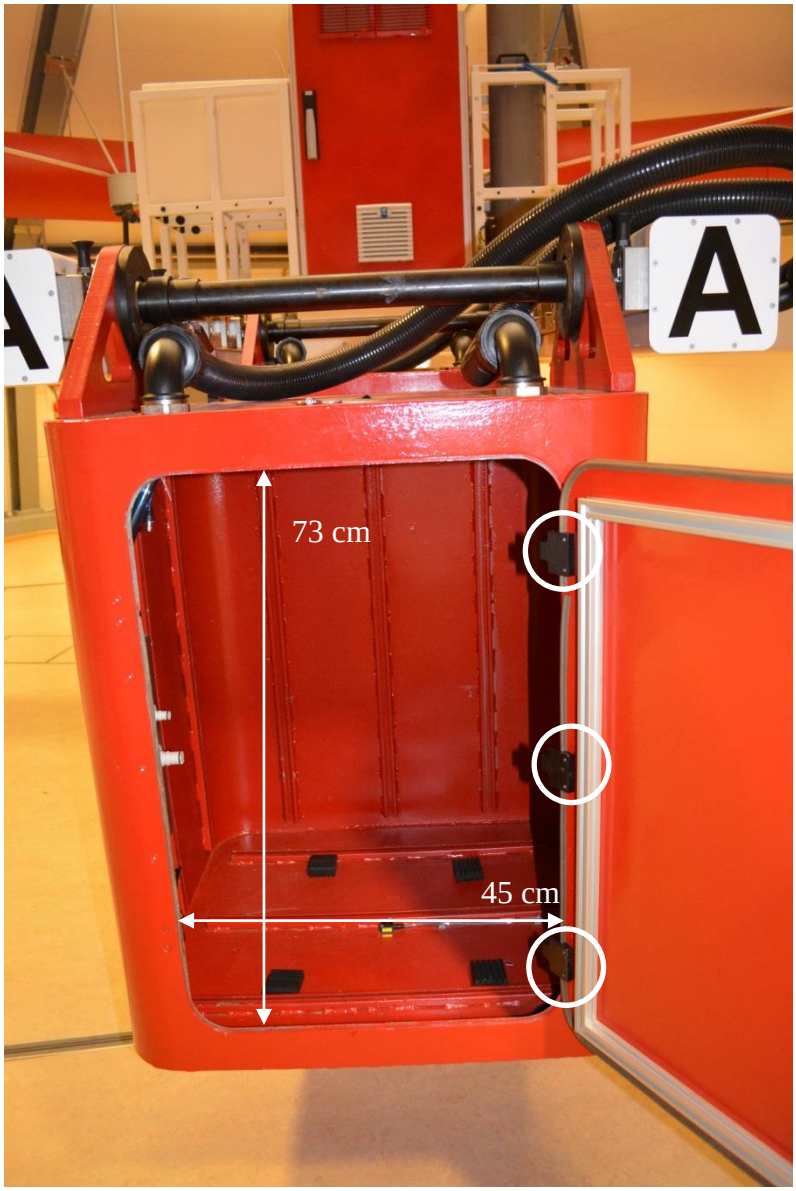

Figure 8.1: The LDC gondola and size constrictions. Note, the hinges (circled in white) also require consideration.

Arguably the most important aspect of all the experiments described in this thesis is the force measurement; we are after all aiming to reduce the required penetration force using ultrasonics. In order for the measurement of penetration force to be accurate, we must ensure that the force transducer is the only point of contact that the probe has with the supporting structure of the rig. If the probe were to be supported at any other regard, then it would be exerting a force that would not get measured, invalidating any results.

Since the penetrator is moved up and down in a straight line, it is most efficient to locate the linear actuator directly above, in line with the probe. This provides a linear force transmission from the actuator, to the probe, and finally into the sand. The schematic of this is shown in Figure 8.2(a), illustrating the linear layout.

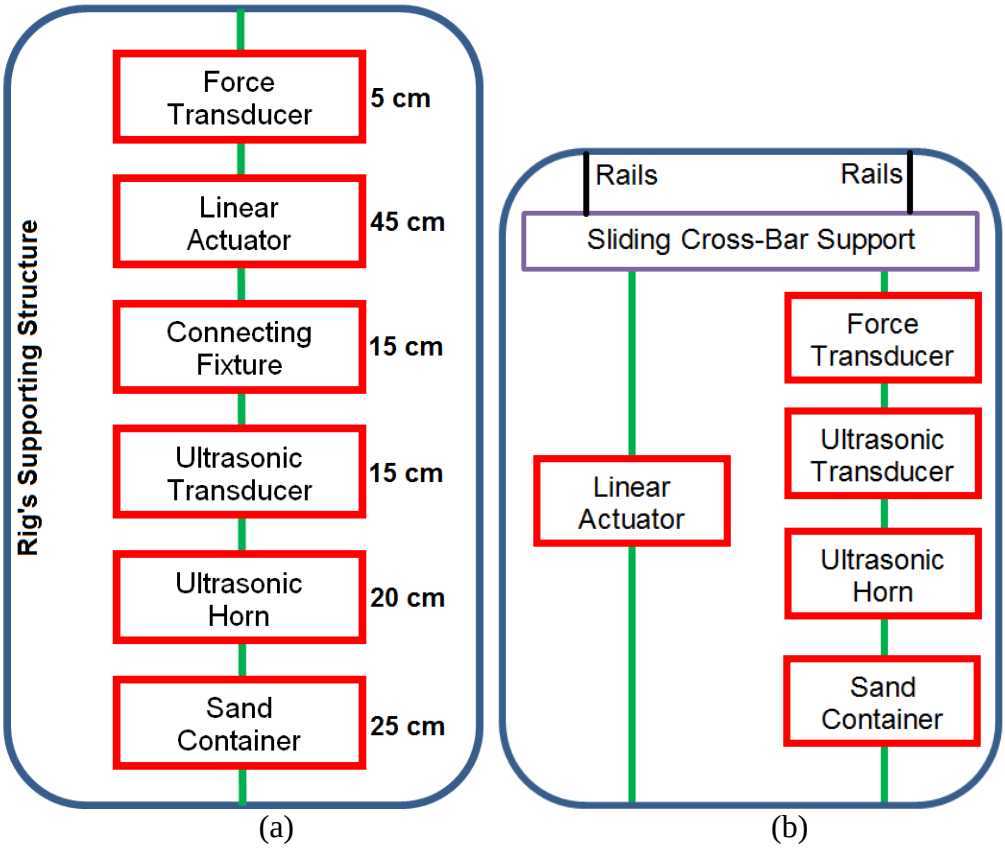

Figure 8.2: The original linear rig, with rough height dimensions is given in (a). Every component must be beneath the other, creating a tall structure. The new parallel design is shown in (b), where the actuator is placed side-by-side to the transducer, horn, and sand container. This reduces the height significantly, but further reductions must be made to adhere to 65cm.

Cuts needed to be made to the arrangement shown in Figure 8.2(a) to fit within the 73 cm height imposed by the gondola entrance, whilst also allowing additional room for ease of manoeuvring. The first design choice was to step away from the linear design, and produce a parallel arrangement where the force transducer, ultrasonic transducer, and horn are connected to a cross piece, with the entire unit pulled down by the linear actuator, Figure 8.2(b). The final revised design for use in the LDC is shown in Figure 8.3. Whilst this method does indeed dramatically reduce the height requirement, it also creates an off-axis torque in the sliding cross-bar support that must be addressed to ensure nothing in the apparatus breaks under the anticipated high g forces. The redesign of this experimental rig was conducted with assistance from MSc student Philip Docherty.

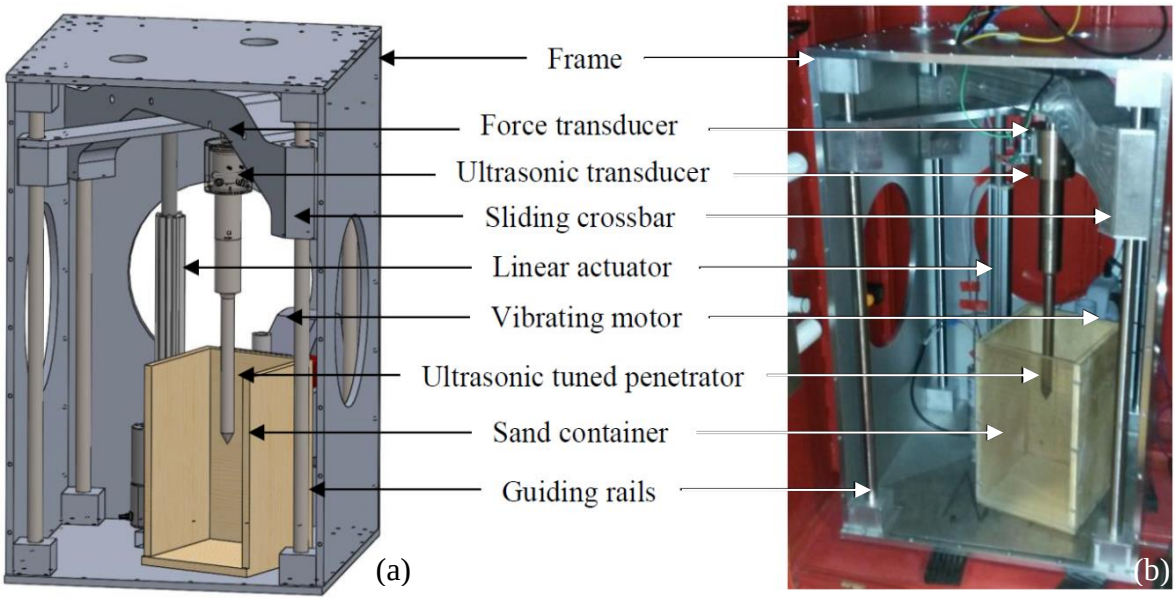

Figure 8.3: The LDC rig.

8.2.2 Transducer case

Further reductions were made by omitting the connecting fixture and machining a custom case for the ultrasonic transducer which integrates a threaded connection within it. As shown in Figure 8.4, this new case also does away with the transducer's internal fan, as this was mostly used to cool the transducer only in very high-power applications. As has been shown in Chapter 7, only a few Watts are consumed at the level of vibration used, so heating is not an issue. Additionally, the wires supplying the transducer were routed to the side of the unit rather than above, enabling a threaded connection at the top of the case which can be used to connect it directly to the force transducer. In this new set up, this stack is at its absolute minimum length of 44 cm. The top and bottom plate, as well as the thickness of the sliding cross-support and sand container, all contribute more height to the rig, leaving 18 cm potential penetration depth.

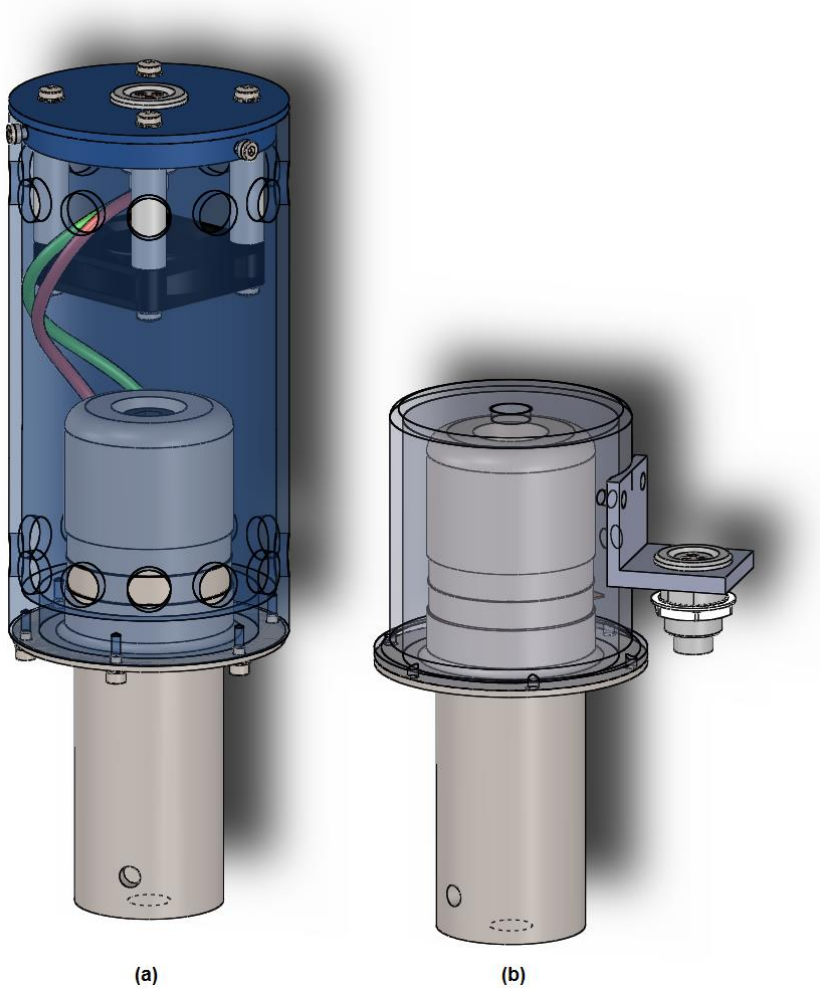

Figure 8.4: Side-by-side comparison of the old transducer case (a) with the new one (b) The fan has been removed, and the cable socket moved to the side of the case to allow the force transducer to fix directly onto the top of the case.

8.2.3 High gravity calculation on the hardware

As the rig will be subjected to high levels of gravity and potentially complex forces from within, detailed stress analysis is vital to ensure that the apparatus does not malfunction or break. In the following subsections, the stress analysis of the three main components: ultrasonic transducer case, sliding crossbar, and rig frame are given. In addition to simulations of high-gravity stresses on components, the sand container was physically loaded with 100 kg weight to ensure that it would not break under the penetration force at high gravity.

8.2.3.1 Ultrasonic transducer case

The redesign of the ultrasonic transducer case puts the force transducer directly at the top, loading this point with thousands of Newtons. Coupled with the relatively small contact area of the force transducer, this could lead to potentially damaging levels of pressure on the ultrasonic transducer case. The initial choice of material was aluminium 6082 T6, but a simulation of the stress analysis using ABAQUS proved that the magnitude and stress values were too high. The material was then changed to stainless steel 1.4305, which meant the stresses were within acceptable limits, shown in Figure 8.5.

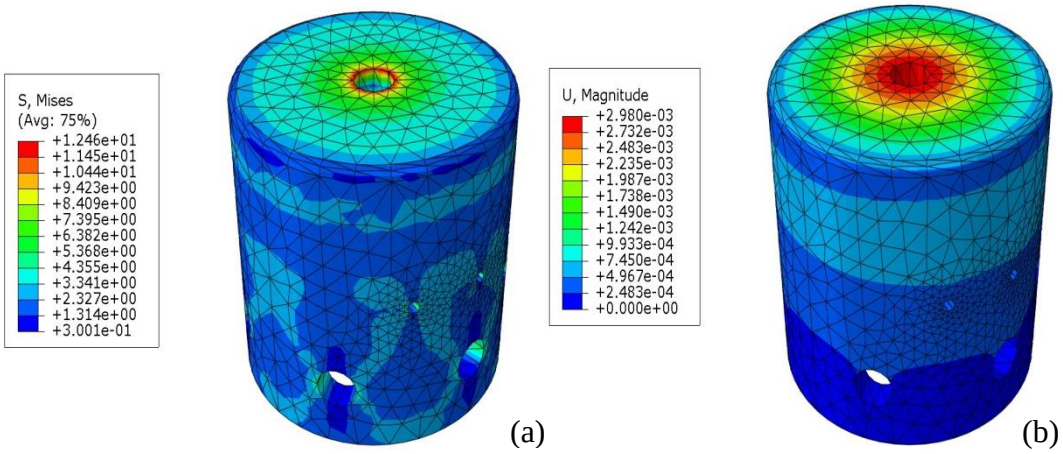

Figure 8.5: Stress analysis of the new design for the ultrasonic transducer case. The Mises stress (a) is in MPa, and the magnitude of displacement (b) is in mm.

The simulated maximum stress of 12 MPa falls well below the tensile strength of this steel (500 to 750 MPa) [117], so a steel case will be strong enough for this experiment. It is also vital that the case does not flex during penetration, as the piezo elements in the force transducer are susceptible to bending forces. As can be seen in Figure 8.5(a), a maximum deflection of 3 µm is low enough that the force transducer would not be affected by any bending moment. Instead of using a fan in this design, cooler holes were incorporated to allow air to flow through the cap in order to cool the piezo ceramics passively during operation. The wires from the electrodes were fed through one of these holes to a cable socket off to one side.

8.2.3.2 Sliding crossbar

Whilst the parallel rig goes a significant way in solving the issue with height constraints, it creates another problem with stresses. Since the actuator is no longer acting directly through the penetration path and is instead off to one side, it creates off-axis forces within the sliding cross-bar, which will act to skew the bar and jam it on the rails if it is not accounted for. The linear actuator is rated to a maximum of 1,000 N, which can create a very large torsional force if measures are not taken. This was dealt with in a number of ways:

1. The actuator was placed as close to the sand container as possible, either side of the centre of the sliding cross bar. This minimised the distance between the pivot point and the force, thereby reducing the moment.
2. The rails, and thus cross-support length, were designed to be spaced as far apart as possible to reduce torque forces. This was achieved by placing them along the diagonal of the 43x43cm base plate permitted by the gondola.
3. The sliding cross-support was designed to be rigid so that it could withstand the bending force created by the actuator force and penetration force being off-set from one another.
4. Similarly, linear bearings were used within the cross-bar support that can withstand the large force, yet still allow the bar to slide freely. There were four linear bearings within the sliding crossbar, and two within the supporting cross piece.

As with the transducer case, a stress and deflection analysis was conducted on the sliding cross-bar to see how much it might bend under maximum loading. This was considered to be a ‘worst case scenario’ by using a maximum loading force of 1,500 N to help accommodate any unanticipated effects due to higher gravity. Since the cross bar is a sliding fixture, it has no fixed points and is thus complex to model. Complicated simulations are unnecessary at this initial phase of testing, so the simulation was simplified in the interest of time by taking the frame of reference with respect to the cross bar, and modelling two different scenarios. In the first scenario, shown in Figure 8.6(a), the actuator is kept stationary and the transducer force is pushing up, whereas in Figure 8.6(b) the transducer is kept stationary and the actuator is pulling down. The movement of the rails was taken into consideration by limiting those portions of the cross bar to only move in the

vertical direction. The main areas of stress in the sliding crossbar were calculated to be located at the connection points for the actuator and force transducer. To mitigate this, rounded corners and fillets were incorporated into the design wherever possible to reduce the concentration of stress. From the analysis it was found that the stresses involved would not be an issue for the design with maximum stresses reaching 18 MPa with the tensile strength of this aluminium alloy quoted at 295 MPa [118].

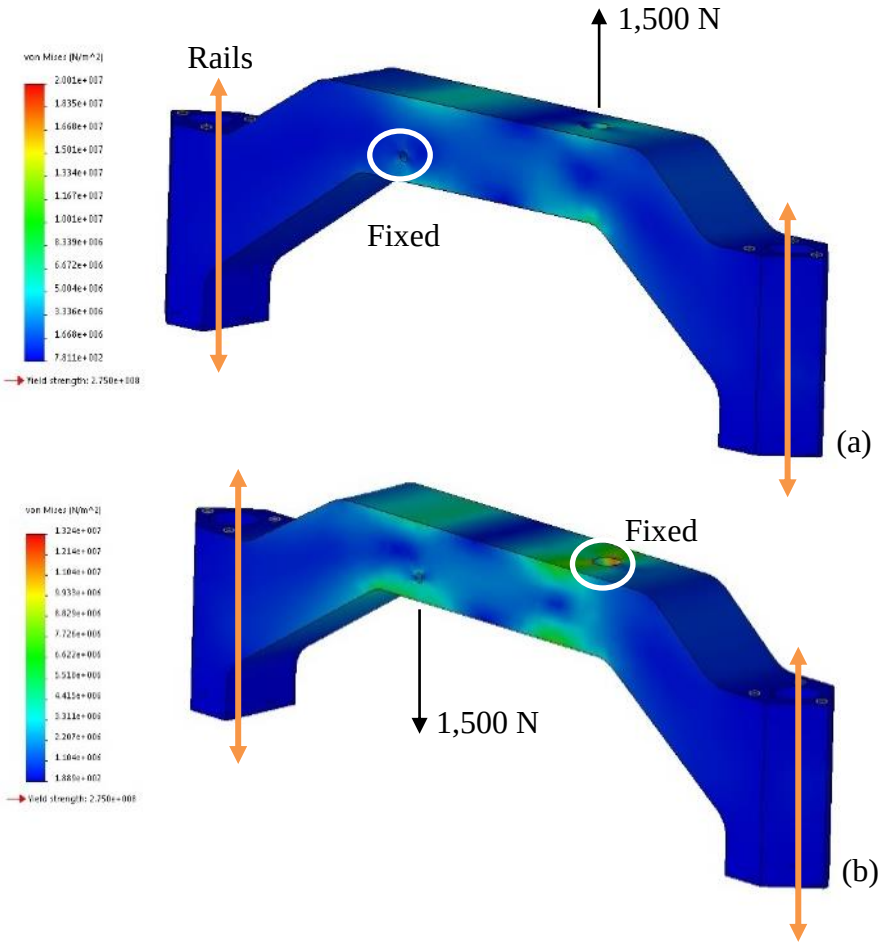

Figure 8.6: Stress analysis of the sliding cross-bar in two scenarios: (a) with the actuator point stationary, and (b) with the force transducer point stationary.

A similar simulation was conducted for any displacement of the crossbar, as a large degree of movement could potentially jam the bar and either prevent movement, or at least overload the linear actuator. From the analysis, shown in Figure 8.7, it can be seen that the magnitude of displacement of the crossbar will only be around 0.4 mm in both scenarios. With a displacement this small, failure of the sliding action should not be an issue.

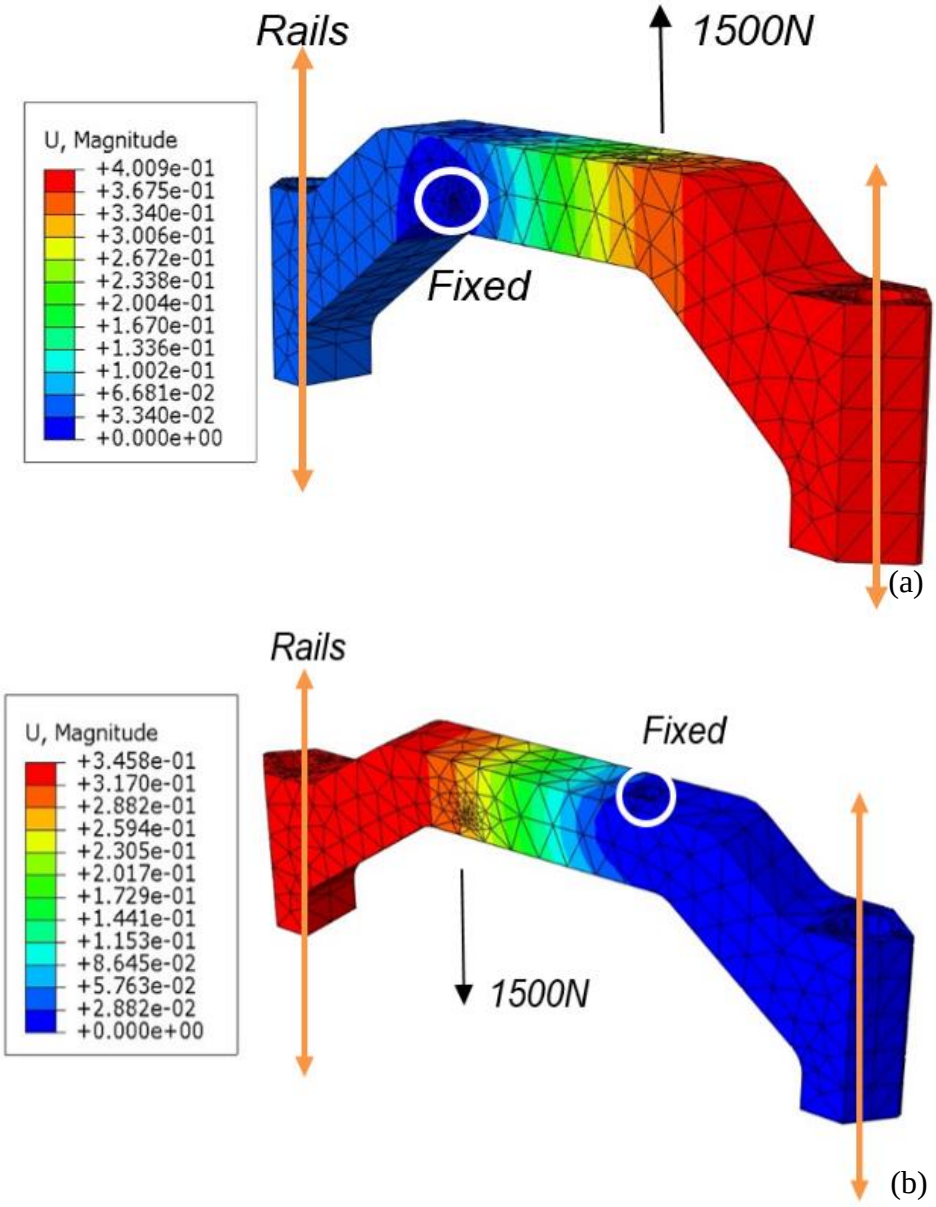

Figure 8.7: Deflection analysis of the sliding cross bar in two scenarios: (a) with the actuator point stationary, and (b) with the force transducer point stationary.

8.2.3.3 Rig frame

Within the centrifuge, the experimental apparatus will be subjected to a maximum of 10 times Earth's gravity, so an additional simulation was conducted on the frame itself. The frame is made of the same aluminium as the sliding cross bar, so an analysis was completed to see if the frame could withstand this force. In higher gravities, all of the structural panels will weigh more, and must still support themselves. Whilst this can be approximated by placing a large weight on a physical object (indeed, this was done after

manufacture), a simulation that increases the level of gravity is better. A stress and displacement analysis was run on the frame, shown in Figure 8.8(a) and (b) respectively. A maximum stress of 850 kPa and maximum deflection of 0.02 mm fall far below any failure limits, and will not be a concern for these experiments.

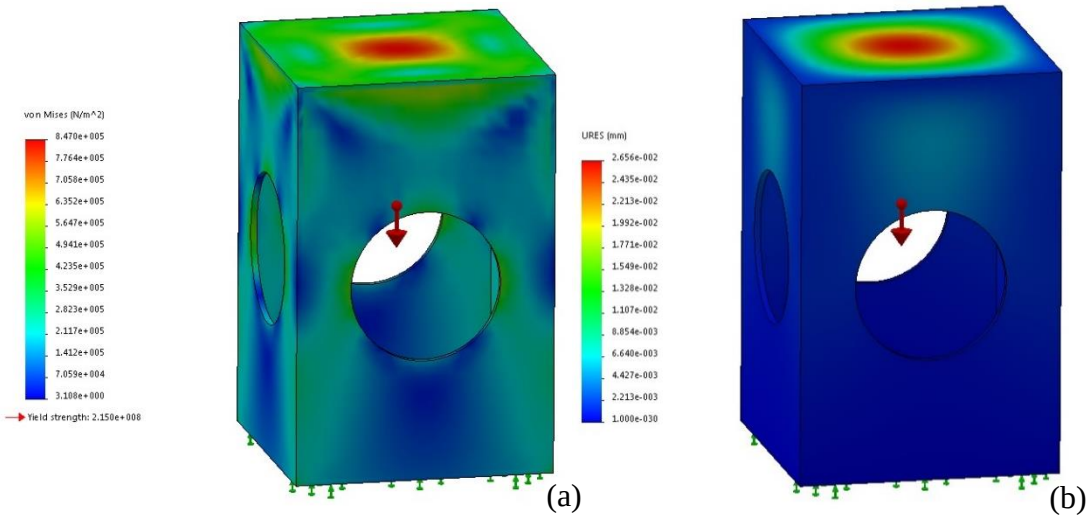

Figure 8.8: Stress and deflection analysis on the aluminium frame under 10 g loading.

8.2.4 Sand preparation

When the centrifuge is in motion, access to the experimental rig is forbidden for obvious reasons. Resetting the container of sand in the usual poured-method in-between each penetration would be too time prohibitive, and removing and re-securing the container from within the rig without knocking or disturbing the sand would be extremely difficult. Therefore, the experimental method needs to be altered to account for this, omitting manual sand sample preparation and requiring remote control of container vibration motor.

Remote vibration of a container of sand poses some difficulties over how the container is secured to the rig. The container must be permanently attached so that no horizontal movement takes place during the experiment, but at the same time must be loose enough to allow the container to vibrate sufficiently. This was solved by attaching a thin aluminium plate to the bottom of the container, which was then in turn loosely bolted to the floor of the rig with a rubber mat underneath. The bolts were glued in place to ensure they would not loosen under the vibration.

Attaching the container to the bottom of the rig in any way would act to reduce the amplitude of vibrations from the shaker, so this semi-permanent fixture was tested under laboratory conditions. The container was filled with sand to 2/3 capacity, and several different durations of vibration and penetrations conducted to see if any variations were apparent. No deviations were noted above 1 minute vibration duration, so a duration of 2 minutes was chosen to allow the container to be vibrated at higher gravity and still adequately reset the sand.

Since the container of sand was not reset by hand and levelled off, the container needs to be less than 100% full in order to accommodate the vibration without any spillages. This reduces the maximum penetration distance as the surface of the sand begins at a lower level. The container was filled with an amount of sand that was small enough so that no sand would be thrown out of the container once vibration started, eventually settling on a weight of 4.57 kg. The final bulk density recorded using this method was 1.790 g/cc, as opposed to the lower density of 1.626 g/cc recorded for other tests. This is due to the different conditions of this method, such as a smaller sand mass and a semi-permanent fixture, resulting in a slightly denser final density. It is expected that this will result in higher peak penetrations than with previous experiments, therefore direct comparisons will not be able to be conducted.

Before arriving at the LDC facilities, the plan had been to vibrate the container of sand at high-gravity, whilst the centrifuge was in motion. However once this was able to be tested in situ, it was found that even at the lowest level tested (1.5 g), the vibration of the container was significantly impaired, and portions of sand were visibly seen via the gondola video link to be ‘jammed’, a phenomena that has been previously noted [85] and indicates that sections of the sand will not be correctly reset. It was understood that the sand would increase in weight at higher g levels and therefore the amount of vibration would be reduced, but it was not anticipated that it would impact the vibration to this degree.

To remedy this, the centrifuge was spun down to a standstill before resetting the sand (i.e. to 1 g). This ensured that all samples of sand would have been reset in the same environment, providing consistency in results. Measurements of the surface levels of the sand showed that the sand did not compact further after having been subjected to 10 g,

giving a constant value for density throughout all the experiments. (Previously the plan was to rely on the video feed to record the levels of the sand after vibration, but this would have been much less accurate than measuring by hand). This method obviously added extra time to the experiment, so the vibration time was decreased from 2 minutes to 1 minute to compensate. A 1 minute vibration time in pre-testing was shown to adequately reset the sand, and since the original 2 minute vibration time was chosen specifically to allow for vibration at higher g levels, this was a reasonable compromise to make.

There were also two additional benefits of using this method. Firstly, there were some concerns over failure of the vibrating motor due to prolonged use. The new method effectively halved the duty-cycle, thus alleviating these doubts. Secondly, this method allowed the linear actuator to raise the penetrator at 1 g, rather than at high g. This significantly reduces the load on the actuator, thereby reducing the probability of failure.

8.2.5 Pre-tests and variable justifications

After the experimental rig was completed, some functionality tests were conducted to examine whether all components and devices were working as intended. The preliminary test involved measuring the perfect actuator motor and ultrasonic power consumption, shown in Figure 8.9, as well as the penetration force as a function of excitation amplitude, shown in Figure 8.10. These tests were using the gravity rig in 1 g using the same amplitude range as in Chapter 7, with values of: 0.4, 0.5, 0.6, 0.7, 0.8, 0.9, 1.0, 1.2, 1.4, 1.6, 1.8, and 2.0 µm. This distribution gives a high resolution of data points at the lowest levels of amplitudes, with a wider range at the higher amplitudes to identify the further reaching effects. In the interest of conducting as many experiments as possible at the LDC and keeping with the concentration at low amplitudes, the 1.8 and 2.0 µm were eventually omitted from the final experimental procedure.

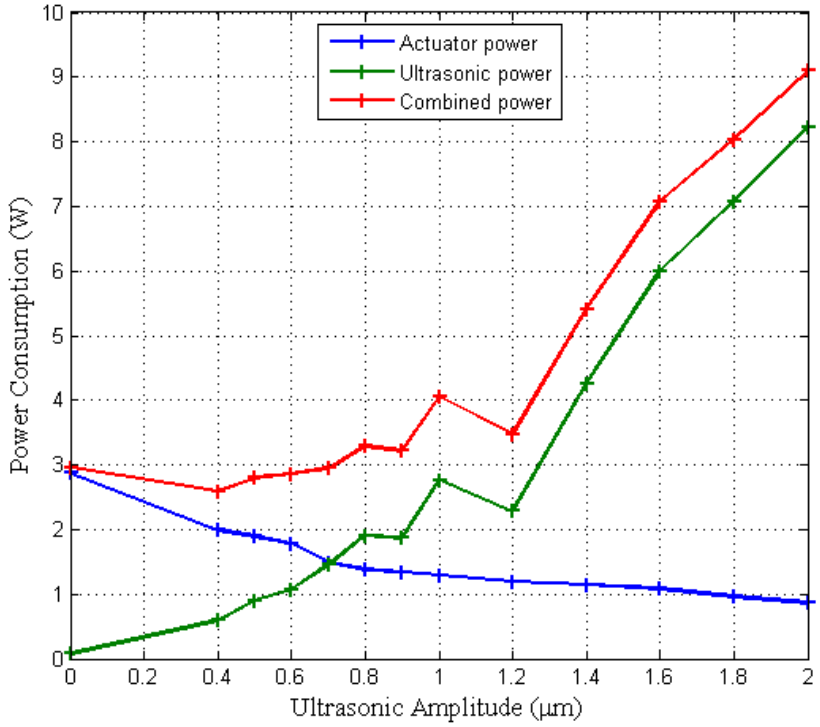

Figure 8.9: Preliminary measurements testing the power experiment capabilities of the newly built gravity rig, penetrating to 12 cm in BP. All experiments were conducted in laboratory conditions at 1 g.

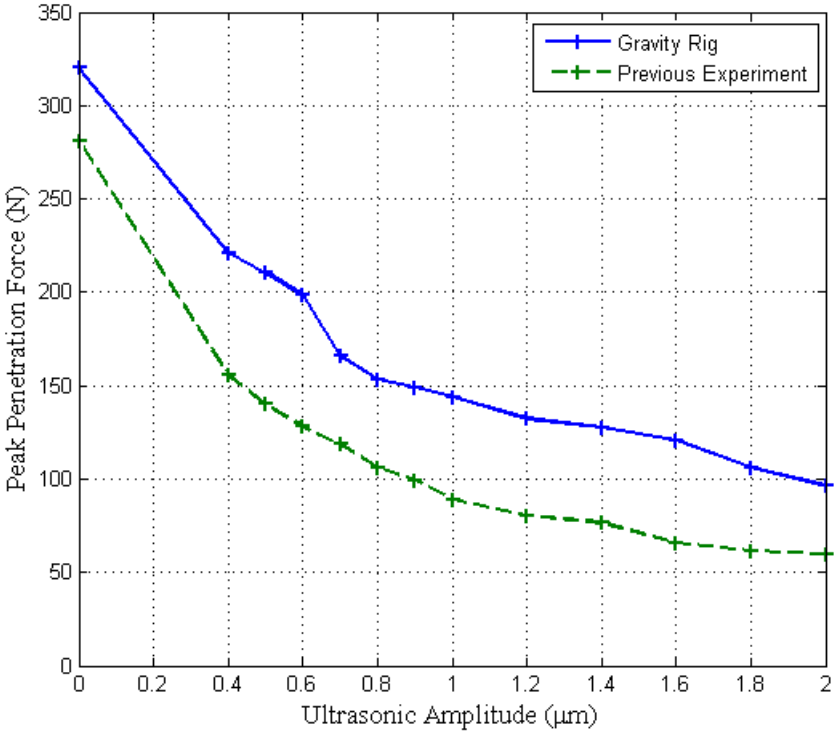

Figure 8.10: Preliminary measurements of the peak penetration force in BP using the gravity rig at 1 g, shown in blue. The penetration forces encountered at 12cm depth from the power experiment are also shown in dashed-green.

Even with a reduced maximum penetration depth of 12 cm, the same general results can be seen, with a clear minimum in total power consumption in Figure 8.9, and a decreasing peak penetration force in Figure 8.10. For comparison purposes, the force encountered at 12 cm depth during penetration in the power experiments is also included in Figure 8.10. These forces are lower than in the gravity rig for all amplitudes, however this is to be expected due to the lower bulk density of sand used in the power experiments (1.626 g/cc). The gravity experiment uses a slightly higher bulk density (1.790 g/cc), due to the different sand preparation method, as outlined in section 8.2.4.

8.2.6 Circuitry and interfaces with ESTEC facilities

8.2.6.1 Experiment control

The penetration experiment is mechanically intensive, requiring a variety of motors and settings to be activated/deactivated at different times, as well as recording the resulting data points. Table 8.1 illustrates the different components that require external input, the method used to control that instrument, and the type of connection.

Table 8.1: Devices and methods of control.

Component	Input/Output	Cable/Port	Method of control
Ultrasonic Amplitude	Input	Serial	MATLAB script
Ultrasonic power	Output	Serial to NI-DAQ	MATLAB script
Actuator (on/off)	Input	Standard wires	MATLAB script
Actuator distance	Output	Standard wires to NI-DAQ	MATLAB script
Force measurement	Output	Co-axial to NI-DAQ	MATLAB script
Sand box vibration	Input	Arduino connection	Off-set motor
Sand density	Output	USB	Camera recording the level of the sand

Most of the control was done through an Arduino device using MATLAB scripts running on a laptop placed within the central gondola; this was then in turn remotely accessed with TeamViewer via the building's network and controlled from a computer in the LDC control room. The measurements themselves were done using a USB NI-DAQ

device, operated through the same MATLAB script. The density of sand was originally going to be measured via a camera in the gondola and volume markings on the container, with the original plan of resetting the container of sand at high gravity. However, after experiments had commenced, this reset procedure was changed to spin down the centrifuge every time and reset the container of sand in 1 g. With this new procedure, densification was constant across all runs, and thus just a single value of bulk density was required.

8.2.6.2 Gondola interface

For ease of transferring the rig in and out of the gondola, the entire rig was designed to be free standing and was largely assembled beforehand. The rig formed a cuboid with outside dimensions of 43 x 43 x 67 cm (width x depth x height). As such, the rig was able to simply be transferred into the gondola and did not need to be bolted to either the side or top. A schematic of the location of the rig within the footprint of the gondola is shown in Figure 8.11 [119].

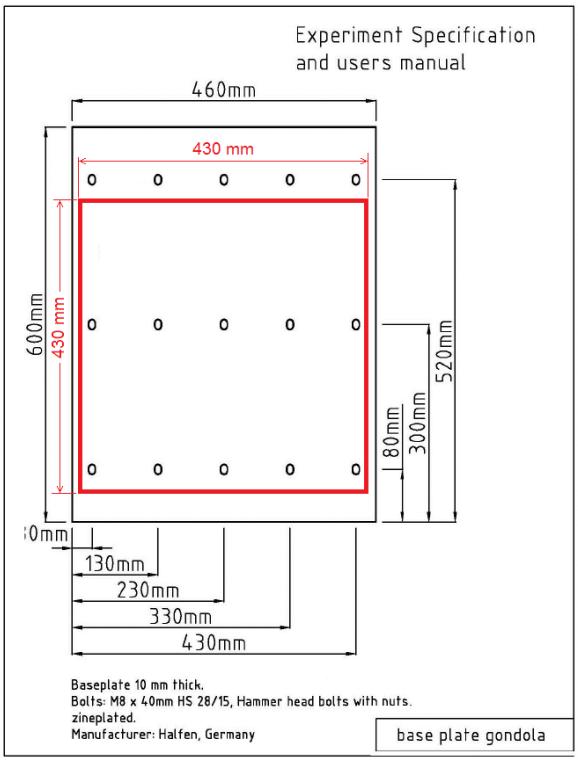

Figure 8.11: Gondola specifications. The footprint of the experimental rig is shown in red.

The ultrasonic power supply, Kistler force sensor supply, NI DAQ (USB-6009) and 12 V DC power supply were placed in the central gondola, along with the control laptop. The

ultrasonic power supply was connected to the laptop via a serial port and the NI-DAQ was connected to the central computer via USB. The experimental apparatus and Arduino circuits were located in the testing gondola, and the Arduino was connected to a serial output, which in turn is connected to the central laptop. A top-level schematic of the system from a data and electrical perspective schematic is given in Figure 8.12. The devices and specifications are defined in Table 8.2.

Table 8.2: Devices and specifications

Device	**Function**	**Specification**	**Gondola Location**
Sander	Vibrates the sand box	230V AC supply, switched	Testing
Kistler Force Sensor	Measures the force of delivered by the system	Specialised system connection.	Testing
Actuator	Raises and lowers the penetrator	LT225-300	Testing
Ultrasonic Transducer	Provides the ultrasonic vibration	Sonic Systems™ model	Testing
Arduino	Data interface and controller for actuator and sander	Uno model	Testing
Relay	Allows control of the sander	G3NA-210B 5-24DC	Testing
H Bridge	Allows control of the actuator	VNH5019	Testing
Kistler Box	Converts signal from the sensor to a readable format		Central
P100 Box	Powers and controls ultrasonic transducer, and relays back info		Central
12 V Power supply	Powers the actuator	Max 3 A	Central
Multiplier box	Provides power readings for the actuator		Central
Current Probe	Converts actuator current into voltage for use with multiplier box	Hall effect sensor	Central
NI USB	Interface for data acquisition between equipment and computer	NI USB-6009	Central
Various Euro Socket Adapters	Allows UK equipment to be powered		Central/ Testing

Central Gondola

Testing Gondola

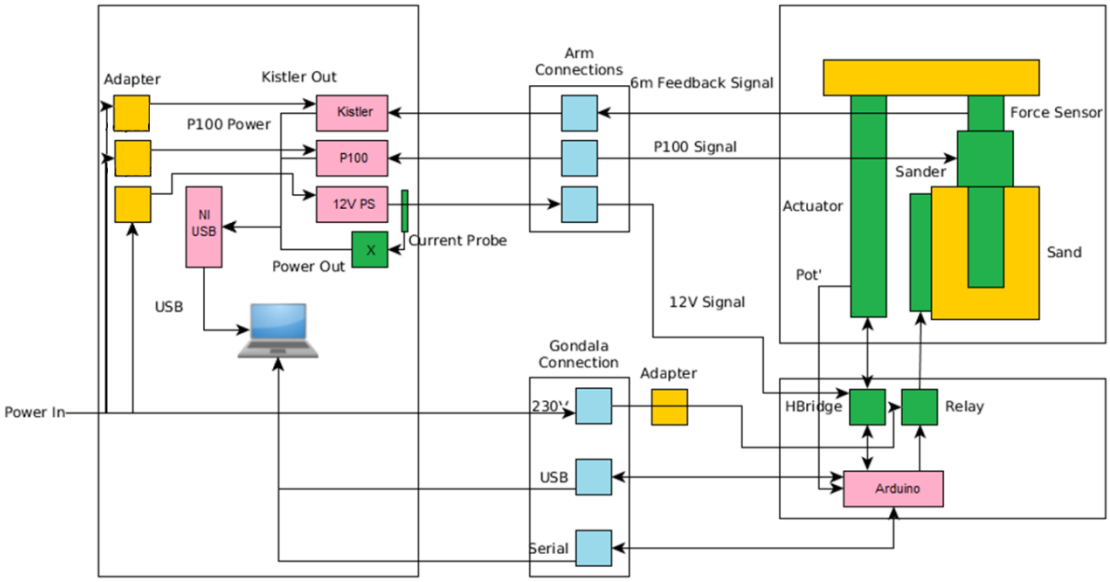

Figure 8.12: Top level connections between the central gondola and the testing gondola.

8.2.7 Testing at the LDC

In total, two and a half days were assigned to each student group to complete all the experiments. Upon arrival, the equipment was set up, but there were significant problems with getting connections to interface correctly with the control PC. Additionally, unforeseen problems with high-gravity levels were encountered, such as the inability of the container of sand to vibrate at high gravity. In the end, no experiments were able to be conducted on the first day, and instead the team focused solely on ensuring that all the equipment worked correctly, and that the procedure was optimised. This included the decision to spin down the centrifuge to 1 g before resetting all containers of sand, significantly increasing the time taken for experiments.

The experimental procedure thus had to be altered. The vibrating container was first attached to the inside of the rig using the semi-permanent fixture to allow some degree of vibration, and filled with 4.57 kg of BP. The rig was then placed in the testing gondola,

and all electrical connections routed out of the gondola, secured to the centrifuge arm, and connected to the powered devices in the central gondola. All personnel were then instructed to vacate the centrifuge room, and the locks on the doors were set in place. Via remote control, the penetrator arm was then raised, and the container set to vibrate for 1 minute to reset the sand. The centrifuge was then spun to the desired gravity level, and the ultrasonic vibration initiated at the desired amplitude. The data was set to record and penetration allowed to commence until the final depth, whereupon the ultrasonics were switched off and the DAQ allowed to finish recording. The centrifuge was then spun down to resting point, the penetrator raised out of the container, and the container set to vibrate once again.

Two minutes were allotted per test, which comprised: 20 seconds penetration, 20 seconds removing the probe from the sand, 60 seconds for vibrating the container of sand to reset it, and 20 seconds for checking everything is correct and in place before proceeding. An additional 2 minutes were allocated for each run to allow the centrifuge to speed up to the desired level of gravity as well as speed back down to allow for sand reset.

Tests were started using the lowest levels of gravity possible, to avoid the risk of damaging the equipment at high g on the first day. Each ultrasonic excitation amplitude was tested consecutively and then repeated three times, rather than testing each amplitude three times before proceeding. This was done to ensure that a broad set of measurements was taken before the repetitions were done, in case any equipment would suddenly fail. All results at a given g level were completed before moving onto the next g level.

Since a significant amount of time had been allowed for unforeseen circumstances, the second day was highly productive, with 84 out of 147 tests completed, once some additional teething issues at the start of the day had been resolved. Since the experiment was highly automated, the main human interaction was simply to stop and start the centrifuge after each run. It was noted during this time that it could have been possible to automate this action as well and let the experiment run overnight, obtaining a significant number of results. There was not enough time during the experiment to program this, however it is a consideration for any potential future experimental plans.

8.2.7.1 Variables tested

The specific variables tested were also changed slightly whilst at the facility. The originally planned testing variables are shown in Table 8.3.

Table 8.3: The variables planned for testing before arrival at the LDC.

G level (g)	2	3	4	6	8	10		
Ultrasonic Amplitude (μm)	0	0.4	0.5	0.6	0.7	0.8	1.2	1.6

These points were chosen in order to split the results evenly over the two days, with each half day testing all g levels and two ultrasonics amplitudes, as well as all three repetitions. However, the issues encountered on the first half day meant that this plan would no longer work, and would have to be altered. The initial testing in high g brought concerns of the survivability of some of the components at these extended levels of acceleration, mostly from fears that the linear actuator would break. It was therefore decided to concentrate more results at the lower amounts of gravitational accelerations, removing 4, 6, and 8 g and replacing them with 1.5, 5, and 7 g. Concentrating tests at lower g levels was also beneficial for potentially extrapolating results to gravities less than 1.

Additionally, it was decided to run a set of tests at 1 g whilst the test rig was in the gondola, rather than externally in a lab as originally planned. This provided a consistent environment for experimentation (temperature, humidity etc.), leading to more accurate results. As a result of increasing the number of g levels, the 0.7 μm value of ultrasonic amplitude was removed, giving a total of 147 runs instead of the original 144. The final tested variables are shown in Table 8.4.

Table 8.4: The variables decided upon after the first day at the LDC.

G level (g)	1	1.5	2	3	5	7	10
Ultrasonic Amplitude (μm)	0	0.4	0.5	0.6	0.8	1.2	1.6

Unfortunately the non-ultrasonic (0 μm) results at 7 g and 10 g were not recorded. A trend was noted from the ultrasonic results at these gravity levels, suggesting that the recorded force would be greater than the maximum rated load of the actuator (1000 N), so the decision was taken to omit these tests for fears of the linear actuator overloading and burning out.

8.3 Results

8.3.1 Non-ultrasonic penetration model comparisons

The first aim of these experiments was to compare the standard non-ultrasonic penetration profiles to the penetration model set out in section 2.3.4. Theoretical penetration forces for lower gravity have been created using these models [95], however these were simulating 50 cm penetration depths, whilst these experiments were only able to do 12 cm.

The model simplifies down to requiring only a few input variables, measured as the following values:

Table 8.5: Measured variables for use with the penetration model.

Bulk Density (g/cc)	Probe Diameter (m)	Friction Angle (º)	Penetration Depth (m)
1790	0.01725	35.6	0.11

Using these values, the predicted penetration profile of non-ultrasonic penetration was calculated shown along with the experimental results in Figure 8.13. Note that the 7 g and 10 g results are absent, as the 0 μm experiments were not conducted at these gravity levels. Comparing the predictive model and experimental data in this way illustrates that perhaps there are improvements that can be sought in the model.

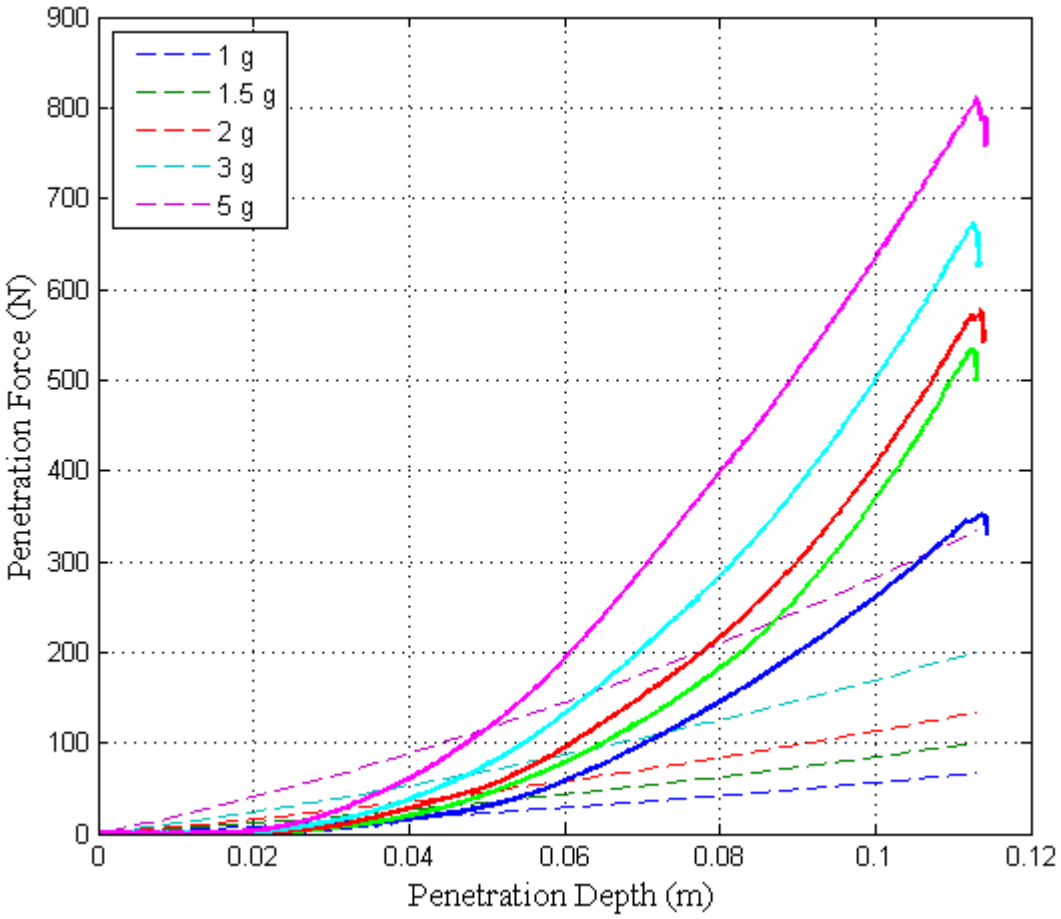

Figure 8.13: Comparison between the non-ultrasonic penetrations at high gravity, shown in solid line, with the predictive model, shown in dotted line.

The experimental data shows a gradual increase in penetration force, resulting in a high degree in curvature. Comparatively, the penetration profiles of the predicted results are much more linear, appearing as almost a straight line at these small depths. The peak penetration forces are also much lower in the model than in experiments by a factor of 3 to 4, depending on the gravity level in question. Additionally, the greatest difference in peak penetration forces with respect to gravity are seen between 3 g and 5 g for the model profiles, whereas for the experimental data it appear to be between 1 g and 1.5 g.

Higher peak penetration forces could potentially be explained by the use of the sand container, as the boundaries of a container will act to increase the penetration resistance [114]. As discussed elsewhere in this thesis, this is inherent in experimental testing, and would be unavoidable in these experiments due to the limiting size of the centrifuge gondola. Also, the model is formulated from a variety of civil engineering and drilling mechanics sources, which deal with depths on much higher scales on the order of tens of

meters to kilometres. Equations at this scale are not designed for small penetration depths, which can often lead to slightly inaccurate results. Further experiments in the centrifuge with solely non-ultrasonic penetration would assist in this regard, however this is outside the scope of this work.

8.3.2 Force reduction trends

The second aim of these tests was to repeat the force reduction tests shown in Chapter 6, establishing any trends with respect to gravity. The peak penetration forces with respect to ultrasonic amplitude are displayed in Figure 8.14 for all the gravity levels used. Since the 0 µm amplitude experiments were not conducted at 7 g and 10 g due to concerns about loading on the linear actuator, these data points were estimated with a linear trend-line for from 0 µm forces for 1.5 – 5 g.

Figure 8.14 shows that the force reduction effect remains at higher levels of gravity, showing that it is not an effect that is only seen in Earth's gravity, but remains at all gravity levels as well. The magnitude of all forces also increases with higher gravity, and it is worth noting that this is not due to the sand compacting at higher gravities, as the surface of sand was recorded during testing and not seen to change in higher gravity. Instead, it is likely due to the *unit-weight* of sand, γ in equation (2.6), increasing with higher gravitational levels. In effect, the heavier the sand, the more difficult it is to 'push it' out of the way as you progress to depths. This effect would also suggest that the magnitude of the penetration forces would decrease on lower gravity bodies accordingly.

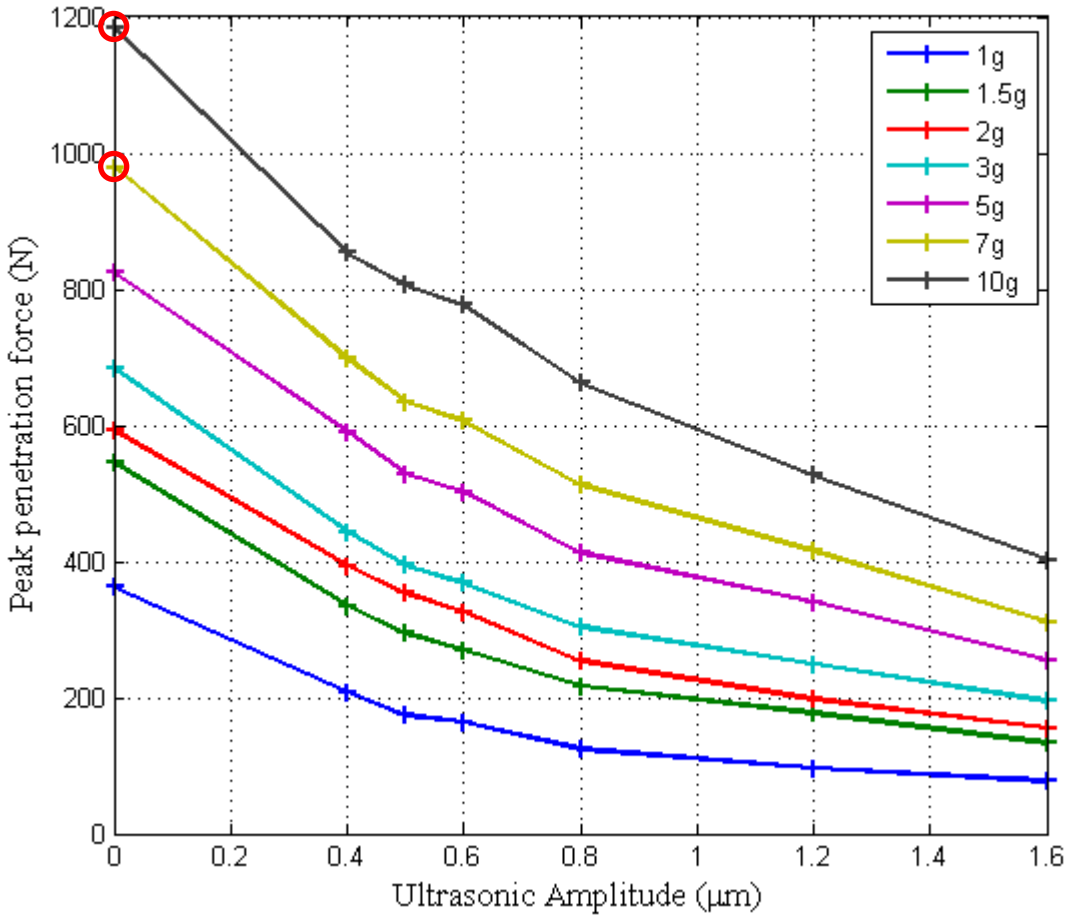

Figure 8.14: Peak penetration forces for all gravity levels as a function of ultrasonic excitation amplitude. The circled values were not experimentally acquired due to over-loading concerns, and indicate anticipated values based on trends.

As outlined in Chapter 6, it can be beneficial to normalise forces to their non-ultrasonic forces in order to directly compare the effectiveness between different environments, in this case between different gravity levels. The results of this are shown in Figure 8.15. Using this graph it is possible to quickly establish by what percentage the peak penetration force has been reduced to in each level of gravity. For example in 1 g, the force reduces by 70% of its original value with 1 µm excitation amplitude, whereas it reduces by just 50% of its original value in 10 g using the same amplitude.

Another way to look at this is to plot the normalised forces against gravity for a specific vibration amplitude, showing the normalised forces for 0.4 µm in Figure 8.16(a) and 1.6 µm in Figure 8.16(b). Viewing the trend in this way and extrapolating for lower gravities, it is possible to see that the effectiveness of ultrasonically assisted penetration would be even greater in lower gravities, reducing the required overhead force by larger fraction than

at high gravity. A slight deviation is seen at 0.4 µm between 2 g and 3 g, caused by the 2 g normalised plots exhibiting larger than anticipated forces at low amplitudes, indicated by the 2 g plot crossing the 3 g plot in Figure 8.15. Care must be taken before reading too much into extrapolated results, but these experiments at least show a promising start for the potential use of ultrasonics, and to spur further investigation.

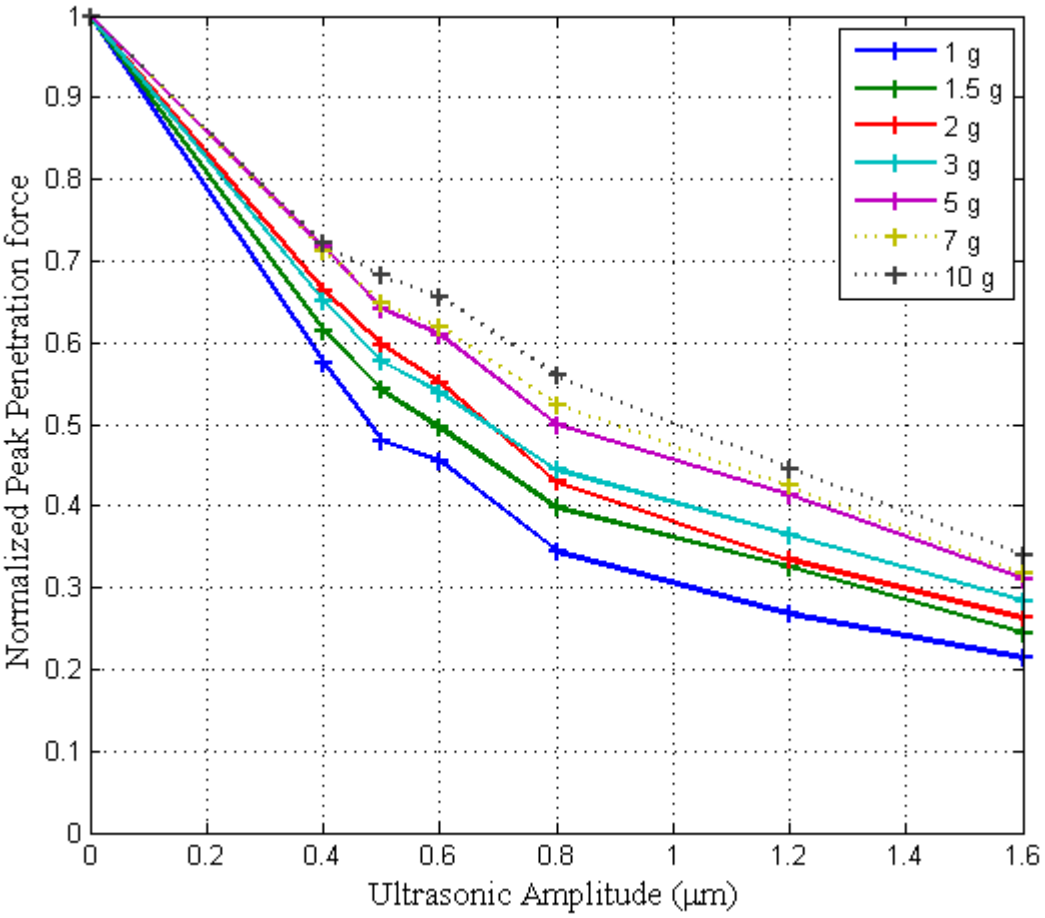

Figure 8.15: Normalised peak penetration forces in high gravity. The dotted line indicate that the estimated 0 µm forces were used in the normalisation process for those plots.

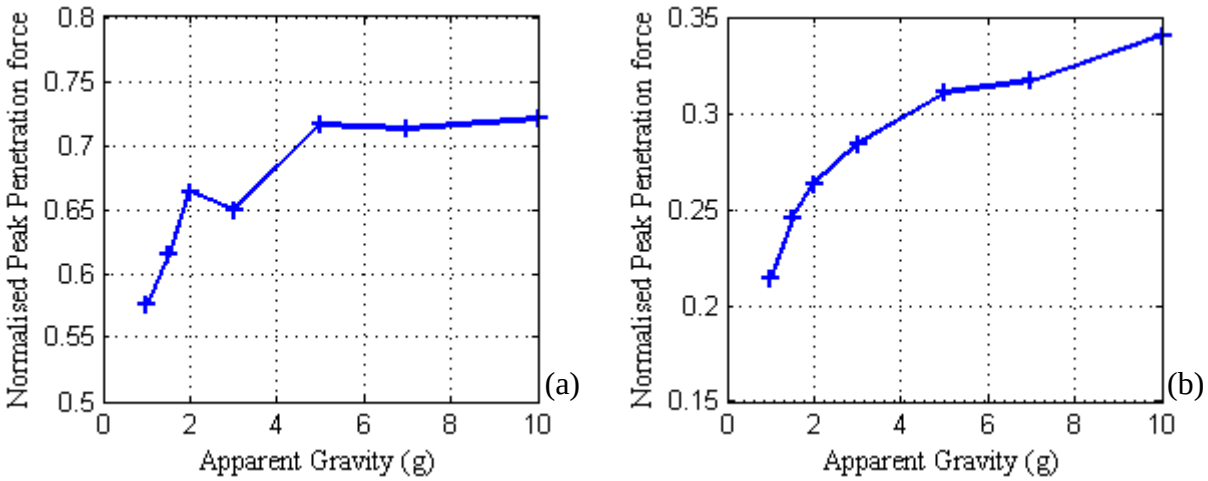

Figure 8.16: Normalised peak penetration profiles with respect to increasing gravity at (a) 0.4 µm, and (b) 1.6 µm ultrasonic excitation amplitude.

8.3.3 Power reduction trends

The third and final aim of the centrifuge tests was to investigate how the power saving capabilities of ultrasonic vibration, previously described in Chapter 7, compare at higher gravities. For all experiments, the physical power draw of the motor was recorded, and the perfect motor power consumption was calculated from the penetration force and rate. These are shown in Figure 8.17(a) for the measured actuator power, and Figure 8.17(b) for the calculated perfect motor power, both of which were conducted in 1 g.

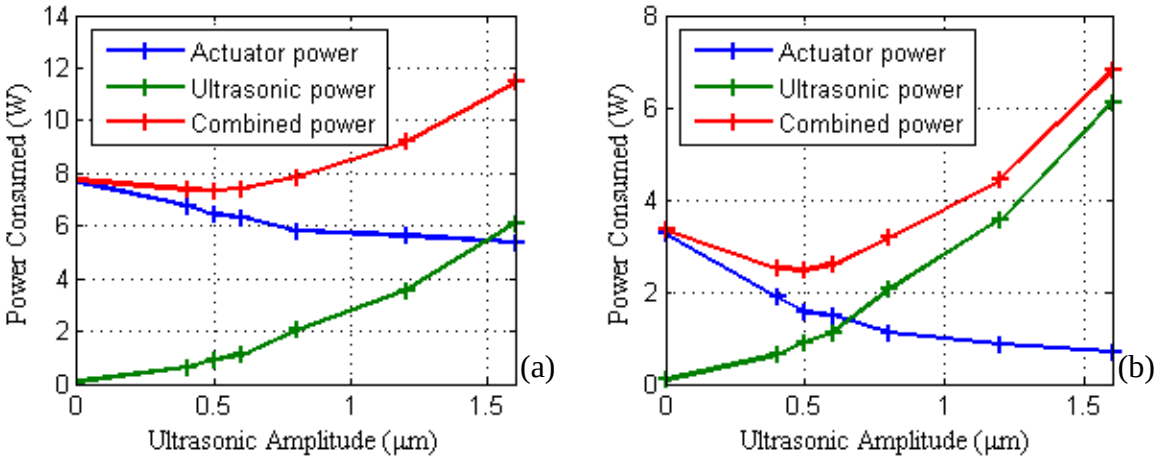

Figure 8.17: Example of the power consumption of the actuator and ultrasonic transducer at 1g. The measured actuator power is shown in (a), whereas the power consumption of a perfect motor (force times the penetration rate) is shown in (b).

As before, the combined power consumption using the measured power only shows a mild decrease in the total power consumption, coinciding with the 0.5 µm runs. The perfect motor plots show the same optimum amplitude, but with a much greater decrease in total power consumed.

This optimum power consumption could be seen at all gravity levels, and the normalised results of all levels are shown in Figure 8.18. There is no clear trend with gravity, but the results show a clear decrease of around 20% of the original power consumption, regardless of gravity.

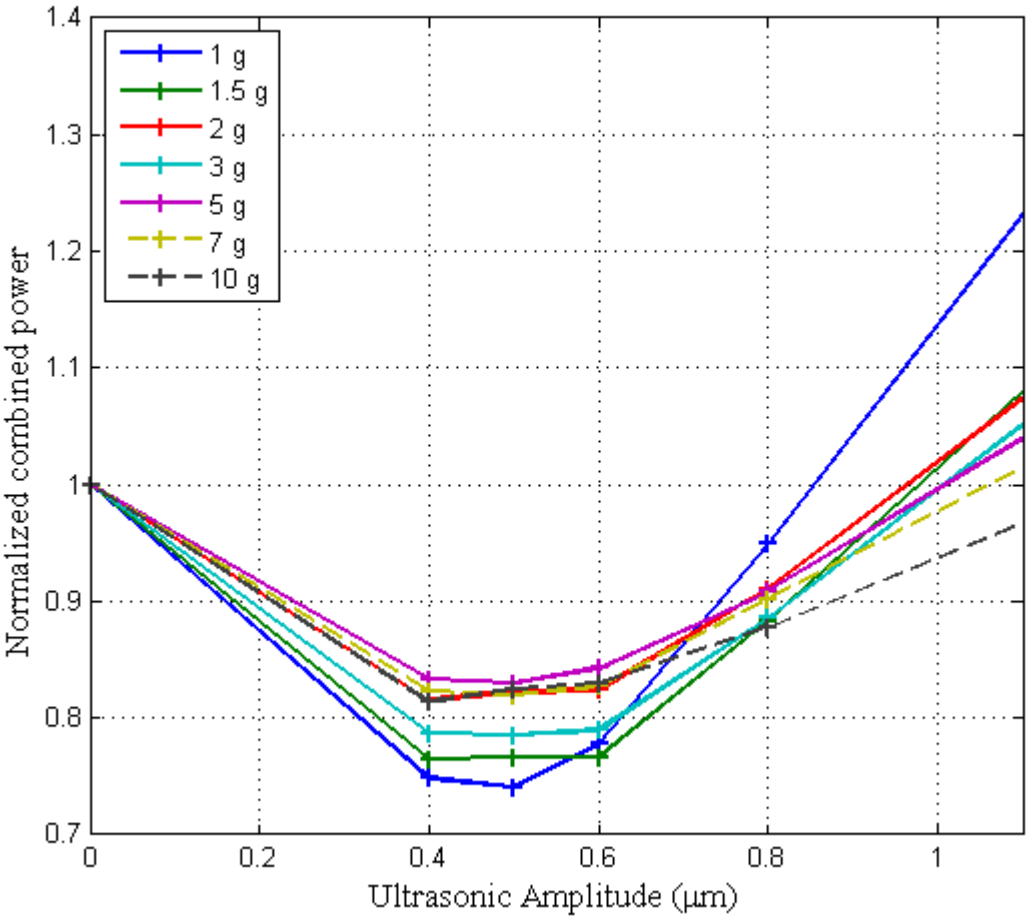

Figure 8.18: Normalised combined power consumption for all gravities, using the 'perfect motor' power.

8.4 Chapter conclusions

This chapter has covered the experiments conducted at the Large Diameter Centrifuge, investigating the effects that high gravity has on the performance of ultrasonically assisted penetration. Additionally, it provided empirical data with which to compare to existing predictive models, showing that at small penetration depths the model was unable to predict the resulting force profiles. This model could serve as a useful rule-of-thumb, but some slight refinement is recommended for it to perform to its full capabilities.

The force reducing properties of ultrasonic vibration were shown to remain at high gravity. Taking it further, by normalising the results to the non-ultrasonic force and comparing this between the different gravity levels, it was discovered that the force reduction efficiency actually increases with lower gravity, suggesting that the force reduction granted by ultrasonic vibration would be enhanced with use for space applications, where all gravity levels are likely to be lower than that of the Earth.

The power reducing capability of ultrasonic penetration was also shown to remain at high gravity levels. The lowest gravities in general displayed the largest reduction in total power consumption, however the differences were not greatly pronounced. All of these experiments have highlighted the importance of empirical information for predicting trends, and it is hoped that these results might spur further investigations into the matter.

Chapter 9

Hammering and Ultrasonic Vibration

9.1 Rationale

So far in this research, it has been proven that ultrasonic vibration can reduce the penetration force and power requirements of the penetration of granular material. Additionally, it has been shown that these effects can be increased at lower levels of gravity. The work has concentrating at establishing the underlying principles, and examining the phenomena; it has not yet been applied to a real world device.

This section deals with these first steps of combining ultrasonic vibration with techniques that have been used on previous missions. Hammering is a common method used in low-gravity environments, such as the PLUTO probe on board the Beagle 2 mission, the MUPUS probe on the Philae lander as part of the Rosetta mission, and the HP^3 probe on the InSight mission.

The basic principle of these probes involves an internal hammer-mass which is compressed against a spring and released, providing a shock and allowing the probe to progress through the granular material. These have proved successful; however the shock loads can potentially cause problems with fragile internal components, reaching impacts of over 8,000 g in some cases [34]. The experiment described in this section will look to see how ultrasonics can be added to this hammering method, what the benefits are (if any), and what limitations might arise. As such, it is the first step to seeing how direct ultrasonic vibration might be applied to real-life situations.

9.2 Experimental design

There are many variables involved in this experiment that could potentially be isolated by using more complicated apparatus, but this particular design kept simplicity at its core. Hammers in low-gravity environments use springs to deliver the required impact; however these require careful considerations of the reacted force, and can cause the penetrator to jump out of the hole. Incorporating suppressors into these spring systems can reduce the reacted force below the skin friction, but this would require significant development and optimisation to be used for these tests. Instead, a simple sliding weight will be used for these tests, using the gravity of Earth to provide the acceleration and impact forces. Additionally, using as many of the components from previous devices as possible will save in design time, and therefore only a few new components needed to be manufactured.

9.2.1 Apparatus

Both the hammer and the anvil were manufactured from mild steel, and the anvil was connected to the penetrator by a threaded connection. A hole through the centre of the hammer allowed it to slide vertically along a loose-fitting rod, ensuring that the contact between the anvil and hammer was always flush.

The penetrator and hammer rig was free to move vertically along a rail using a linear bearing attached to one side of the anvil. The initial design included a bearing on each side to reduce any torque forces on the bearing. This did not result in a smooth motion however, as it requires the rails to be perfectly aligned. Upon further examination, it was discovered that a single bearing was sufficient for the penetrator, as the distances between the bearing and centre of mass were very small, with a negligible the torque on the bearing. The rail was attached to a supporting aluminium structure, enabling easy assembly.

An electro magnet, fixed to the top of an aluminium support, provided the catch and release mechanism for the hammer, ensuring it could be released electronically with accurate timing and consistent starting position.

The penetration distance was measured by eye with a needle attached to the bearing and a steel rule with 0.5 mm accuracy. Any attached component could have added unwanted friction into the system, and this experiment did not call for real-time measurement of the

penetration depth as in the previous experiments, so this method was deemed sufficient for these purposes.

The probes on which this experiment is based upon use an internal spring-loaded mechanism to provide the hammer strike. This experiment instead allowed the hammer to free-fall under its own weight before striking the penetrator. Due to the reduced gravity on other planetary bodies this method is obviously not feasible; however by dropping the hammer from a consistent height it is possible to get consistent hammer-blows. The development of the HP^3 mole determined that a total hammer impact energy of 0.8 J was required to fulfil the depth requirements of the mission [42]. To replicate this energy, the 952.4 g hammer would need to fall a distance of 8.6 cm. The mass of the combined penetrator was 4.0895 kg. An Arduino was programmed to release the hammer and turn on ultrasonic vibration simultaneously. The whole set up can be seen in Figure 9.1.

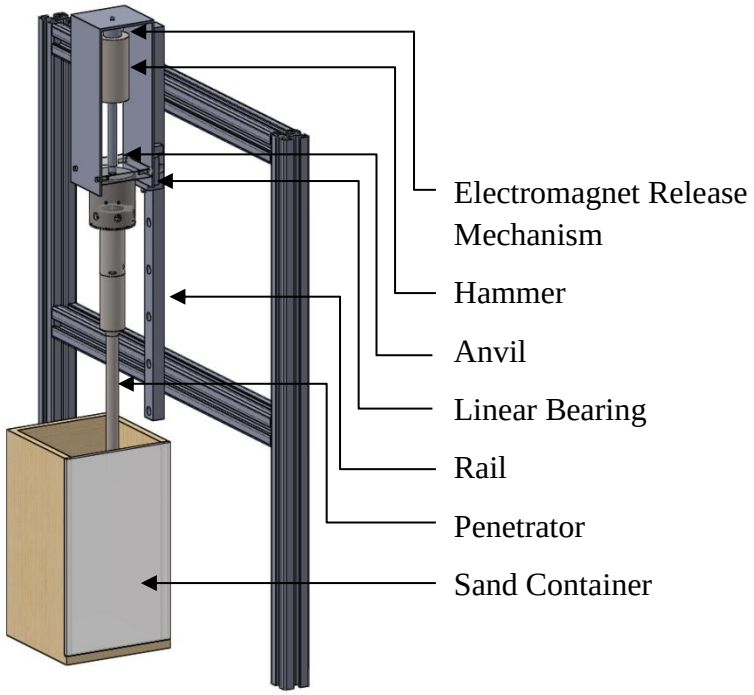

Figure 9.1: Overview of the hammer rig. The rest of the aluminium supporting frame has been removed for ease of viewing.

Under ultrasonic vibration, the penetrator would continue to travel through granular material if left under its own weight, albeit at a slow rate, due to the active fluidisation of the surrounding sand. Preliminary tests in BP were done to investigate this effect, showing penetration rates between 0.2 and 1.5 mm/s, depending on the amplitude of vibration used. Due to this effect, care must be taken when deciding when to begin the vibration, and what

duration to use. The hammer theoretically takes 132 ms to fall 8.6 cm, putting a minimum time on the duration of vibration. A total vibration time of 400 ms was chosen, allowing sufficient time for the hammer to drop, as well as for the penetrator to travel after being struck by the hammer. Further tests could potentially expand on this effect, however the most important feature for this experiment was that vibration duration was constant throughout the tests.

Before the tests started, the empty container was located in position with a steel plate placed on top. The penetrator was gently lowered onto this plate, and the height reading taken. Subtracting the thickness of the plate from this value gives the exact starting height of the sand, establishing the surface position for subsequent depths.

9.2.2 Frictional analysis

As can be seen in Figure 9.1, the hammer-penetrator is guided by a single linear bearing. Any friction between the bearing and the rail could potentially cause loss of transmission of the hammer blow to penetrating the sand, so measurements were conducted to allow for this and determine how influential it might be.

The friction in the bearing was experimentally calculated by suspending the penetrator and hammer mass from a set of scales by an elasticated line. The penetrator was gently lowered under its own weight until the scale reading came to a stable value, which theoretically should display the weight of the penetrator *minus* the friction in the bearings, as the friction would be acting upwards in this case.

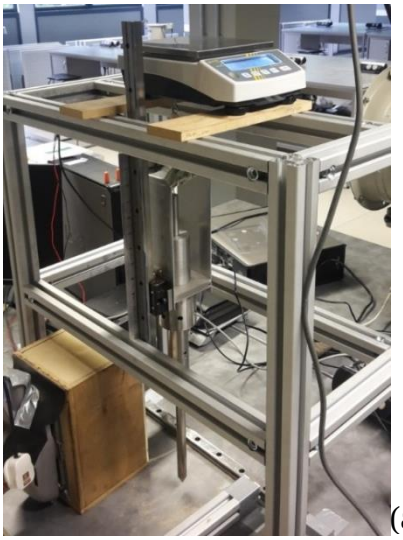
(a)

(b)

Figure 9.2: Measuring the friction in the rails.

The penetrator was then pulled slightly past this resting point, and slowly allowed to rise back up until it came to a stop, again waiting until the scale reading came to a stable value. This set up can be seen in Figure 9.2. Theoretically, this reading should be the weight of the penetrator *plus* the friction in the bearings, as in this situation the friction would be acting downwards.

This was repeated three times and the resulting force readings averaged. The difference between these values is double that of the friction in the rails (since we have measured the friction both in the upwards and downwards direction), giving a final value of 0.435 N. Since this level of friction is so low, it can be considered negligible for the purposes of this experiment. If this technique were to be repeated in lower gravity however, this might be an issue that would need addressing.

9.2.3 Choice of variables

Staying consistent with the power experiment described in Chapter 7, the sands SSC-3 and BP were used for these tests. Low density tests were omitted however, as the weight of the penetrator was too large and simply went through the entire depth of the container under its own weight without coming to a halt.

Following on from the gravity experiments in Chapter 8, the same amplitudes of ultrasonic vibration were used (including a control test using pure hammering and no vibration, noted by the ‘0 μm’ runs). This run of experiments is referred to as the

'simultaneous hammer and ultrasonic vibration tests' as ultrasonics is switched on immediately before hammering occurs. This will help to distinguish this experiment from other similar experiments in the chapter.

Additionally, a set of experiments involving no hammering was run, using pulses of pure ultrasonic vibration to penetrate the sand. The vibration pulse duration was kept at 400 ms, and the depth noted after each pulse. This will help enable a comparison by setting a benchmark by which to compare hammered strikes through the fluidised sand. A total of 96 separate experiments were run in this regard.

9.3 Experimental technique

The sand was prepared in accordance with the technique described in section 3.5 in the same way as for the force and power experiments. The entire set of experiments for each sand was run over the course of a single day, in order to avoid as many external influences on the final bulk density (such as humidity) as much as possible. Five measurements on sand mass were made at various stages during the day. Using a container volume of 5.219 litres, the bulk and relative density could be calculated, and are shown in Table 9.1. These bulk density values are very close to the densities from previous experiments, however since small changes in the density can have large impacts on the effects of penetration, it was prudent to establish the specific density value on the day.

Table 9.1: Bulk and relative density of SSC-3 and BP for the hammering tests.

Sand		Mass of sand (g)	Bulk density (g/cc)	Average density (g/cc)	SD	Relative density (%)
SSC-3	Run 1	8280.3	1.587	1.586	0.00169	43.1
	Run 2	8287.7	1.588			
	Run 3	8277.6	1.586			
	Run 4	8268.6	1.584			
	Run 5	8266	1.584			
BP	Run 1	8509.7	1.631	1.631	0.000615	48.3
	Run 2	8513.8	1.631			
	Run 3	8505.1	1.630			
	Run 4	8511.6	1.631			
	Run 5	8509.8	1.631			

The sand container was then placed directly underneath the penetrator within the rig. Stoppers on the table guaranteed that the container was positioned in the same place each time, ensuring the penetrator consistently travelled through the centre of the container.

The penetrator was then gently lowered into the sand until it came to a stop, and the initial starting point measured. The value of ultrasonic vibration was set, and the hammer raised to the active electro-magnet until it was held in position. Starting the Arduino code, the ultrasonic power was measured for 200 ms (to get a baseline reading in case of any DC offset), then started the ultrasonic vibration and turned off the electro magnet simultaneously, allowing the hammer to fall. The ultrasonic vibration was turned off after 400 ms and the electro-magnet turned back on. Ultrasonic power was measured for an additional 200 ms (for off-set purposes), and then the hammer was raised back to the magnet by hand, ready to repeat the process. A timeline of this process is provided in Figure 9.3.

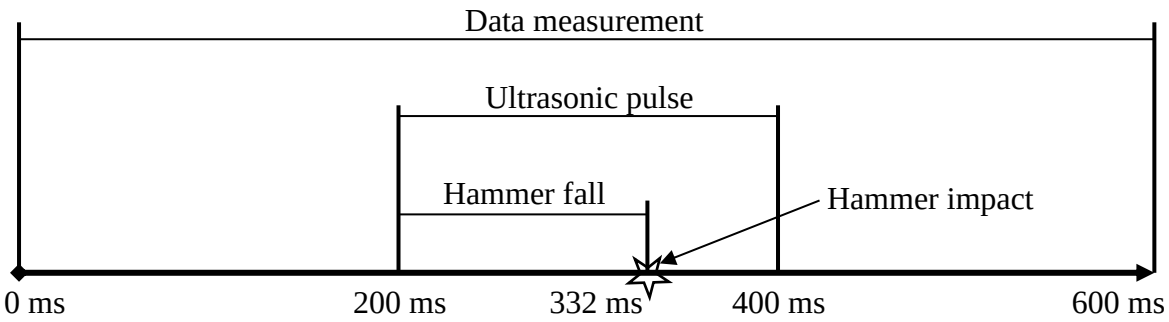

Figure 9.3: Timeline of the hammering process. The hammer was calculated to fall the 8.6 cm distance in 132 ms.

The hammering process was repeated until a depth of 190 mm was reached, which was the maximum length of the straight section of the penetrator.

The ultrasonic pulsing experiments were less complex in design. These tests did not involve raising the hammer to a specific height and letting it drop, however the hammer was still left in position to ensure that the weight of the penetrator was the same across all experiments. With the penetrator lowered into position and the starting depth measured, the same code was run as before, however the hammer was not in position to be released. This ensured an identical pulse duration and measurement time. These pure-puling runs took a significant amount of time to reach this depth, with the 0.4 μm amplitude of vibration estimated to take 900 pulses, based upon the total time it took to fully penetrate with the ultrasonics left on. Due to the manual method of reading the depth and saving the power data this would take an impractical amount of time, so these tests were instead run to a maximum of 50 pulses, with the depth and power recorded after each pulse. This would still result in a large number of data point on which to conduct analysis, and a more

automated experimental method could be designed if the final results warrant it. All tests were also repeated three times in new preparations of sand to obtain an averaged final result. The depth was then read off in the same way, until either a depth of 190 mm was reached, or a set of 50 data points were obtained (49 pulses and 1 starting depth measurement).

9.3.1.1 Timed run

The tests described above describe the majority of the experiments, focussing on a hammer strike, an ultrasonic pulse, or both. To put these results in context, an additional set of experiments, solely in BP, were run to measure the progression of penetration whilst ultrasonic vibration was on continuously.

As discussed in section 9.2.1, the ultrasonic vibration of granular material is a dynamic process. When left on, the ultrasonic probe will continue to sink further into the sand. This test aimed to see whether there was a physical limit to the achievable depth, or if a steady-state of penetration rate could eventually be reached. Similar variables to the pulse test were used, such as the density of sand, ultrasonic amplitude, and maximum penetration depth. However, due to the time constraints and the length of the test, three repetitions were not conducted, and only the sand BP was used. The penetration depth was again measured by eye, but unlike in the main set of experiments, the penetrator was in motion for these measurements, making accurate readings difficult. An automatic method of measuring the distance, such as a linear potentiometer, would have solved this issue; however this particular test was not envisioned in the original design and it will just serve as an additional indicator of ultrasonic effects.

For each of these timed runs, as in the main experiment, the penetrator was lowered into the sand and allowed to come to rest. An ultrasonic amplitude was chosen, and a stopwatch started when ultrasonics were switched on. Since this measurement was done by eye, readings could only be taken every 10 seconds, to allow for the depth to be recorded. For the low levels of amplitude, the penetration rate was so slow that this 10 s special resolution was enough. However, the high-amplitude runs finished very quickly, resulting in a low number of data points.

9.4 Results and analysis

9.4.1 Simultaneous hammering and ultrasonic vibration

This is the core experiment in this chapter, investigating the effects of combining ultrasonic vibration with the commonly used hammering technique. The 0 µm represent pure hammering, forming the control test for the experiment.

The penetration depth as a function of hammer blows in SSC-3 and BP is shown in Figure 9.4. As an aside, it is important to note that the axes are flipped in respect to figures shown previously in this thesis, with the penetration depth shown on the y-axis. This was intentional, as the hammer-strikes were the independent variable in this situation, whereas the penetration depth in previous tests was determined by the constant penetration rate, and thus was an independent variable. As will be seen in some of the other figures in this section, this ordering also allows a clearer analysis of the results.

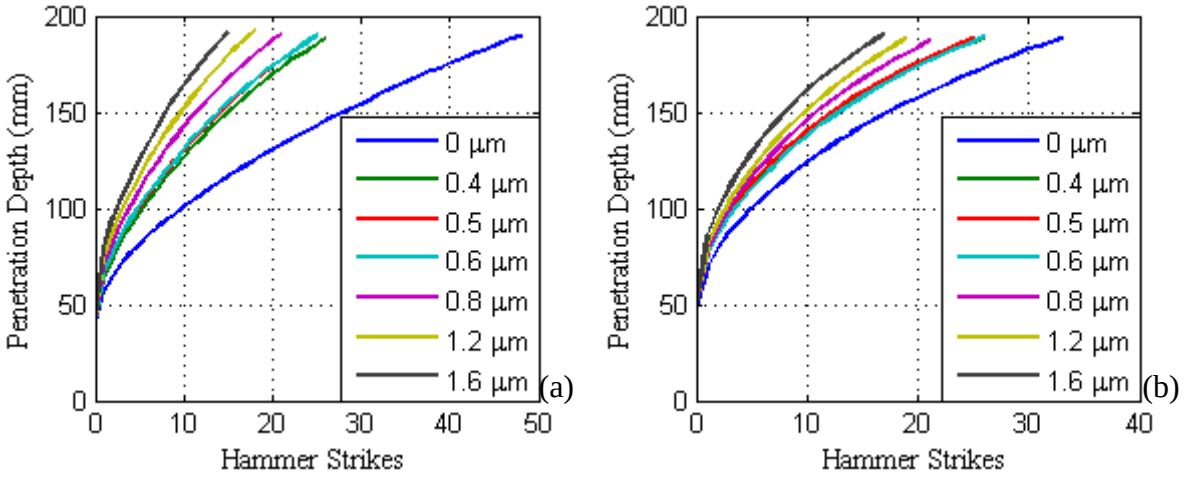

Figure 9.4: Penetration depth with increasing hammer blows for (a) BP and (b) SSC-3.

Predictably, the higher values of ultrasonic amplitude resulted in fewer hammer strikes to reach the final depth of 190 mm. Additionally, more strikes were required with BP than SSC-3, which is in agreement with the higher relative density of BP (48.2% compared to 43.1%), as well as the higher peak penetration forces discussed in Chapter 6.

9.4.1.1 Investigating the effects around 0.6 µm

Interestingly, there seems to be very little variance in depth profile for the three lowest amplitudes, 0.4, 0.5, and 0.6 µm. This feature was not noted until after the experiments were completed and the data plotted and analysed, and was originally thought to be an issue with the experimental set-up. The apparatus was checked, especially the Arduino code that governed the amplitude command to ensure it was not sending an incorrect amplitude signal, but no issue was found. Additionally, not only was this effect seen in both SSC-3 and BP, but each run was also repeated three times and averaged, and each repetition showed the same result.

To better visualise this, it is perhaps beneficial to view the penetration depth reached after a specific number of strikes, and plot these points against the ultrasonic amplitude value used. This is shown for BP in Figure 9.5, and for SSC-3 in Figure 9.6. Note that these plots display all three of these runs in order to illustrate the consistent nature of this effect, whilst the plots shown in Figure 9.4 show the average results from these three tests.

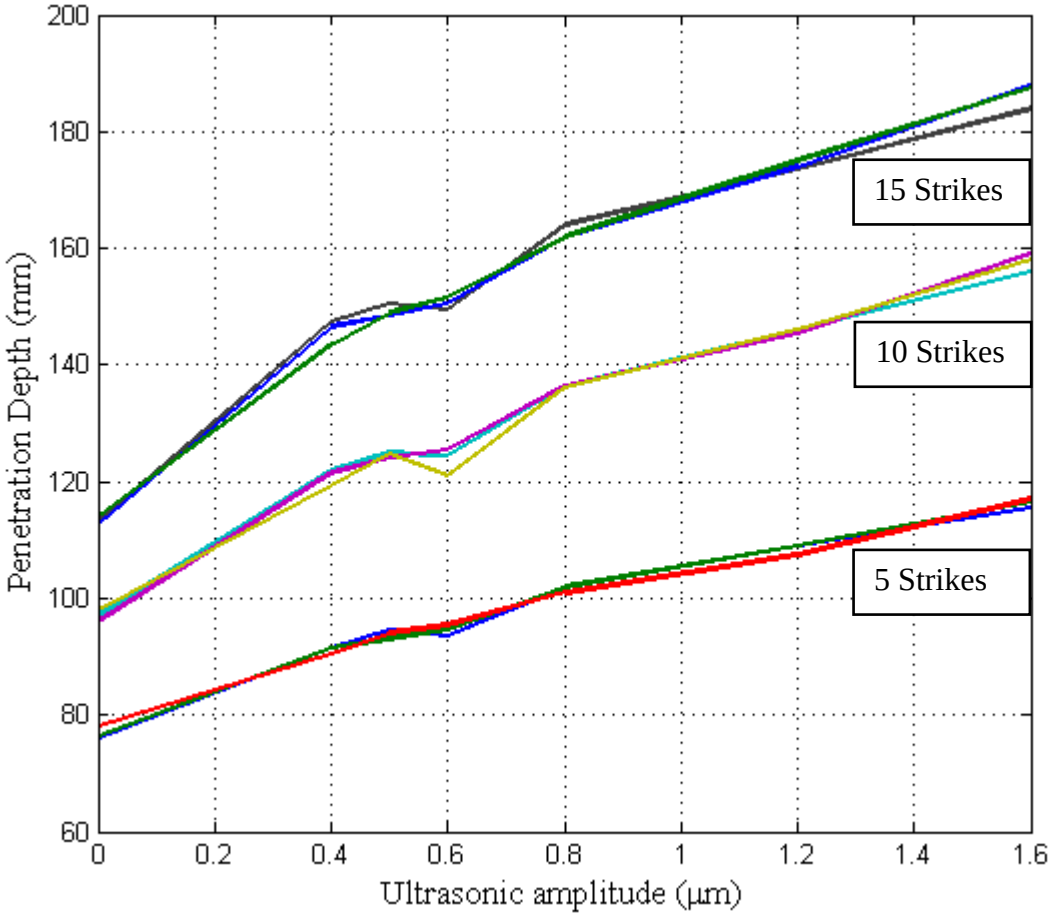

Figure 9.5: Depth reached after a specific number of hammer strikes for BP, showing all three of the runs.

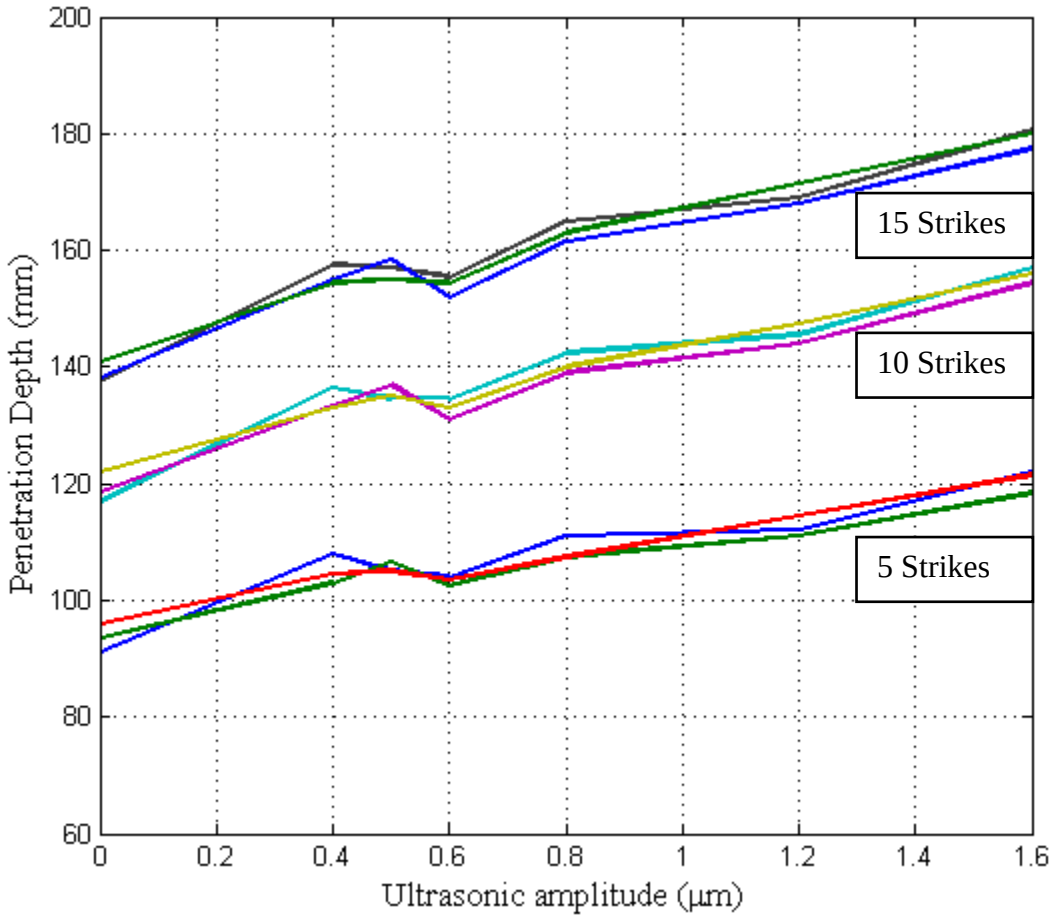

Figure 9.6: Depth reached after a specific number of hammer strikes for SSC-3, showing all three of the runs.

In general, there is a trend that increasing the ultrasonic amplitudes results in a further depth of penetration with the same number of hammer strikes. With the data presented in this way however, it is clear that an inflection point appears in the range of 0.4 – 0.6 µm with the depth levelling off to some degree, and in some cases actually decreasing slightly with increasing amplitude. Whilst some effects are apparent in BP, it is most notably seen in SSC-3, with nearly all of the plots experiencing a decrease in penetration depth.

What this suggests is that initially a slight *increase* in amplitude from 0.4 to 0.6 µm can result in a slight *decrease* in hammering penetration performance. This is in clear conflict with the results obtained in all experiments using a contact penetration rate, as one would expect higher levels of vibration to result in larger penetration depths across all amplitudes. Perhaps coincidentally, this inflection occurs around the same point as the optimum amplitude for minimum power consumption. It is important to note, however, that the hammering technique does not rely on a linear actuator like the constant rate experiments

did, and therefore does not fall under the same optimised-power premise as do the previous experiments, so this optimum amplitude does not inherently apply here.

In relative terms, the difference in depth in this ultrasonic region is about a centimetre, or 10% of the penetration depth after 5 strikes. This is a relatively large discrepancy, and if it had occurred in just one of the runs then it could have been put down to slight differences in the final bulk density of the sample of sand. However, with this effect being present across all runs, it is more likely that this is a genuine effect of the amplitude of ultrasonic vibration.

9.4.2 Ultrasonic pulsing

The ultrasonic pulsing tests functioned in a similar way; however they did not include hammering and focussed solely on the depth acquired from pulsing ultrasonic vibration for the same duration. As such, the figures look similar, except there are no 0 µm plot lines. The results for BP are shown in Figure 9.7, and for SSC-3 in Figure 9.8.

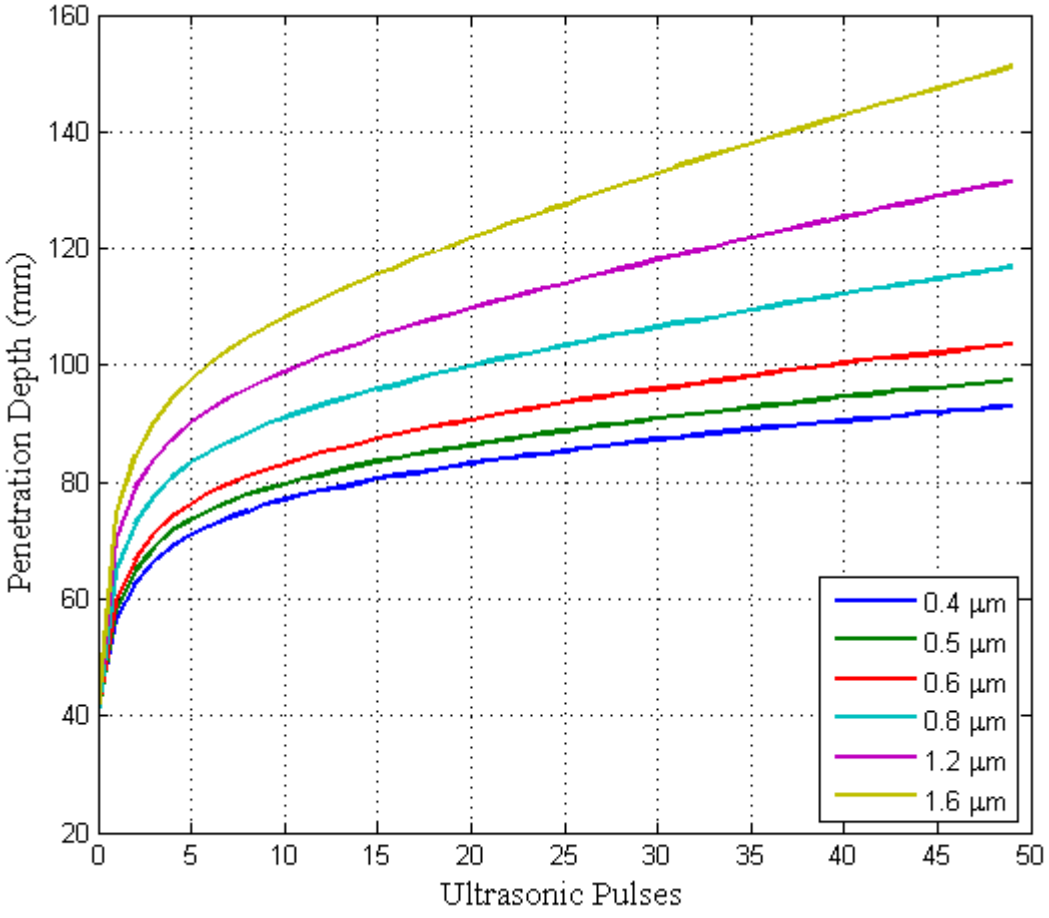

Figure 9.7: Ultrasonic pulsing in BP. Each pulse lasts 0.4 s.

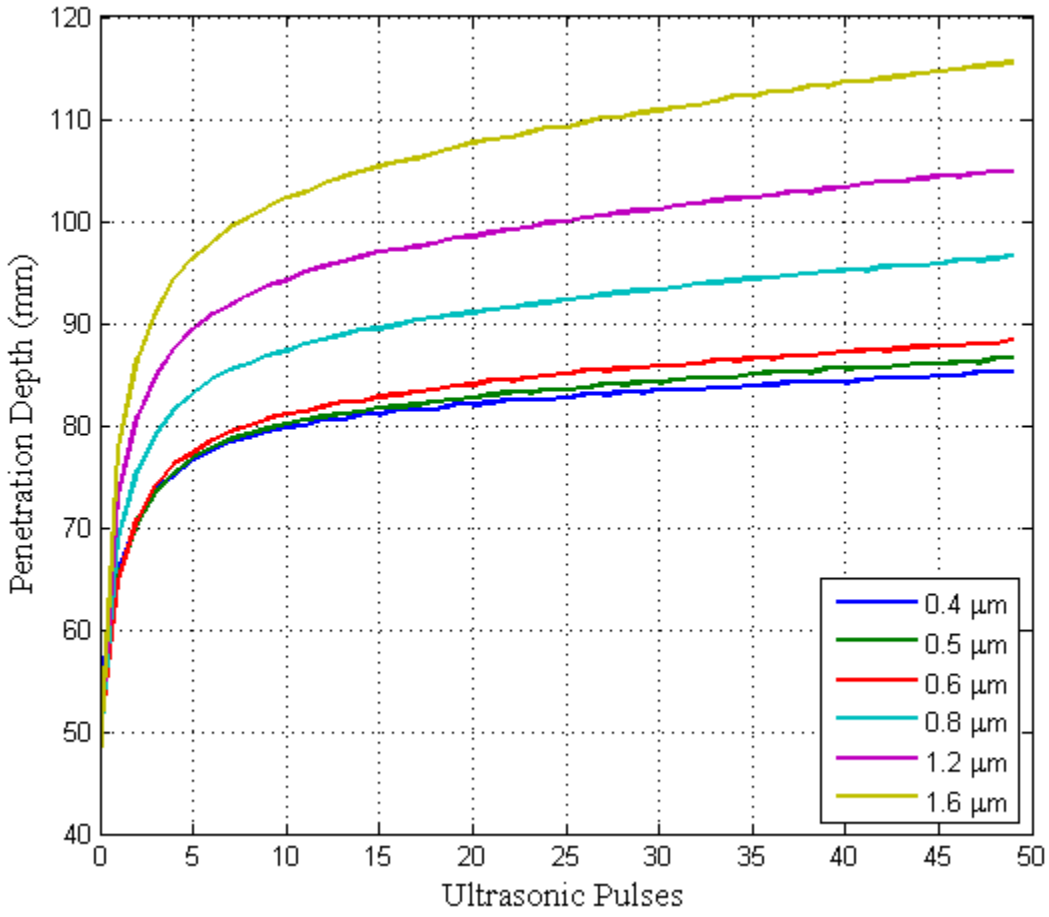

Figure 9.8: Ultrasonic pulsing in SSC-3.

Pulsing ultrasonics in this way resulted in much less efficient penetration, with none of the experiments reaching the maximum depth of 190 mm. Based on these results, it appears that the progression becomes almost linear, with each pulse providing the same change in depth. A larger number of pulses would help confirm whether this trend continues at larger depths.

Additionally, the inflection effect seen in simultaneous hammering and pulsing is not nearly as pronounced, in particular for BP which shows much more distinction between the different vibration amplitudes. SSC-3, however, still has the 0.4 – 0.6 µm results grouped closer together, especially at a low number of pulses. Again, the comparison of penetration depth against ultrasonic amplitude for 5, 10, and 15 pulses can be seen in Figure 9.9 and Figure 9.10 for BP and SSC-3 respectively.

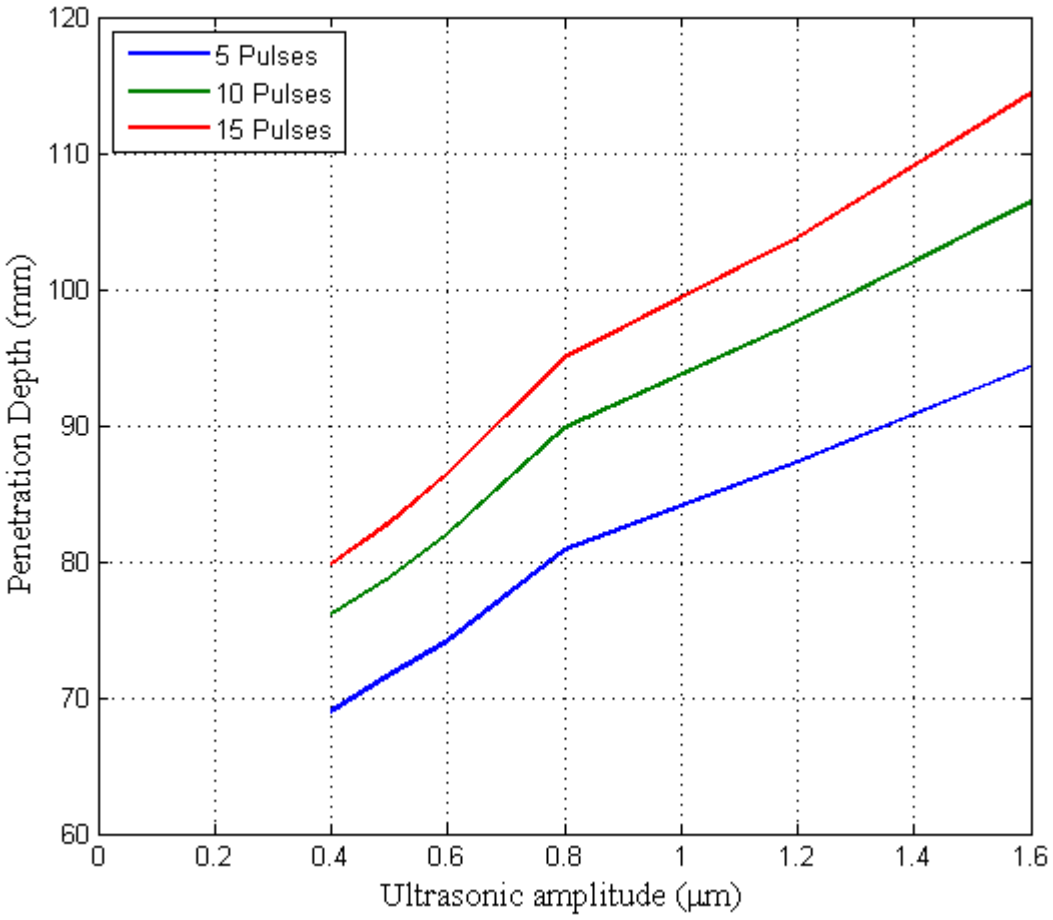

Figure 9.9: Ultrasonic pulsing in BP, showing the average depth of the 3 runs.

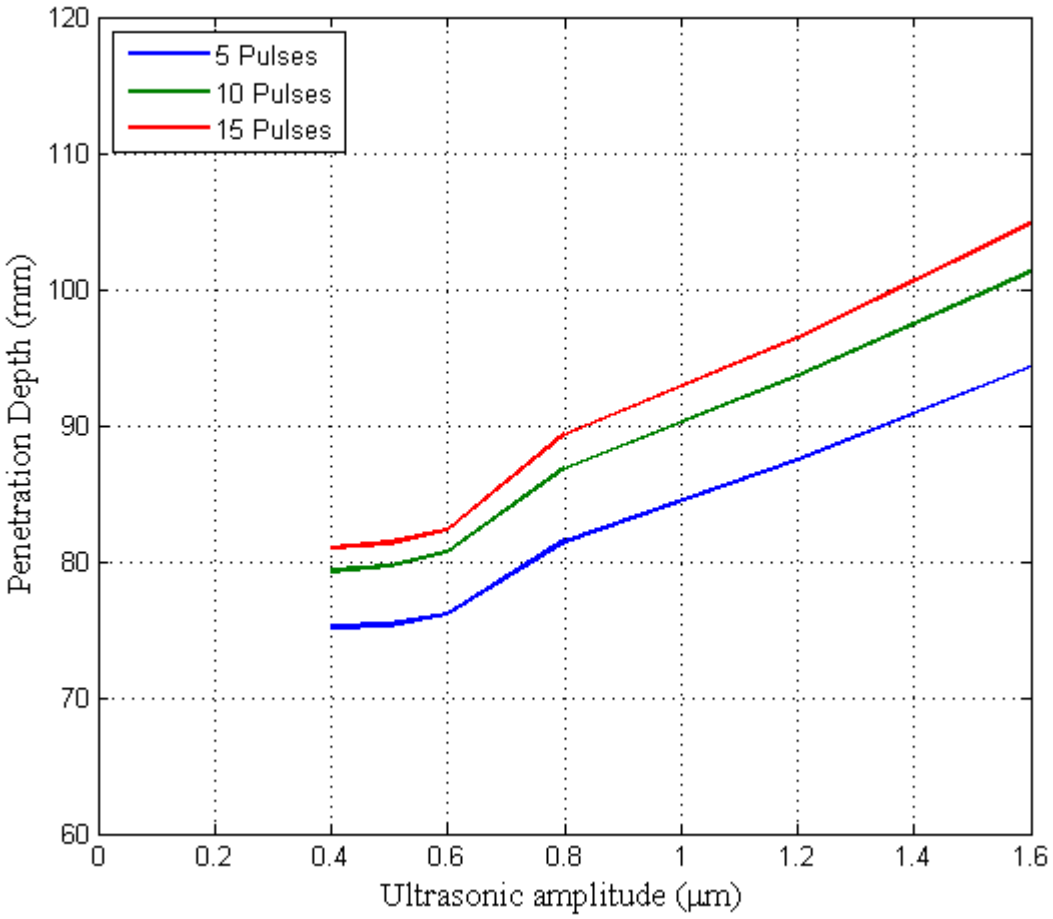

Figure 9.10: Ultrasonic pulsing in SSC-3, showing the average of the 3 runs.

For these figures, the average of the three runs is shown, as the depths are so close together that it is difficult to distinguish between all the plot lines if all three runs were shown on one graph. Note also that these plots differ from Figure 9.5 and Figure 9.6 in that there is no 0 µm data, as these were all done purely with ultrasonic pulsing.

With the data presented in this way, it can clearly be seen that BP increases in a much more linear fashion than with simultaneous hammering and ultrasonics, with no inflection point apparent. SSC-3 on the other hand displays only minor improvements in penetration depth in the range 0.4 – 0.6 µm, and then follows a similar trend as BP in higher amplitudes. These pulsing experiments are designed to investigate the contribution to the overall penetration that ultrasonic vibration provides, and will be investigated further in section 9.5.1.

9.4.3 Timed experiments

Ultrasonic vibration is a dynamic process, and thus can provide penetration on its own. The pulsing experiments above replicated the same duration of vibration as in the combined hammering and ultrasonics experiments. However, it can be useful to investigate how the penetrator would function if the vibration was continuously on. The distance was noted every 10 seconds for each of the six ultrasonic amplitudes and repeated three times, with the average results shown in Figure 9.11.

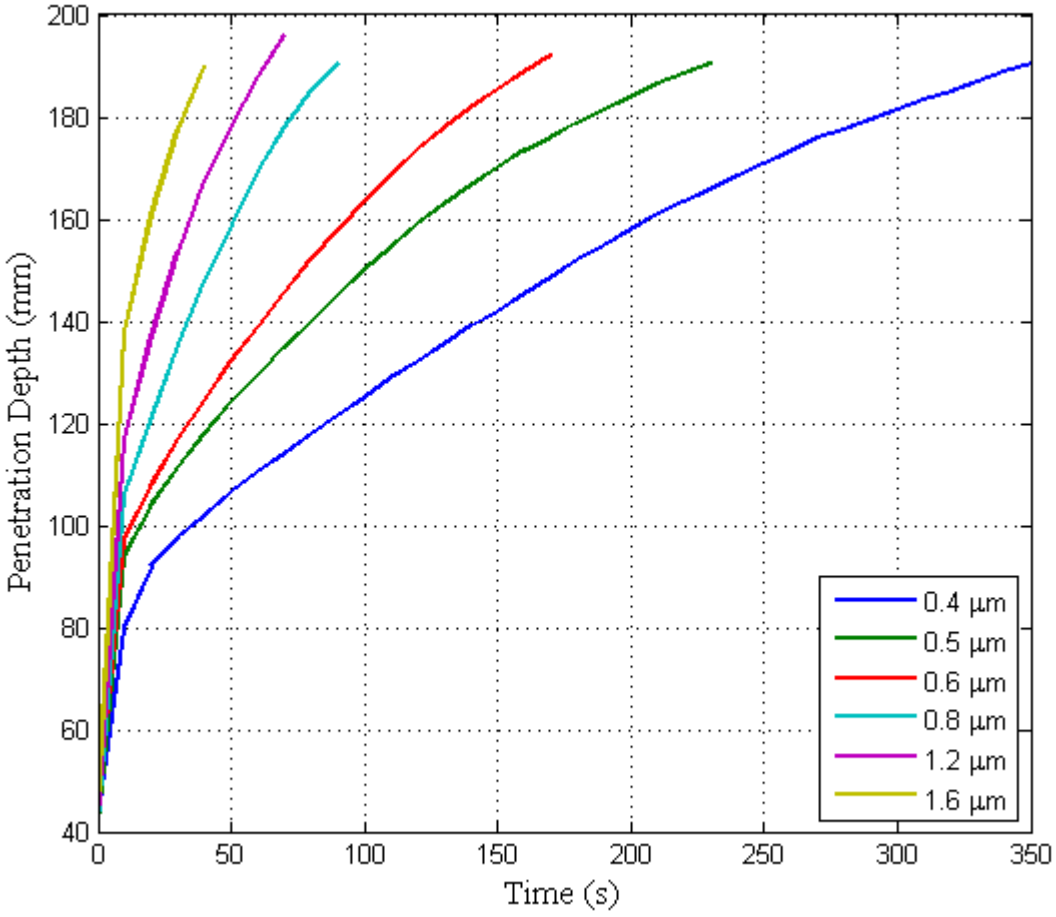

Figure 9.11: Continuous ultrasonic vibration in BP.

The distinction between the different amplitudes is even clearer, with a very even progression of penetration depth with increasing amplitude. Due to high amplitudes progressing very quickly through the sand, only four measurements were able to be taken for the 1.6 µm run, reaching the 190 mm depth in 40 seconds, compared to 350 seconds for the 0.4 µm run.

9.5 Comparisons of data

With this data collected, it is clear that adding ultrasonic vibration to hammering can assist in the penetration of granular material, resulting in a lower number of strikes to reach the same penetration depth. However, two questions arise from this data, and it is possible to combine some of the results to get a new look at this effect. These questions are:

1. Does the penetration depth of simultaneous hammering and ultrasonics give the same depth as the sum of depths from hammering and ultrasonic pulsing separately?
2. Does the penetration depth after 50 ultrasonic pulses of 0.4 seconds duration result in the same depth after 20 seconds of continuous vibration?

These questions are answered in the following subsections.

9.5.1 Comparing simultaneous hammering and ultrasonics with the depth of pure hammering plus ultrasonic pulses

So far, these experiments have covered the penetration of granular material using three different methods: purely hammering, purely ultrasonic pulsing, and both simultaneously. The simultaneous hammering and ultrasonics method resulted in the least amount of strikes/pulses to reach the full 190 mm penetration depth, which is to be expected since it is the combination of both of the other methods. However, it will be useful to determine how the two methods interact with each other, and whether the combination of hammering and ultrasonics is greater than the sum of hammering and ultrasonics separately.

To visualise this, the following graphs each display results of each of the six different ultrasonic amplitudes, shown in Figure 9.12 for BP and Figure 9.13 for SSC-3. Each graph contains four plots, showing the penetration depth profile of pure hammering, pure ultrasonic pulses, both methods used together, and finally the sum of the penetration profiles of both, starting from the same initial penetration depth.

For BP, the difference between the simultaneous runs and the summed runs is remarkably small, reaching the final penetration depth with very little difference in the number of strikes/pulses. The gradient between the two methods varies slightly, with the summed results showing a slightly faster penetration initially. SSC-3 on the other hand

displays a significant difference in every case, with the summed results reaching maximum penetration depth between 5-8 strikes/pulses earlier than the simultaneous results. The shape of the curve, however, is much more similar between the two methods, with the summed results at 0.4 µm excitation amplitude matching very well with the simultaneous results at 0.8 µm. These results indicate that whilst simultaneous hammering and ultrasonic does reduce the number of strikes needed to reach a given depth, there is some loss of penetration efficiency when they are combined together. A small loss in efficiency, however, would not discount this as a viable option, as the most important factor is that the total number of strikes is reduced, thereby reducing stresses and damage potential in a final tool.

With the data showing both hammering and pulsing results for a given amplitude in the same plot, it is easy to compare the two directly. It was noted in section 9.4.2 that the final penetration depth for pure pulsing was significantly lower than that for pure hammering, even at the highest amplitude of 1.6 µm. What can be seen in some figures, particularly for the 0.8 – 1.6 µm BP and the 1.6 µm SSC-3 runs, is that initially the purely pulsing technique can out-perform the purely hammering technique at a low number of strikes/pulses, but at larger number of pulses the depth gained per pulse is too small to match the capabilities of the hammering technique. This is seen starting at lower amplitudes in BP, which along with the greater overall penetration depth over SSC-3 could suggest that BP reacts more favourably to ultrasonic penetration than SSC-3 does. The opposite appears to be true for non-ultrasonic hammering, as the full penetration depth was reached in 50 strikes for BP, whilst only requiring 33 strikes for SSC-3. The specific reason for the cause of this is unknown, and could be due to a variety of reason such as bulk density, relative density, particle sizes etc.

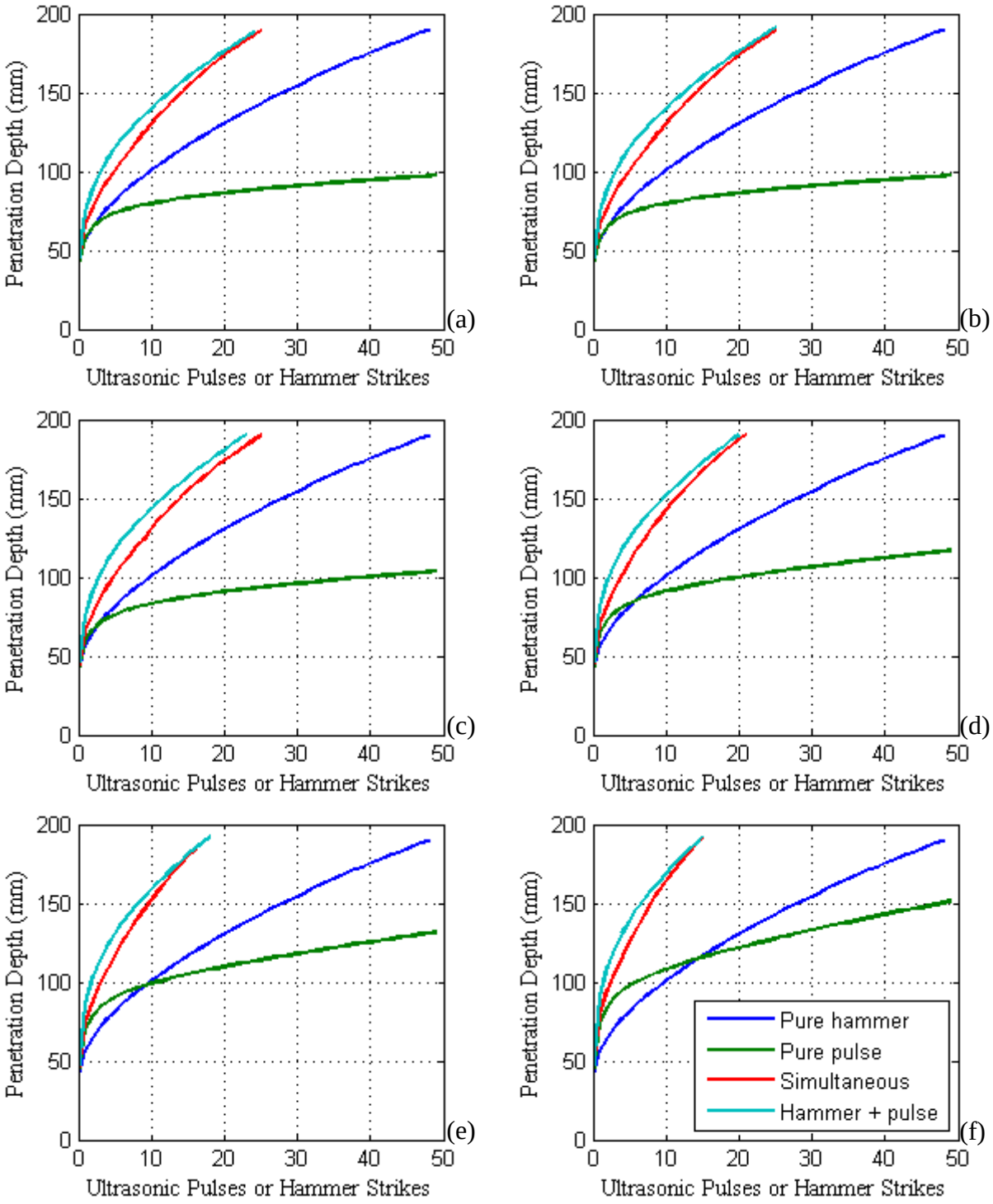

Figure 9.12: Simultaneous hammer strike and ultrasonic pulsing, pure striking pure pulsing, and the sum of the two in BP using an excitation amplitude of (a) 0.4 µm, (b) 0.5 µm, (c) 0.6 µm, (d) 0.8 µm, (e) 1.2 µm, and (f) 1.6 µm.

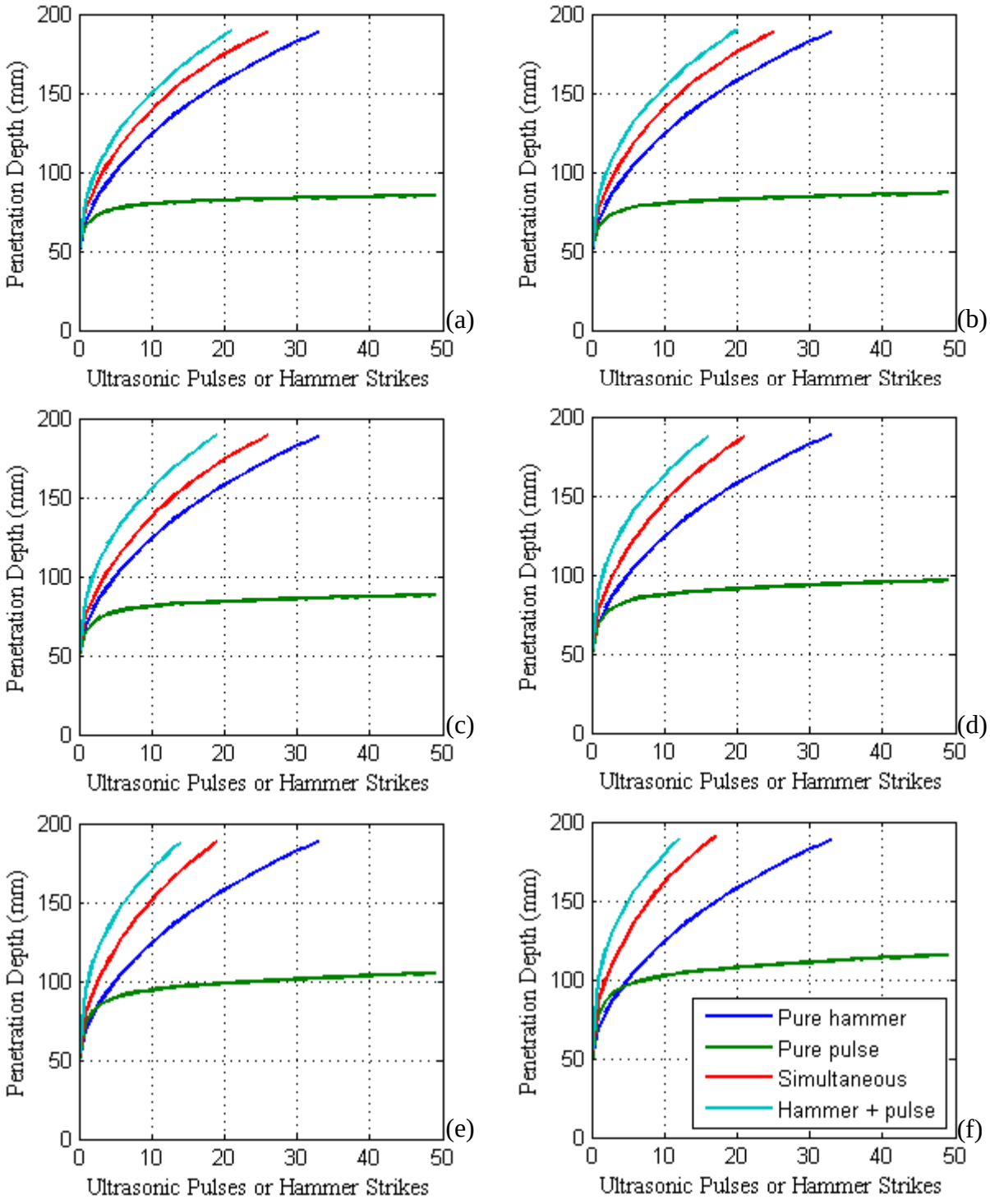

Figure 9.13: Simultaneous hammer strike and ultrasonic pulsing, pure striking pure pulsing, and the sum of the two in SSC-3 using an excitation amplitude of (a) 0.4 µm, (b) 0.5 µm, (c) 0.6 µm, (d) 0.8 µm, (e) 1.2 µm, and (f) 1.6 µm.

9.5.2 Comparing continuous and pulsed ultrasonics

As discussed in the previous section, in some cases it transpired that ultrasonic pulsing resulted in a greater initial penetration depth than the hammering technique for the same number of strikes/pulses. A potential explanation for this could be due to the penetrator gaining a large amount of momentum at shallow depths, as the sudden ultrasonic vibration and subsequent fluidised sand would result in little resistance during entire 400 ms pulse, with the probe in effect 'free-falling' through the sand. The momentum gained by the penetrator during this free-fall phase would then help drive the probe to a greater depth in the soil than if the pulse had been split up into shorter segments, thereby shortening the time that the falling penetrator could build up momentum. Comparing the difference between pulse durations would therefore be extremely valuable to understanding how vibration interacts with hammering,

A new set of experiments is not necessarily required to investigate this, as it is possible to compare the penetration depths of the timed experiment to the pulsed experiment, with the equivalent time represented by the sum of the 400 ms pulses. This is shown in Figure 9.14 only for BP, as a timed experiment was not conducted for SSC-3. Due to measurements being taken by hand, the timed experiments have a temporal resolution of 10 seconds compared to the 400 ms resolution of the pulsed experiment, so only three data points from the timed experiment are able to be displayed, representing 20 seconds of continuous vibration. Also note that the 50 data points for the pulsed experiment comprised of 49 pulses and 1 initial starting value, so the sum of the ultrasonic pulse time is in fact 19.6 seconds, resulting in the final point of the timed experiment not precisely lining up with the last point of the pulsed experiment data plots. Despite this small discrepancy and the low resolution of data points from the timed experiment, it is still possible to use this comparison to great effect.

The first thing to note from this figure is that all vibrations amplitudes except 0.4 μm result in the timed experiment to have a higher penetration depth than the corresponding summed pulse time. This would suggest that the extra initial momentum afforded by the continuous ultrasonic vibration caused the penetrator to travel further, whilst the stop-start nature of the pulsed experiments prevented this. This initial momentum boost would not be a significant factor once the probe had reached a steady-state, progressing solely under its own weight through the fluidised sand. This is clearly illustrated by the fact that the

gradients of the pulsed plots after 25 pulses, again barring the 0.4 µm plot, match very closely with the gradient of the timed experiment plots after 10 seconds, albeit at a slightly lower penetration depth. It follows that a higher vibration amplitude would result in a larger amount of fluidisation, and potentially a greater length of time for momentum to build up and push the probe further. This is illustrated by the 1.6 µm tests showing the largest difference in penetration depth, however the 0.5 µm runs seem to have the second largest difference between penetration depths, so it might be that more effects are at play.

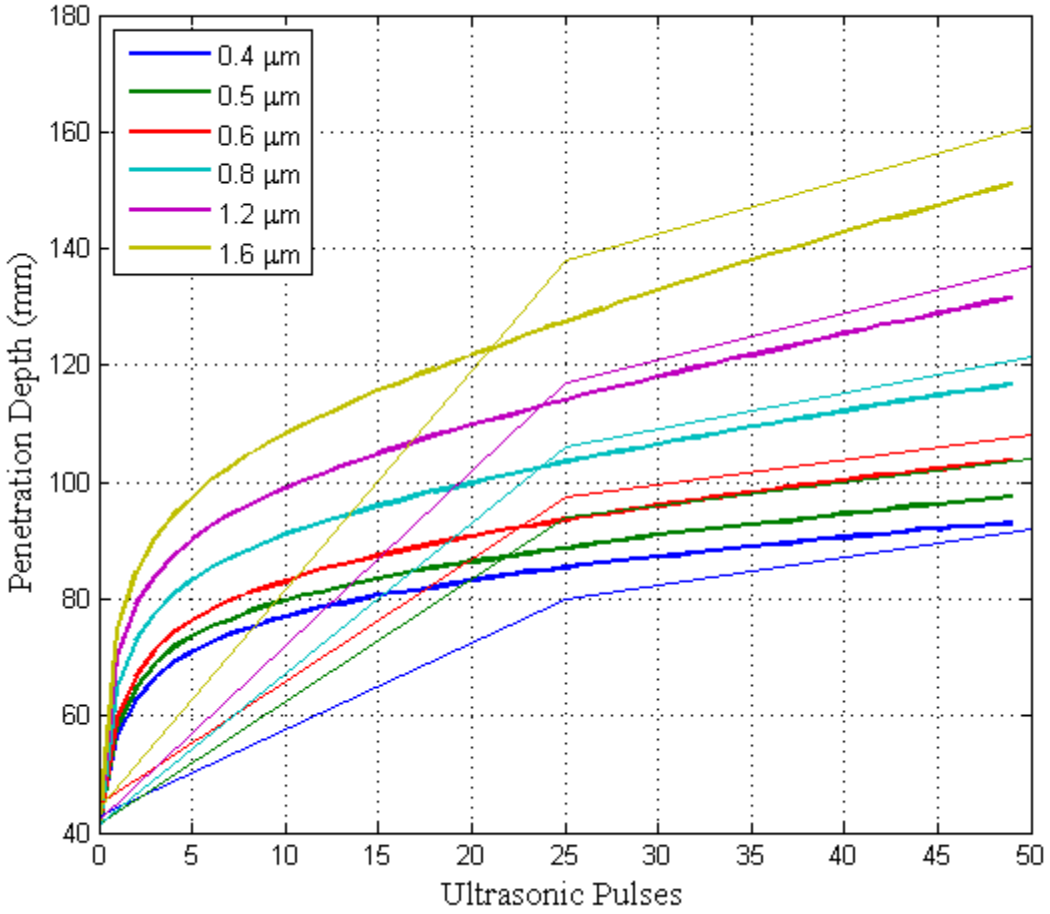

Figure 9.14: Comparison between the pulsed experiments (shown in thick line), and the equivalent time for the continuous vibration experiments (shown in thin line with just 3 data points, due to the low sample rate of the timed experiments).

The 0.4 µm plot is peculiar, as the timed experiment plot lies below the pulsed plot and the final gradient for the timed experiment is higher, both of which are at odds with the rest of the results. It is possible that the low amplitude of vibration would not fluidise the sand to as great of an extent as the higher amplitudes, or the stop-start nature of the pulsing tests could be a benefit at lower amplitudes.

Unfortunately the low resolution of data points for the timed experiments prevents definitive conclusions to be drawn regarding the transition point between free-fall and steady-state penetration. A future experiment that would incorporate an automated method of depth measurement could be extremely valuable to investigate this. What can be determined, however, is that this transition occurs at some point below 10 seconds, and is likely to appear as a sharp change in gradient of the penetration depth curve.

9.6 Chapter conclusions

This chapter has laid out the final set of experiments taken during this PhD, utilising all of the information gained from the previous investigations and applying it to a penetration technique that has flown on previous space missions. As such, these experiments take the first steps into using ultrasonic vibration as a viable device for penetration granular material.

The combination of simultaneous hammering and ultrasonic pulsing showed that the addition of ultrasonic vibration can reduce the total number of strikes required on a probe to reach a specific depth, in this case 190 mm. In BP this was reduced from 48 strikes to 15 strikes at the highest excitation amplitude of 1.6 μm, and from 33 strikes to 17 strikes in SSC-3. Reducing the number of strikes for a hammering device can significantly extended its operational lifetime, and this technique could potentially be used to great effect in this regard.

Additionally, it was discovered that at low penetration depths, ultrasonic vibration can fluidise the sand to such an extent that the penetrator undergoes a brief moment of near free-fall, where it progresses for a short time unhindered. This effect was not seen at larger depths, where progression due to ultrasonic vibration was much more linear. In applications for a probe that is allowed to progress through terrain under its own weight, it would be beneficial to extend the duration of ultrasonic vibration at shallower depths to take advantage of this effect. This will no doubt be heavily affected by the local gravity, and further tests could be done to investigate the relationship between gravity and ultrasonic pulse duration.

Chapter 10

Conclusions

10.1 Overview

A summary of the conclusions from each chapter are provided here.

Chapter 2

Ultrasonic penetration of granular materials is a multi-disciplinary field, involving aspects from many different areas of research. An overview of the principles of ultrasonic vibration was given, ultimately guiding the design of the ultrasonic penetrator. Sand is a very complex material, and an overview of some bearing capacity theory was also covered. As an area of civil engineering, these principles are normally applied to large structures, and so specific equations are not intended to hold up at the macro scale. However, it can provide information about some of the physical processes involved with the insertion of objects into granular material, and one model was described that aimed to predict the penetration performance of static probes through soil. Terrestrial applications of drilling and pile-driving, as well as their associated mechanics, were also covered.

As this work is aimed towards space applications, a summary of previous, ongoing, and future missions was described. Of particular note were the missions involving accessing the subsurface of planets through regolith, as these illustrate clearly the obstacles that must be overcome in order to conduct scientific analysis. Available weight-on-bit and power requirements were at the forefront of considerations for all of these devices, showing that this field is still ongoing, with new methods and devices being created in continuing research. Some more novel concepts involving biomimetics were also discussed.

Chapter 3

This chapter set out to measure and define the sands used throughout the rest of the research. Three sands from the University of Surrey (SSC-1, SSC-2, and ES-3), were already fully characterised. A fourth sand from Surrey, SSC-3, was only partially characterised, and an additional sand from the University of Glasgow, BP, was also included. These last two sands underwent the full process of characterisation, measuring the key mechanical properties of the regoliths: particle size distributions, particle density, minimum and maximum densities, loose and compact density of preparations (and therefore relative densities), and the critical and peak friction angle.

In addition to these measurements, a definitive protocol for creating loose and compact preparations of sand was established. This was designed to be as hands-off as possible, thus creating a high degree of consistency and repeatability. Consistent preparations of sand allowed subsequent penetration tests to be directly compared against one another.

Chapter 4

This short chapter laid out the processes of the design of an ultrasonically active penetrator. Horns are often used to increase and amplify the vibration supplied by piezoelectric transducers, however this particular design also required the horn to include features that would allow it to sufficiently penetrate through sand. The penetration depth was limited to the length of the shaft up to the step-profile, which in turn is governed by factors such as the operational frequency, material choice, and volume of material. By designing the horn to resonate at the second longitudinal mode, L2, the effective penetration depth was increased three-fold over a horn designed to resonate at L1, all other factors being the same. The experimental modal analysis (EMA) matched up well with the finite element analysis (FEA), and showed that the horn had a gain of 3.5, meaning all excitation amplitudes were amplified by this factor at the very tip of the probe. This penetrator design was used for all tests.

Chapter 5

This chapter provided a qualitative examination of the motion of sand particles under ultrasonic vibration. Visualising the motion of sand during a full penetration test was not possible, due to the opaque nature of sand. Instead, the probe was laid horizontally and half-buried in a 50/50 mix of white and black sand, and examined with a high speed

camera and microscope. When ultrasonic vibration was initialised, sand immediately surrounding the penetrator began to fluidise. Regions directly in front were dispelled several centimetres away, whilst the sand along the side of the shaft was observed to travel in the opposite direction, towards the nodal point of the probe.

Fluidisation of sand surrounding the probe is likely the leading cause of the force reductions seen elsewhere in the thesis, in a similar way to quicksand causing objects to sink into it. The phenomenon of sand collecting around the nodal points could potentially be utilised for evacuation purposes, removing cuttings away from a drilling surface.

Chapter 6

These were the very first tests into using direct ultrasonic vibration in the penetration of granular material. A rig was designed to measure the reacted force throughout penetration at a slow and fast penetration rate into ten different regolith environments (five different regoliths, each at loose and compact densities). In all environments, the peak penetration force decreased with increasing amplitude. Some regoliths displayed a higher sensitivity to the vibration, reducing force by a greater amount than others. Loose density preparations also showed a lower overall sensitivity than compacted sand, suggesting that the greatest benefits would be in tougher substrates. The higher levels of vibration displayed diminishing returns, only reducing the force requirements by a small amount compared to the lower levels of vibration.

Additional effects involving consecutive penetrations also arose in these tests, suggesting that repeated penetrations into the same area of sand would require less force up to a certain depth, whereupon the peak force would rapidly increase.

Chapter 7

After the force experiments were conducted, it became apparent that the power consumption of the ultrasonic transducer would warrant investigation, particularly at lower amplitudes. A new ultrasonic supply was used for these tests that provided a smaller minimum ultrasonic excitation amplitude, allowing experiments to be conducted down to 0.4 µm. A reduction in the penetration force results in a lower power consumption in the linear actuator; however the ultrasonic vibration requires power itself to maintain. By measuring the power consumption of both the actuator and the ultrasonic transducer, the

total power consumption with respect to excitation amplitude was realised. It was discovered than there was an optimum excitation amplitude of 0.6 μm for high density BP, where the total power consumption was minimised, proving that using ultrasonic vibration in penetrating devices could in some cases reduce the overall power requirements.

Chapter 8

These experiments looked at the impact that gravity has on the effectiveness of ultrasonically assisted penetration, by conducting the previous experiments in a large centrifuge. The penetration force and power consumption were measured in gravity levels between 1 – 10 g, and the relations with gravity examined. The total power consumption levels appeared to vary very little with increasing gravity, continually displaying optimum excitation amplitude around 0.6 μm.

Force requirements on the other hand increased dramatically with higher gravity levels. Additionally, the effectiveness of ultrasonic vibration (i.e. how much the force is reduced as a percentage of the non-ultrasonic force) appeared to decrease at higher gravity. Extrapolating this result, it is possible to infer that using ultrasonic vibration in the penetration of granular material would be even *more* effective in lower gravity, giving larger decreases in penetration force compared to non-ultrasonic forces.

Chapter 9

All other experiments in this thesis looked at categorising and establishing the limits and benefits of ultrasonic vibration on granular material. The experimental technique used was simply to cut out as many variables as possible, and it is not expected that this would be used in situ. The tests covered in this chapter however formed the first steps into incorporating ultrasonic onto an actual device, using the ‘hammer-action’ method used on previous space missions.

Coordinating pulses of ultrasonic vibration with a hammer striking yielded significantly fewer impacts required to reach a depth of 190 mm than by pure hammering. These advantages can manifest in two ways. Firstly, increasing the depth per strike would enable a penetration vehicle to reach its desired depth in a much shorter time frame, allowing a longer duration for scientific measurements. Secondly, the force of impact can be immense, potentially leading to damages within the device. By allowing a lower impact force, the penetrating mole could theoretically be loaded with more sensitive scientific

equipment, opening up an increased suite of scientific instruments that can be delivered to the sub-surface of a planet.

To summarise, ultrasonically assisted penetration through granular material is a fledgling field, and the results indicate that it could potentially significantly beneficial in its application to low gravity or low mass penetrators.

10.2 Contributions

Brief descriptions of the main contributions that this work has given to the scientific community are given here, illustrating the new information and knowledge gained

Ultrasonics and WOB reduction

Ultrasonic vibration of a penetrating probe impacts the surrounding media by fluidising the sand within a very short range. Through this effect, the weight-on-bit (WOB) required for penetration has experimentally been shown to reduce, up to an order of magnitude in these specific cases, illustrating its potential worth for either low gravity environments such as on planets or asteroids, or for low weight environments, such as submerged exploration.

Ultrasonics and power reduction

Simultaneously it has been shown that this vibration, whilst requiring power to sustain, can reduce the overhead forces to such a degree that the total power consumption of the whole system is reduced.

Performance with gravity

Initial tests with a high gravity centrifuge have shown, through extrapolating trends, that the WOB reduction performance seen with ultrasonic penetration could increase at lower gravities. This would be attractive for any penetration in low gravity.

Increasing performance of hammering probes

Applying ultrasonic vibration to an existing penetration method, impact hammering, has shown that ultrasonic vibration is a versatile method, which can be used simultaneously with other mechanisms. Tests showed that combining ultrasonic vibration and impact

hammering resulted in a significantly higher penetration performance, accessing depths in fewer impacts.

10.3 Publications

The work in this thesis has been published and presented at several conferences, as well as in a journal article. The references of these papers are listed here, as well as the corresponding chapters that relate to the content within each paper.

10.3.1 Journal publications

D. Firstbrook, K. Worrall, R. Timoney, F. Suñol, Y. Gao, and P. Harkness, "An Experimental Study of Ultrasonic Vibration and the Penetration of Granular Material," *Proc. R. Soc. A*, vol. 473, no. 2198, pp. 1–16, 2017. (Chapters 3, 4, 6, 7, and 8)

10.3.2 Conference publications

D. Firstbrook, P. Harkness, and Y. Gao, "High-powered ultrasonic penetrators in granular material," in *AIAA Space 2014 Conference, 4-7 Aug 2014, San Diego, CA, USA.*, 2014, pp. 1–11. (Chapters 3, 4, and 6)

D. G. Firstbrook, P. Doherty, R. Timoney, P. Harkness, and F. Suñol, "Preparations for variable-gravity regolith penetration with an ultrasonically-active probe," in *12th International Planetary Probe Workshop*, 2015, no. 1. (Chapter 8)

D. Firstbrook, P. Harkness, and Y. Gao, "Power optimization for an ultrasonic penetrator in granular materials," in *AIAA Space 2015 Conference, 31 Aug - 2 Sept 2015, Pasadena, CA, USA.*, 2015, pp. 1–8. (Chapter 7)

D. Firstbrook, K. Worrall, P. Doherty, R. Timoney, P. Harkness, and F. Suñol, "Ultrasonic Penetration of Granular Materials in Varying Gravity," in *ASCE Earth & Space 2016*, 2016. (Chapter 8)

D. Firstbrook, K. Worrall, R. Timoney, P. Harkness, F. Suñol, and Y. Gao, "Ultrasonically Assisted Penetration Through Granular Materials," (poster) in *13th International Planetary Probe Workshop*, 2016, p. 1. (Chapters 3, 6, 7, and 8)

10.3.3 Other articles

Interviewed article for STV

http://glasgow.stv.tv/articles/315159-space-team-glasgow-to-work-on-mars-rover-drill-at-european-space-agency/

The "Team Dynamics" as part of the ESA Educations 'Spin Your Thesis!' campaign

http://www.esa.int/Education/Spin_Your_Thesis/Meet_the_teams_Dynamics

Chapter 11

Recommended Future Design and Research

Research time for PhD has inevitable limitations and the work is never truly completed, with more questions than answers often arising. The work in this PhD is no different, and several questions and curious results arose that would benefit from further examination, which unfortunately were not able to be covered during the time available.

This chapter will present a few of the areas that warrant further scientific investigation, followed by a short discussion as to the possible applications of the work covered in this thesis. It is important to note that the possible applications are simply ideas that are based on the observations and experience of the author. As such they are not aimed to be taken as a final design, but rather as a seed for inspiration on possible applications.

11.1 Future work

11.1.1 Optimisation of ultrasonics

The ultrasonic transducer used for these tests was the L500 from Sonic Systems™; an off-the-shelf product used for a wide variety of tasks. As such, it is not strictly tailored for the penetration of granular materials. The transducer is capable of tracking a small frequency range of 19.5 – 20.5 kHz, however it is entirely possible that different frequencies might perform differently with respect penetration, perhaps exciting some sort of resonance with the sand. Future work could potentially look into this, manufacturing a range of ultrasonic transducers that resonate at a range of frequencies.

11.1.2 In situ monitoring

Due to the opacity of sand, the high-speed camera experiments described in Chapter 5 were limited to viewing the surface, with a horizontally positioned penetrator secured in place. This helped with the understanding of the general mechanics of vibration and granular material, but it is not a true representation of ultrasonic vibration during penetration. Previous work using Magnetic Resonance Imaging (MRI) has been done to allow the user to probe the flow of grains within a material [120], [121]. Ultrasonic penetration experiments could be performed with these MRI machines. This is not a trivial task however, as extreme care is required when using metals in these high-magnetic-field machines, especially with any magnetic metals such as iron, nickel, or cobalt.

11.1.3 Low gravity tests

The high-gravity experiments described in Chapter 8 provided a valuable insight into the effects of gravitational acceleration on ultrasonic vibration. However, the authors were well aware that the Earth possesses the highest gravity of any rocky body in the solar system, meaning that any extra-terrestrial surface exploration would be conducted in gravity less than 1 g. Despite this, the high-gravity experiments allowed a vast amount of experiments to be conducted, and a trend line to be extrapolated.

The next step in progression of this work would be to conduct experiments in low gravity. Due to the time taken for penetration, it is likely that a parabolic flight would be required. Micro-gravity is too low to keep the sand sample intact, so dedicated partial-g flights would be needed, which have been previously achieved for penetration experiments [122]. If a future experiment were able to get a placement on one of these flights, then it would be possible to test out the theory inferred from Chapter 8, and provide valuable empirical feedback for future missions involving ultrasonic penetration.

11.1.4 Expanding hammering tests

The hammering experiments of Chapter 9 concluded that ultrasonic vibration allowed a higher rate of penetration per strike than just pure hammering. The benefit is that the hammering force could be reduced, allowing more delicate instruments to be included within the device. During these experiments, a variety of different hammering masses were

considered, thus providing different impact energies. However, these were not able to be implemented due to time. For pure hammering, a lower impact energy results in a lower depth of penetration, all other things being equal. With the introduction of ultrasonic vibration, it would be interesting to see where the balance lies, and whether the impact mass can be reduced to a point where the penetration profiles of simultaneous vibration and hammering eventually match that of pure hammering, albeit it with a larger mass. This information would be invaluable in the design of an ultrasonic mole, guiding the operator the amplitude to use for comparable penetration performance, and answering how much the internal impacts can be reduced by to achieve comparable penetration depths.

11.1.5 Wasp horn tests

One goal of this PhD was to combine the ultrasonics knowledge of the University of Glasgow, and the wasp-drill concept from the University of Surrey, described in section 2.1.4.1. One of the problems with this task is the half-cylinder shape of the wasp drill. If such a shape were to vibrate ultrasonically it would create a large bending force, which at large amplitudes could possibly break the device. For this reason, it was decided to create a rotationally symmetric version of the wasp drill to start investigating its properties. This is known as a Mono-block Drill Head (MDH) [56], as is essentially the same shape as if the two halves of the wasp drill were fused together. This horn was rotationally symmetric, with barbs designed at the surface, tapering in a conical fashion, shown in Figure 11.1.

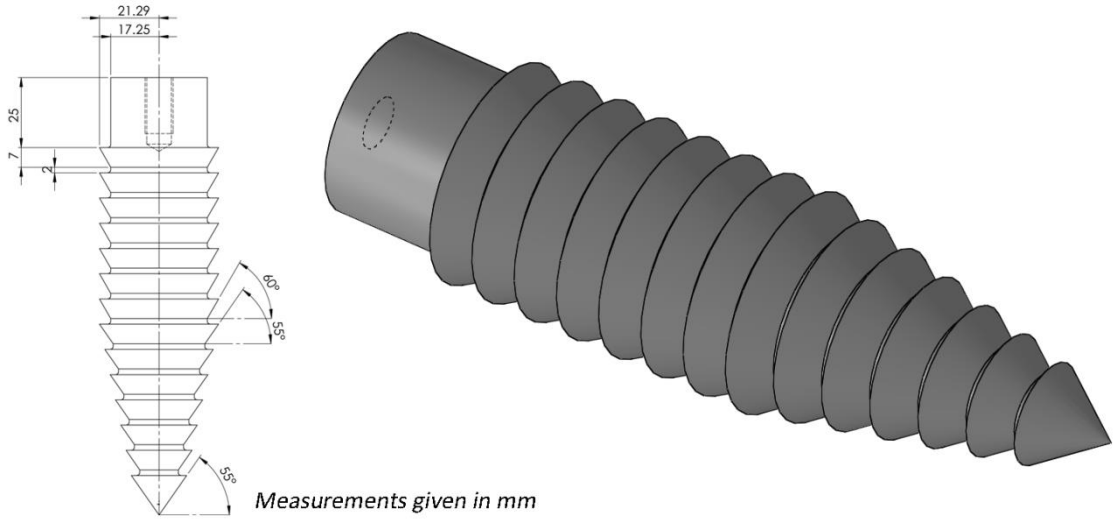

Figure 11.1: Overview of the ultrasonic wasp horn.

The design was based as much as possible on an existing MDH (described in the thesis by Gouache [56]), with the additional constraint that it must fit the Langevin transducer and vibrate at 20 kHz. Additionally, the 3D laser used in the experimental modal analysis is required to be perpendicular to the surface it is measuring. The simplest way to do this was to introduce short flat sections between the barbs, still keeping the general shape the same as the original MDH.

11.1.5.1 Wasp horn Experimental Modal Analysis

The horn was tested using the same EMA method as described in Chapter 4. Unlike the previous horn, this horn was designed to resonate at the L1 mode at 20 kHz. This design does not utilise a step, and thus is not as constrained in penetration depth. However, this also results in a much lower gain compared to the previous horn, requiring more power input to reach the same amplitude. The larger cross-sectional area would also result in much higher penetration forces comparatively, but as this was intended to investigate the effects at an initial level, this was not a huge concern.

During the EMA testing, attempts at measuring the vibration on a barb using the 3D laser proved more difficult than anticipated due to the angles involved. The flat sections

incorporated into the design on the other hand proved to give a much clearer results, showing the flat-sections in the design were essential. The results of the frequency response are shown in Figure 11.2, with a clear peak at 20 kHz.

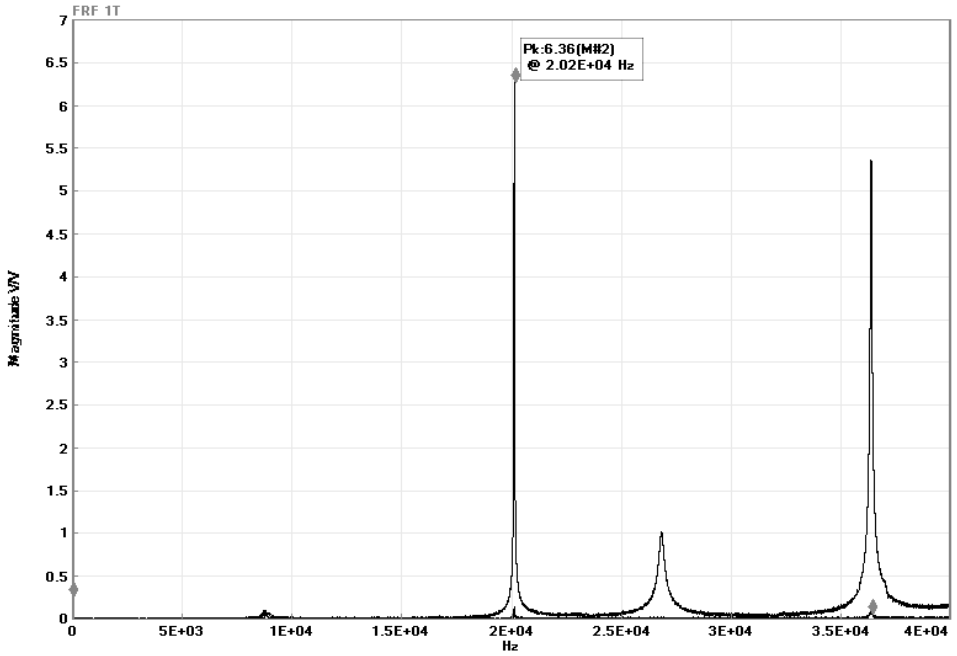

Figure 11.2: EMA results of the wasp horn

The placement of points of measurement is shown in Figure 11.3, resulting in 48 total points using a 6-way symmetry. The complex shape of the horn was not reproduced in the simulation as there is no vibration data from the tips of the barbs. However the underlying vibration was recorded, and showed a perfectly longitudinal vibration. The gain of the horn can be calculated from the ratio of tip vibration to base vibration, resulting in a final gain of 1.5. This is much lower than the gain of the previous horn (3.5); however this is to be expected due to the shape of the horn being more like a cone, rather than a step function.

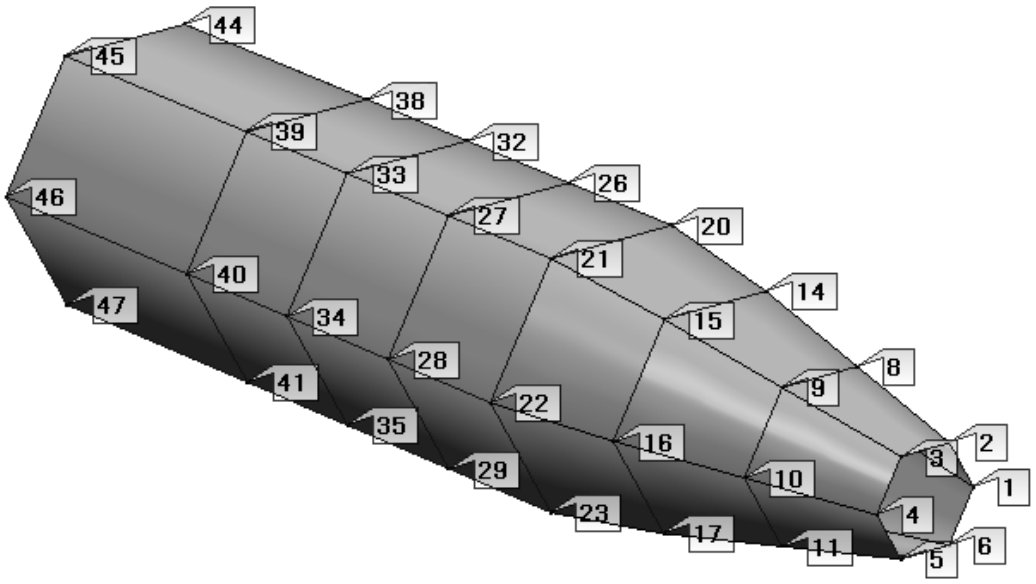

Figure 11.3: EMA model of the wasp horn. The nodes are numbered in the order they were measured.

Investigations using this horn could be extremely valuable in combining ultrasonics and wasp-drilling technologies, however due to time constraints, experiments with it were not able to be conducted. The horn has been manufacture and fully characterised, so it could easily form the basis of a future project.

11.2 Applications

11.2.1 Ultrasonic mole

As discussed in Chapter 9, ultrasonic vibration could potentially be incorporated with the existing mole technology. Due to the fragile nature of piezo-ceramics, care would need to be taken in ensuring the shocks are kept away from these elements. A hammering strike would not be able to impact the back-mass of a Langevin transducer directly, however by using a case that encapsulates the ultrasonic elements, the shock could be spread out and around, directing energy towards the mole tip. An example of this design is shown in Figure 11.4.

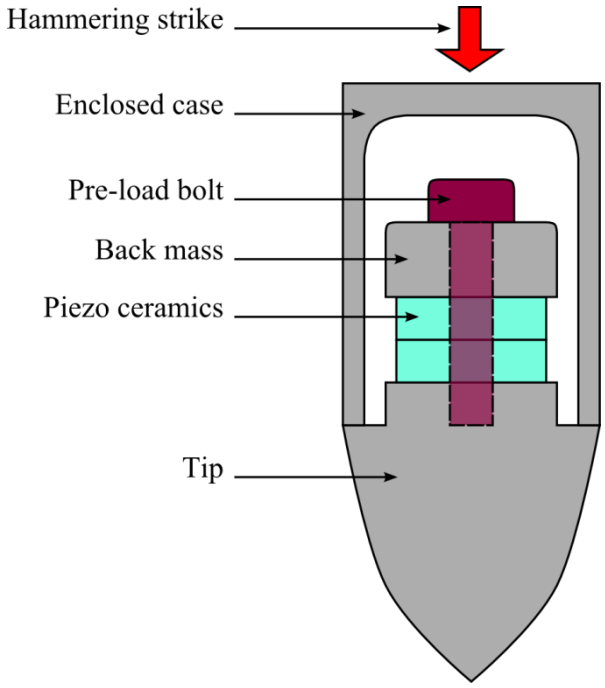

Figure 11.4: Example of a mole-tip schematic that incorporates ultrasonic vibration.

In this design, a case is connected to the tip via a flange. Designing the nodal point of vibration to coincide with this flange allows mechanical fixtures to be made without vibration propagating through it. The tip acts as several components simultaneously; the tip of the penetrating mole, the front mass of the Langevin transducer, and the horn to amplify vibration. It is important to note that the shape of the tip would require to be designed to maximise mole penetration performance and not to maximise the vibration gain. However, previous tests showed significant reduction in force at the lowest level of excitation amplitude, 0.4 µm, which corresponds to a tip amplitude of 1.4 µm with the 3.5 gain of the penetrator. This level of vibration can easily be achieved; however a slightly larger power draw would be expected.

This design is just a preliminary example of how ultrasonic could be incorporated into the hammering mole technique, and it is hoped future research could develop this further.

11.2.2 Anchoring

For small landers in low gravity, anchors offer an attractive method to increase the effective weight that can be applied to drills or penetrators. The same force that keeps the anchor in place and which provides increased traction is the same force that would need to

be overcome if the anchor needs to be retrieved. As the traction force is often intended to be maximised, this results in the anchor simply being cut loose after use, due to the high retrieval force. Ultrasonic vibration, with its ability to fluidise sand under controlled circumstances could potentially alleviate this retrieval problem by creating a 'smart' anchor. For example, using a barbed horn and activating ultrasonics, it would be able to progress to further depths compared to non-ultrasonic penetration. By deactivating this horn, it effectively acts as an anchor, potentially providing a higher anchoring force due to its deeper depth. For retrieval, the ultrasonics can once again be activated, fluidising the sand around the anchor and reducing the retrieval force. The anchor could then be stored within the lander, ready to be used again. An overview of an example of this procedure is described in Figure 11.5.

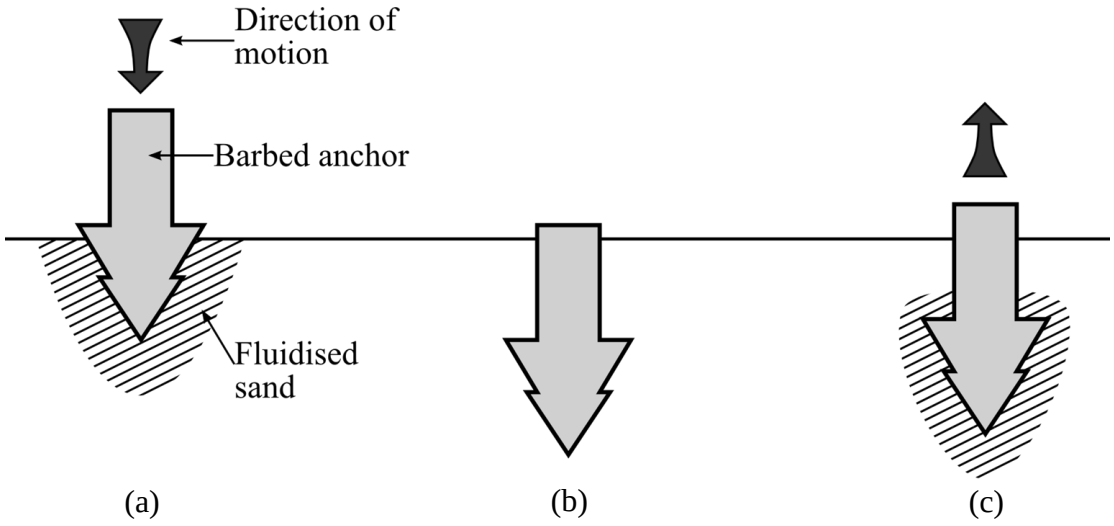

Figure 11.5: Illustrated example of a 'smart' anchor. (a) The anchor is ultrasonically activated and progresses through the regolith with reduced friction due to the fluidised sand. (b) The ultrasonics are switched off, and the anchor allowed to function as normal, at a greater depth than previously possible. (c) For retrieval, the ultrasonics are once again activated, fluidising the surrounding sand and reducing the retrieval force required.

11.2.3 Ultrasonic spoil removal

An interesting effect seen during the high-speed camera experiment in Chapter 5 occurred when the sand began to move and pile up around the nodal point of the horn. This effect was also seen in qualitative testing when pushing the penetrator through wet sand by hand, where clumps of sand would stick to the sides of the probe and move up the shaft against gravity. It is still not clear exactly how the sand vibrates in situ during penetration, however it could be possible that this nodal effect still occurs within the sand.

An example of how this phenomenon could be exploited is shown in Figure 11.6. During penetration, sand would move along the shaft and collect around the nodal point. As this particular horn is tuned to the second longitudinal mode, L2, this point is roughly located a third-way up the shaft. By lowering the frequency of vibration to coincide with the first longitudinal mode, approximately half the frequency at 10 kHz, the nodal point rises up to roughly two-thirds up the shaft. The collection of sand would potentially then travel up the shaft to this new nodal point. Here, the vibration could switch back to the second longitudinal mode, where the sand would then progress up to the second node at the top of the shaft.

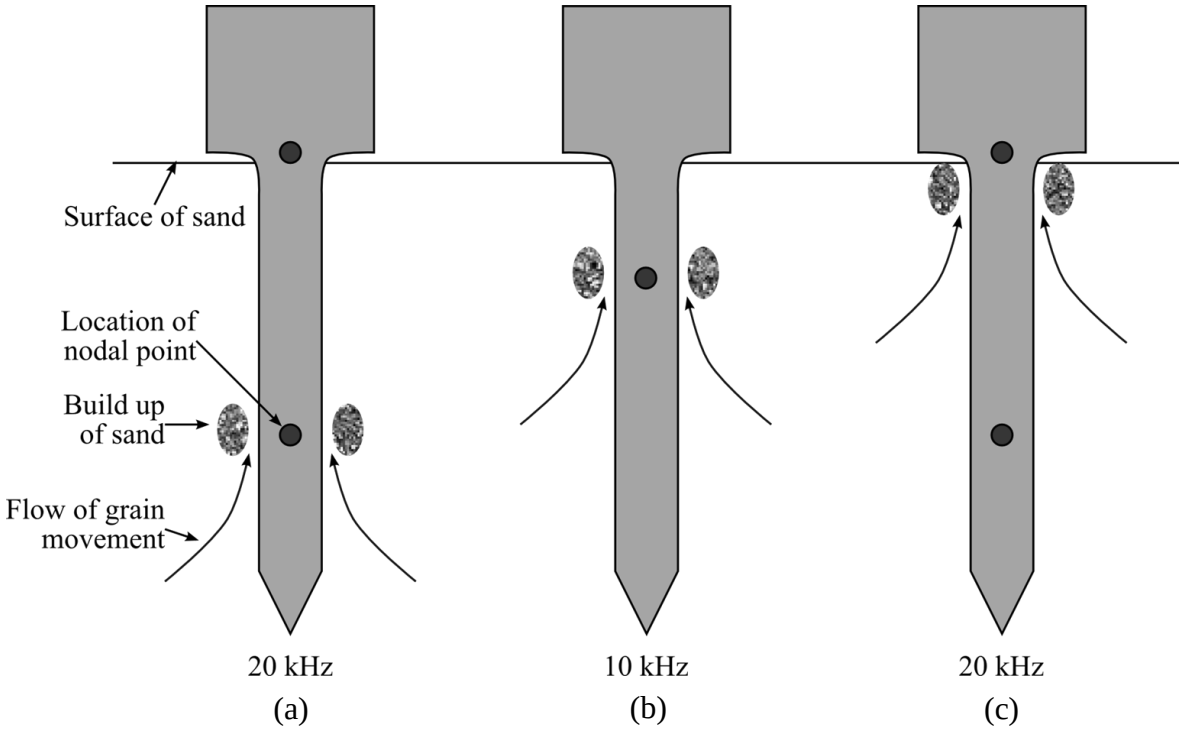

Figure 11.6: Example of exploiting the collection of sand at the nodal points of vibration for locomotion of regolith. Switching the applied frequency would change the operating resonant mode to (a) the L2 mode, (b) the L1 mode, and (c) back to the L2 mode. The rough frequencies of these modes are given for the penetrator used in this particular work.

Theoretically, this effectively would be excavating sand from the tip of the penetrator to the surface, without the probe having to move position. This is highly speculative however, as the interaction of sand next to a vertical vibrating probe deep within the sample is currently unknown, and would rely heavily on the specific interactions with the soil. It is likely that this would have a greater effect in saturated sand, as the cohesive nature of wetted soil would cause a great degree of adhesion to the probe surface.

Additionally, operating the penetrator at a lower frequency could potentially have damaging consequences, as the flange of the Langevin transducer that supports the case would no longer be located at a nodal point. If this idea were to be taken further, significant development would be required, possibly using other vibrational modes such as bending or torsional.

11.3 Chapter conclusions

This chapter combines the knowledge acquired from the experiments taken previously, and suggests further research that could be developed. Many questions remain unanswered, and as this is a relatively young research field there is a great scope for ultrasonically assisted penetration to evolve.

Based on the experiences of the author, different possible applications were also suggested. Expanding on work covered with the hammering experiments in Chapter 9, suggestions towards incorporating this on a mole device were proposed. Reducing the hammering impacts or allowing the device to travel further for the same impact could be extremely beneficial for subsurface exploration. Ideas for a controllable ‘smart’ anchor were also suggested, potentially allowing a rover or lander to increase its effective weight-on-bit, whilst also allowing it to recommence locomotion when desired. Finally, a highly conceptual idea for using the collection of sand around nodal points for evacuation purposes was discussed.

Bibliography

[1] K. E. Herkenhoff, J. J. Plaut, and S. A. Nowicki, "Surface age and resurfacing rate of the north polar layered terrain on Mars," in *28th Lunar and Planetary Conference*, 1997, p. 1575.

[2] D. M. Hassler, C. Zeitlin, R. F. Wimmer-Schweingruber, B. Ehresmann, S. Rafkin, J. L. Eigenbrode, D. E. Brinza, G. Weigle, S. Böttcher, E. Böhm, S. Burmeister, J. Guo, J. Köhler, C. Martin, G. Reitz, F. A. Cucinotta, M.-H. Kim, D. Grinspoon, M. A. Bullock, A. Posner, J. Gómez-Elvira, A. Vasavada, J. P. Grotzinger, and M. S. Team, "Mars' Surface Radiation Environment Measured with the Mars Science Laboratory's Curiosity Rover," *Science (80-.).*, vol. 343, no. 6169, p. 1244797, 2014.

[3] ESA Exobiology Team Study, "Exobiology in the Solar System and the search for life on Mars," ESA Publication Division, ESTEC, Noordwijk, The Netherlands, 1999.

[4] D. Persson, K. A. Halberg, A. Jørgensen, C. Ricci, N. Møbjerg, and R. M. Kristensen, "Extreme stress tolerance in tardigrades: surviving space conditions in low earth orbit," *J. Zool. Syst. Evol. Res.*, vol. 49, no. supplement 1, pp. 90–97, 2011.

[5] G. Horneck and P. Rettberg, *Complete course in astrobiology*. Weinheim, Germany: Wiley-VCH, 2007.

[6] K. R. Sridhar, C. S. Iacomini, and J. E. Finn, "Combined H2O/CO2 Solid Oxide Electrolysis for Mars In Situ Resource Utilization," *J. Propuls. Power*, vol. 20, no. 5, pp. 892–901, 2004.

[7] G. B. Sanders and W. E. Larson, "Integration of in-situ resource utilization into lunar/Mars exploration through field analogs," *Adv. Sp. Res.*, vol. 47, pp. 20–29, 2011.

[8] M. Anand, I. A. Crawford, M. Balat-Pichelin, S. Abanades, W. van Westrenen, G. Péraudeau, R. Jaumann, and W. Seboldt, "A brief review of chemical and mineralogical resources on the Moon and likely initial in situ resource utilization (ISRU) applications," *Planet. Space Sci.*, vol. 74, pp. 42–48, Dec. 2012.

[9] K. Zacny, P. Chu, J. Craft, M. M. Cohen, M. Field, W. W. James, and B. Hilscher, "Asteroid Mining," in *AIAA SPACE 2013 Conference & Exposistion*, 2013, pp. 1–16.

[10] Y. Bar-Cohen and K. Zacny, *Drilling in Extreme Environments*. Weinheim, Germany: Wiley-VCH, 2009.

[11] R. Bement, "Ground compaction due to vibrodriving of piles," Durham University, 1996.

[12] M. W. O'neill, C. Vipulanandan, and D. Wong, "Laboratory Modeling of Vibro-Driven Piles," *J. Geotech. Eng.*, vol. 116, no. 8, pp. 1190–1209, 1990.

[13] D. L. Glaser, A. J. Ball, and K. A. Zacny, "A review of penetrometers for subsurface access on comets and asteroids," *Meteorit. Planet. Sci.*, vol. 43, no. 6, pp. 1021–1032, 2008.

[14] W. T. Huntress Jr. and M. Y. Marov, *Soviet Robots in the Solar System: Mission Technologies and Discoveries*. New York, New York: Springer, 2011.

[15] Robert Godwin, *Apollo 11: The NASA Mission Reports Volume 1*. Ontario, Canada: Apogee Books, 1999.

[16] NASA Manned Spacecraft Center, "Apollo 15: Preliminary Science Report," Washington D.C., 1972.

[17] K. Zacny, Y. Bar-Cohen, M. Brennan, G. Briggs, G. Cooper, K. Davis, B. Dolgin, D. Glaser, B. Glass, S. Gorevan, J. Guerrero, C. McKay, G. Paulsen, S. Stanley, and C. Stoker, "Drilling Systems for Extraterrestrial Subsurface Exploration," *Astrobiology*, vol. 8, no. 3, pp. 665–706, 2008.

[18] J. P. Grotzinger, J. Crisp, A. R. Vasavada, R. C. Anderson, C. J. Baker, R. Barry, D. F. Blake, P. Conrad, K. S. Edgett, B. Ferdowski, R. Gellert, J. B. Gilbert, M. Golombek, J. Gómez-Elvira, D. M. Hassler, L. Jandura, M. Litvak, P. Mahaffy, J. Maki, M. Meyer, M. C. Malin, I. Mitrofanov, john J. Simmonds, D. Vaniman, R. V Welch, and R. C. Wiens, "Mars Science Laboratory mission and science investigation," *Space Sci. Rev.*, vol. 170, pp. 5–56, 2012.

[19] R. C. Anderson, L. Jandura, A. B. Okon, D. Sunshine, C. Roumeliotis, L. W. Beegle, J. Hurowitz, B. Kennedy, D. Limonadi, S. McCloskey, M. Robinson, C. Seybold, and K. Brown, "Collecting samples in Gale Crater, Mars; an overview of the Mars Science Laboratory sample acquisition, sample processing and handling system," *Space Sci. Rev.*, vol. 170, pp. 57–75, 2012.

[20] A. B. Okon, "Mars science laboratory drill," in *40th Aerospace Mechanisms Symposium*, 2010.

[21] J. Biele and S. Ulamec, "Capabilities of Philae, the Rosetta Lander," *Space Sci. Rev.*, vol. 138, pp. 275–289, 2008.

[22] K. Zacny, G. Paulsen, C. P. Mckay, B. Glass, A. Davé, A. F. Davila, M. Marinova, B. Mellerowicz, J. Heldmann, C. Stoker, N. Cabrol, M. Hedlund, and J. Craft,

"Reaching 1 m Deep on Mars: The Icebreaker Drill," *Astrobiology*, vol. 13, no. 12, pp. 1166–1198, 2013.

[23] B. J. Glass, C. McKay, S. Thompson, and K. Zacny, "Automated Mars drilling for 'Icebreaker,'" in *IEEE Aerospace Conference Proceedings*, 2011, pp. 1–7.

[24] J. Vago, O. Witasse, P. Baglioni, A. Haldemann, G. Gianfiglio, T. Blancquaert, D. McCoy, R. de Groot, and E. Team, "ExomarsESA's next step in Mars exploration," *ESA Bull.*, 2013.

[25] J. Vago, O. Witasse, H. Svedhem, P. Baglioni, A. F. C. Haldemann, G. Gianfiglio, T. Blancquaert, D. McCoy, and R. de Groot, "ESA ExoMars program: the next step in exploring Mars," *Sol. Syst. Res.*, vol. 49, no. 7, pp. 518–528, 2015.

[26] Y. Bar-Cohen, Z. Chang, S. Sherrit, M. Badescu, and X. Bao, "The Ultrasonic/Sonic Driller/Corer (USDC) as a subsurface drill, sampler and lab-on-a-drill for planetary exploration applications," in *Proceedings of the SPIE Smart Structures Conference*, 2005, vol. 5762–22, pp. 1–8.

[27] M. Badescu, S. Sherrit, X. Bao, Y. Bar-Cohen, and B. Chen, "Auto-Gopher-a wire-line rotary-hammer ultrasonic drill," in *Proceedings of SPIE Smart Structures and Materials Conference*, 2011, vol. 7981, pp. 1–8.

[28] P. Harkness, M. McRobb, Y. W. Loh, M. Hyde, and M. Lucas, "A Rock-Coring Campaign in an Analogue Environment," in *AIAA SPACE 2014 Conference & Exposistion*, 2014, pp. 1–9.

[29] R. Timoney, P. Harkness, K. Worrall, X. Li, A. Bolhovitins, and Lucas, "The Development of the European Ultrasonic Planetary Core Drill (UPCD)," in *AIAA Space 2015 Conference & Exposistion*, 2015, pp. 1–11.

[30] ASTM, "ASTM D3441-98 Standard Test Method for Mechanical Cone Penetration Tests of Soil." pp. 1–5, 1998.

[31] P. K. Robertson and R. G. Campanella, "Interpretation of cone penetrationtests. Part I: Sand," *Can. Geotechincal J.*, vol. 20, pp. 718–733, 1983.

[32] M. R. Sims, C. T. Pillinger, I. P. Wright, J. Dowson, S. Whitehead, A. Wells, J. E. Spragg, G. Fraser, L. Richter, and H. Hamacher, "Beagle 2: a proposed exobiology lander for ESA's 2003 Mars Express mission," *Adv. Sp. Res.*, vol. 23, no. 11, pp. 1925–1928, 1999.

[33] L. Richter, P. Coste, V. Gromov, H. Kochan, S. Pinna, and H.-E. Richter, "Development of the 'planetary underground tool' subsurface soil sampler for the Mars express 'Beagle 2' lander," *Adv. Sp. Res.*, vol. 28, no. 8, pp. 1225–1230, 2001.

[34] S. Pinna, F. Angrilli, H. Kochan, and L. Richter, "Development of the mobile

penetrometer (Mole) as sampling tool for the Beagle2 Lander on Mars Express 2003," *Adv. Sp. Res.*, vol. 28, no. 8, pp. 1231–1236, Jan. 2001.

[35] L. Richter, P. Coste, V. Gromov, and A. Grzesik, "The mole with sampling mechanism (MSM)–Technology development and payload of Beagle 2 mars lander," in *Proceedings, 8th ESA Workshop on Advanced Space Technologies for Robotics and Automation (ASTRA 2004), Noordwijk, The Netherlands, November*, 2004, pp. 2–4.

[36] T. Spohn, M. Grott, J. Knollenberg, T. van Zoest, G. Kargl, S. E. Smrekar, W. B. Banerdt, and T. L. Hudson, "InSight: Measuring the Martian Heat Flow Using the Heat Flow and Physical Properties Package (HP^3)," in *International Workshop on Instrumentation for Planetary Missions*, 2012, vol. 1124, pp. 1–2.

[37] K. Seweryn, M. Banaszkiewicz, S. Bednarz, M. Ciesielska, A. Gonet, J. Grygorczuk, T. Kucinski, T. Rybus, M. Rzyczniak, R. Wawrzaszek, L. Wisniewski, and M. Wojcikowski, "The experimental results of the functional tests of the mole penetrator KRET in different regolith analogues," in *Aerospace Robotics: Robotics in Aeronautics and Astronautics*, 2013.

[38] T. Spohn, K. Seiferlin, A. Hagermann, J. Knollenberg, A. J. Ball, M. Banaszkiewicz, J. Benkhoff, S. Gadomski, W. Gregorczyk, J. Grygorczuk, M. Hlond, G. Kargl, E. Kührt, N. Kömle, J. Krasowski, W. Marczewski, and J. C. Zarnecki, "Mupus – A Thermal and Mechanical Properties Probe for the Rosetta Lander Philae," *Space Sci. Rev.*, vol. 128, pp. 339–362, Feb. 2007.

[39] H. Rickman, E. Słaby, J. Gurgurewicz, M. Śmigielski, M. Banaszkiewicz, J. Grygorczuk, M. Morawski, K. Seweryn, and R. Wawrzaszek, "CHOMIK: a multi-method approach for studying Phobos," *Sol. Syst. Res.*, vol. 48, no. 4, pp. 279–286, 2014.

[40] J. Grygorczuk, M. Dobrowolski, and L. Wisniewski, "Advanced mechanisms and tribological tests of the hammering sampling device CHOMIK," in *14th European Space Mechanisms & Tribology Symposium*, 2011, pp. 271–278.

[41] L. Richter, P. Coste, V. V Gromov, H. Kochan, R. Nadalini, T. C. Ng, S. Pinna, H.-E. Richter, and K. L. Yung, "Development and testing of subsurface sampling devices for the Beagle 2 lander," *Planet. Space Sci.*, vol. 50, pp. 903–913, 2002.

[42] H. Hansen-Goos and M. Grott, "Predicted Penetration Performance of the InSight HP^3 Mole," in *45th Lunar and Planetary Science Conference*, 2014, p. 1325.

[43] JPL, "Mars Exploration Program - New Insight on Mars Expected From New NASA Mission," 2012. [Online]. Available: http://mars.jpl.nasa.gov/news/whatsnew/index.cfm?FuseAction=ShowNews&NewsID=1318. [Accessed: 23-Aug-2016].

[44] R. Lichtenheldt, B. Schäfer, and O. Krömer, "Hammering beneath the surface of Mars-Modeling and simulation of the impact-driven locomotion of the HP^3-Mole by

coupling enhanced multi-body dynamics," in *58th Ilmenau Scientific Colloquium*, 2014, pp. 1–20.

[45] R. F. Scott and F. I. Roberson, "Soil mechanics surface sampler: Lunar surface tests, results, and analyses," *J. Geophys. Res.*, vol. 73, no. 12, pp. 4045–4080, 1968.

[46] R. F. Scott and F. I. Roberson, "Soil mechanics surface sampler," *J. Geophys. Res.*, vol. 74, no. 25, pp. 6175–6214, 1969.

[47] H. P. Klein, "The Viking mission and the search for life on Mars," *Rev. Geophys. Sp. Phys.*, vol. 17, no. 7, pp. 1655–1662, 1979.

[48] NASA, "Phoenix Landing. Mission to the Martian Polar North," *Press Kit/ May 2008*, no. May, 2008.

[49] R. G. Bonitz, L. Shiraishi, M. Robinson, R. E. Arvidson, P. C. Chu, J. J. Wilson, K. R. Davis, G. Paulsen, A. G. Kusack, D. Archer, and P. Smith, "NASA Mars 2007 Phoenix lander robotic arm and icy soil acquisition device," *J. Geophys. Res.*, vol. 113, no. EEA01, pp. 1–10, 2008.

[50] R. E. Arvidson, R. G. Bonitz, M. L. Robinson, J. L. Carsten, R. A. Volpe, A. Trebi-Ollennu, M. T. Mellon, P. C. Chu, K. R. Davis, J. J. Wilson, A. S. Shaw, R. N. Greenberger, K. L. Siebach, T. C. Stein, S. C. Cull, W. Goetz, R. V Morris, D. W. Ming, H. U. Keller, M. T. Lemmon, H. G. Sizemore, and M. Mehta, "Results from the Mars Phoenix lander robotic arm experiment," *J. Geophys. Res.*, vol. 114, no. E00E02, pp. 1–21, 2009.

[51] M. A'Hearn, M. Belton, W. Delamere, and J. Kissel, "Deep Impact: Excavating Comet Tempel 1," *Science (80-.).*, vol. 310, no. 258, pp. 258–264, 2005.

[52] A. Mukherjee, Ed., *Biomimetics Learning from Nature*. Vukovar, Croatia: In-Teh, 2010.

[53] C. Menon, J. F. V Vincent, N. Lan, L. Bilhaut, A. Ellery, Y. Gao, D. Zangani, S. Carosio, C. Manning, M. Jaddou, and S. Eckersley, "Bio-inspired micro-drills for future planetary exploration," in *CANEUS2006*, 2006, pp. 1–12.

[54] M. H. Rahman, M. G. Fitton, and D. L. J. Quicke, "Ovipositor internal microsculpture in the Braconidae (Insecta, Hymenoptera)," *Zool. Scr.*, vol. 27, no. 4, pp. 319–332, 1998.

[55] T. P. Gouache, Y. Gao, P. Coste, and Y. Gourinat, "First experimental investigation of dual-reciprocating drilling in planetary regoliths: Proposition of penetration mechanics," *Planet. Space Sci.*, vol. 59, pp. 1529–1541, 2011.

[56] T. Gouache, "Dual reciprocating drilling in planetary regoliths: evolution of a bio-inspired solution," University of Surrey, 2011.

[57] T. Gouache, Y. Gao, P. Coste, and Y. Gourinat, “Experimental study of dual-reciprocating-drilling mechanism using design of experiment approach,” in *13th European Space Mechanisms and Tribology Symposium*, 2009, vol. 670.

[58] T. Gouache, Y. Gao, P. Coste, and Y. Gourinat, “Experimental parametric evaluation of dual-reciprocating drilling mechanism performance,” in *Proceedings of the 11th European Conference on Spacecraft Structures, Materials and Mechanical Testing*, 2009.

[59] T. Gouache, Y. Gao, T. Frame, P. Coste, and Y. Gourinat, “Identification of the force between regolith and a reciprocating drill-head: Perspectives for the exploration of Martian regolith,” in *62nd International Astronautical Congress*, 2011, pp. 1–9.

[60] Y. Gao, A. Ellery, M. Jaddou, J. Vincent, and S. Eckersley, “A novel penetration system for in situ astrobiological studies,” *Int. J. Adv. Robot. Syst.*, vol. 2, no. 4, pp. 281–286, 2005.

[61] Y. Gao, A. Ellery, M. Jaddou, J. Vincent, and S. Eckersley, “Planetary micro-penetrator concept study with biomimetric drill and sampler design,” *IEEE Trans. Aerosp. Electron. Syst.*, vol. 43, no. 3, pp. 875–885, 2007.

[62] C. Pitcher and Y. Gao, “Analysis of drill head designs for dual-reciprocating drilling technique in planetary regoliths,” *Adv. Sp. Res.*, vol. 56, pp. 1765–1776, 2015.

[63] A. G. Winter, A. E. Hosoi, A. H. Slocum, and R. L. H. Deits, “The Design and Testing of RoboClam: A Machine Used to Investigate and Optimize Razor Clam-Inspired Burrowing Mechanisms for Engineering Applications,” in *ASME 2009 International Design Engineering Technical Conferences & Computers and Information in Engineering Conference*, 2009, pp. 1–6.

[64] A. G. Winter, R. L. H. Deits, D. S. Dorsch, A. E. Hosoi, and A. H. Slocum, “Teaching RoboClam to Dig: The design, testing, and genetic algorithm optimization of a biomimetic robot,” in *2010 IEEE/RSJ International Conference on Intelligent Robots and Systems (IROS)*, 2010, pp. 4231–4235.

[65] A. G. Winter, V, R. L. H. Deits, D. S. Dorsch, A. H. Slocum, and A. E. Hosoi, “Razor clam to RoboClam: burrowing drag reduction mechanisms and their robotic adaptation.,” *Bioinspiration & Bomimetics*, vol. 9, no. 3, p. 36009, Apr. 2014.

[66] A. F. Holland and J. M. Dean, “The Biology of the Stout Razor Clam Tagelus plebeius: I. Animal-Sediment Relationships, Feeding Mechanism, and Community Biology,” *Chesap. Sci.*, vol. 18, no. 1, pp. 58–66, Mar. 1977.

[67] S. P. Gorevan, T. M. Myrick, C. Batting, S. Mukherjee, P. Bartlett, and J. Wilson, “Strategies for future mars exploration: An infrastructure for the near and longer-term future exploration of the subsurface of mars,” in *6th International Conference on Mars*, 2003, p. 3196.

[68] S. Yasuda, K. Komatsu, and S. Tanaka, “Self-turning screw mechanism for burying geophysical sensors under regolith,” in *11th International Symposium on Artificial Intelligence, Robotics and Automation in Space (i-SAIRAS 2012)*, 2012, pp. 1–8.

[69] A. Mizushina, H. Omori, and H. Kitamoto, “Study on Geotechnical Tests with a Lunar Subsurface Explorer Robot Using a Peristaltic Crawling Mechanism,” *SICE J. Control. Meas. Syst. Integr.*, vol. 8, no. 4, pp. 242–249, 2015.

[70] F. Becker, S. Boerner, and R. Lichtenheldt, “Enabling Autonomous Locomotion into Sand - A Mobile and Modular Drilling Robot,” in *International Symposium of Robotics*, 2016, pp. 307–312.

[71] K. F. Graff, “Ultrasonics: Historical Aspects,” in *Ultrasonics Symposium*, 1977, pp. 1–10.

[72] K. Graff, “Historical highlights in ultrasonics - 2,” in *2004 IEEE International Ultrasonics, Ferroelectrics, and Frequency Control Joint 50th Anniversary Conference*, 2004, pp. 5–10.

[73] J. A. Gallego-Juarez, “Piezoelectric ceramics and ultrasonic transducers,” *J. Phys. E.*, vol. 22, no. 10, pp. 804–816, Oct. 1989.

[74] W. P. Mason, “Sonics and Ultrasonics: Early History and Applications,” *IEEE Trans. Sonics Ultrason.*, vol. 23, no. 4, pp. 224–232, Jul. 1976.

[75] S. G. Amin, M. H. M. Ahmed, and H. A. Youssef, “Computer-aided design of acoustic horns for ultrasonic machining using finite-element analysis,” *J. Mater. Process. Technol.*, vol. 55, no. 3, pp. 254–260, 1995.

[76] S. Sherrit, S. A. Askins, M. Gradziol, B. P. Dolgin, X. Bao, Z. Chang, and Y. Bar-Cohen, “Novel horn designs for ultrasonic/sonic cleaning welding, soldering, cutting and drilling,” in *Proceedings of SPIE*, 2002, vol. 4701, p. 353.

[77] S. Sherrit, M. Badescu, X. Bao, Y. Bar-Cohen, and Z. Chang, “Novel horn designs for power ultrasonics,” in *2004 IEEE International Ultrasonics, Ferroelectrics, and Frequency Control Joint 50th Anniversary Conference*, 2004, vol. 3, pp. 2263–2266.

[78] P. Harkness, M. Lucas, and A. Cardoni, “Maximization of the effective impulse delivered by a high-frequency/low-frequency planetary drill tool,” *IEEE Trans. Ultrason. Ferroelectr. Freq. Control*, vol. 58, no. 11, pp. 2387–2396, 2011.

[79] Z. Chang, S. Sherrit, X. Bao, and Y. Bar-Cohen, “Design and analysis of ultrasonic horn for USDC (Ultrasonic/Sonic Driller/Corer),” in *SPIE Smart Structures Conference*, 2004, vol. 5388–34, p. 321.

[80] D. J. Hoigne, S. Stübinger, O. Von Kaenel, S. Shamdasani, and P. Hasenboehler, “Piezoelectric osteotomy in hand surgery: first experiences with a new technique,”

BMC Musculoskelet. Disord., vol. 7, no. 36, p. 4, 2006.

[81] Polytec, "No Title." [Online]. Available: http://www.polytec.com/us/company/technologies/. [Accessed: 20-Mar-2017].

[82] P. Evesque, "Shaking dry powders and grains," *Contemp. Phys.*, vol. 33, no. 4, pp. 245–261, 1992.

[83] E. Ben-Naim, J. B. Knight, E. R. Nowak, H. M. Jaeger, and S. R. Nagel, "Slow relaxation in granular compaction," *Phys. D Nonlinear Phenom.*, vol. 123, no. 380, pp. 1–4, 1998.

[84] A. Raihane, O. Bonnefoy, J.-L. Gelet, J.-M. Chaix, and G. Thomas, "Experimental study of a 3D dry granular medium submitted to horizontal shaking," *Powder Technol.*, vol. 190, no. 1–2, pp. 252–257, 2009.

[85] A. Raihane, O. Bonnefoy, J. M. Chaix, J. L. Gelet, and G. Thomas, "Analysis of the densification of a vibrated sand packing," *Powder Technol.*, vol. 208, no. 2, pp. 289–295, 2011.

[86] S. Aumaitre, C. Puls, J. N. McElwaine, and J. P. Gollub, "Comparing flow thresholds and dynamics for oscillating and inclined granular layers," *Phys. Rev. E*, vol. 75, no. 6, p. 61307(9), 2007.

[87] F. Darve, "Liquefaction phenomenon of granular materials and constitutive stability," *Eng. Comput.*, vol. 13, no. 7, pp. 5–28, 1995.

[88] T. Gouache, Y. Gao, P. Coste, and Y. Gourinat, "Lunar regolith simulant preparation and its impact on static penetration resistance and DRD penetration," in *European Planetary Science Congress*, 2010, pp. 1–2.

[89] J. Kolbuszewski and R. Jones, "The preparation of sand samples for laboratory testing," *Proc. Midl. Soil Mech. Found. Eng. Soc.*, no. 4, pp. 107–123, 1961.

[90] A. ElShafie, R. Ulrich, and L. Roe, "Penetration forces for subsurface regolith probes," in *40th Lunar and Planetary Science Conference*, 2009, p. 1205.

[91] T. P. Gouache, C. Brunskill, G. P. Scott, Y. Gao, P. Coste, and Y. Gourinat, "Regolith simulant preparation methods for hardware testing," *Planet. Space Sci.*, vol. 58, pp. 1977–1984, 2010.

[92] D. G. Fredlund and H. Rahardjo, *Soil mechanics for unsaturated soils*. New York, New York: John Wiley & Sons, Inc., 1993.

[93] A. Myslivec and Z. Kysela, *The bearing capacity of building foundations*. Amsterdam, The Netherlands: Elsevier Scientific Publishing Company, 1978.

[94] G. Meyerhof, "The Ultimate Bearing Capacity of Foundations," *Géotechnique*, vol.

2, no. 4, pp. 301–332, 1951.

[95] A. ElShafie, V. F. Chevrier, R. Ulrich, and L. Roe, “Penetration testing for the Optical Probe for Regolith Analysis (OPRA),” *Adv. Sp. Res.*, vol. 46, no. 3, pp. 327–336, Aug. 2010.

[96] Y. Shen, X. Hou, Y. Qin, S. Jiang, and Z. Deng, “Shape of mole nose providing minimum axial resistance,” *Robot. Biomimetics*, vol. 1, no. 10, pp. 1–10, 2014.

[97] “Philae settles in dust-covered ice,” *Rosetta blog*, 2014. [Online]. Available: http://blogs.esa.int/rosetta/2014/11/18/philae-settles-in-dust-covered-ice/.

[98] J. J. Marlow, Z. Martins, and M. A. Sephton, “Mars on Earth: soil analogues for future Mars missions,” *Astron. Geophys.*, vol. 49, no. 2, pp. 20–23, 2008.

[99] D. S. McKay and J. D. Blacic, “Workshop on production and uses of simulated lunar materials,” in *Lunar and Planetary Institute*, 1991, pp. 1–83.

[100] K. Seiferlin, P. Ehrenfreund, J. Garry, K. Gunderson, E. Hütter, G. Kargl, A. Maturilli, and J. P. Merrison, “Simulating Martian regolith in the laboratory,” *Planet. Space Sci.*, vol. 56, no. 15, pp. 2009–2025, 2008.

[101] C. C. Allen, R. V Morris, D. J. Lindstrom, M. M. Lindstrom, and J. P. Lockwood, “JSC Mars-1: Martian regolith simulant,” in *28th Lunar and Planetary Conference*, 1997, p. 1797.

[102] L. W. Beegle, G. H. Peters, G. S. Mungas, G. H. Bearman, J. a. Smith, and R. C. Anderson, “Mojave Martian Simulant: A New Martian Soil Simulant,” *38th Lunar Planet. Sci. Conf.*, p. 2005, 2007.

[103] G. H. Peters, W. Abbey, G. H. Bearman, G. S. Mungas, J. A. Smith, R. C. Anderson, S. Douglas, and L. W. Beegle, “Mojave Mars simulant—Characterization of a new geologic Mars analog,” *Icarus*, vol. 197, no. 2, pp. 470–479, 2008.

[104] R. D. Holtz, W. D. Kovacs, and T. C. Sheahan, *An introduction to geotechnical engineering*. London, U.K.: Pearson, 1981.

[105] G. H. Heiken, D. T. Vaniman, and B. M. French, *The Lunar sourcebook: A user’s guide to the Moon*. Cambridge, U.K.: Cambridge University Press, 1991.

[106] ASTM, “ASTM D854-02 Standard Test Methods for Specific Gravity of Soil Solids by Water Pyncometer.” pp. 1–7, 2006.

[107] ASTM, “ASTM D4254-00 Standard Test Methods for Minimum Index Density and Unit Weight of Soils.” pp. 1–9, 2014.

[108] M. E. Möbius, B. E. Lauderdale, S. R. Nagel, and H. M. Jaeger, "Brazil-nut effect: Size separation of granular particles," *Nature*, vol. 414, no. 6861, p. 270, 2001.

[109] C. F. Harwood, "Powder segregation due to vibration," *Powder Technol.*, vol. 16, pp. 51–57, 1977.

[110] K. Head, *Manual of soil laboratory testing Volume 2: Permeability, Shear Strength and Compressibility Tests*. Plymouth, Devon, U.K.: Pentech Press, 1986.

[111] J. Briaud, *Geotechnical Engineering: Unsaturated and Saturated soils*. New York, New York: John Wiley & Sons, Inc., 2013.

[112] R. Thiel, "A technical note regarding interpretation of cohesion (or adhesion) and friction angle in direct shear tests," *Geosynthetics*, pp. 10–19, 2009.

[113] H. Perko and J. Nelson, "Mars Global Surveyor Soil Mechanics Data Analysis," in *Eighth International Conference on Engineering, Construction, Operation, and Business In Space; Fifth International Conference and Exposition and Demonstration on Robotics for Challenging Situations and Environments*, 2002.

[114] M. D. Bolton and M. W. Gui, "The Study of Relative Density Effects of Cone Penetration Tests in Centrifuge," Cambridge, U.K., 1993.

[115] T. D. Rossing, "Chladni's law for vibrating plates," *Am. J. Phys.*, vol. 50, no. 3, pp. 271–274, Mar. 1982.

[116] Y. Bar-Cohen, S. Sherrit, X. Bao, M. Badescu, J. Aldrich, and Z. Chang, "Subsurface sampler and sensors platform using the ultrasonic/sonic driller/corer (USDC)," in *SPIE Smart Structures and Materials Symposium*, 2007, pp. 1–8.

[117] Aalco, "Stainless Steel 1.4305 Bar." [Online]. Available: http://www.aalco.co.uk/datasheets/Stainless-Steel-14305-Bar_107.ashx.

[118] Aalco, "Aluminium Alloy 6082 T6-T651 Plate." [Online]. Available: http://www.aalco.co.uk/datasheets/Aluminium-Alloy- 6082-T6T651-Plate_148.ashx.

[119] J. J. W. A. van Loon and A. Dowson, "Large Diameter Centrifuge (LDC) Experimenter Users Manual," Noordwijk, The Netherlands, 2014.

[120] E. E. Ehrichs, H. M. Jaeger, G. S. Karczmar, J. B. Knight, V. Y. Kuperman, and S. R. Nagel, "Granular convection observed by magnetic resonance imaging.," *Science (80-.).*, vol. 267, no. 5204, pp. 1632–1634, 1995.

[121] E. Fukushima, "Nuclear Magnetic Resonance As a Tool," *Annu. Rev. Fluid Mech.*, vol. 31, pp. 95–123, 1999.

[122] C. Krause, M. Gehlen, A. Jaquemet, S. Heller, M. Sperl, and R. Willnecker,

"Penetration Experiments under Reduced Gravity," in *European Planetary Science Congress*, 2013, p. 1.

[123] E. A. Thomson, "Dig this: RoboClam," 2008. [Online]. Available: http://news.mit.edu/2008/roboclam-1125. [Accessed: 27-Feb-2017].